First- and Second-Principles Studies of Perovskites

A thesis presented to obtain the academic grade of *Doctor in Science*

by Michael Marcus Schmitt

September 2020

Jury Committee

Pr. Philippe Ghosez (Supervisor)	Université de Liège
Dr. Jean-Yves Raty (President)	Université de Liège
Dr. Eric Bousquet (Secretary)	Université de Liège
Dr. Bertrand Dupé	Université de Liège
Pr. Pablo García-Fernández	Universidad de Cantabria
Pr. Marta Gibert	Universität Zürich

Preface - Acknowledgements

If you want to make God laugh, tell him about your plans.

Wenn du Gott zum Lachen bringen willst, erzähle ihm von deinen Plänen.
Si tu veux faire rire Dieu, parle-lui de tes projets.

Blaise Pascal or Woody Allen

I heard the above quote for the first time in a German radio interview during the last weeks of writing this manuscript. It made me smile, as it softly and charmingly points out that there are much more things that we don't know than we do know when we make plans. And of course it fits well into this pandemic times that threw over a lot of things we thought to be unchangeable. I tried to figure out from who the quote stems. Sometimes (mostly in German) it gets attributed to the mathematician Blaise Pascal, and sometimes (mostly in other languages) to Woody Allen. Eventually, it made me reflect on my *PhD*-time that is now coming to an end. Everything started with a *plan*. Philippe and I wrote a doctoral project to apply for a FRS-FNRS FRIA grant that would guarantee financing over four years. I will forever be grateful to Philippe having supported me in this application after I declined several offers from his side for a *PhD* position and a year of personal crisis. Furthermore, I consider myself very lucky that the FRS-FNRS FRIA committee granted me this scholarship, which made this thesis possible.

Having received the scholarship I started to work enthusiastically on the project. Finally, after having defined a *plan* with a detailed working schedule for four years, nothing could go wrong... However, it took just a few months to work out that the mechanism that we hoped to be strong in our original proposal, is indeed very weak. Thus I'm afraid to say that not much of the original plan's proposal made it into the manuscript. On the other hand, this early set-back eventually turned my attention to much more fundamental questions and I'm happy if this manuscript can make a small contribution to a more unified understanding of metal-insulator transitions in perovskites.

I want to take this opportunity here to thank everybody who accompanied, motivated, and sometimes suffered with me along this path. First to my supervisor Philippe Ghosez whose incredible optimism will always fascinate me. Then to all colleagues of the Phythema group and the office corridor. To Alain, Jordan, Eric, Fabio, Antoine, Alireza, to have been always available for discussions, feedback, and restorative coffee and lunch brakes (that I may have detiorated sometimes, when I couldn't leave a problem behind in the office). To Yajun with whom I shared office for more than two years and who I admire for his braveness to come to Europe and start a family and his work ethic. To all other

colleagues with whom I crossed paths in Liege, Camillo, Karan Deep, Louis, Alam, He Xu, Danila, Alex, Sebastien. To Javier and Pablo, who welcomed me warmly for a research stay in the beautiful city of Santander. In great seminars I learned about the core concepts of pseudopotentials, the Berry phase, and much more. I'm grateful for the discussions with Pablo that introduced my to the Kugel-Khomskii model and the cooperative Jahn-Teller effect. I thank Yann who shared a lot of his great informatics knowledge. Finally, I learned that also in some regions of Spain it often rains. Last but not least, I'm grateful to all international friends I got to know at scientific conferences and doctoral schools. I think that the relative insignificance of national frontiers is one of the greatest assets of fundamental research.

Finally, I have to thank all other persons outside of science that make life worth living and thus equally helped me to finish this thesis manuscript. À touts mes amis wallons, je veux vous remercier en français. D'abord à mon grand amour Hélène qui j'ai trouvé par un coup de fortune a Liège et avec qui j'ai vécu la formidable aventure d'apporter quatre petits chiens dans ce monde. Dans les moments durs de l'écriture de ce manuscrit tu as souffert avec moi mais tu m'as jamais laissé craquer. À son père Albert Grailet qui nous a rendu des inestimables services pendant le lockdown et qui nous a permis de vivre dans une belle petite maison au cœur des hautes Ardennes dans laquelle ce manuscrit a été écrit au calme. À sa mère Marie-Pierre qui m'a tenu la morale quand ça n'allait pas. Je remercie tous les amis à Liège. Gaël, Mélanie, Olivier, Sarah, Daniela, Lucas et tous les amis de l'escalade. I thank all my friends in Germany and elsewhere that I do not see as often as I wished to. Tim, Johannes, Hannes and Ash, Kolja, Jenny, Annika, Stefan, Nicole and many more. Last I want to thank my family, my parents and my sister Julia for always being at my side. The older I get the more I realize that I started life from a privileged position and how hard my parents Franz-Josef and Christine worked to give me the best possible start to life.

A doctoral thesis is thought to be a personal project and it is only one name that is written on the cover, but in reality everybody that I mentioned contributed to it.

A last acknowledgement to somebody that I don't know personally goes to Federico Marotta who wrote the beautiful LaTeX template* on which this manuscript is based.

* https://github.com/fmarotta/kaobook

Abstract

The Metal-Insulator transition (MIT) upon cooling at elevated temperatures is a fascinating effect that is observed in some ABX_3 perovskite compounds with specific electronic configurations on the transition metal B cation d states. These compounds behave completely oppositional to ordinary metals who become better conductors upon cooling. At the MIT temperature these specific perovskite compounds show electron localization accompanied by cooperative lattice distortions that deform the BX_6 corner shared octahedral network. Since the discovery of these MITs, theoretical concepts about its origin have been proposed and debated. In this work we study from ab initio density functional theory (DFT) calculations $LaMnO_3$ and the alkaline earth ferrite series $AFeO_3$ who all have a formal d^4 occupation. As a basis to our discussion we introduce canonical notations, that were missing until now, for lattice distortions in perovskites that distort the X anion octahedra and are connected to MITs. While $LaMnO_3$ shows electron localization through orbital ordering - the appearance of a static order of Mn d orbital occupations-, $CaFeO_3$ shows electron localization through charge ordering - the appearance of a static order of formal Fe charges-. From DFT calculations we can show that both mechanisms are compatible with the concept of a *Peierls transition* and are enabled by octahedral rotations. From Monte-Carlo simulations we show furthermore that spin disorder in the paramagnetic phase is a key ingredient to explain the high MIT temperatures. Last we study the influence of external epitaxial strain on these compounds. Here, our canonical notations help to discriminate internal relaxations and external constraints. Our calculations show that in $LaMnO_3$ epitaxial strain alone can provoke a change from an *anti*ferromagnetic to an ferromagnetic order without the necessity of Oxygen vacancies as has been often speculated. In $CaFeO_3$ epitaxial strain can provoke a change from the bulk charge ordering MIT to an orbital ordering MIT, which explains the experimental finding of a strongly elevated MIT in $CaFeO_3$ thin films.

In the second part of this work, we present methodological developments for generating effective lattice potentials by a polynomial expansion that describe electronic potential energy surfaces in which atomic nuclei move. This is the so-called second-principles approach. The aim thereby is to replace the computational intensive self consistent DFT procedure by an lightweight evaluation of a polynomial depending on nuclear positions. If successful, this approach provides a mean to achieve a scale-transfer retaining the accuracy of ab initio calculations applicable to large scale systems with many thousand atoms and statistical simulations. In a proof of concept study we apply this approach to the perovskite $CaTiO_3$. The retained effective potential reproduces with good accuracy a number of ab initio quantities. Moreover, in the low to average temperature range (T<=1000K) the lattice dilatation of $CaTiO_3$ is well described. In the highest temperature range the effective potential deviates from the experimentally measured lattice dilatation and proposed phase transition sequence that is itself, however, debated. We conclude that the lattice dilatation properties can be refined by extending the lattice expansion and that a reexamination of the high temperature phase sequence of $CaTiO_3$ due the the information of our effective potential might be meaningful. Finally, we also highlight that there exists a strongly ferroelectric low energetic phase of $CaTiO_3$ whose stabilization through external constraints is part of ongoing research.

Résumé

La transition métal-isolant (MIT) lors du refroidissement à hautes températures est un effet fascinant observé dans certains composés perovskite ABX_3 pour des configurations électroniques spécifiques des états d du cation B qui fait partie des métaux de transition. Ces composés ont un comportement complètement opposé aux métaux ordinaires qui deviennent de meilleurs conducteurs lorsqu'ils sont refroidit. A la transition métal-isolant, ces composés perovskites spécifiques montrent une localisation électronique accompagnée d'une déformation collective de la maille via la déformation du réseau d'octaèdres BX_6 partagés aux coins. Depuis la découverte de ces transitions métal-isolant, différents/plusieurs concepts théoriques concernant leur origine ont été proposés et débattus. Dans cette étude, nous utilisons les calculs ab initio basés sur la théorie de la fonctionnelle de la densité (DFT for density functional theory) pour le composé $LaMnO_3$ et la série ferrites de terre alcalines $AFeO_3$ qui ont tous une occupation formelle d^4. Comme point de départ de notre discussion, nous introduisons des notations canoniques, jusqu'ici manquantes, pour définir les distorsions de réseaux dans les perovskites pour lesquelles les octaèdres d'anions X sont distordus et connectés à la transition métal-isolant. Alors que $LaMnO_3$ montre une localisation électronique au travers d'un ordre orbitalaire (apparition d'un ordre statique des occupations des orbitales d du Mn), $CaFeO_3$ quant à lui, montre une localisation électronique au travers d'un ordre de charge (apparition d'un ordre statique de charges formelle pour le Fe). Grâce aux calculs DFT, nous pouvons montrer que ces deux mécanismes sont compatibles avec le concept de *transition de Peierls* et sont rendus possibles par les rotations des octaèdres. De plus, les simulations Monte-Carlo montrent que le désordre de spin dans la phase paramagnétique est un primordial pour expliquer les hautes températures de ces transitions métal-isolant. Pour finir, l'influence de la déformation épitaxiale externe sur ces composés est étudiée. A cette occasion, nos notations canoniques servent à discerner les contraintes externes et les relaxations internes. Nos calculs montrent que la déformation épitaxiale de la maille de $LaMnO_3$ seule peut provoquer une transition d'un ordre *anti*ferromagnétique vers un ordre ferromagnétique sans nécessiter de lacune d'oxygène comme souvent suggéré. En comparaison, cette déformation épitaxiale de le maille dans $CaFeO_3$ massif peut provoquer un passage d'une transition métal-isolant en ordre de charge vers une transition en ordre orbitalaire, ce qui explique la découverte expérimentale de la transition métal-isolante à très hautes températures pour le film mince de $CaFeO_3$.

Dans la seconde partie de ce travail, nous présentons les développements méthodologiques pour générer des potentiels effectifs de réseaux qui décrivent les surfaces d'énergie potentielle électronique dans lesquelles les déplacements des noyaux atomiques sont décrits par un développement polynomiale. C'est ce que l'on nomme l'approche en second-principes. L'objectif, à cette étape, est de remplacer la procédure auto-cohérente de la DFT qui est gourmande en ressources de calculs par une évaluation peu coûteuse d'un polynôme qui ne dépend que des positions atomiques. Sous condition de réussite, cette approche fournit un moyen de réaliser un transfert d'échelle de la précision des calculs ab initio pour de grands systèmes avec des milliers d'atomes. Afin de valider cette approche, nous l'appliquons à la perovskite $CaTiO_3$. Le potentiel effectif obtenu reproduit avec une bonne précision plusieurs données ab initio. De plus, il décrit correctement la dilatation des paramètres de maille de ce $CaTiO_3$ pour une gamme de températures allant jusqu'à 1000K. Pour la région des plus hautes températures, le potentiel effectif dévie des mesures expérimentales de dilatation de réseau mais prédit une séquence de transitions de phase qui est source de débat. Nous concluons que les propriétés de dilatation thermique peuvent être raffinées en étendant le développement polynomiale et

qu'une réévaluation expérimentale de l'enchaînement des transitions de phase à hautes températures du $CaTiO_3$ pourrait mettre en évidence l'intêret prédictif du potentiel effectif. Finalement, nous mettons également en évidence le fait qu'il existe une phase fortement ferroélectrique à basse énergie pour $CaTiO_3$ dont la stabilisation aux travers de contraintes externes est un sujet de recherche encore non élucidé.

Contents

1 Introduction

The objective of the studies presented in this manuscript is to understand how properties of crystals are made up from interactions at the atomic scale. The tool for our studies is in its essence the fundamental equation of quantum mechanics: the time independent *Schrödinger equation*

$$H\Psi = E\Psi, \tag{1.1}$$

where H is the Hamilton operator that contains operators for kinetic and potential energy acting on particles described by a wave-function Ψ yielding a specific energy *eigenvalue* E. Upon its solution all properties of mater in a specific state associated to a specific energy E are defined. Sadly, solving this equation is in general very tough.

But to dive into this exciting subject let us start with the description of a crystal. A crystalline solid is at its heart a periodic arrangement of atoms. Fig. 1.1 shows a two dimensional example of a periodic arrangement of two types of atoms (red and black dots). To describe the atomic structure of a crystalline solid it is sufficient to find a cell that upon a translation of it itself, translates all atoms that it contains onto periodic images of themselves. This cell is called unit cell and the property is called translational invariance. If we have found a unit cell, the crystal structure is completely defined by the vectors that make up the unit cell and the position of the atoms within the unit cell, which is the so-called lattice motif. There is an infinite number of possible unit cells under the condition that we think about an idealized crystal that repeats itself until infinity. The smallest possible unit cell is called primitive cell and of special interest as it is the smallest volume which completely describes a crystal structure.

A direct consequence of the translational invariance of the atomic positions in a crystal is the translational invariance of all other local properties

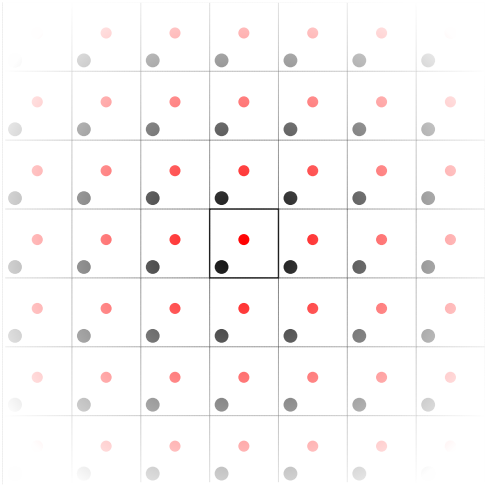

Figure 1.1: Schematic representation of a 2 dimensional crystal, which is a periodic arrangement of atoms represented by black and red dots that repeats until infinity. The crystal can be described by choosing a unit cell that upon a translation by its constituent vectors translates all atoms that it contains to periodic images of themselves. This property is called translational invariance.

as for example the electrostatic potential created by the atomic nuclei, local charge density, local magnetic- and local dipole-moments etc.. This insight leads directly to the theorem of *Felix Bloch* [1] who showed that the wave function of electrons moving in a periodic potential that solves the *time independent Schrödinger equation* must be of the form

$$\Psi(x) = u_k(x)e^{ikx}, \tag{1.2}$$

where $u_k(x)$ is a function that succumbs to the same periodicity as the crystal lattice, x is a positional vector in Cartesian space and k is the momentum vector of the electronic wave. The electronic wave function is thus a planar wave that is modulated by the periodicity of the crystal. Such planar wave functions are used in today's advanced computer programs that have been very successful in calculating approximations of electronic wave functions solving the time independent Schrödinger equation without any empirical input. Those methods are thus called *first-principles* or *ab initio* and we use them throughout this work.

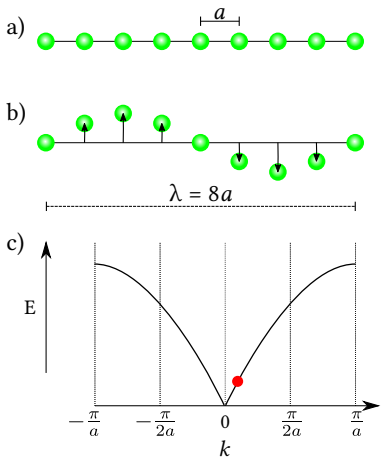

Figure 1.2: a) shows a monoatomic chain with equispaced atoms of distance a. b) shows a transversal wave of the atomic positions, a so-called phonon, in this monoatomic chain. c) shows the dispersion relation between the energy of the wave and the momentum vector $k = \frac{2\pi}{\lambda}$. The red dot marks the position of the phonon shown in b). All possible wavelengths are incorporated in the momentum vector range $[-\frac{\pi}{a}, +\frac{\pi}{a}]$, which is the first Brillouin zone in reciprocal space of the monoatomic equidistanced chain.

A second property that follows from the periodicity of a crystal is the possibility to perform Fourier analysis. The Fourier transformed space is called reciprocal space or momentum space as its variable is the momentum vector k and the unit is one over length. The equivalent of the unit cell in real space is the Brillouin zone in reciprocal space. An entity with a non zero momentum vector k in reciprocal space corresponds to a wave of wavelength $2\pi/k$ in real space. The application of such a wave to a crystal replaces the original periodicity by the wavelength and is associated with an energy. The relation between this energy and the momentum vector k is called dispersion relation. Any local property in a crystal can form waves that are described by their dispersion relation in the Brillouin zone. In this work we will be specifically interested in electronic waves that form the electronic band structure of a crystal and atomic displacement waves (see Fig. 1.2), so-called phonons, and their static interactions. I.e. how does the dispersion relation of the electronic waves change if a phonon distortion is applied to the crystal. We will see that in some crystals this interaction is the origin of an unusual transition from metallic to insulating behavior (metal-insulator transition: MIT) upon cooling at elevated temperatures (several hundred K). This MIT is completely opposite to the behavior of ordinary metals that show decreasing resistivity (a better metallic behavior) upon cooling.

Although, ab initio calculations have come a long way from being one of the most advanced calculation tools that only its inventors knew how to use to a quasi standard tool of solid state research today, they are computationally intensive and can thus only be applied to a limited set of problems restricted by the amount of atoms included. For this reason we attempt in the second part of our work to transform the results of ab initio calculations into light weight polynomial descriptions that can subsequently be used in larger simulations achieving a scale transfer. This approach is called second-principles and resembles in many ways machine learning techniques. Our main interest will be to describe the energy associated to atomic displacements in a crystal by this technique. In a proof of concept study we show its applicability to simulate the temperature dependence of average atomic positions in a crystal upon heating.

1.1 The Perovskite Materials Family

The crystals that we study in this work belong to the perovskite materials family. Perovskites are ternary compounds usually made up of two metallic cations A and B, and one anion X (very often oxygen O or fluorine F). The structures of all crystals belonging to this family are derived from the ideal perovskite structure. The primitive unit cell of the ideal perovskite structure is a cube defined by an edge length a. The lattice motif consist of the cation A sitting on the edge of the cube, the cation B at the center of the cube surrounded by an octahedra formed of the anions X sitting on the faces of the cube. The periodic repetition of this cell forms thus a network of X octahedra connected by their corners. The space group of this structure is $Pm\bar{3}m$ and composition formula is ABX_3. Besides silicon and similar technical relevant semiconductors, the perovskite materials family is most likely the most studied class of crystals in the last century. This interest by solid state scientists stems from the ability of the perovskite structure to accommodate almost any metal cation. Therefore, perovskites show almost any imaginable property that crystals can display and the structure is thus the perfect host to study how those different macroscopic properties originate from interactions at the atomic scale.

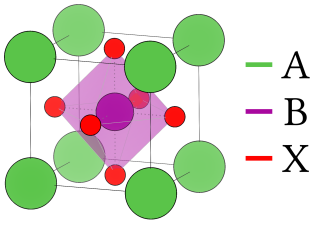

Figure 1.3: Cubic unit cell of the ideal perovskite structure of ternary compounds with space group $Pm\bar{3}m$.

1.1.1 Structure and Distortions

Although the perovskite materials family is very large only a small subsets of perovskites actually show the ideal cubic perovskite structure at ambient pressure and room temperature. On the contrary, most perovskites show some sort of slight deviation from the ideal perovskite structure that keeps the network of corner shared X octahedra in place. *Goldschmidt* [2] explained this deviations by seeing the constituent atoms as balls with given radii that touch each other. In this picture it is easy to derive that these balls form a cubic structure if the sum of the atomic radii that touch along the faces of the ideal perovskite cube equals the sum of the atomic radii that touch along the octahedral axis times square root of two. The ratio of those two quantities is known as the *Goldschmidt tolerance factor*

$$t = \frac{r_A + r_X}{\sqrt{2}(r_B + r_X)}, \tag{1.3}$$

where r_A,r_B, and r_X are the radii of the ions A, B, and X respectively.

If $t < 1$ the A atom is too small for the ideal cubic perovskite structure. The crystal typically compensates this misfit by cooperative rotations of the X anion octahedra. Thereby, the corner shared octahedral network leaves a freedom along the rotation axis. Octahedra in adjacent layers along the rotation axis can exhibit either the same (*in-phase rotation*) or opposite rotation direction (*anti-phase rotation*). Throughout this work we label the former one ϕ_α^+ and the latter one ϕ_α^- (See Fig. 1.4 b and c). The index α labels the axis around which the octahedra rotate. It takes the indices x, y, z referring to Cartesian directions parallel to the cubic axis of the undistorted perovskite (see Fig. 1.4 a). This octahedral rotations can appear simultaneously around different octahedral axis with different amplitudes. To label the character and amplitude of a distinct rotation pattern *Glazer* introduced a notation of the form $a^{+,-,0}b^{+,-,0}c^{+,-,0}$

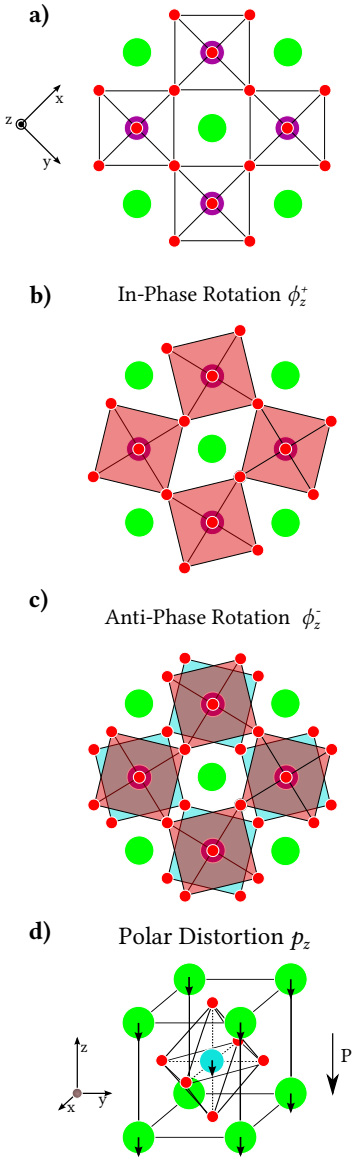

Figure 1.4: a) Top view on the cubic perovskite structure along the z-axis. b) In-phase rotation of the octahedra around the z axis labeled ϕ_z^+. Octahedra in adjacent layers in the z-direction rotate in the same direction. c) Out-of-phase rotation of the octahedra around the z axis labeled ϕ_z^-. Octahedra in adjacent layers in the z-direction rotate in the opposite direction. d) Polar displacement of A and B cations against the octahedral cage labeled p_z producing a dipole moment P.

[3]. There, a,b, and c label the amplitudes of rotations around the axis x, y, z and the superscripts $+, -, 0$ indicate in-phase, anti-phase or no rotation. From this notation *Glazer* identified 23 distinct rotation patterns. From those 23 the $a^-a^-c^+$ rotation pattern is adopted by most perovskites [4]. The $a^-a^-c^+$ rotation pattern leads to a reduction of the spacegroup symmetry from cubic $Pm\bar{3}m$ to orthorhombic $Pnma$ and triggers spontaneous orthorhombic strains that deform the cubic unit cell.

In perovskites with $t > 1$ it is the B cation that is too small to adopt the ideal perovskite structure. These perovskites adopt to the misfit often with a displacement of the cations along one or several Cartesian axes against the X anion octahedra. We label this distortion p_α (see Fig. 1.4 d). Similar to the octahedral rotations, in this label the index α takes the values x, y, z and shows the axis along the polar distortions takes place.

The distortion of a given perovskite with respect to the ideal cubic perovskite structure can be expressed in a atomic displacement field **u**

$$r_{i\alpha} = r^0_{i,\alpha} + u_{i,\alpha}, \tag{1.4}$$

where $r_{i\alpha}$ denotes the Cartesian component α of the position of atom i belonging to the lattice motif of the distorted perovskite and $r^0_{i\alpha}$ the same for the undistorted ideal cubic perovskite. It is consequently very useful to decompose the atomic displacement field **u** in terms of an orthonormal displacement basis ϵ_τ

$$|u\rangle = \sum_\tau \langle u|\epsilon_\tau\rangle \, |e_\tau\rangle = \sum_\tau A_\tau \, |\epsilon_\tau\rangle \,, \tag{1.5}$$

which allows to describe the distortion of a perovskite with respect to the ideal cubic structure by the distortion amplitudes A_τ of modes τ contained in the displacement field **u**. The minimal orthonormal basis is given by the decomposition of the space group of the ideal cubic perovskite structure into *irreducible representations* (irreps). The strain defined as the difference between the lattice vectors of the ideal cubic perovskite and the distorted phase can be decomposed in the same way. We will use this approach extensively in this work to study the influence of each individual orthonormal distortion onto properties that we calculate using ab initio techniques as for example the electronic dispersion relation or the stability of one magnetic order about another.

1.1.2 Properties: Chemistry and Size Effects

As we pointed out in the preceding section the structure of a perovskite is closely related to the size of the constituting atoms. Unsurprisingly, some macroscopic properties are in turn closely related to the structure. E.g. a perovskite with $t > 1$ that shows a local polar distortion exhibits macroscopic ferroelectric behavior, while a perovskite with $t < 1$ that shows local octahedral rotations doesn't show macroscopic ferroelectricity, since the rotations protect inversion symmetry*.

However, the size of atoms is not the only ingredient that determines the macroscopic properties of a perovskite. Especially for magnetic properties and the conductivity of a perovskite the size of the atoms is at first order completely irrelevant as those properties constitute themselves from the electronic structure. For those properties the detrimental ingredient is the number of unpaired electrons in the B atoms transition metal d shell, since those orbitals constitute the highest occupied states if they are occupied, and the lowest unoccupied ones if they are empty. In an isolated transition metal atom the d states are fivefold degenerate. If the transition metal atom is placed in the octahedral environment of the X anions in the perovskite structure, the fivefold degenerate d states are split by the cubic symmetry into three lower lying states with t_{2g} symmetry and two higher energetic states with e_g symmetry (see Fig. 1.5). The energy difference stems from the different electron densities associated to the t_{2g} and e_g states. While the t_{2g} states localize electrons between the transition metal $B - X$ bonds the e_g localize the electrons along the $B - X$ bonds. Therefore, the e_g states localize the electrons close to the density of the X p states and electrons in the e_g states experience a stronger Coulomb repulsion than the t_{2g} states. The energy splitting between the e_g and t_{2g} states is called crystal field splitting.

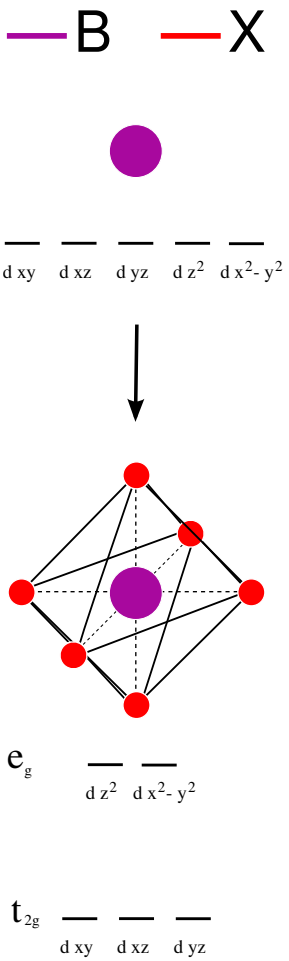

Figure 1.5: Top: Lone transition metal atom with spherical symmetry in which the d states are degenerate. Bottom: If the same transition metal atom is put in the center of an X octahedra as in the perovskite structure, the fivefold degeneracy of the d states is lifted by the reduction from spherical to cubic symmetry of the X anions. The five d states are split into three lower lying states with t_{2g} symmetry and two higher energetic states with e_g symmetry. The energy difference between both is called crystal field splitting.

An interesting example of how the properties change with the transition metal d filling can be given by comparing $BaTiO_3$ with an empty d shell (d^0), $BaVO_3$ with one electron in the d-shell (d^1), and $BaFeO_3$ with four electrons in the d shell (d^4). All three compounds have a similar Goldschmidt tolerance factor larger than one (between 1.06 and 1.08). However, $BaTiO_3$ is a prototypical wide band gap ferroelectric [5], $BaVO_3$ a paramagnetic metal [6], and $BaFeO_3$ is a metal showing complex spin-spiral structures [7]. While $BaTiO_3$ experiences significant distortions in the ferroelectric phases below 400K [5], $BaVO_3$ [6] and $BaFeO_3$ [7] stay cubic until the lowest temperatures.

In this work we will put a focus on perovskites having four electrons in the $3d$ shell. As we will see this electronic configuration is prone to a close connection between structural and electronic properties and most perovskites having this specific electronic configuration show metal-insulator transitions accompanied by structural distortions.

* For this reason the octahedral rotational distortions of the ideal cubic perovskite structure are also called *antiferrodistortive* (AFD).

Part I

Methodical Background

Introduction

In the following first chapters we introduce some formal background regarding the methods used in the calculation applications in this work. Specific parameters and settings within those methods are however mentioned in the appropriate results chapter. In chapter 2 we briefly introduce some methods that aim for a approximate solution of the stationary Schrödinger equation which are called *first-principles* or *ab initio*. From the approximate electronic density and derivatives of the energy *eigenvalue* many physical properties of solid state materials can be determined. We remain mainly qualitative with respect to those methods as no additional development has been contributed to those methods in the preparation of this manuscript, but have been used in studying the perovskite oxides $LaMnO_3$ and the ferrite series $AFeO_3$.
In chapter 3 we introduce the so-called *second-principles* technique that aims in its essence to reproduce first-principles quantities by a polynomial expansion. Here, we will be a bit more exhaustive as a central focus of this work has been to implement automatic procedures in the Multibinit software package to generate polynomial expansions capturing the important higher order contributions to the polynomial expansion of lattice degrees of freedom. Moreover, we introduce briefly in section 3.3 the polynomial expansion of one-body electronic interactions that is developed at the *University of Cantabria* and implemented in the Scale-Up software package. During a research stay at the *University of Cantabria* an interface between Multibinit and Scale-Up was developed that allows to create lightweight second-principles polynomial expansion including some relevant electronic degrees of freedom.

First-Principles Methods 2

The fundamental properties of matter in general and solid-state materials are determined by the interaction of the electrons and atomic nuclei they are made of. In the static limit those are described by the time independent Schrödinger equation

$$H\Psi = E\Psi, \tag{2.1}$$

where Ψ is the total (*many-body*) wave-function depending on the positions of nuclei and electrons, E is an energy eigenvalue, and H is the Hamilton operator containing the kinetic energy operator for the nuclei and the electrons as well as the potential energy operators between all charged particles (nuclei-nuclei,nuclei-electron, electron-electron). Unfortunately, there is no direct way to solve (2.1) for many particles. Therefore, approximations and numerical methods have been introduced to give approximate solutions. Such methods solely based on finding approximate solutions for Eq. (2.1) are called *first-principles* or *ab initio*. The first approximation is the Born-Oppenheimer approximation [8] that writes the total wave-function as a product of a nuclear wavefunction and an electronic wavefunction

$$\Psi(\mathbf{R}, \mathbf{r}) = \psi(\mathbf{R}, \mathbf{r})\chi(\mathbf{R}), \tag{2.2}$$

where $\mathbf{R}$ and $\mathbf{r}$ represent the complete sets of nuclear positions $\{R_I\}$ and electronic positions $\{r_i\}$, respectively. By assuming that there is one definite ground state for the electronic system[1] at a given positions of the nuclei $\mathbf{R}$, eq. (2.1) can be split into an electronic and a nuclear subsystem

$$H_e\psi(\mathbf{R}, \mathbf{r}) = \epsilon(\mathbf{R})\psi(\mathbf{R}, \mathbf{r}) \tag{2.3}$$
$$H_n\chi(\mathbf{R}) = E\chi(\mathbf{R}), \tag{2.4}$$

where H_e is the electronic Hamilton operator that contains the kinetic electronic energy and the Coulomb interactions between electrons, electrons and nuclei, and nuclei and nuclei

$$\begin{aligned} H_e =& -\frac{1}{2}\sum_{i=1,N_e}\nabla_i^2 + \frac{1}{2}\sum_{i\neq i'}\frac{1}{|r_i - r_{i'}|} - \sum_{i,I}\frac{Z_I}{|r_i - R_I|} + \frac{1}{2}\sum_{I\neq I}\frac{Z_I Z_{I'}}{|R_I - R_{I'}|} \\ =& T_e + V_{ee} + V_{en} + V_{nn}, \end{aligned} \tag{2.5}$$

and H_n is the Hamilton operator for the nuclei

$$\begin{aligned} H_n =& \sum_{I=1,N_n}\frac{-1}{2M_I}\nabla_I^2 + \epsilon(\mathbf{R}) \\ =& T_n + \epsilon(\mathbf{R}), \end{aligned} \tag{2.6}$$

where N_e and N_n are the number of electrons respectively nuclei contained in the problem, Z_I and M_I are the charge and the mass of nucleus I, and we have employed atomic units. The wave function of the electrons

1: Thereby, energy transfers between different electronic states are neglected. This is justified in the limit of a large energy difference between the electronic ground-state and the first excited state at a given set of nucleic position $\mathbf{R}$. Therefore, the Born-Oppenheimer approximation is also called adiabatic approximation since the entire energy is in the ground state.

and the energy eigenvalue $\epsilon(\mathbf{R})$ depend parametrically on the positions of the nuclei. $\epsilon(\mathbf{R})$ builds an effective potential of the electron in which the nuclei move and is called the Born-Oppenheimer potential energy surface (PES). Minimizing the potential energy of the electrons with respect to the nuclei's positions leads to the equilibrium structure for the nuclei. However, there is still no direct way to solve the reduced electronic subsystem due to the number of electrons in a solid ($N_e \sim 10^{23}$) and further approximations have to be introduced. One of the most successful method is *Density Functional Theory* (DFT). We give a brief introduction to DFT and associated methods used throughout the manuscript below.

2.1 Density Functional Theory

Walter Kohn together with *Pierre Hohenberg* [9], and *Walter Kohn* with *Lu Jeu Sham* [10] laid down in the 1960s the theoretical foundation of DFT. The first work showed that the energy and all associated fundamental properties of the electronic ground state are a functional of the electronic ground state density. The second work showed that the electronic density of the interacting electrons can in principle exactly be reproduced by a fictitious non-interacting particle system moving in an effective potential that depends on the density of the non-interacting system. Through the second work a self-consistent solution of the many-body electronic problem through the non-interacting system was shown. The density of the fictitious system is given by the sum of the density of the single-body wave functions of the non interacting particles

$$n(r) = \sum_{i=1,N_{occ}} \left|\phi_i(r)\right|^2, \tag{2.7}$$

where N_{occ} is the number of occupied states and ϕ_i are the one particle wave functions (also called *Kohn-Sham orbitals*) that have to fulfill the orthonormality constraint

$$\delta_{ij} = \left\langle \phi_i \middle| \phi_j \right\rangle . \tag{2.8}$$

The total ground state energy of the independent particle system can be calculated by the minimization of the following equation with respect to the Kohn-Sham orbitals

$$E[\phi_i] = \sum_{i}^{N_{occ}} \left\langle \phi_i \middle| T + V_{en} \middle| \phi_i \right\rangle + \frac{1}{2} \int \frac{n(r)n(r')}{|r - r'|} dr dr' + E_{XC}[n(r)], \tag{2.9}$$

where the first term gives the kinetic and potential energy of the electrons moving in the field of the ions, the second term gives the Coulomb interaction of the electronic density (also called Hartree energy:E_H) and the last term captures exchange and correlation effects between the electrons. Using the Lagrange multiplier method, the orthonormality constraint (2.8) can be imposed upon minimization of

$$F[\phi_i] = E[\phi_i] - \sum_{ij}^{N_{occ}} \Lambda_{ij} (\left\langle \phi_i \middle| \phi_j \right\rangle - \delta_{ij}), \tag{2.10}$$

with Λ_{ij} the Lagrange multipliers. The associated Euler-Lagrange equation is

$$H\left|\phi_i\right\rangle = \Lambda_{ij}\left|\phi_j\right\rangle \tag{2.11}$$

with the Hamiltonian being

$$H = T + V_{en} + V_H + V_{XC}, \tag{2.12}$$

where T is the kinetic enrgy operator, V_{en} is the electron-nuclei potential, V_H the Hartree and V_{XC} the exchange-correlation potential. The Hamiltonian and the ground state density are determined through a self consistent procedure starting from a given density, since the exchange correlation potential and the Hartree potential itself depend on the particle density

$$V_H = \frac{\partial E_H}{\partial n(r)}; V_{XC} = \frac{\partial E_{XC}}{\partial n(r)}. \tag{2.13}$$

There is no unique solution of Eq. (2.11) as a unitary transformation can be applied to the wavefunctions

$$\left|\phi_i\right\rangle \rightarrow \sum_j^{N_{occ}} U_{ij}\left|\phi_j\right\rangle, \tag{2.14}$$

that leaves the density or energy invariant. This freedom is called a *gauge transformation*. Due to the Hermetian property of the Hamilton operator the gauge can be fixed to the diagonal gauge, where the Lagrange multiplier matrix becomes diagonal

$$\lambda_{ij} = \left\langle\phi_i\middle|H\middle|\phi_j\right\rangle = \epsilon_i\delta_{ij}. \tag{2.15}$$

The self-consistent solution of eq. (2.9) would provide the exact ground-state energy and density of the *true* interacting electron system if all terms were known. Unfortunately, there is no known way to calculate the exchange-correlation part. Hence, approximations are introduced. The most basic and widely used one is the *Local-Density-Approximation* (LDA) [11, 12] that estimates the exchange-correlation energy by locally evaluating the exchange correlation energy of the homogeneous electron gas

$$E_{XC}^{LDA} = \int n(r)\epsilon_{xc}^{hom}[n(r)]dr, \tag{2.16}$$

where ϵ_{xc}^{hom} contains the exchange and correlation energies of the homogeneous electron gas. The exchange part is known analytically and the correlation part parameterized to the results of Monte-Carlo simulations [13]. Further, there exist a vast amount of formulations of the E_{XC} with increasing complexity taking into account local gradients of the electronic density (*generalized gradient approximation* - GGA) and even further the local gradients plus kinetic energy of the non-interacting Kohn-Sham particles (*meta-GGA*). One of the reasons of the successes of DFT can be attributed to the fact that the simple LDA and GGA approximations work surprisingly well. However, for electronic states that are strongly localized (in general occupations of d and f orbitals) the LDA and GGA formalisms underestimate the electronic correlation between localized states.

To improve the description of localized states corrections are introduced

that evaluate the local occupation and calculate additional associated exact exchange or an associated local correlation corrections (the so-called +U method that we describe briefly below). Functionals that include some degree of exact-exchange are called hybrid-functionals. The basis functions to solve Eq. (2.11) can be separated into two categories. Local atomic centered functions representing the atomic orbitals (Gaussians or Numerical Atomical Orbitals) or a Fourier expansion of plane-waves that we use throughout this manuscript

$$\phi_{n,\mathbf{k}}(\mathbf{r}) = \frac{1}{\sqrt{\Omega}} \sum_{G} C_{n,\mathbf{k}}(\mathbf{G}) e^{i(\mathbf{k}+\mathbf{G})\mathbf{r}}, \tag{2.17}$$

where n is the band index, $\mathbf{k}$ a wavevector, $\mathbf{G}$ a vector of the reciprocal space of the studied system, $\mathbf{r}$ the position vector in real-space, and Ω the unit-cell volume. The Fourier expansion of plane waves is especially appropriate for periodic solids through its numerical representations of Bloch-Functions [1]. The summation over reciprocal space vectors is in principle infinite, but is practically cut at some energy

$$E_{Cut} \geq \frac{\hbar^2}{2m_e} |\mathbf{k} + \mathbf{G}|^2. \tag{2.18}$$

In practice convergence studies have to be performed to ensure the convergence of the energy (Eq. (2.9)) with respect to E_{Cut}. To limit the number of plane waves to include in the expansion in Eq. (2.17) pseudopotential methods have been developed that include some of the core electrons into the potential of the nucleus. The physical justification of this simplification lies in the presumption that the core electrons show almost no interaction with electrons of neighboring atoms so that their state closely resembles the state of the isolated atom. Thereupon, they should not contribute to the physical properties of the molecule or material and are *frozen* in the core.

Two popular pseudopotential methods are used in this work. The *norm-conserving* pseudopotentials [14] and the *projector augmented wave* (PAW) method [15]. The construction of norm-conserving pseudopotentials starts from an all-electron (AE) DFT calculation of the isolated atom in question. The pseudopotential is then constructed under the constraint that the wave function of a valence state is outside of a core radius precisely the same as for the AE calculation. Inside the core region the AE wave-function is replaced by a smoothly varying function (without nodes) that keeps the norm of the AE-function. In the PAW method the plane wave Fourier expansion resulting from a pseudopotential calculation is augmented in a sphere around the atom by the projection of the plane waves to the AE wave functions containing all the nodes of states with higher principal quantum numbers that are dismissed in the pure norm-conserving approach.

2.2 The +U correction

As mentioned above, conventional DFT methods with E_{XC} functionals based only on the evaluation of the electronic density fail to correctly predict electronic properties especially for materials with open shell electronic d and f states (which are often called *strongly correlated*). It is especially well-known that GGA and LDA functionals fail to correctly predict electronic band gaps and sometimes predict *strongly correlated* materials to be metallic while they are experimentally found to be insulators (e.g. in transition metal monoxides [16]). A popular correction to this problem is the $+U$ method [17–20] that adds an additional correlation energy - the Hubbard or "U" term - to the occupation of the strongly correlated states. Furthermore, a double-counting term is subtracted, to account for the correlation energy that has already been included in the DFT energy. The abstract formulation of the total energy within the $DFT + U$ realm thus is

$$E_{DFT+U} = E_{DFT}[n(\mathbf{r})] + E_{Hub}(n^{I\sigma}_{m,m'}) - E_{DC}(n^{I\sigma}), \tag{2.19}$$

where E_{DFT} is the uncorrected DFT energy, E_{DC} is the double-counting energy, and E_{Hub} is the Hubbard U correction depending on the occupation matrix $n^{I\sigma}_{m,m'}$, where I is the space of correlated orbitals (e.g. the $3d$ states), m and m' denote states with different angular momentum in that space and σ denotes the spin. The occupation matrix can be calculated by the projection of the Kohn-Sham orbitals on the states of the localized manifold

$$n^{I\sigma}_{m,m'} = \sum_{\mathbf{k},n} f^{\sigma}_{\mathbf{k}n} \left\langle \phi^{\sigma}_{\mathbf{k}n} \middle| \Phi^{I}_{m'} \right\rangle \left\langle \Phi^{I}_{m} \middle| \phi^{\sigma}_{\mathbf{k}n} \right\rangle , \tag{2.20}$$

where $\phi_{\mathbf{k}n}$ is the Kohn-Sham orbital of band n at the wavevector $\mathbf{k}$, $f_{\mathbf{k}n}$ is the occupation number of that orbital, and Φ^{I}_{m} is the atomic wavefunction of the correlated state on which the Hubbard correction is applied. Within the PAW method the occupation numbers are readily available trough the augmentation part of the total Kohn-Sham wave function. There exist different formulations of the Hubbard correction and double-counting terms. Since there is no diagrammatic expression of the DFT energy, there is especially no unique definition of E_{DC}, which is modeled through a mean field approximation [21]. The $+U$ correction is hence often used as semi-empirical correction to the DFT energy, where different values of the parameters that appear in the Hubbard and double-counting expression are tested with respect to experimental results. While this semi-empirical approach is sometimes criticized, it could be said that the use of most exchange correlation functionals is justified by semi-empirical testing. Nonetheless, there are methods for a *self-consistent* calculation of U parameter that scales the electronic correlation (See ref. [22] and ref. [21] and references therein). Within this work we use the rotational invariant formulation of the *Hubbard U* correction introduced by *Liechtenstein* et al. [18] in our calculations of $LaMnO_3$ and $CaFeO_3$. Therein, two parameters occur that we tune empirically: The Hubbard U scaling the electronic correlations, and in the double-counting a Hund's like J.

2.3 Density Functional Perturbation Theory

A range of properties of materials can be determined as derivatives of the total energy. From perturbation theory the total energy of a system under a perturbation λ can be expressed in a power series around the energy of a reference

$$E(\lambda) = E^0 + \sum_i \left.\frac{\partial E}{\partial \lambda_i}\right|_0 \lambda_i + \sum_{i,j} \left.\frac{\partial^2 E}{\partial \lambda_i \partial \lambda_j}\right|_0 \lambda_i \lambda_j + \ldots, \tag{2.21}$$

that we cut here at second order.

Table 2.1: Overview of physical quantities related to first- and second-order derivatives of the total energy accessible on the first-principles level through DFPT. The perturbation parameter λ takes the values of an atomic displacement u, a homogeneous strain η, or an electric field $\mathscr{E}$.

λ	1st Order	2nd Order		
		u	η	$\mathscr{E}$
u	F	C	Λ	Z^*
η	σ	Λ	c	e^0
$\mathscr{E}$	P	Z^*	e^0	ϵ^∞

The application of perturbation theory within DFT is called *Density Functional Perturbation Theory* (DFPT). *Gonze* and coworkers showed how to accurately calculate the derivatives appearing in the perturbative expansion with first-principles techniques [23–27]. Therein, the $2N$ theorem for even perturbations and $2N+1$ theorem for odd perturbations shows that through the knowledge of the Nth wavefunction the $2Nth$ respectively $2Nth+1$ energy derivative can be calculated. Today accessing second-order and some third-order derivatives through DFPT calculations is state of the art and implemented in the Abinit software package. Typical perturbations of interest are atomic displacements u, homogeneous strain η, and an static external electric field $\mathscr{E}$. Tab. 2.1 shows the physical quantities given by first- and second-order energy derivatives with respect to those perturbations. At first order, the atomic displacement derivative results in the forces on the atoms F, the derivative of η is the stress tensor acting on the unit-cell σ, and the derivative with respect to $\mathscr{E}$ gives the spontaneous-polarization vector P of the investigated structure. The second-order derivatives give the linear response of the solid to the external perturbations. The second-order derivative with respect to u gives the interatomic force constants matrix C, the second-order derivative with respect to η gives the elastic tensor c, and the second-order derivative with respect $\mathscr{E}$ the electronic dielectric constant at fixed atomic positions ϵ^∞. The mixed derivative with respect to u and η gives the internal strain-displacement coupling Λ that characterizes the forces on the atoms under a given strain state and vice versa, the mixed derivative with respect to u and $\mathscr{E}$ the Born-Effective charges Z^* that characterize the polarization induced by a given displacement and the forces induced on the atoms by the application of an external electric field, and the mixed derivative with respect to η and $\mathscr{E}$ gives the piezoelectric tensor at fixed atomic positions e^0 that characterize the polarization induced by a given strain and vice versa. Within our work the DFPT quantities at second-order serve as a starting point of higher order polynomial development of the total energy with respect to atomic displacements u and homogeneous strain η, which is called the *second-principles* approach and explained in the next chapter. The philosophy of this development is however somewhat different from the perturbative approach that is mainly interested in finding the derivatives that are valid for small perturbations around the reference, because we will seek to describe a whole potential energy surface including somewhat large perturbations through the polynomial.

Second-Principles Approach: Polynomial Representation of First-Principles Data

3

Significant advances in calculation power over the last 20 years and the ever increasing availability of calculation resources have made ab initio calculations more and more affordable. This development has been so successful that ab initio calculations have not only been one of the most growing research method in condensed matter physics and physical chemistry but also in science overall [28]. A result of this development is a huge amount of ab initio data that is being produced non-systematically in individual studies or systematically and collected in impressive data bases like the *materials project* [29]. However, the number of atoms that can be considered in a practical state-of-the-art everyday use case is still limited to few tens to a few hundred*. Hence, studying objects away from the purely atomic scale as domains, interfaces, or polarons is a time intensive task from an ab initio point of view. Furthermore, the study of thermodynamical properties through ab-initio molecular dynamics simulations are still today rather limited, since for significant statistical averages many thousand atoms and lattice configurations have to be calculated.

It was therefore early on conceived that it is desirable to transfer the results of ab initio calculations into a lightweight mathematical representation whose evaluation is much cheaper than performing a self-consistent density functional theory cycle at a given nuclear configuration. Such mathematical representations are generally called effective models and rely on different mathematical formulations to represent a potential energy surface (PES) that is calculated by a ab initio method. The common ground of different approaches is that the electronic problem is integrated out, such that no explicit calculation of the electronic structure is needed, but their effect is captured in *effective parameters* that build the *effective potential*. Then, to perform lattice dynamical simulation only the nuclear positional degrees of freedom are treated in a classical or stochastical way.

The most popular form of such effective potentials are chemically motivated and try to reproduce pairwise atomic interactions in the form of Lennard-Jones potentials [32], reactive force-fields [33, 34], bond-valence models [35, 36], shell models [37, 38] and others. All these approaches have in common that the total energy of a system is defined by a sum of local atomic energies that depend on the local environment. As such these models are not limited to a certain bond-topology or symmetry. Hence, they can be applied to phase-transitions in which the bond topology is

* One should mention that DFT implementations based on local basis sets as numerical atomic orbitals used in SIESTA [30] or Gaussian orbitals used e.g. in CRYSTAL [31] have led to ab initio studies with several thousand or ten thousands of atoms. However, even those very efficient DFT implementations demand large computational facilities (several thousand cores) to perform such large scale calculations and are not considered *standard* here. Moreover, they are still not capable of calculating rapidly thousands of different lattice configurations with a few thousand atoms, which is what we try to achieve with the second-principles approach.

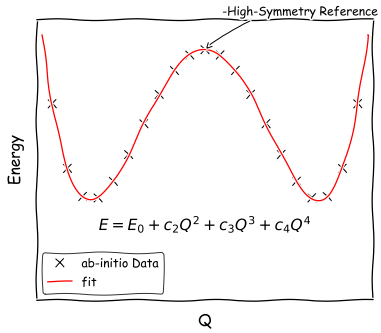

Figure 3.1: The central idea of effective Hamiltonian method and the second-principals approach is to represent ab initio data points (crosses) by a fitted polynomial expansion (red line). Here shown the ab initio energy in dependence of an arbitrary parameter Q. The fit is performed around a reference Q_0 with energy E_0, which has the property a zero gradient with respect to Q. Within this work Q will typically be a variable describing a lattice distortion, but principally it could be any other order-parameter. Also, the fitted quantity can be any other than the energy as forces on atoms or electronic quantities.

lost (e.g. a solid to liquid transition) or used to try to estimate reaction barriers or complex interactions of molecules with surfaces [34].

Another less widely used approach also developed in the 1990s was to integrate out not only the electronic degrees of freedom, but also all lattice degrees of freedom irrelevant to a given solid-to-solid phase transition. Then, the PES of the relevant degrees of freedom (the order parameter of the phase transition) has been expressed in a Taylor like polynomial expansion around a reference, which corresponds to a high symmetry structure before the phase transition. This approach is called the *effective Hamiltonian method*. Its principal idea is illustrated in Fig. 3.1. It has been almost exclusively but very successfully applied to ferroelectric phase transitions in the perovskite structure (see e.g. references [39–43]), where the order parameters are a polar distortions and spontaneous lattice strains. While the effective Hamiltonian method is inherently much more restricted than aforementioned force field methods its advantage lies in its clear connection to the Ginzburg-Landau theory of phase transition.

Recently, there has been an effort - branded the second-principles approach - to generalize the effective Hamiltonian method to describe all lattice degrees of freedom [44, 45] and to extend the approach of a polynomial expansion to electronic quantities as the one electron interaction parameters in and effective Mott-Hubbard model [46]. This push has led to development of the Scale-Up and Multibinit software packages. Due to the underlying Taylor like polynomial expansion the second-principles approach can only treat somewhat small deviations of the reference structure, which means in practice that the bond-topology around a phase transition needs to be preserved. Moreover, it relies on a periodic repetition of the reference unit cell in its current implementation. This means that only single crystal structures can be simulated. The second-principles approach is thus more restricted than aforementioned force-fields. However, this approach seems very suited for the perovskite materials class, where many crystal phases with different space-group symmetry but the same bond topology compete with only small energy differences between them. As we show, the method is, in contrast to the force-fields relying on empirical pair-wise interactions, well defined and expandable and the most important goal of the recent push is to provide a software for the automatic generation of second-principles models from ab initio data.

The chapter is organized as follows. The first part introduces the Multibinit software package, the second describes the polynomial expansion of lattice degrees of freedom around a reference structure, and the third the polynomial expansion of lattice-electronic interactions.

A large part of the work performed in preparation of this manuscript has been devoted to further develop the existing implementations in Multibinit. Besides many miscellaneous improvements, the biggest efforts were a reviewing, reorganization, and parallelization of the symmetry reduction of anharmonic polynomial coefficients (see section 3.2.3) and the addition of an automized bounding approach (see section 3.2.5). Moreover, an interface between the lattice effective part of Multibinit and the electronic part of Scale-Up has been set up during a research stay at the University of Cantabria (see section 3.3.2).

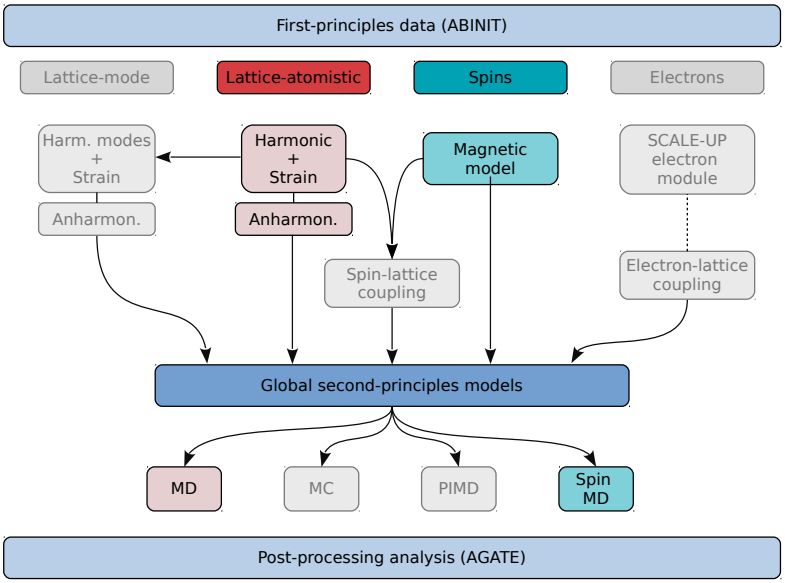

Figure 3.2: Overview of the Multibinit Project. Colored parts are available in the distributed package. Grey pats are under development. Figure taken from [47].

3.1 The Multibinit Project

Multibinit is a software package that aims to be an integrated tool for generating and utilizing second-principles models - i.e. polynomial expansions - of different degrees of freedom to enable large simulations up to a few 100.000 atoms. It is released within the Abinit software package [47]. Multibinit closely integrates in the Abinit eco-systems by utilizing the results of ab initio DFT and DFPT calculations performed by Abinit to create second-principles models. Fig. 3.2 shows the current status of the project with available functionalities and those currently under development. The first completed implementation is the creation of harmonic and anharmonic atomistic lattice models that recover all lattice degrees of freedom. The harmonic part is thereby directly extracted from DFPT calculations produced by Abinit and stored in the *derivative database format* (ddb). The anharmonic part is fitted to first principle data provided in the *_HIST.nc netCDF* format used by Abinit to store energy forces at given lattice configurations. Currently under development is an option to restrict the lattice model to a subspace of lattice one or multiple Wannier functions (Lattice Mode in 3.2) and recover the effective Hamiltonian method with scalable dimensionality. The second completed part is the automated construction of an effective Heisenberg like spin Hamiltonian including magnetic exchange Dzaloshinskii Moriya [48], single ion anisotropy and dipole-dipole interactions. In the near future it is aimed to combine the lattice atomistic and spin parts to create spin-lattice coupled models. Finally, the SCALE-UP electronic module provides a way to create effective electronic models by including some electronic states in a Mott like tight binding Hamiltonian in a Wannier basis extracted from ab initio data including electron lattice coupling of the tight binding elements. A basic modular design common to all degrees of freedom was put in place inside Multibinit to guarantee extensibility. All models are stored in common datatype *.xml* format.

For the finite temperature simulations of the lattice degrees of freedom the molecular dynamic (MD) implementations of Abinit can be used.

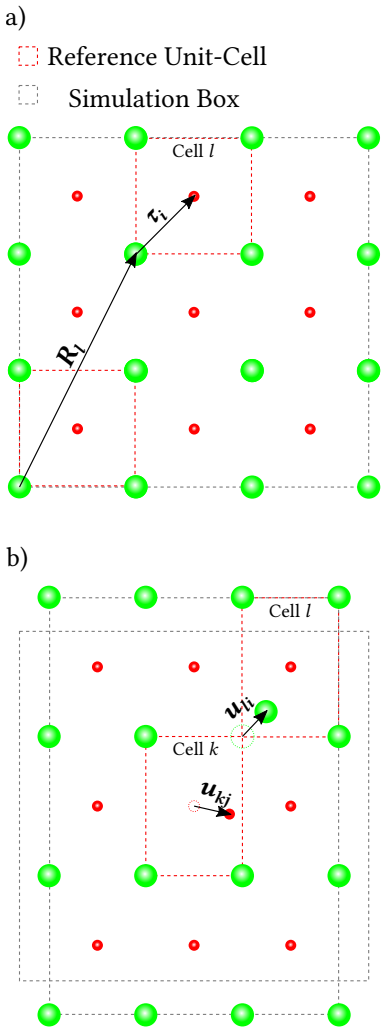

Figure 3.3: a) Illustration of the reference structure. The simulation box is made of repetitions of the Reference structure unit cell. The position of a general atom i in cell l within the reference structure is found by the sum of the vector to the origin of cell l $\mathbf{R_l}$ and the lattice motif vector of atom i $\tau_\mathbf{i}$. b) General deviations from the reference structure. Homogeneous lattice strain η acting on the simulation box shape (the original shape is drawn for clarity) and two local displacement vectors of $\mathbf{u_{li}}$ and $\mathbf{u_{kj}}$ of atoms i and j located in cells l and k.

Moreover, the lattice relaxation algorithms available in ABINIT can be used to relax large scale lattice structures (domain-walls, interfaces etc.). Finally, we also implemented a hybrid molecular dynamics Monte-Carlo approach (HMC) [49] using an isothermal/isoenthalpic molecular dynamics algorithm [50] (readily implemented in ABINIT) to generate new steps in the Markov Chain.

Post-processing and visualization is ensured by the AGATE tool developed by *Jordan Bieder* [51] that is interfaced with a number of file formats provided by ABINIT and MULTIBINIT. Its main features are the visualization of lattice or spin dynamics and their analyses by the calculation of mean square displacements, velocity autocorrelation functions, pair distribution function, projection of general lattice structures on phonon modes, visualization of the evolution of temperature, pressure, lattice constants and other properties.

Within the preparation of the manuscript we worked extensively on the lattice atomistic model part and the interface between MULTIBINIT and *Scale-UP* as summarized below.

3.2 Polynomial Expansion of Lattice Degrees of Freedom

The first step of constructing a second-principles effective lattice model is the choice of a reference structure around which we develop a polynomial expansion in all lattice and strain degrees freedom. This reference has to be a stationary point of the PES where all gradients vanish. Depending on the aim of the model the appropriate reference might be a local minimum or a local maximum. If the goal of the model is to describe and study the anharmonicity of a given phase the preferred choice of the reference structure would be the local minimum of that phase. If, however, the goal is to describe phase transitions, competition between phases or domain structures the choice of the reference should be a local maximum and is typically a common high-symmetry structure of different lower symmetry phases. In any case the total energy of the model can be split in the energy E^0 of the reference configuration R^0 and the energy of the effective polynomial E_{eff} that depends on the general set of position of the atoms in the crystal $\mathbf{R}$

$$E_{tot}(\mathbf{R}) = E_0(\mathbf{R^0}) + E_{eff}(\mathbf{R}). \tag{3.1}$$

In the second-principles approach it is convenient to see a material as periodic repetition of the reference structure's unit cell. The reference position of an individual atom i of the repetition of the references lattice motive in cell l and the Cartesian direction α can be written as

$$R^0_{li\alpha} = R_{l\alpha} + \tau_{i\alpha}, \tag{3.2}$$

where $R_{l\alpha}$ is the Cartesian component α of the vector pointing to the origin of the unit cell l inside the simulation box and $\tau_{i\alpha}$ is the α component of the position of the atom i inside cell l (see also Figure 3.3). Then, an individual entry of the set of general positions of an atom in the

simulation box is defined by its deviation of the reference structure

$$R_{li\alpha} = \sum_{\beta=1}^{3}(\delta_{\alpha\beta} + \eta_{\alpha\beta})R^0_{li\beta} + u_{li\alpha}, \tag{3.3}$$

where the deviating entities are η the homogeneous strain tensor acting on the shape of the simulation box and $\mathbf{u_{li}}$ the displacement vector of atom i in cell l (see also Figure 3.3). Since we develop a polynomial in terms of the difference of the reference structure, E_{eff} depends on η and the set of atomic displacements vectors contained in the simulation box $\{\mathbf{u}\}$. Further, it will be useful to split E_{eff} into harmonic and higher-order anharmonic parts

$$E_{eff}(\{\mathbf{u}\}, \eta) = E_{Har}(\{\mathbf{u}\}, \eta) + E_{Anh}(\{\mathbf{u}\}, \eta). \tag{3.4}$$

In the following two sections we will describe all contributions to $E_{Har}(\{\mathbf{u}\}, \eta)$ and $E_{Anh}(\{\mathbf{u}\}, \eta)$ and their peculiarities. The parameters entering E_{har} will be extracted from common DFPT calculations done with the Abinit software package, while all coefficients in E_{Anh} will be fitted by Multibinit so that E_{eff} reproduces the energy, forces of stresses resulting ab initio calculations on a given set of nuclear configurations, which we call the training set (TS).

3.2.1 Harmonic Contributions

In this section we describe all the contributions to the harmonic energy of the effective potential. It is natural to split the harmonic energy into three terms separating the atomic displacement and the strain variables

$$E_{Har}(\{\mathbf{u}\}, \eta) = E^P_{Har}(\{\mathbf{u}\}) + E^S_{Har}(\eta) + E^{SP}_{Har}(\{\mathbf{u}\}, \eta), \tag{3.5}$$

where E^P_{Har} is the phonon contribution that only depends on atomic displacements in the simulation box, E^S_{Har} is the strain part that only depends on the homogeneous strain deformation of the simulation box, and E^{SP}_{Har} is the strain-phonon part that couples strain and atomic displacements. The harmonic phononic contribution is directly related to the interatomic force constant matrix C, that is the second derivative of the total energy with respect to the atomic displacement around the reference structure R^0

$$C_{i\alpha j\beta}(a, b) = \left.\frac{\partial^2 E^{DFT}_{tot}}{\partial u_{ai\alpha}\partial u_{bj\beta}}\right|_{R^0}, \tag{3.6}$$

where i, j denote atoms in cells (a, b), α, β denote the Cartesian directions, and E^{DFT}_{tot} denotes the total ab initio energy. Then, the exact harmonic energy becomes

$$E^P_{Har} = \frac{1}{2}\sum_{i\in SC}\sum_{\alpha=1}^{3}\sum_{b=1}^{\infty}\sum_{j\in SC}\sum_{\beta=1}^{3} C_{i\alpha j\beta}(0, b)u_{0i\alpha}u_{bj\beta}, \tag{3.7}$$

where the factor $\frac{1}{2}$ takes into account the double counting and SC indicates the sum over all atoms in the simulation box. The index b indicates periodic repetitions of the simulation box until infinity. It should be

noted that the index b is different from index l used in equations Eq. (3.2) and Eq. (3.3) that refers to the reference unit cell. In Eq. (3.7) we mapped the indexes l and i from Eq. (3.2) onto on single index i to denote all atoms that are inside the simulation box. The interatomic force constants can be trivially calculated from standard DFPT or finite differences calculations. The range of the force constant matrix C is directly determined by the density of the q-point mesh respectively the supercell size in such calculations. Practically it is limited to a few reference unit cells (typically <= 10). However, if the reference structure is an insulator, long-ranging atomic interactions created by electronic dipoles upon displacements can be analytically calculated beyond the supercell size or q-point density of the initial calculation. This approach let us split the interatomic force constant matrix in a short-range (SR) and a dipole-dipole (DD) part,

$$C_{i\alpha j\beta}(a,b) \approx C^{SR}_{i\alpha j\beta}(a,b) + C^{DD}_{i\alpha j\beta}(a,b), \tag{3.8}$$

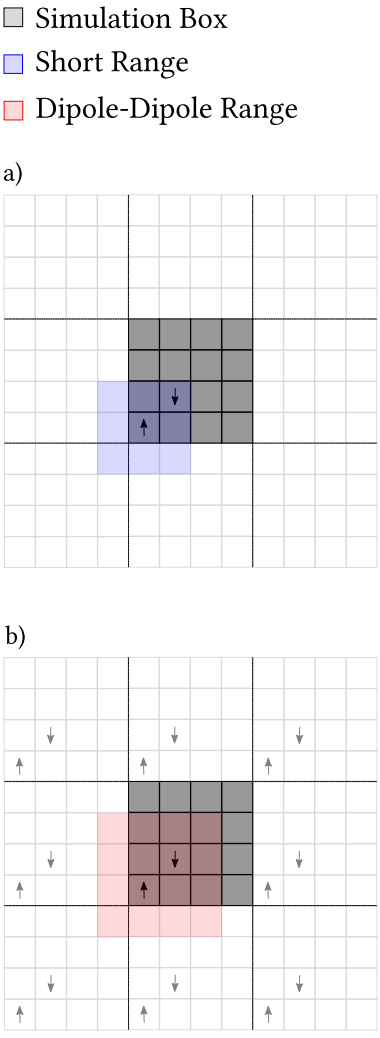

Figure 3.4: Illustration of different harmonic atomic displacement interaction ranges of the second-principles implementation in MULTIBINIT. In grey the simulation box and in transparent its periodic replicas around. a) Illustration of the harmonic short range interaction (blue box). b) Illustration of dipole-dipole interaction. The interaction of two atoms and their periodic replica until infinity (shaded arrows) is mapped onto one single interaction (bold arrows). The size of the dipole-dipole interaction box (red box) is always the same as the simulation box.

where the SR part is non zero in the size of the supercell or the q-point mesh in DFPT calculations and zero outside, while the DD part is defined up to infinity. With this we can rewrite Eq. (3.7)

$$E^P_{Har} = \frac{1}{2}\sum_{i\in SC}\sum_{\alpha=1}^{3} u_{0i\alpha}\sum_{\beta=1}^{3}\left(\sum_{j\in SR} C^{SR}_{i\alpha j\beta}(0,b) + \sum_{j\in SC}\sum_{b=1}^{\infty} C^{DD}_{i\alpha j\beta}(0,b)\right) u_{bj\beta}, \tag{3.9}$$

where SR signifies the short-range box. Finally, it turns out that the DD interatomic force constant C^{DD} can also be calculated in reciprocal space by an Ewald summation technique [26]. With that the second sum in the brackets in Eq. (3.9) can be replaced the dynamical matrix in reciprocal space calculated in the Brillouin-zone center ($q = \Gamma$)

$$\sum_{b=1}^{\infty} C^{DD}_{i\alpha j\beta}(0,b) = \widetilde{C}^{DD}_{i\alpha j\beta}(q=\Gamma). \tag{3.10}$$

The signification of $\widetilde{C}^{DD}(q=\Gamma)$ is illustrated in Fig. 3.4 b). An individual element of $\widetilde{C}^{DD}(q=\Gamma)$ maps the interaction of atom i and atom j *and all their periodic images* until infinity onto one single interaction. Inserting Eq. (3.10) into Eq. (3.9) replaces the sum over supercells to infinity and limits the indexes of atom i and atom j by the size of the largest box (simulation or short-range box)[†]

$$E^P_{Har} = \frac{1}{2}\sum_{i\in SC}\sum_{\alpha=1}^{3} u_{0i\alpha}\sum_{\beta=1}^{3}\left(\sum_{j\in SR} C^{SR}_{i\alpha j\beta}(0,b) + \sum_{j\in SC} \widetilde{C}^{DD}_{i\alpha j\beta}(q=\Gamma)\right) u_{bj\beta}. \tag{3.11}$$

Practically this means that all atoms inside the simulation box are harmonically coupled to each other. Implementation it can, however, be meaningful to apply a cutoff on the DD interaction as the double loop

[†] There is no limitation for the short-range box to be smaller than the simulation box. During the fitting process the situation can be such that the SR interactions have been calculated in an interaction range larger than the simulation box of the TS. Then, the short-range box protrudes the simulation box. In this case the dipole-dipole interaction is only defined inside the simulation box and zero outside, where the short range interaction is finite. In a typical large scale Molecular Dynamics or Monte-Carlo simulation scenario the situation is just inverse where the simulation box is larger than the short-range box.

over all atoms in the simulation box can become heavy to evaluate for large simulation boxes that the second-principles simulations aim for. Moreover so, as the DD interaction becomes negligible for large distances between atoms i and j.

In practice Multibinit extracts the interatomic force constants from the output of a Abinit DFPT calculation (the so-called derivative database (ddb) - file) done at the reference structure for the second-principles model and extracts the full force constant matrix C. Then, the dipole-dipole interaction $\widetilde{C}^{DD}$ for the unit cell of the reference structure is calculated and subtracted from C to get C^{SR}. $\widetilde{C}^{DD}$ is then recalculated for the simulation box of the second-principles run and added to C^{SR}. For the rest of the run only the sum of both is stored.

Finally, the force constant matrix has to comply with the well-known Acoustic Sum Rule (ASR). That is, that the total energy is invariant upon a rigid translation of the crystal as a whole, where

$$u_{i\alpha} = u_{j\alpha} \; \forall \; i, j \in SC \; and \; \alpha \in [1, 3]. \tag{3.12}$$

This rule is fulfilled when the sum over one atom index vanishes

$$\sum_i C_{i\alpha j\beta}(0, b) = 0 \; \forall \; \alpha, j, \beta, b, \tag{3.13}$$

which is generally not the case for the matrices calculated by DFPT. A strategy to fulfill this rule is to derive the self interaction elements ($i = j$) to be the negative sum of the pairwise interactions ($i \neq j$) and impose the symmetry of C

$$\forall \; i \; C_{i\alpha i\beta}(0, b) = \sum_{j \neq i} C_{i\alpha j\beta}(0, b) \tag{3.14}$$

$$C_{i\alpha j\beta}(0, b) = C_{j\beta i\alpha}(b, 0). \tag{3.15}$$

Multibinit uses an implementation from Abinit of Eq. (3.14) and Eq. (3.15) to impose the ASR.

The second contribution to the harmonic energy is the elastic energy depending on the homogeneous strain of the simulation box η. The general strain tensor η contains symmetric and antisymmetric parts, where the antisymmetric part refers e.g. to rigid rotations of the material. We exclude such antisymmetric strains from second-principles simulations. Hence, we can use the Voigt notation based on the symmetry of the strain tensor to reduce the two Cartesian indices α, β to one index labeling the six independent strains (three normal-,three shear strains) with one index $\kappa = 1...6$. Then, the total harmonic elastic energy becomes

$$E^S_{Har} = \frac{N_{SC}}{2} \sum_{\kappa}^{6} \sum_{\lambda}^{6} c_{\kappa\lambda} \eta_\kappa \eta_\lambda, \tag{3.16}$$

where N_{SC} is the number of reference unit cells in the simulation box supercell and c is the elastic tensor for fixed atomic positions that can be trivially calculated from DFPT or finite differences calculation as the second derivative of the total energy with respect to the six independent

strain components

$$c_{\kappa\lambda} = \left.\frac{\partial^2 E_{tot}^{DFT}}{\partial\eta_\kappa \partial\eta_\lambda}\right|_{R^0} \tag{3.17}$$

around the reference configuration R^0. It shall be mentioned that we assume the stresses to vanish around R^0, which implies that there is no linear term in the strain coordinates in our polynomial expansion. However, in contrast to forces on individual atoms the stress does never vanish by symmetry. Hence, it is essential to carefully relax the unit cell of the reference structure.

The last term contributing to the harmonic energy is the strain-phonon coupling depending on both the atomic displacements $\{\mathbf{u}\}$ and the homogeneous strain η

$$E_{Har}^{SP} = \sum_{i\in SC}\sum_{\alpha}^{3}\sum_{\kappa}^{6} \Lambda_{i\alpha\kappa} u_{i\alpha}\eta_\kappa, \tag{3.18}$$

where Λ is the force-response internal strain tensor. Equivalently to C and c it is calculated from DFPT or finite difference calculations as the mixed second-order derivative with respect to homogeneous strain and the atomic displacements

$$\Lambda_{i\alpha\kappa} = \left.\frac{\partial^2 E_{tot}^{DFT}}{\partial u_{i\alpha}\partial\eta_\kappa}\right|_{R^0}. \tag{3.19}$$

It describes the forces acting on the atoms upon a given strain state and the stresses in the unit cell upon a given set of atomic distortions $\{\mathbf{u}\}$. In some cases, like the cubic perovskite structure that is the reference structure for the second-principles model developed in the preparation of this manuscript, Λ vanishes by symmetry.

3.2.2 Anharmonic Contributions

In this section we describe all the contributions to the anharmonic energy of the effective potential. In the same way that we split the harmonic energy, it is also natural to split the anharmonic energy in three different terms depending on their dependency on the atomic displacements $\{\mathbf{u}\}$ and homogeneous strain η

$$E_{Anh} = E_{Anh}^{P}(\{\mathbf{u}\}) + E_{Anh}^{S}(\eta) + E_{Anh}^{SP}(\{\mathbf{u}\},\eta). \tag{3.20}$$

The main difference between the anharmonic and the harmonic terms is the order of the variables they depend on, which can be three or higher in the case of the anharmonic terms. For the anharmonic phonon, strain, and

strain phonon contributions truncated at third order order we write

$$E^P_{Anh} = \sum_{i\alpha}\sum_{j\beta}\sum_{k\gamma} C^3_{i\alpha j\beta k\gamma} u_{i\alpha} u_{j\beta} u_{k\gamma} + \dots \tag{3.21}$$

$$E^S_{Anh} = \sum_{\kappa\lambda\mu} c^3_{\kappa\lambda\mu} \eta_\kappa \eta_\lambda \eta_\mu + \dots \tag{3.22}$$

$$E^{SP}_{Anh} = \sum_{i\alpha}\sum_{j\beta}\sum_{\lambda} \Lambda^{(1,2)}_{i\alpha j\beta\lambda} u_{i\alpha} u_{j\beta} \eta_\lambda + \sum_{i\alpha}\sum_{\lambda}\sum_{\kappa} \Lambda^{(1,2)}_{i\alpha\kappa\lambda} u_{i\alpha} \eta_\lambda \eta_\kappa + \dots \tag{3.23}$$

C^n,c^n are the n^{th} order tensors and $\Lambda^{(n,m)}$ is the strain-phonon tensor with n^{th} displacement and m^{th} strain order. Individual elements of these tensors are defined as

$$C^m_{i\alpha j\beta k\gamma\dots} = \left.\frac{\partial^n E^{DFT}_{tot}}{\partial u_{i\alpha}\partial u_{j\beta}\partial u_{k\gamma}\dots}\right|_{R^0} \tag{3.24}$$

$$c^n_{\kappa\lambda\mu\dots} = \left.\frac{\partial^n E^{DFT}_{tot}}{\partial \eta_\kappa \partial \eta_\lambda \partial \eta_\mu \dots}\right|_{R^0} \tag{3.25}$$

$$\Lambda^{(n,m)}_{i\alpha\kappa\lambda\dots} = \left.\frac{\partial^{n+m} E^{DFT}_{tot}}{\partial u_{i\alpha}\partial \eta_\kappa \partial \eta_\lambda \dots}\right|_{R^0}, \tag{3.26}$$

However, a first difficulty arises from the number of independent entries of those tensors, which, as we will see in the next section, is generally much too large to systematically calculate all independent elements. Therefore, we do not only have to cut the range of interatomic anharmonic interactions, but also find an algorithmic efficient way do determine and calculate some *important* elements in the anharmonic energy contribution. It is therefore instructive to see the higher-order contributions as a set of coefficients rather than complete tensors.

A second difficulty arises from the fact that the set of C^n and $\Lambda^{(n,m)}$ coefficients have to comply with the ASR like their harmonic counterparts. Imposing the ASR on the higher-order quantities is more difficult than on the harmonic order, especially as we will only determine some entries of C^n and $\Lambda^{(n,m)}$. To circumvent this difficulty we write the atomic coordinates as a set of difference of displacement instead of displacement so that Eq. (3.21) and Eq. (3.23) become

$$E^P_{Anh} = \sum_{ijklmn}\sum_{\alpha\beta\gamma} \widehat{C}^3_{ijklmn\alpha\beta\gamma} (u_{i\alpha} - u_{j\alpha})(u_{k\beta} - u_{l\beta})(u_{m\beta} - u_{n\beta}) + \dots \tag{3.27}$$

$$E^{SP}_{Anh} = \sum_{ijkl}\sum_{\alpha\beta}\sum_{\kappa} \widehat{\Lambda}^{(2,1)}_{ijkl\alpha\beta\kappa} (u_{i\alpha} - u_{j\alpha})(u_{k\beta} - u_{l\beta})\eta_\kappa + \dots \tag{3.28}$$

Evaluating the product of differences of displacements rather than the product of displacements automatically fulfils the ASR because a rigid translation of the crystal will result in a zero contribution of Eq. (3.27) and Eq. (3.28) as all factors that contain a differences of displacement turn out to be zero. While introducing differences of displacements allows to directly fit the anharmonic coefficients to reproduce a set of ab initio data, they also unfortunately increase the number of independent anharmonic coefficients. E.g. in a third order term in the expansion of E^P_{Anh} there are only three atomic indices in C^3. In the product of differences of

displacements formulation of the same expansion there are six atomic indices in $\widehat{C}^3$. In the forthcoming we will show how to generate the complete set of independent anharmonic coefficients and an algorithmic approach to fit and select important coefficients out of this set.

3.2.3 Anharmonic Term Generation

In the preceding sections we laid out the polynomial expansion of lattice degrees of freedom. Thereby, we showed the advantage to evaluate the anharmonic expansion by products of differences of displacements rather than products of displacements to comply with the ASR. In this section we show how to define the set of irreducible set of *independent* anharmonic coefficients by utilising the crystal symmetry of the reference structure R^0 around which we develop the polynomial expansion. The irreducible anharmonic coefficients will in the result be applied to a set of symmetry equivalent terms, which have been called *symmetry adapted terms* (SAT) [44]. In preparation of the manuscript we reviewed and optimized the implementation of the generation of the SAT in Multibinit.

We write a general symmetry operation as $\{S|t\}$, where S is a 3×3 matrix representation of a point operation, while t is a translation vector in the Cartesian reference frame. For $\{S|t\}$ to be a symmetry operation of the reference structure R^0 it has to fulfil

$$\{S|t\}(R_{li} + \tau_{li}) = (R_{l'i'} + \tau_{l'i'}). \tag{3.29}$$

Eq. (3.29) states that for each atom i situated in cell l there must exist another atom i' in cell l' into which i transforms upon the application of the symmetry operation $\{S|t\}$. The symmetry of the reference structure is defined by a set of symmetry operations. E.g. the space group of the cubic perovskite structure $Pm\bar{3}m$, which serves as a high-symmetry reference in our case, is defined by 48 symmetry operations.

Further, the symmetry operations determine how the deviations of the reference structure - the atomic displacements and homogeneous strains - transform into each other by

$$u_{i'\alpha} = \sum_{\beta} S_{\alpha,\beta} u_{i\beta} \tag{3.30}$$

$$\eta'_{\alpha\beta} = \sum_{\gamma\delta} S_{\alpha\gamma}\eta_{\gamma\delta}S^{-1}_{\delta\beta} \tag{3.31}$$

Eqs. (3.30) and (3.31) allow us to group together sets of symmetry equivalent displacements and strains. This grouping is at the center of the generation of the SATs. In Multibinit the SATs are generated in four steps.

Firstly, the set of irreducible strains and atomic displacements pairs $(u_{i\alpha} - u_{j\alpha})$ are created by applying Eqs. (3.30) and (3.31). To do so, we create first a list of all atomic pairs within a given cutoff radius r_{cut}, which is controlled by the input variable *fit_cutoff* in Multibinit. Then, we apply the set of symmetry operations to each atomic displacement pair and strain to find the set of equivalent pairs and strains. We establish the transformation for each symmetry operation of the atomic pairs and strains and store them. A representative irreducible pair and strain is selected for each set of equivalent pairs and strains, which is illustrated in Fig. 3.5 for the first neighbors in the BX_2 and AX planes in the perovskite structure. We list the number of irreducible atomic displacement pairs for a given cutoff around each irreducible atom i in the perovskite structure as well as the sum of all irreducible pairs for a given cutoff in Tables 3.1 and 3.2. The number of irreducible strains with respect to a cubic

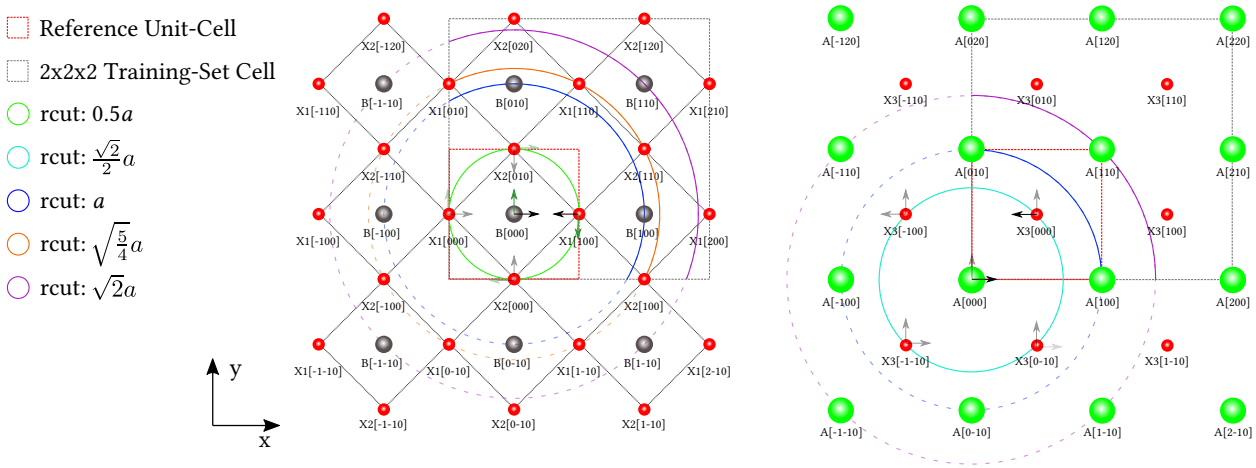

Figure 3.5: Illustration of irreducible atomic displacement pairs for different cutoff radii in BX_2 and AX planes in the perovskite structure. The irreducible atomic displacement pairs are shown by arrows for the shortest cutoff radii. While there are two (black and green arrows) in the BX_2 plane there is only one in the AX plane. The set of symmetry equivalent atomic displacement pairs is indicated by faded arrows. For cutoff-radii equal or larger than half the TS cell lattice parameter only a part of the set of symmetry equivalent atomic displacement pairs can be combined to form a SAT as a SAT can not contain an atom and its translational image, which is illustrated by the partly dashed circles.

reference is trivially two (one-normal and one shear strain) and could be maximum six for a triclinic reference (three normal and three shear strains).

In the second step we recursively combine the irreducible atomic displacement pairs and strains from a lower start to a higher finish polynomial order p controlled by the input keyword *fit_rangePower* (typically order 3 to order 4). The number of combinations of irreducible entities can be easily calculated by an unordered sampling with replacement from combination theory

$$n_{irred.comb.} = \binom{p + n_{irred} - 1}{p}, \tag{3.32}$$

where n_{irred} is the sum of irreducible atomic displacements pairs and strains, and p is the polynomial order. In Tables 3.1 and 3.2 we list number of combinations of irreducible atomic displacement pairs for a given cutoff. Thereby, we impose that one of the irreducible atoms of the perovskite structure has to appear in all of the products, so that we only create terms in the form of

$$\widehat{C}^3_{ijkl\alpha\beta\gamma}(u_{i\alpha} - u_{j\beta})(u_{i\beta} - u_{k\beta})(u_{i\gamma} - u_{j\gamma}), \tag{3.33}$$

which reduces the atomic indices for a third order atomic displacement term from six to four. Anharmonic coefficients generated in this way can be seen as generating all anharmonic interactions on a circle around one central atom, which is illustrated for the A and B cations in the AX and BX_2 planes in Fig. 3.5.

The third step, to get the complete set, is the most cumbersome one. It is easy to follow that a specific combination of p irreducible pairs of atomic displacements does not represent all irreducible combinations that can be formed of the set of symmetry equivalent pairs of atomic displacements from the p irreducible pairs. To generate the missing coefficients that can be traced back to one specific combination of irreducible atomic displacement pairs, we developed a two step procedure. First, we apply

a symmetry operation to one of the p irreducible atomic displacement pairs to transform it into a symmetry equivalent one. Then, we form a new combination of the transformed displacement pair with the $p-1$ untransformed displacement pairs[1]. Then, we apply successively all symmetry operations to the new combination (all p displacement pairs get transformed) to check if the new combination can be transformed into an already existing combination. If yes, it is not stored, if not we store it as a new irreducible combination. The first step is recursively applied over all symmetries of the reference structure and the p irreducible entities of the specific combination (atomic displacement pairs and strains). The number of created irreducible terms is strongly dependant on the coordination of one atom and it's first neighbors. This procedure has been parallelized so that the $n_{irred.comb.}$ combinations of irreducible entities get distributed over the number of available processors at run-time.

1: Thereby we take care that no combination contains an atom and its periodic image with respect to the training cell size. This means that the TS cell size restricts the number of SATs that can be calculated and is illustrated by the partly dashed circles in Fig. 3.5 for cutoff radii equal or larger than half the TS lattice parameter.

In the final step of the generation of the SATs we create for each representative irreducible combination the set of symmetry equivalent combinations and associate them to one single coefficient. Thereby, we might find SATs which cancel out by symmetry at odd order, which reduces further the number of irreducible coefficients.

As an example, the final number of SATs in the perovskite structure and a 2x2x2 TS cell is given in Tables 3.1 and 3.2 for a given cutoff r_{cut} at third and fourth order labeled n for only atomic displacement terms associated to coefficients $\widehat{C}^n$ and strain-phonon terms that mix atomic displacements and homogeneous strains together associated to $\widehat{\Lambda}^{(n-m,m)}$, with m the order of the strain variable either limited to one or two. r_{cut} ranges from the first neighbor distance in the perovskite structure to $\sqrt{3}{a_p}^2$, which is the maximum cutoff for a 2x2x2 TS supercell. Tables 3.1 and 3.2 show that the final number of SATs not only depends on r_{cut}, but also on the coordination of the central atom i that we choose. For instance in the perovskite structure, if r_{cut} is chosen to only contain the first neighbors there are only two irreducible displacement pairs independent of the central atom i that we chose. However, for the twelvefold coordinated cation A we find 175 irreducible displacement terms at third order, while we find only 29 for the sixfold coordinated cation B. Finally, comparing the number of irreducible anharmonic displacement coefficients for choosing a central atom i over combining all possible terms (lower part of Table 3.2) with $2 \cdot n$ atomic indices, shows a significant reduction of independent coefficients. All of the above explanations and algorithms can be applied in the same way to homogeneous strain coordinates to generate an expansion of E^S_{Anh}, which can be activated by the keyword *fit_anha_strain* in Multibinit.

2: a_p is the cubic lattice parameter of the reference perovskite structure

As mentioned before our goal in creating a second-principles model is not to define a *complete* polynomial expansion up to a given order and a given anharmonic interaction cutoff, but to rather select a few *important* anharmonic coefficients. Attempting, to define the complete lattice expansion would be in any way impractical because of the rapidly growing number of SATs coefficients outlined in Tables 3.1 and 3.2. The algorithmic approach to finding and fitting these important anharmonic coefficients, with respect to some ab initio data is outlined in the next section.

Table 3.1: Count of number of irreducible atomic displacement pairs (n_{irred}), combinations of irreducible atomic displacement pairs at order n ($n_{irred.comb.}$), atomic displacement SATs ($n_{\widehat{C}^n}$) and strain phonon SATs ($n_{\widehat{\Lambda}^{(n-m,m)}}$) at order n and strain power m in the perovskite structure with A cation (top) and B-cation (bottom) as the fixed atom in dependence on the cutoff radius r_{cut}. r_{cut} is expressed in terms of the cubic primitive lattice parameter a_p. Note the divergence of independent SATs with growing r_{cut}.

A-Cation Terms

Order n	r_{cut} (a_p)	n_{irred}	$n_{irred.comb.}$	$n_{\widehat{C}^n}$	$n_{\widehat{C}^n} + n_{\widehat{\Lambda}^{(n-m,m)}}$	
					$max\ m = 1$	$max\ m = 2$
3rd	$\frac{\sqrt{2}}{2}$	2	4	175	276	293
	$\frac{\sqrt{3}}{2}$	3	10	797	1058	1088
	1	5	35	1607	2032	2072
	$\sqrt{2}$	9	165	14146	16140	16231
	$\sqrt{3}$	10	220	17223	19577	19681
4th	$\frac{\sqrt{2}}{2}$	2	5	1651	2668	3006
	$\frac{\sqrt{3}}{2}$	3	15	11481	16140	17025
	1	5	70	26229	35642	37090
	$\sqrt{2}$	9	495	365318	449384	456280
	$\sqrt{3}$	10	715	451181	553477	561621

B-Cation Terms

Order n	r_{cut} (a_p)	n_{irred}	$n_{irred.comb.}$	$n_{\widehat{C}^n}$	$n_{\widehat{C}^n} + n_{\widehat{\Lambda}^{(n-m,m)}}$	
					$max\ m = 1$	$max\ m = 2$
3rd	0.5	2	4	29	60	70
	$\frac{\sqrt{3}}{2}$	3	10	143	238	261
	1	5	35	521	740	773
	$\frac{\sqrt{5}}{2}$	8	120	5103	6139	6206
	$\sqrt{2}$	10	220	8569	10115	10199
	1.5	12	364	18346	21105	21223
	$\sqrt{3}$	13	455	21289	24408	24539
4th	0.5	2	5	146	293	393
	$\frac{\sqrt{3}}{2}$	3	15	931	1726	2046
	1	5	70	4852	7829	8572
	$\frac{\sqrt{5}}{2}$	8	330	86390	116454	120027
	$\sqrt{2}$	10	715	157619	208256	213599
	1.5	12	1365	401195	510107	519675
	$\sqrt{3}$	13	1820	473549	599913	610729

Table 3.2: Count of number of irreducible atomic displacement pairs (n_{irred}), combinations of irreducible atomic displacement pairs at order n ($n_{irred.comb.}$), atomic displacement SATs ($n_{\widehat{C}^n}$) and strain phonon SATs ($n_{\widehat{\Lambda}^{(n-m,m)}}$) at order n and strain power m in the perovskite structure with X anion (top) as the fixed atom and all cross terms (bottom) with $2 \cdot n$ atomic indices per $\widehat{C}^n$ in dependence on the cutoff radius r_{cut}. r_{cut} is expressed in terms of the cubic primitive lattice parameter a_p. Note the divergence of independent SATs with growing r_{cut}.

X-Anion Terms

Order n	r_{cut} (a_p)	n_{irred}	$n_{irred.comb.}$	$n_{\widehat{C}^n}$	$n_{\widehat{C}^n} + n_{\widehat{\Lambda}^{(n-m,m)}}$	
					$max\ m = 1$	$max\ m = 2$
3rd	0.5	2	4	2	9	19
	$\frac{\sqrt{2}}{2}$	6	56	231	415	463
	1	11	286	998	1482	1557
	$\frac{\sqrt{5}}{2}$	14	560	2967	3994	4103
	$\sqrt{2}$	23	2300	19371	23299	23535
	1.5	25	2925	26733	31726	31996
	$\sqrt{3}$	27	3654	32459	38364	38668
4th	0.5	2	5	4	13	35
	$\frac{\sqrt{2}}{2}$	6	126	1208	2537	3165
	1	11	1001	8175	14001	15663
	$\frac{\sqrt{5}}{2}$	14	2380	32499	49992	53538
	$\sqrt{2}$	23	14950	347943	463334	476990
	1.5	25	20475	515308	674606	691973
	$\sqrt{3}$	27	27405	640492	833930	854477

All Cross Terms

Order n	r_{cut} (a_p)	n_{irred}	$n_{irred.comb.}$	$n_{\widehat{C}^n}$	$n_{\widehat{C}^n} + n_{\widehat{\Lambda}^{(n-m,m)}}$	
					$max\ m = 1$	$max\ m = 2$
3rd	0.5	2	4	29	60	70
	$\frac{\sqrt{2}}{2}$	6	56	1635	2095	2143
	$\frac{\sqrt{3}}{2}$	7	84	3616	4370	4431
	1	16	816	20192	22795	22903
	$\frac{\sqrt{5}}{2}$	19	1330	43976	48470	48612
	$\sqrt{2}$	32	5984	304034	322507	322810
	1.5	34	7140	394599	416751	417088
	$\sqrt{3}$	38	9880	558532	587312	587709
4th	0.5	2	5	146	293	393
	$\frac{\sqrt{2}}{2}$	6	126	25022	34558	36122
	$\frac{\sqrt{3}}{2}$	7	210	73242	94472	97050
	1	16	3876	570177	688908	697871
	$\frac{\sqrt{5}}{2}$	19	7315	1490716	1750649	1766180

3.2.4 Anharmonic Term Selection and Fitting

In the preceding sections we laid out the polynomial expansion of lattice degrees of freedoms that is the second-principles approach. In the section above we have explained in some detail how to generate the set of independent anharmonic coefficients for given anharmonic atomic interaction radius. Thereby, it became apparent that for a realistic cutoff (at least second neighbor) the number of independent anharmonic coefficients is by orders of magnitude too large to be fitted entirely as getting sufficient data points from ab initio calculations would need an immense amount of time. Moreover, a large number of anharmonic coefficients in the polynomial expansion would counteract to some degree our goal of a light weight polynomial description of the PES.

The approach to reduce the number of anharmonic coefficients is to select only a few *important* ones from the whole set. An algorithmic approach for this anharmonic term selection has been presented by *Escorihuela-Sayalero et al.* [45] and reimplemented in Multibinit. Here, we will briefly present their approach and show an addition to the fit process that has been implemented in Multibinit in the preparation of this manuscript.

The algorithm of *Escorihuela-Sayalero et al.* has two essential ingredients. First the anharmonic coefficient calculation and second the selection of anharmonic coefficients. The determination of the anharmonic coefficients is done by least squares fitting approach. The fitted quantity is ab initio data calculated on a set on various nuclear configurations, which we call the training set (TS). To perform the fit we write a goal function (GF) that depends on a given set of anharmonic coefficients $\Theta_p := \theta_1, ..\theta_p$ [3], as the square difference between anharmonic energy, forces and stresses from the TS and the energy, forces and stresses of the anharmonic polynomial expansion

3: The coefficients θ_i in the set Θ_p correspond to any of the anharmonic coefficients $\widehat{C}^n$,$\widehat{\Lambda}^{(n-m,m)}$, or c^n defined in section 3.2.2

$$\begin{aligned} G(\Theta_p, TS) =& \frac{1}{N_1}\sum_s (E^{TS}_{Anh}(s) - E_{Anh}(\Theta_p, s)) \\ &+ \frac{1}{N_2}\sum_{si\alpha} (F^{TS}_{Anh,i\alpha}(s) - F_{Anh,i\alpha}(\Theta_p, s)) \\ &+ \frac{1}{N_3}\sum_{s\kappa} \Omega^2(s)(S^{TS}_{Anh,\kappa}(s) - S_{Anh,\kappa}(\Theta_p, s)), \end{aligned} \tag{3.34}$$

where E,F, and S refer to energy, forces and stresses, N_1, N_2, and N_3 are normalization constants, s are the TS configurations, i, α are atomic indices and Cartesian directions, κ are the strain degrees of freedom in Voigt notation, and $\Omega(s)$ is a factor proposed by *Sheppard et al.* to balance forces and stresses [52]. N_1, N_2, N_3 are set to 1, $3 \cdot N^{TS}_{at}$, and 6, where N^{TS}_{at} is the number of atoms in the TS. In this way, the greater number of force and stress values per TS data point are balanced with respect to just one energy value per TS data point. The GF $G(\Theta_p, TS)$ can be seen as a p-dimensional parabola. We minimize it with respect to the set of anharmonic coefficients Θ_p. At the minimum the GF satisfies

$$\frac{\partial G(\Theta_p, TS)}{\partial \theta_i} = 0 \forall i \in p. \tag{3.35}$$

For more comprehensive information about the properties of the GF we refer to Ref. [45]. The implementation of the GF in Multibinit deviates

slightly from the one proposed by *Escorihuela et al.* as only the anharmonic contribution is minimized. The harmonic contribution is determined accurately by DFPT calculations and reduced from the total ab initio quantity. E.g. $E^{TS}_{Anh}(s)$ at a given configuration $s := (\{\mathbf{u}\}, \eta)$ is calculated as

$$E^{TS}_{Anh}(s) = E^{DFT}_{tot}(s) - E_0(R^0) - E_{har}(s), \tag{3.36}$$

where similar relations hold for $F^{TS}_{Anh}(s)$ and $S^{TS}_{Anh}(s)$. Finally, the Multibinit user has the freedom to choose on which quantity the GF shall be minimized by specifying the keyword *fit_EFS*. For instance it can be more important to minimize the GF on forces on stresses for the dynamical properties of the lattice model than minimizing the GF on the energy differences. The second part of the algorithm of *Escorihuela-Sayalero et al.* is the anharmonic coefficient selection. In the established second-principles models [44, 45] it has been shown to be sufficient to select few tens of anharmonic coefficients at 3rd and 4th orders to generate a realistic model. However, selecting this few tens of terms poses a great challenge, since the number of possible combinations from the whole set of the anharmonic coefficients is

$$N_{comb} = \binom{N_{SAT}}{p}, \tag{3.37}$$

where N_{SAT} is the number of SAT defined by cutoff range r_{cut} and polynomial order, N_{comb} is the number of different combinations of p SATs that we want to select. N_{comb} is even for short cutoffs an untreatable large number. For instance if we want to select $p = 30$ SATs from the set of 3rd and 4th order terms including strain-phonon coupling and a cutoff $r_{cut} = \frac{\sqrt{3}}{2}a_p$ in the perovskite structure (where a_p is the cubic lattice parameter) then N_{comb} is approximately $2.7 \cdot 10^{147}$. Hence, the naive way of testing all different N_{comb} possibilities to find the best one is practically impossible.

The algorithm proposed by *Escorihuela-Sayalero et al.* reduces the number of combinations to test using an iterative procedure and is illustrated in Fig. 3.6. In the first iteration the coefficient θ_i of all N_{SAT} SAT are determined by minimizing the GF $G(\theta_i, TS)$. Then, the SAT which reduces $G(\theta_i, TS)$ the most is selected to be θ_1. In the next iteration $N_{SAT} - 1$ sets of SATs $\Theta^i_2 =: \{\theta_1, \theta_i\}$ are created and the coefficients are newly determined by reducing $G(\Theta^i_2, TS)$. Then, the set Θ^i_2 is selected that reduces $G(\Theta_2, TS)$ the most. This procedure is repeated until p anharmonic SATs have been selected. In Multibinit p can either be specified by the keyword *fit_ncoeff* or the loop is broken by a convergence criterion on $G(\Theta_p, TS)$. This algorithm reduces the number of combinations to test $N_{comb,test}$ for selecting p SATs to

$$N_{comb,test} = p \cdot N_{SAT} - \sum_{i=1}^{p-1} i, \tag{3.38}$$

which leads for the example in the perovskite structure given above to $N_{comb,test} \approx 2.9 \cdot 10^6$ and hence to an enormous reduction of the problem size compared to $N_{comb} \approx 10^{147}$. Similarly to the keyword *fit_EFS* the user has the freedom to choose the selection of the anharmonic terms based on energy, forces, or stresses or the sum of those quantities by specifying the keyword *sel_EFS*.

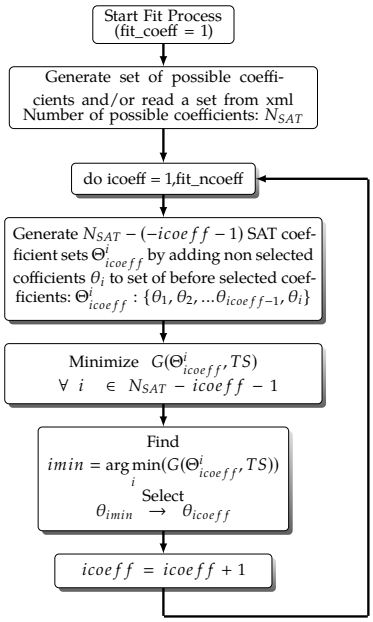

Figure 3.6: Illustration of the term selection algorithm proposed by *Escorihuela-Sayalero et al.* [45] as implemented in Multibinit. In *fit_ncoeff* iterations *fit_ncoeff* SATs are selected from a set of N_{SAT} SATs. In each iteration $N_{SAT} - (icoeff - 1)$ sets of SATs Θ^i_{icoeff} are generated adding individually the non selected SAT coefficients θ_i to the set of before selected SAT coefficients $\Theta_{icoeff-1}$. Then, the coefficient sets Θ^i_{icoeff} are fitted with respect to the TS by minimizing $G(\Theta^i_{icoeff}, TS)$. Finally, the coefficient θ_i is selected whose set Θ^i_{icoeff} reduces the most the GF $G(\Theta^i_{icoeff}, TS)$.

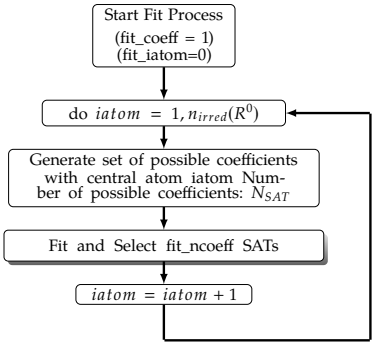

Figure 3.7: Loop over irreducible atoms in the reference structure R_0. At the beginning of each iteration the set of possible SAT with a given r_{cut} and polynomial order and the irreducible atom $iatom$ as the central atom of the set of SATs are generated. In each iteration *fit_ncoeff* SATs are selected by the fitting and selection algorithm (see also Fig.3.6).

A second way to reduce the number of combinations to test is to reduce the pool of SATs N_{SAT}. As laid out in section 3.2.3 for the same cutoff r_{cut} and polynomial order N_{SAT} is about one order magnitude smaller by specifying one central atom that repeats in all products and only generating SATs in the form of Eq. (3.33) than producing all cross terms. Therefore, we implemented a loop over all irreducible atoms in the reference structure. At each iteration the SATs for the corresponding atom are generated and the SAT fitting and selection procedure is started. SATs selected in the preceding iteration are passed. Using such a loop is also meaningful from physical perspective as fitting a certain number of SAT in the form of Eq. (3.33) can be seen as fitting the anharmonic interaction of each atom with respect to the lattice in the cutoff r_{cut}. This can be easily understood by expanding the product of terms in the form of Eq. (3.33), which always contains a term like u_i^n, where n is the polynomial order.
The loop over the irreducible atoms can be controlled with the keyword *fit_iatom*. If it is set to its default value zero the loop over all reducible atoms is started, if it is set to a positive integer the atom with that index in the reference structure is set to the central atom for the generation of the SATs, and if it is set to -1 all cross terms are generated.

3.2.5 Algorithmic Approach for Bounding the Polynomial Expansion

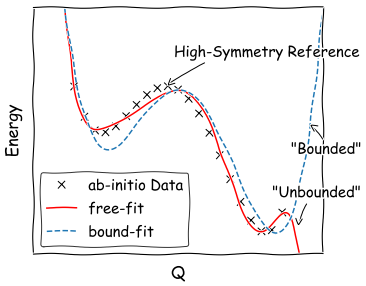

Figure 3.8: Schematical draw of the boundedness problem. A free polynomial fit (red line) might reproduce the provided ab initio data with a suitable precision, while diverging to minus infinity outside the provided data range. A preferable second-principle models would be a *bounded* one that diverges to positive infinity for all extremal values of the order coordinate Q even if it is less precise than the free-fit (blue dashed line).

Very often the polynomial expansion (we call it free-fit from here on) generated by the procedure described in the preceding section reproduces the TS data with sufficient precision to describe correctly the minima of the PES. However, it is at the same time very often not bounded from below, which means it diverges to minus infinity for large distortions (see Fig. 3.8). We call such a polynomial unbounded. To practically use a polynomial expansion in lattice dynamic simulations we need to guarantee that it is *bounded* i.e. that it diverges to positive infinity in all its degrees of freedom. One might think that this problem could be solved by simply sampling the phase space with ab initio calculations up to high energy large amplitudes of distortion, which then should automatically impose a bounded free-fit. However, the dimensionality of the phase space is generally too large to practically produce such a sampling. E.g. a 2x2x2 TS cell of the perovskite structure contains 40 atoms. Consequently, the phase space contains 120 degrees of freedom. Trying to sample all the degrees of freedom with a regular grid that contains just a few data points per degree of freedom would result in an intreatable number of ab initio calculations. Hence, the TS data that we provide for the fitting will always be relatively sparse with respect to the entire dimensionality of the phase space and a free-fit will often contain degrees of freedom that diverge to negative infinity.

In the preparation of this manuscript we implemented an algorithmic approach to impose boundedness on a free-fit potential. The basic idea of that approach is to add higher-order even SATs with positive coefficients to the free-fit potential that have a negligible contribution inside the already fitted data range, but guarantee boundedness outside. Therefore, we investigate each SAT in the free-fit potential for its possibility to introduce a negative divergence for large distortion amplitudes. A SAT

is decided to be divergent if it contains factors with odd power or has a negative coefficient.

Then, for a divergent SAT a set of higher-order even bounding SATs is created. The set of higher-order SATs contains even SATs for all multipliers of the divergent SAT as well as even analogs of the divergent SAT that fit into the bounding order (see also Fig. 3.6). The start and stop order of the bounding SATs is controlled by the keyword *bound_rangePower* in MULTIBINIT. Typical bounding orders range from six to eight.

Finally, to enforce the boundedness we have to enforce a positive coefficient on the higher-order bounding SATs while keeping the precision with respect to the TS. The general approach to such a problem would be to perform a constrained optimization of all the SAT coefficients (free-fit and bounding), where the bounding SATs' coefficients are constrained to positive values. In the preparation of the manuscript we experimented with the bounded-variable least squares algorithm [53] that provides an implementation of such a constrained optimization. However, we found that the solutions were unstable, which might be related to an insufficient sampling of the phase space.

Therefore, we implemented alternatively a simple iterative optimization algorithm. At the beginning we fix the Θ_p SAT coefficients of the free-fit polynomial. Then, a loop over the free-fit SATs is started. If a free-fit SAT is divergent its set of NB_i high order equivalent SATs is generated. Second, a loop over the high order equivalent terms is started. At each iteration, a bounding SAT is added to the set of SATs and its coefficient θ_i^{Bj} is optimized (where i is the i^{th} free-fit SAT coefficient of the p initial SATs and j is the j^{th} bounding SAT coefficient). Before the optimization a check is performed if the bounding SAT is already present in the polynomial as the multipliers of different free-fit SATs are often equivalent. For the optimization we define the parabola of the ratio of the GF depending on the value of the new SAT coefficient $G(\theta_i^{Bj}, TS)$‡. with respect to the GF's initial value at the beginning of the bounding term iteration G_0. Therefore, we calculate the GF at two positive values of θ_i^{Bj}. The third value necessary to construct the parabola is trivially found at $G(\theta_i^{Bj} = 0, TS)/G_0 = 1$. Once the parabola is constructed its minimum is trivially found. A minimum value at $\theta_i^{Bj} > 0$ means that a positive bounding coefficient improves the description of the training set data by the polynomial expansion and we take this value as the optimized one for θ_i^{Bj}. If the minimum of the goal function is at a value $\theta_i^{Bj} < 0$, we chose a value θ_i^{Bj} at a penalty $G(\theta_i^{Bj}, TS)/G_0 = G_P > 1$ (see Fig. 3.10). Choosing this penalty implies that we sacrifice the precision of the polynomial expansion for imposing boundedness. After choosing θ_i^{Bj} the value of G_0 is updated and the loop over high order bounding SATS for the initial SAT i is continued. The value of G_P has to be rather close to 1 to avoid a deterioration of the precision of the initial free-fit by successively adding bounding coefficients with a precision penalty. Currently a value of 1.001 for G_P is hard coded inside MULTIBINIT.

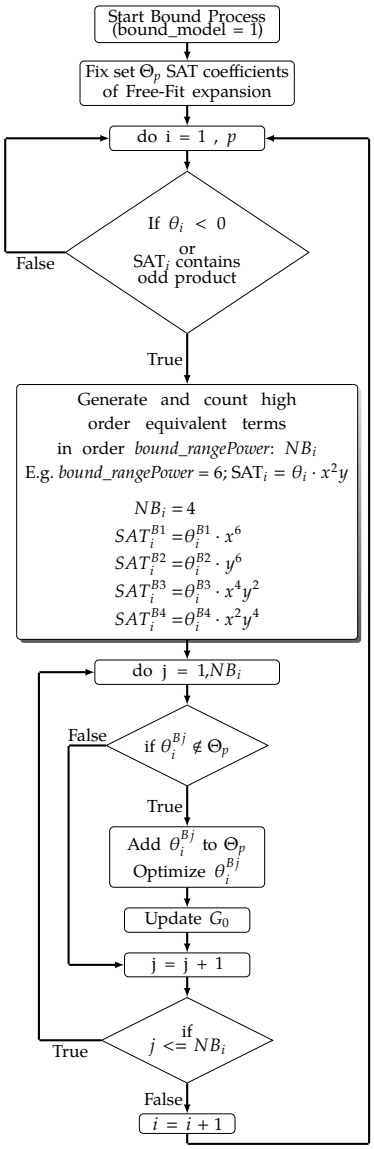

Figure 3.9: Illustration of the bounding algorithm. The algorithm is activated by the keyword *bound_model* in MULTIBINIT. At the beginning an input set Θ_p of anharmonic SAT coefficients are fixed. For each divergent term θ_i a set NB_i of equivalent even higher-order term is added. x and y are representatives of any irreducible atomic displacement pair or homogeneous strain in the example. In a second loop the NB_i SAT bounding coefficients are added to the initial set and optimized.

‡ Here the GF becomes one dimensional, since we fix all other SAT coefficients and only vary θ_i^{Bj}.

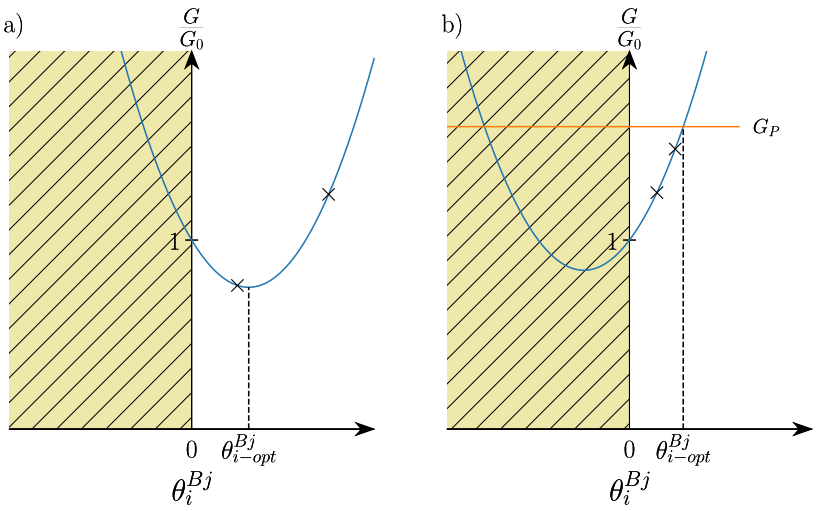

Figure 3.10: Illustration of optimization approach for bounding coefficients. The GF $G(\theta_i^{Bj}, TS)$ is calculated at two positive values (crosses) of the bounding coefficient θ_i^{Bj}. Then, a parabola through the ratio of those two GF values over the initial GF G_0 value and $\frac{G}{G_0}(\theta_i^{Bj} = 0, TS) = 1$ is constructed (blue line). If the minimum of that parabola lies at a positive value of θ_i^{Bj} it is taken as the coefficient value θ_{i-opt}^{Bj} (corresponds to a)). If the minimum of the parabola lies at a negative value of θ_i^{Bj} a positive value of θ_i^{Bj} at a GF penalty G_P (orange line) is taken as θ_{i-opt}^{Bj} (corresponds to b)).

3.3 Coupled Lattice/Electronic second-principles Models

In constructing second-principles lattice polynomial expansions we integrate out all the electronic degrees of freedom. All the electronic effects forming the shape of the PES are captured implicitly in the lattice harmonic and anharmonic coefficients. Such a polynomial expansion gives us a powerful lightweight tool to study lattice dynamics at large scale. However, in some cases where there is a strong interlocking between the electronic structure and the lattice structure it would be desirable to preserve some relevant degrees of electronic freedom to study their interaction with the lattice degrees of freedom. Such strong interlockings exist for example in perovskites showing metal-to-insulator transitions. The states of interest are typically the highest occupied and lowest unoccupied states around the Fermi level. *García-Fernández et al.* [46] presented a *second-principles* method to reintroduce some electronic degrees of freedom back to a lattice polynomial expansion whose central ideas we present here. Their method has been implemented in the Scale-Up package. During the preparation of this Thesis we set up an interface between the Multibinit and Scale-Up packages to create coupled lattice electronic second-principles models. The interface will be introduced at the end of the section.

3.3.1 Polynomial Expansion of Electron Lattice Interactions in a Wannier-Basis

In analogy to effective lattice energy E_{eff} that is developed as function of the deviation of the lattice structure from a reference structure the method of *García-Fernández et al.* develops the electronic energy E_{el} as a function of the deviation of the electronic density from a reference electronic density that is given by

$$n^0(\mathbf{r}, \mathbf{R}) = \sum_{ab} d^0_{ab} \chi_a(\mathbf{r}, \mathbf{R}) \chi_b(\vec{r}, \mathbf{r}), \tag{3.39}$$

where $\chi_a(\mathbf{r}, \mathbf{R})$ and $\chi_b(\mathbf{r}, \mathbf{R})$ denote a local electronic state a and b centered on a given atom i in a unit cell l in a Wannier basis calculated by

$$|\chi_a\rangle \equiv |\chi_{lia}\rangle = \frac{V}{(2\pi)^3} \int_{BZ} d\vec{k} e^{-i\vec{k}\cdot\vec{R}_l} \sum_{m=1}^{J} T^{\vec{k}}_{ma} \left|\Psi^0_{m\vec{k}}\right\rangle, \tag{3.40}$$

where V is the unit cell volume R_l is the lattice translation vector to unit cell l (compare Eq. (3.3)), $\left|\Psi^0_{m\vec{k}}\right\rangle$ are Bloch like Hamiltonian eigenstates that define a manifold of J bands and $T^{\vec{k}}$ are matrices representing unitary transformations between the J Bloch orbitals at a given wavevector $\vec{k}$. The reference electronic density n^0 and the localized Wannier functions χ are defined at any given lattice structure $\mathbf{R}$ and depend parametrically on it. However, the reference occupation matrix d^0_{ab} is independent of the lattice structure and characterizes the reference Born-Oppenheimer PES. Consequently, the central quantity on which we develop the electronic energy E_{el} is the *deformation occupation matrix*

$$D_{ab} = d_{ab} - d^0_{ab}, \tag{3.41}$$

where d refers to a general density

$$n(\mathbf{r}, \mathbf{R}) = \sum_{ab} d_{ab} \chi_a(\mathbf{r}, \mathbf{R}) \chi_b(\mathbf{r}, \mathbf{R}). \tag{3.42}$$

D_{ab} captures the difference of two given densities at a given lattice structure. Furthermore, for magnetic systems we introduce the up- and down-spin *deformation occupation matrix*

$$D^{\uparrow}_{ab} = d^{\uparrow}_{ab} - \frac{1}{2} d^0_{ab} \tag{3.43}$$

$$D^{\downarrow}_{ab} = d^{\downarrow}_{ab} - \frac{1}{2} d^0_{ab}, \tag{3.44}$$

where we presuppose a *non-magnetic* reference occupation matrix d^0. Further, it is convenient to introduce the total deformation occupation matrix

$$D^U_{ab} = D^{\uparrow}_{ab} + D^{\downarrow}_{ab} \tag{3.45}$$

and spin difference deformation occupation matrix

$$D^I_{ab} = D^{\uparrow}_{ab} - D^{\downarrow}_{ab} \tag{3.46}$$

with which we can write after some algebra that can be found in [46] the electronic energy as a Hubbard model [54] tight binding Hamiltonian depending on D^U_{ab} and D^I_{ab}

$$\begin{aligned} E_{el}(\{\mathbf{u}\}, \eta, D) = &\sum_{ab} D^U_{ab} \gamma_{ab}(\{\mathbf{u}\}, \eta) \\ &+ 1/2 \sum_{ab} \sum_{a'b'} D^U_{ab} D^U_{a'b'} U_{aba'b'} - D^I_{ab} D^I_{a'b'} I_{aba'b'}, \end{aligned} \tag{3.47}$$

where the first term gathers the one electron tight binding interactions γ_{ab} and the second term the two electron interactions depending on Hubbard U and Stoner I parameters. The matrix elements γ_{ab} gather electrostatic interactions created by the electrons and nuclei acting on the

Wannier functions χ_a and χ_b. At the reference geometry it is calculated by

$$\begin{aligned}\gamma_{ab}(R^0) &= \left\langle \chi_a(R^0) \middle| \widehat{h}_0(R^0) \middle| \chi_b(R^0) \right\rangle \\ &= \int d^3r \chi_a(\vec{r}, R^0) h_0(\vec{r}, R^0) \chi_b(\vec{r}, R^0),\end{aligned} \tag{3.48}$$

where $\widehat{h}_0(R^0)$ and $h_0(\vec{r}, R^0)$ refer to the one electron Kohn-Sham Hamiltonian at the reference structure R^0. Eventually, γ_{ab} is the target property of the second-principles fitting by a polynomial function. Therefore, Eq. (3.48) is evaluated on a given set of nuclear configurations $\{\mathbf{r}\}$ to create a TS of γ matrices whose dependence on the nuclear configuration can then be fitted by

$$\gamma_{ab}(\mathbf{r}) = \gamma_{ab}(R^0) + \sum_{\lambda\nu} \left[-\vec{f}^T_{ab,\lambda\nu} \Delta\vec{r}_{\lambda\nu} + \sum_{\lambda'\nu'} \Delta\vec{r}^T_{\lambda\nu} \overleftrightarrow{g}_{ab,\lambda\nu\lambda'\nu'} \Delta\vec{r}_{\lambda'\nu'} \right], \tag{3.49}$$

where λ,ν,λ',ν' refer abbreviated to atoms i in cells l, $\Delta\vec{r}_{\lambda\nu}$ is the relative displacement between atoms λ and ν, and $\vec{f}$ and $\overleftrightarrow{g}$ are the first and second-rank tensors that describe the one-electron interactions coupling to the lattice at linear and harmonic order. The relative displacement of atoms λ and ν can be decomposed into atomic displacements $\vec{u}$ and homogeneous strain components η,

$$\Delta\vec{r}_{\lambda\nu} = \eta(\vec{R}_l - \vec{R}_k + \tau_i + \tau_j) + \vec{u}_i - \vec{u}_j, \tag{3.50}$$

which gives the actual dependence of γ on atomic displacements and homogeneous strain. Finally, we can write the total energy of an second-principles model including some electronic degrees of freedom by the sum of the energy of the reference structure, the lattice effective energy and the electronic energy

$$E_{tot}(\{\mathbf{u}\}, \eta, D) = E_0(\mathbf{R^0}) + E_{eff}(\{\mathbf{u}\}, \eta) + E_{el}(\{\mathbf{u}\}, \eta, D). \tag{3.51}$$

We note that if E_{eff} and E_{el} have been constructed by fitting the same Born-Oppenheimer PES characterized by a specific occupation D the electronic contribution to the total energy is zero at any given lattice structure when the electronic system is in its reference state due to $D = 0$. E_{el} only gives a finite electronic correction energy for electronic excitations away from the reference electronic density. This means that an electronic model description can be added to an established lattice model *a-posteriori* and both can be constructed independently as they have no overlapping energy contribution.

However, the definition of a reference density is only trivial if there is a clear ground state Born-Oppenheimer PES as for non-magnetic band insulators. In more complex electronic situations like metallic and/or magnetic materials with closely competing electronic configurations the definition and enforcement of a specific electronic configurations in *ab initio* calculations to extract reference electronic and lattice parameters is less trivial and the target of ongoing research.

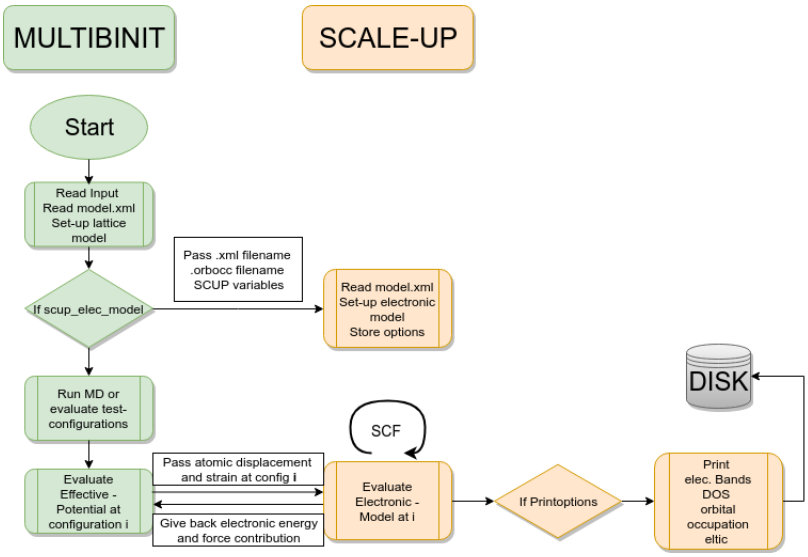

Figure 3.11: Illustration of the MULTIBINIT SCALE-UP interface.

3.3.2 The MULTIBINIT SCALE-UP Interface

The Interface between the lattice atomistic and effective electronic part between MULTIBINIT and SCALE-UP has been set up during a research stay at the University of Cantabria. Essentially it puts Eq. (3.51) to practice where *Multibint* calculates E_{eff} and SCALE-UP E_{el}[4].

MULTIBINIT uses SCALE-UP as a library extension to which it has to be linked during compilation. MULTIBINIT and SCALE-UP use both the *.xml* format to store the effective lattice respectively electronic parameters. Therefore, a global model file is defined in which lattice and electronic parameters are stored and whose name is passed from MULTIBINIT to SCALE-UP. The principal working mechanism for the evaluation of the energy, forces, and stresses at a given lattice configuration is that MULTIBINIT passes the atomic displacements $\{\mathbf{u}\}$ and homogeneous strain tensor η to SCALE-UP where Eq. (3.47) is solved self consistently and the electronic energy, force, and stress contribution is given back to MULTIBINIT. The occupations of the Wannier functions might be specifically initialized to e.g. force the relaxation of a specific magnetic order by specifying a file that contains the values of the *deformation occupation matrix* D. Finally, print options for electronic quantities calculated by SCALE-UP can be set in the input of MULTIBINIT, which will be written to the disk by SCALE-UP. Current possibilities to be saved include the electronic band structure, the electronic Density of Sates, the orbital occupation D, and the so-called eltic file containing information on local dipoles.

4: The same applies to the forces and stresses. Forces and stresses stemming from E_{eff} are derived inside MULTIBINIT and those from E_{el} inside SCALE-UP.

Part II

Degenerate Electronic States Interacting with Lattice Degrees of Freedom

Introduction

The calculation applications on $LaMnO_3$ and on the alkaline earth ferrite perovskites series $AFeO_3$ with A=Ca, Sr, Ba that we present in chapters 6 and 7 deal with perovskites that are metals at high temperature but become insulating at lower temperatures. As such these materials behave entirely oppositely to ordinary metals whose conductivity increases with decreasing temperature. At the metal-insulator transition (MIT) these materials show a joint appearance of electronic localization through ordered local orbital occupations and a cooperative lattice distortion. A couple of closely connected theories have been proposed to understand this MIT. We present them here in shorthanded manner to situate our own work.

The first theory proposed to understand these MITs is the Jahn-Teller Effect (JTE) which shows the existence of a strong coupling between degenerate electronic states in a molecule and its nuclear degrees of freedom [55]. The work by *Hermann Jahn* and *Edward Teller* whose principal idea goes back to a discussion between Teller and *Lev Landau* [56] has to be recognized as one of the greatest exploits of group theory to quantum mechanical problems. We introduce their work and the consecutive application to the transition metal octahedron relevant to the perovskite structure in chapter 4.

The JTE has been thereupon straightforwardly applied to perovskites like $LaMnO_3$, where the octahedra with locally degenerate states are connected through their corners. The appearance of the lattice distortion at the MIT is then explained by a cooperative arrangement of the locally induced distortions and has been called the cooperative Jahn-Teller effect (CJTE). We introduce the ideas of the CJTE in section 5.3.1. In some slight opposition to the CJTE stays the work of *Kugel* and *Khomskii* [57] that instead highlights the inter-site electronic interactions through super-exchange that can introduce a spontaneous localization of electrons by orbital ordering without distortions of the lattice. The work has been branded the Kugel-Khomskii model and is introduced in section 5.3.2. Finally, in section 5.3.3 we introduce the work of *Rudolf Peierls* that explains the MIT from a different perspective. He showed that for certain band fillings a distortion that breaks the translational symmetry of the lattice can lower the total electronic band energy by opening a band gap at the Fermi level.

Moreover, in section 5.1 we introduce a canonical notation for all distortions in the perovskite structure that deform the oxygen octahedral cages and are connected to MITs. We apply this new notations to our study on $LaMnO_3$ and the $AFeO_3$ series.

Distortions Induced by Degenerate Electronic States: The Jahn-Teller Effect

4

In 1937 *Jahn* and *Teller* published a work stating that in a molecule "*stability and* (orbital) *degeneracy are not possible simultaneously unless the molecule is a linear one* [...]." [55]. The geometric instability of a molecule containing an orbitally degenerate state is introduced by the so-called vibronic-coupling terms. These couple the degenerate electronic state linearly to a vibrational mode coordinate Q_k. The strength of the coupling is expressed in

$$\alpha_{JT} = \left\langle \Psi_i^0 \middle| \frac{\partial H_0}{\partial Q_k} \middle| \Psi_j^0 \right\rangle, \tag{4.1}$$

where Ψ_i^0, Ψ_j^0 are degenerate electronic states in a high symmetry structure R^0 of the molecular system and H_0 is the Hamiltonian of the unperturbed system. The intuitional idea of the vibronic coupling terms is that the vibrational coordinate Q_k must be such that its application to the molecular geometry removes the degeneracy and brings the molecule to an energetically lower lying non-degenerate state.

At the center of the work of *Jahn* and *Teller* is the symmetrical analysis of the matrix elements of Eq. (4.1). To do so, they express the vibrational mode coordinate Q_k in irreducible representations of the group of the reference structure R^0. Then, one can recognize that the variation of the nuclear potential and therefore the variation of the Hamiltonian H_0 transforms with the same symmetry as the vibrational coordinate Q_k. Eq. (4.1) is then finite under the condition that the direct product of the symmetry representations of the electronic states and the vibrational coordinate contains the identical symmetric representation in the reference group

$$a_{1g} \subset \Gamma_{ikj} = \Gamma_i^* \otimes \Gamma_k \otimes \Gamma_j, \tag{4.2}$$

where Γ are irreducible symmetric representations of the degenerate electronic state Ψ_i^0, Ψ_j^0 and the vibrational coordinate Q_k and the asterisk denotes the complex conjugate. As long as we are only interested in the orbital degeneracy we can skip the spin coordinates of the wave function and chose them to be real. Then, the characters $\chi_{ikj}(R)$ for each symmetry element R of the reference group of the product Γ_{ikj} are given by

$$\chi_{ikj}(R) = \chi_i(R)\chi_k(R)\chi_j(R) \tag{4.3}$$

and can be calculated by using the character table of the reference group. To find the symmetric representation Γ_k of the vibrational coordinate Q_k that fulfils (4.2) one can alternatively define that Γ_k must be contained in the direct product of the symmetric representations of the wave functions

$$\Gamma_k \subset \Gamma_i \otimes \Gamma_j, \tag{4.4}$$

which is possible since the product (4.2) is commutative as long as the wavefunctions are real. Finally, in the orbitally degenerate case Γ_i and Γ_j belong necessarily to the same multidimensional irreducible representation γ. Moreover, trivially (4.1) must be Hermitian under the

exchange of i and j. With these two properties the right hand side of (4.4) can replaced by the direct symmetric product of multidimensional irreducible subspace γ with itself

$$\Gamma_k \subset [\Gamma_{\gamma i} \otimes \Gamma_{\gamma j}]^+ = [\Gamma_\gamma^2]^+. \tag{4.5}$$

The characters of $[\Gamma_\gamma^2]^+$ at the symmetry element R of the reference group are calculated by

$$[\chi_\gamma^2(R)]^+ = \frac{[\chi_\gamma(R)]^2 + \chi_\gamma(R^2)}{2}. \tag{4.6}$$

To identify the symmetry of vibrational coordinate Γ_k the reducible representation $[\Gamma_\gamma^2]^+$ can then be decomposed into irreducible representations of the reference representation

$$[\Gamma_\gamma^2]^+ = \bigoplus_{j=1,n_k} a_j \Gamma_j, \tag{4.7}$$

where n_k is the number of classes of the reference group. The coefficients a_j are then calculated by a scalar product between direct symmetrical product $[\Gamma_\gamma^2]^+$ and the irreducible representations of the reference group Γ_j by using the respective characters

$$a_j = \frac{1}{h} \sum_{k=1}^{n_k} N_k \chi_j(R_k) [\chi_\gamma^2(R_k)]^+, \tag{4.8}$$

where h is the order of the reference group and N_k is the number of elements in the class of the symmetry element R_k. For a good comprehensive introduction to the symmetric analysis of orbitally degenerate molecular states with an introduction to group theory we refer to a lecture of *Pavarini* [58] and an introductory chapter of *Breza* [59] on which this section is mainly based.

4.1 The Jahn-Teller Effect in Action: The Octahedral Transition Metal Complex

Jahn and *Teller* wrote down the possible vibrational symmetries in all point groups and the direct symmetrical product of degenerate representations for all space groups. In conjunction with their theorem outlined in the section above one can then easily identify the symmetry representation of a specific vibrational coordinate that is instable in a molecule of a given point group and degenerate electronic state. What was left to do for researchers was then to work out the actual vibrational coordinates for a given molecule that have the necessary symmetry property and work out the ground state amplitude of a given distortion. *Van Vleck* studied the octahedral transition metal complex MX_6, where the transition metal cation M builds the center and the anions X the corners of an octahedron (point group: O_h), embedded in an external crystal field [60]. The fivefold degenerate d states of the transition metal M within the ligand field of the anions X will be split into a threefold degenerate set of lower lying orbitals (d_{xy}, d_{xz}, d_{yz}) with t_{2g} symmetry and a twofold degenerate set of higher energetic orbitals ($d_{z^2-r^2}, d_{x^2-y^2}$) with e_g symmetry. The direct

symmetrical product of the e_g and t_{2g} representation with the point group O_h with themselves are

$$[e_g^2]^+ = a_{1g} \oplus e_g \tag{4.9}$$

$$[t_{2g}^2]^+ = a_{1g} \oplus e_g \oplus t_{2g}. \tag{4.10}$$

Therefore, degeneracy of the e_g electronic states can be lifted by the application of a distortion with e_g symmetry and the degeneracy of the t_{2g} by a distortion of e_g or t_{2g} symmetry.

From the 21 degrees of freedom of the octahedral complex *Van Vleck* wrote down six normal mode coordinates that belong to irreducible representations a_{1g}, e_g, and t_{2g} and labeled them from Q_1 to Q_6 (see Fig. 4.1).

The mode Q_1 belongs to the a_{1g} representation and can be described as the volume expansion/contraction mode of the octahedron (see Fig. 4.1 a). However, Q_1 does obviously not play a role in removing the degeneracy of the transition metal's d states. For the treatment of the octahedron it can be assumed that the reference structure R_0 resides at relaxed volume respectively relaxed Q_1 amplitude.

The modes Q_2 and Q_3 belong to the e_g representation and are hence degenerate in the ideal octahedron. Q_2 can be described as a two-dimensional rhombic distortion reducing the symmetry of the octahedron from O_h to D_{2h} (see top of Fig. 4.1 b). The mode Q_3 is a tetragonal elongation/-contraction (depending on the sign of the distortion) with the tetragonal unique axis being the normal axis of the rhombic plane of the Q_2 mode (see bottom of Fig. 4.1 b). The application of Q_3 reduces the symmetry of the octahedron from O_h to D_{4h}.

The modes Q_4, Q_5, and Q_6 belong to the t_{2g} representation and are degenerate in the ideal octahedron. They can be described as the three possible shears of the octahedron. We show one of the possible shears in Fig. 4.1 c). The others are imagined easily by changing the normal axis of the shearing plane.

In what follows we describe how to find the ground state of the octahedral transitional metal complex with a degenerate electronic e_g state. Such a state is given if either one or three electrons (respectively one hole) occupy the e_g states in the ideal octahedron.

To start, we write perturbative development of the electronic Hamiltonian until second order in the two dimensional normal mode basis $Q = \{Q_2, Q_3\}$

$$H_e(Q) = H_0 + \sum_{i=2,3} \frac{\partial H_0}{\partial Q_i} Q_i + \sum_{i=2,3} \sum_{j=2,3} \frac{\partial^2 H_0}{\partial Q_i \partial Q_j} Q_i Q_j, \tag{4.11}$$

$$H_e(Q) = H_0 + H_e^1(Q) + H_e^2(Q), \tag{4.12}$$

where H_0 is the electronic Hamiltonian of the reference structure (the ideal octahedron with O_h symmetry). The second order perturbative sum can be directly reduced to diagonal elements in the vibrational

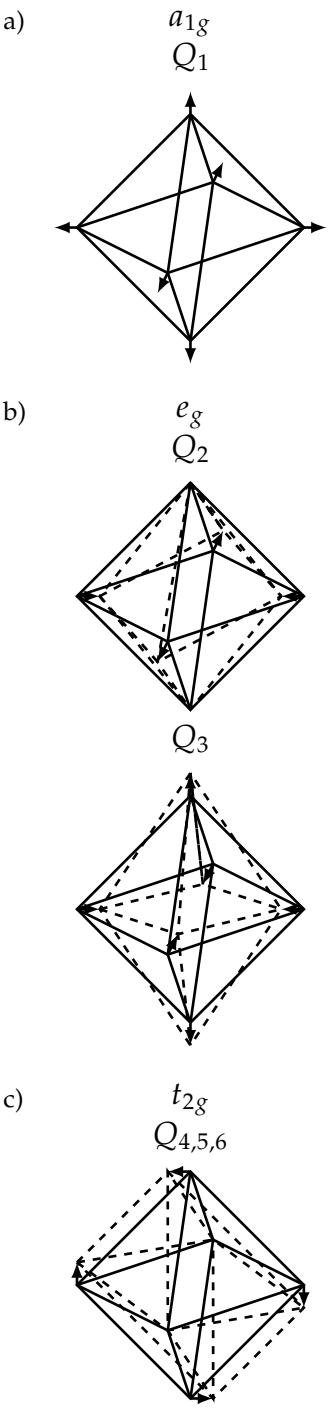

Figure 4.1: Symmetrized normal modes in the octahedron (point group O_h) as noted by *Van Vleck* relevant to transition metal octahedra with degenerate t_{2g} or e_g states. a) Mode Q_1 volume expansion/contraction belonging to irreducible representation a_{1g}. b) Mode Q_2 and Q_3 belonging to the irreducible representation e_g. Q_2 is a two-dimensional rhombic distortion and Q_3 a tetragonal distortion of the octahedron. c) Q_4,Q_5, and Q_6 the three possible shears of the octahedron belonging to the irreducible representation t_{2g}.

coordinates due to their orthogonal properties

$$H_e^2(Q) = \sum_{i=2,3} \frac{\partial^2 H_0}{\partial Q_i^2} Q_i^2. \tag{4.13}$$

To get the energy eigenvalue of (4.12) we multiply from the right $\left|\phi_k\right\rangle$ and from the left $\left\langle\phi_{k'}\right|$, where $\left|\phi_k'\right\rangle, \left|\phi_k\right\rangle \in \{\left|x^2-y^2\right\rangle, \left|z^2-r^2\right\rangle\}$

$$\begin{aligned} E_{k'k}(Q) &= \left\langle\phi_{k'}\middle|H_e(Q)\middle|\phi_k\right\rangle \\ &= E^0_{k'k} + \underbrace{\sum_{i=2,3}\left\langle\phi_{k'}\middle|\frac{\partial H_0}{\partial Q_i}\middle|\phi_k\right\rangle Q_i}_{=E^1_{k'k}(Q)=\sum_{i=2,3}\alpha_{JT}^{k'k,i}Q_i} + \underbrace{\sum_{i=2,3}\left\langle\phi_{k'}\middle|\frac{\partial^2 H_0}{\partial Q_i^2}\middle|\phi_k\right\rangle Q_i^2}_{E^2_{k'k}(Q)=\sum_{i=2,3}\beta^{k'k,i}Q_i^2}. \end{aligned} \tag{4.14}$$

The values $E^0_{kk'}$ are the energy eigenvalues of the electronic states $\left|\phi_k\right\rangle$ in the reference structure. Their degeneracy is expressed by a unique value E^0 for every combination of k and k'. For the further discussion we can drop them by introducing

$$\epsilon(Q) = E(Q) - E^0 = E^1(Q) + E^2(Q). \tag{4.15}$$

In the first order perturbative energy term E^1 we recognize the vibronic coupling terms as introduced by *Jahn* and *Teller*. By using the *Slater-Koster* integrals [61] in combination with the normal mode coordinates the E^1 matrix can be completely determined [58] with a unique vibronic coupling constant α_{JT}

$$E^1(Q) = \begin{pmatrix} E^1_{kk}(Q) & E^1_{kk'}(Q) \\ E^1_{k'k}(Q) & E^1_{k'k'}(Q) \end{pmatrix} = \alpha_{JT}\begin{pmatrix} Q_3 & Q_2 \\ Q_2 & -Q_3 \end{pmatrix}. \tag{4.16}$$

Eq. (4.16) can be further decomposed to

$$E^1(Q) = \alpha_{JT}(Q_3\sigma_z + Q_2\sigma_x) \tag{4.17}$$

using the Pauli matrices

$$\sigma_z = \begin{pmatrix} 1 & 0 \\ 0 & -1 \end{pmatrix} \tag{4.18}$$

$$\sigma_x = \begin{pmatrix} 0 & 1 \\ 1 & 0 \end{pmatrix}. \tag{4.19}$$

The second order perturbative energy is given by

$$E^2(Q) = \beta(Q_2^2 + Q_3^2), \tag{4.20}$$

which is the potential of a two dimensional harmonic oscillator with a unique force constant β, which in general is positive. To find the ground state it is finally sufficient to minimize the potential energy[1]

$$\epsilon(Q) = \alpha_{JT}(Q_3\sigma_z + Q_2\sigma_x) + \beta(Q_2^2 + Q_3^2). \tag{4.21}$$

To do so, it is useful to transform Q_3 and Q_2 into polar coordinates

1: In doing so we omit the kinetic energy of the nuclei as well as non-adiabatic couplings between the two Born-Oppenheimer energy sheets associated to the states k and k'

$Q_3 = q\cos\theta$ and $Q_2 = q\sin\theta$. Putting these definitions in (4.21) gives

$$\epsilon(Q) = \alpha_{JT} q(\cos\theta\sigma_z + \sin\theta\sigma_x) + \beta q^2. \tag{4.22}$$

Eq. (4.22) has two eigenvalues $\{+1, -1\}$ so that for each angle θ we find two branches

$$\epsilon^-(q) = -\alpha_{JT} q + \beta q^2, \tag{4.23}$$
$$\epsilon^+(q) = +\alpha_{JT} q + \beta q^2, \tag{4.24}$$

corresponding to the two states k, k' that were originally degenerate in the ideal octahedron and are split upon the application of a distortion q. The potential energy surface is hence invariant with respect to the angle θ and called the *mexican hat* (see Fig. 4.2). There is an infinite number of minima lying on a circle with the radius $q_{min} = \frac{\alpha_{JT}}{2\beta}$ with a stabilization energy $E_{JT} = \frac{-\alpha_{JT}^2}{2\beta}$. The eigenfunctions corresponding to (4.23) and (4.24) are [58, 62]

$$|\Psi^-\rangle = \cos\frac{\theta}{2}\left|z^2 - r^2\right\rangle - \sin\frac{\theta}{2}\left|x^2 - y^2\right\rangle, \tag{4.25}$$
$$|\Psi^+\rangle = \sin\frac{\theta}{2}\left|z^2 - r^2\right\rangle + \cos\frac{\theta}{2}\left|x^2 - y^2\right\rangle .. \tag{4.26}$$

Thus, the angle θ is a direct measure of the nature of the electronic ground state. For $\theta = 0°$ the ground state is a pure occupation of the $d_{z^2-r^2}$ orbital and for $\theta = 180°$ of the $d_{x^2-y^2}$ orbital. For $\theta = 90°$ a mixed $d_{z^2-r^2}/d_{x^2-y^2}$ state is observed. Since θ can be calculated by

$$\theta = \arctan\frac{Q_2}{Q_3}, \tag{4.27}$$

the occurring distortions are a direct measurement of the stabilized electronic state.

However, the result of the expansion until harmonic order would mean that although the distortion removes the electronic degeneracy there is no unique ground state. Later, *Öpik* and *Pryce* [63] extended the potential energy expansion to the third order by adding the term

$$E^3(Q) = \gamma(Q_3^3 - 3Q_3Q_2^2) = \gamma q^3\cos 3\theta, \tag{4.28}$$

which at third order is the sole invariant term in the space $Q = \{Q_2, Q_3\}$. This term leads to a warping of the mexican hat potential energy surface with three distinct minima 120° away from each other (see Fig. 4.3). If γ is negative the minima lie at $0°, 120°, 240°$ with saddle points in between. The minima correspond to the three possible tetragonal elongations of the octahedron. If γ is positive the positions of minima and saddle points inverse. Then, the minima are lying at $180°, 300°, 60°$ and are corresponding to the three possible compressions of the octahedron. γ is often observed to be negative and the ground state of the ideal octahedron with a degenerate e_g state is tetragonally elongated [63]. The derivations presented here are mainly based on a lecture of *Pavarini* [58], but can be found in many textbooks and scientific articles (e.g. without seeking completeness in Refs. [62–67] and naturally in the work of *Van Vleck* [60]).

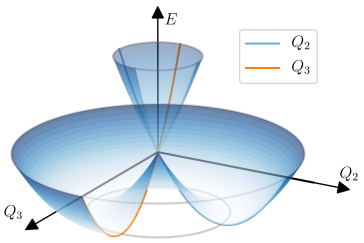

Figure 4.2: Mexican hat potential energy surface in the Q_2/Q_3 plane as defined by Eq. (4.22). The minima are lying on circle (shown in grey) with the radius $q_{min} = \frac{\alpha_{JT}}{2\beta}$ with a stabilization energy $E_{JT} = \frac{-\alpha_{JT}^2}{2\beta}$.

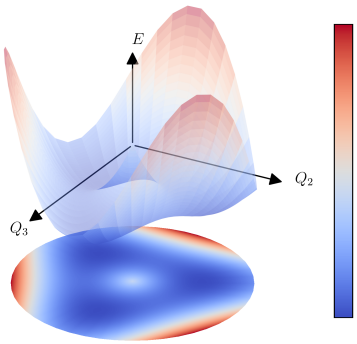

Figure 4.3: Warped Mexican Hat potential energy surface defined with negative third order coupling constant γ (see Text). The minima are lying at 0°,120°,and 240° corresponding to the three possible tetragonal elongations of the ideal octahedron.

Connected Jahn-Teller Centers 5

In the preceding chapter we laid out the group theoretical foundation of the JTE and its specific consequence to an *isolated* transition metal octahedron with a degenerate e_g state. The ground state of such an octahedron is a tetragonal elongation with the occupation of the $d_{z^2-r^2}$ state. In this chapter we give an introduction to perovskite materials where transition metal octahedra with degenerate e_g states are connected through their corners. Those materials show a metallic behavior at high temperature and experience a MIT upon cooling. At the MIT a cooperative distortion of the octahedra occurs. As we will see, there are several distinct cooperative distortions found in different material systems. Although these cooperative distortions have been extensively studied at least since the 1950s (see Ref. [68] and references therein) no common notation of cooperative distortions associated to MITs has been established. Therefore, we present in section 5.1 a canonical notation that defines a *unique* symbol for *all* cooperative Jahn-Teller like distortions based on *Van Vleck's* notation (see section 4.1) taking into account the translational character. In section 5.2 we give a shorthand overview to some materials with degenerate e_g states and the cooperative distortions appearing at the MIT, which do in general *not* experience a tetragonal elongation of the octahedra but a strong rhombic Q_2 distortion with a small tetragonal Q_3 compression. Finally, we give a short overview of three theoretical concepts related to the MIT: the cooperative Jahn-Teller effect (CJTE) (section 5.3.1), the Kugel-Khomskii model (section 5.3.2), and the Peierls transition (section 5.3.3).

5.1 A Canonical Notation for Cooperative Jahn-Teller distortions in Perovskites

The problem of the Jahn-Teller instability in isolated MX_6 octahedra was soon transferred to periodic solids, in which each unit cell contains a Jahn-Teller ion. Amongst them are the ABX_3 perovskites with their corner-shared BX_6 octahedral network. Jahn-Teller instabilities occur in ABX_3 perovskites with an odd occupation of the B-cation's e_g orbitals, such as rare-earth manganites $RMnO_3$ ($d^4 = e_g^1$), $KCrF_3$ ($d^4 = e_g^1$) [69], $KCuF_3$ ($d^9 = e_g^3$) [70], or with an incomplete occupation of the t_{2g} orbitals such as rare-earth titanates $RTiO_3$ ($d^1 = t_{2g}^1$) [71, 72] and rare-earth vanadates RVO_3 ($d^2 = t_{2g}^2$) [73]. The key difference between the isolated problem studied by *Van Vleck* and the perovskites with connected Jahn-Teller centers lies in the direct neighboring of the Jahn-Teller ions. As a first consequence, the lattice of sites implies that the degenerate electronic states form continuous electronic bands instead of well-defined orbital states. As a second consequence, individual distortions are transferred between octahedral sites. The network allows nonetheless for some phase freedom in the cooperative arrangement of the distorted octahedra. This

additional freedom enables the system to achieve the same individual octahedral distortion from different cooperative orderings. Regardless, in perovskites where each of the interconnected octahedron contains a Jahn-Teller active ion, it is usual to quantify the amplitude of Q_2 and Q_3 distortions based on $B-O$ distances in absolute coordinates. This notation quantifies the distortion of one *individual* octahedron. It does not indicate the cooperative arrangement of the distorted octahedra nor distinguish condensed phonon-type distortions from homogeneous lattice strain. At the same time, the quantification and notation of $Q_4 - Q_6$ distortions seems to have been dropped in latter years (the last occurrence we found dates back to 1997 [74]).

Carpenter and *Howard* gave a different notation based on the ISOTROPY software suite and associating Jahn-Teller ordering schemes with labels of irreducible representations (irrep) and ordering parameters [75]. These symmetry labels are unique and distinguish between strain and phonon modes. Moreover, the symmetry-adapted analysis allows to quantify the amplitudes of Jahn-Teller distortions in their own subspace, such that they can be separated from other distortions in the crystal lattice as octahedral rotations or antipolar motions. Finally, by creating invariant polynomial terms between the subspace of the Jahn-Teller distortions and other lattice distortions, the order, sign and strength of couplings between those different distortions can be studied. This makes the decomposition of lattice distortions into orthogonal irreducible subspaces a very powerful approach. However, the application of the symmetry analysis has not found widespread application. A reason might be that the connection between the *Van-Vleck*-numbering and the irrep labels is not obvious.

In the context of a first-principles study of $RNiO_3$ rare-earth nickelates, *He* and *Millis* [76] defined labels Q_x^k (which could be said to be inspired by *Kanamori* [67]) with x a number indicating a local pattern (different from *van Vleck's*) and k the label associated to high symmetry k-points in the cubic Brillouin zone. Through the phase factor $e^{i\vec{k}\vec{x}}$, the k-label emphasizes the cooperative arrangement. However, they only labeled the modes of interest in their study, without labeling all possibilities.

Here, we introduce canonical notations defining a unique symbol for all possible cooperative Jahn-Teller distortions in the perovskite structure. Our canonical symbols have the form $Q_{i\alpha}^{\vec{q}}$. The subscript i indicates the local distortion pattern and takes the enumeration of the octahedral normal modes from *Van-Vleck*. The second subscript α is necessary for non-isotropic local patterns that break the cubic symmetry of the octahedra (all besides Q_1): it identifies the alignment of the unique feature of the local distortion pattern with respect to the perovskite lattice. It takes the values x, y, z, which are defined to lie along the cubic perovskite lattice axes. For a two-dimensional local distortion pattern, the unique feature is the axis orthogonal to the two-dimensional distortion plane (applies to Q_2 and Q_4). For a one or three dimensional local distortion pattern it shows the Cartesian axis along the unique feature. Finally, the superscript $\vec{q}$ is the label of the reciprocal space vector according to which the local mode is translating in the crystal. Within this work, we limit $\vec{q}$ to zone center ($\mathbf{\Gamma} = (0,0,0)$) and zone boundary modes at high symmetry $\vec{q}$ points. The zone center $\mathbf{\Gamma}$ is thereby associated to lattice strains. However, there is no inherent limitation of the notation to the high symmetry $\vec{q}$ -points. In the cubic Brillouin zone, the high-symmetry $\vec{q}$ points at the zone

boundary are **X** = (½, 0, 0), **M** = (½,½, 0), and **R** = (½,½,½). The power of using such high-symmetry $\vec{q}$ points lies in their unique definition of the cooperative arrangement of the local distortion pattern and thereby also the related orbital ordering. In analogy to magnetic orderings, **Γ** leads to *ferro*, **X** to a planar or *A-type*, **M** to a columnar or *C-type*, and **R** to a checkerboard or *G-type* arrangement. The freedom of the phase-factor depends on the local distortion pattern, since the corner-shared atoms imply the opposite displacement of neighboring octahedra. The resulting notations for all local patterns at the high symmetry points are shown in Table 5.1. Additionally, Table 5.1 shows the crystal symmetry achieved by condensing the individual cooperative modes in the $Pm\bar{3}m$ space-group, the local octahedral symmetry only taking into account the MX_6 complex, and the label of the irreducible subspace with the origin of the cubic perovskite unit cell set on either *A* or *B* cation.

The Q_1 mode is related to a homogeneous expansion/contraction of the volume of individual octahedra. It appears as a lattice strain at **Γ**. As in the molecular case, it can be omitted by choosing a reference stationary with respect to $Q_1^{\mathbf{\Gamma}}$. Since the local distortion pattern is three dimensional, Q_1 is limited to $\vec{q}$ between **Γ** and **R**. $Q_1^{\mathbf{R}}$ is often called the breathing type distortion and associated to charge ordering [77, 78]. Two additional modes changing the volume of local octahedra can be thought of. First, a mode that alters one bond axis (uniaxial volume change) and, second, two octahedral axis (planar volume change). In the molecular case, these distortions do not appear as normal modes as they are not orthogonal to Q_1 and Q_3. Since in solids these modes have been shown to be connected to charge ordering [79], we associate equally a Q_1-label to them. In the periodic perovskite crystal, the uniaxial volume change appears as a irreducible mode at **X** ($Q_{1\alpha}^{\mathbf{X}}$) and the planar volume change at **M** ($Q_{1\alpha}^{\mathbf{M}}$ in Table 5.1). At the other high-symmetry q-points of the cubic Brillouin zone, the uniaxial and planar volume changes are (equivalently to the case of an isolated octahedron) not orthogonal to the other modes presented in Table 5.1. Indeed, at the **M** point, the uniaxial volume change is represented by a sum of $Q_{1\alpha}^{\mathbf{M}}$ and $Q_{2\alpha}^{\mathbf{M}}$ while, at the **R** and **Γ** points, the volume changes are represented by sums of $Q_1^{\mathbf{R/\Gamma}}$, $Q_{2\alpha}^{\mathbf{R/\Gamma}}$ and $Q_{3\alpha}^{\mathbf{R/\Gamma}}$ (respectively the subspaces R_2^-/R_3^- and Γ_1^+/Γ_3^+).

The Q_2 modes are two-dimensional and can hence translate with **Γ**, **M**, and **R**. They reduce the local symmetry to D_{2h} stabilizing a mixed $d_{z^2-r^2}/d_{x^2-y^2}$ state.

The Q_3 modes are three-dimensional and hence appear at **Γ** and **R**. They reduce the local symmetry to D_{4h} stabilizing, either a $d_{x^2-y^2}$ or a $d_{z^2-r^2}$ state for tetragonal compression or extension respectively.

At **Γ** and **R**, Q_2 and Q_3 form a two-dimensional subspace equivalent to the Q_2/Q_3 space of the isolated Jahn-Teller center. However, an intriguing difference to the isolated center is the appearance of $Q_{2\alpha}^{\mathbf{M}}$ in its own subspace. This gives an additional degree of freedom for cooperative Jahn-Teller distortions of connected Jahn-Teller centers.

Table 5.1: Canonical labels $Q_{i\alpha}^{\vec{q}}$ for cooperative Jahn-Teller distortions in solids with octahedral corner shared networks. The first subscript i refers to the *Van Vleck's* numbering of normal modes in the isolated octahedron. The second subscript α defines the unique axis of the local distortion pattern. α is not necessary for the isotropic deformations $Q_1^{\mathbf{\Gamma}}$ and $Q_1^{\mathbf{R}}$. The superscript $\vec{q}$ refers to the reciprocal space vector with which the mode is translating. Shown are $\mathbf{\Gamma} = (0,0,0)$, $\mathbf{X} = (½,0,0)$, $\mathbf{M} = (½,½,0)$, and $\mathbf{R} = (½,½,½)$. $\mathbf{\Gamma}$ is associated to lattice strains. Octahedra drawn in red and blue experience opposite distortions.

Q_1 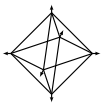		$Q_1^{\mathbf{\Gamma}}$	$Q_1^{\mathbf{R}}$	$Q_{1\alpha}^{\mathbf{X}}$ 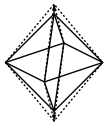	$Q_{1\alpha}^{\mathbf{M}}$ 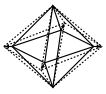
Origin in	A	$\Gamma_1^+\ (a)$	$R_2^-\ (a)$	$X_3^-\ (a,0,0)$	$M_4^+\ (a,0,0)$
Ref. $Pm\bar{3}m$	B	$\Gamma_1^+\ (a)$	$R_1^+\ (a)$	$X_1^+\ (a,0,0)$	$M_1^+\ (a,0,0)$
Displacement Pattern		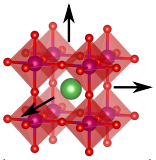	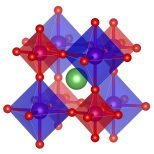	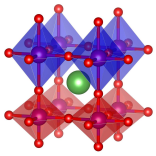	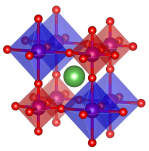
Strain Vector		$(a,a,a,0,0,0)$	-	-	-
Crystal Space Group (Schönflies)		$Pm\bar{3}m$ (O_h^1)	$Fm\bar{3}m$ (O_h^5)	$P4/mmm$ (D_{4h}^1)	$P4/mmm$ (D_{4h}^1)
Local Octahedral Symmetry		O_h	O_h	D_{4h}	D_{4h}

Q_2 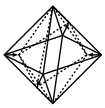		$Q_{2\alpha}^{\mathbf{\Gamma}}$	$Q_{2\alpha}^{\mathbf{M}}$	$Q_{2\alpha}^{\mathbf{R}}$	Q_3 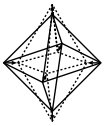	$Q_{3\alpha}^{\mathbf{\Gamma}}$	$Q_{3\alpha}^{\mathbf{R}}$
Origin in	A	$\Gamma_3^+\ (0,a)$	$M_3^+\ (a,0,0)$	$R_3^-\ (0,a)$		$\Gamma_3^+\ (a,0)$	$R_3^-\ (a,0)$
Ref. $Pm\bar{3}m$	B	$\Gamma_3^+\ (0,a)$	$M_2^+\ (a,0,0)$	$R_3^+\ (0,a)$		$\Gamma_3^+\ (a,0)$	$R_3^+\ (a,0)$
Displacement Pattern		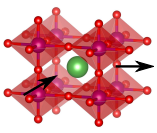	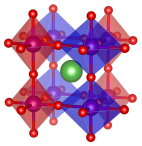	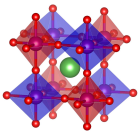		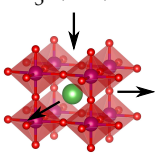	
Strain Vector		$(0,-a,a,0,0,0)$	-	-		$(-2a,a,a,0,0,0)$	-
Crystal Space Group (Schönflies)		$Pmmm$ (D_{2h}^1)	$P4/mbm$ (D_{4h}^5)	$I4/mcm$ (D_{4h}^{18})		$P4/mmm$ (D_{4h}^1)	$I4/mmm$ (D_{4h}^{17})
Local Octahedral Symmetry		D_{2h}	D_{2h}	D_{2h}		D_{4h}	D_{4h}

$Q_{4,5,6}$ 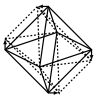		$Q_{4\alpha}^{\mathbf{\Gamma}}$	$Q_{4\alpha}^{\mathbf{M}}$	$Q_{4\alpha}^{\mathbf{R}}$
Origin in	A	$\Gamma_5^+\ (a,0,0)$	$M_1^+\ (a,0,0)$	$R_4^-\ (a,0,0)$
Ref. $Pm\bar{3}m$	B	$\Gamma_5^+\ (a,0,0)$	$M_4^+\ (a,0,0)$	$R_5^+\ (a,0,0)$
Displacement Pattern		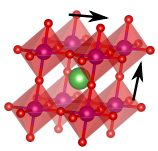	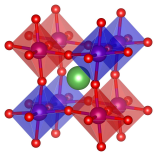	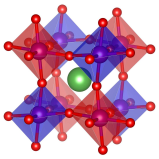
Strain Vector		$(0,0,0,a,0,0)$	-	-
Crystal Space Group (Schönflies)		$Cmmm$ (D_{2h}^{19})	$P4/mmm$ (D_{4h}^1)	$I4/mmm$ (D_{4h}^{17})
Local Octahedral Symmetry		D_{2h}	D_{2h}	D_{2h}

Finally, the Q_4 modes label the shear distortions. As they are two-dimensional, they appear at **Γ**,**M**, and **R**, being at each point threefold degenerated. This threefold degeneracy reflects the modes Q_5 and Q_6 in *Van Vleck's* numbering. The necessity of Q_5 and Q_6 falls away using the second subscript α in our notations. Q_4 modes reduce the local symmetry to D_{2h} albeit in a different way than Q_2 since the $B-O$ distances in the sheared plane stay degenerate.

All irreducible subspaces besides X_3^-/X_1^+ and R_4^-/R_5^+ given in Table 5.1 are formed exclusively by the corresponding Jahn-Teller displacements of the ions at the octahedral corners. In the subspaces X_3^-/X_1^+ and R_4^-/R_5^+ additional antipolar motions of A-cations are found. In X_3^-/X_1^+ the A-cations of [100]-planes move along the corresponding cubic axes. In the R_4^-/R_5^+ subspace, it is the case for A-cations of the [111]-planes (see also Fig. 6.1). Hence, it is expected that the condensation of a $Q_1^{\mathbf{X}}$ or $Q_4^{\mathbf{R}}$ distortion will induce the corresponding antipolar motion and vice versa.

Finally, we notice that the strains $Q_1^{\mathbf{\Gamma}}$, $Q_{2\alpha}^{\mathbf{\Gamma}}$, $Q_{3\alpha}^{\mathbf{\Gamma}}$, and $Q_{4\alpha}^{\mathbf{\Gamma}}$ represent a complete strain basis for the cubic perovskite system.

This canonical notation, defining a unique symbol for each cooperative Jahn-Teller distortion while distinguishing phonon-modes and lattice strains, will facilitate the discussion of perovskite systems experiencing static Jahn-Teller distortions. As it will be shown in the forthcoming of this work, the orthogonality of the decomposition is most powerful in the study of the interplay of Jahn-Teller distortions with other lattice distortions and strains.

5.2 Perovskite Materials with Connected e_g Jahn-Teller Centers

In this section we present the structural distortions of some characteristic perovskites with formally the degenerate e_g states that experience cooperative Jahn-Teller distortions in the low temperature orbitally ordered insulating phase. We present the distortions in the Q_2/Q_3 notation and then in our canonical Jahn-Teller distortion notation (CJTN) to emphasize the use of those. The materials are $KCrF_3$, $KCuF_3$, and $LaMnO_3$. All posses

Table 5.2: Cooperative Jahn-Teller distortions and MIT temperatures of three perovskite compounds with formally degenerate e_g states. The distortions are given in the Q_2/Q_3 notation as well as in the canonical Jahn-Teller distortion notation emphasizing the cooperative arrangement. $KCuF_3$ and $KCrF_3$ are cubic in the average befor the MIT, while $LaMnO_3$ shows a $a^-a^-c^+$ rotation pattern (in Glazer's notation [3]) before and after the transition.

Material	d^n	Q_2	Q_3	θ	CJTN[a]	rot. pattern	T_{JT}
$KCrF_3$	d^4	0.44[b]	-0.22[b]	116.84°, 243.16°	$0.24Q_{2z}^{\mathbf{R}} - 0.052Q_{3z}^{\mathbf{\Gamma}}$	-	923K[b]
$KCuF_3$	d^9	0.51[c]	-0.18[c]	109.00°, 251.00°	$0.25Q_{2z}^{\mathbf{R}} - 0.043Q_{3z}^{\mathbf{\Gamma}}$	-	800K[d]
$LaMnO_3$	d^4	0.38[b]	-0.12[b]	107.61°, 252.39°	$0.19Q_{2z}^{\mathbf{M}} - 0.040Q_{3z}^{\mathbf{\Gamma}}$	$a^-a^-c^+$	750K[e]

[a] Normalized with respect to cubic 5-atoms reference unit cell.
[b] Q_2 and Q_3 calculated from bond distances taken from Ref. [69]
[c] Q_2 and Q_3 calculated from bond distances taken from Ref. [80]
[d] Ref. [81]
[e] Ref. [82]

a formally degenerate e_g state at the cation B-site. In the case of $KCrF_3$ and $LaMnO_3$ the Cr^{2+} and Mn^{3+} d-states are occupied by four electrons. Due to strong Hund's coupling in the 3d shell a high spin configuration is preferred and the e_g states are occupied by one electron. In the case of $KCuF_3$ the d-states are occupied by 9 electrons which leads one hole in the e_g states. All materials experience a metal-insulator transition at an elevated temperature T_{JT} between 750K and 923K. At the transition strong cooperative Jahn-Teller distortions appear. $KCuF_3$ and $KCrF_3$ show the appearance of a strong Q_2 distortion that alternates between neighboring octahedra and somewhat smaller tetragonal compression that is the same for all octahedra. There are hence two different octahedral sublattices with equivalent distortions. The angle in the Q_2/Q_3 plane corresponding to the minima are in somewhat proximity to the 120° and 240° minima expected from the isolated octahedral problem. In the CJTN this reduces to a sum of $Q_{2z}^{\mathbf{M}}$ and a compressive (negative) strain $Q_{3z}^{\mathbf{\Gamma}}$. $LaMnO_3$ shows a similar local distortion with large alternating Q_2 distortion and smaller universal Q_3 compression. The Q_2 distortion is however ordered in a columnar arrangement. In the CJTN this reduces to $Q_{2z}^{\mathbf{M}}$ and a compressive tetragonal strain $Q_{3z}^{\mathbf{\Gamma}}$. In the calculation application section on $LaMnO_3$ (see ch. 6) we show that this change of ordered distortion is related to the rotation pattern that is present in $LaMnO_3$ but absent around the MIT in $KCuF_3$ and $KCrF_3$.

5.3 Theoretical Concepts Related to Cooperative Distortions at Metal-Insulator Transitions

5.3.1 The Cooperative Jahn-Teller Effect

The idea of the cooperative Jahn-Teller effect (CJTE) was first rigorously formulated by Kanamori [67]. In its essence the CJTE postulates to see a solid state material with connected Jahn-Teller centers as an accumulation of molecules that each experience a local Jahn-Teller effect and are coupled harmonically [62, 64]. The Hamiltonian is thus written as

$$H = \sum_N H_{JT}(Q_n) + \frac{1}{2}\sum_{n\neq m} Q_n^T K(n,m) Q_m, \tag{5.1}$$

where n and m reference to different lattice sites with a degenerate electronic state, Q_n is a normal coordinate vector at lattice site n and Q_n^T its transpose, H_{JT} is a local *Jahn-Teller* Hamiltonian as for example the Hamiltonian of the ideal octahedron with a degenerate e_g state that we presented in section 4.1, and $K(n,m)$ is a interaction matrix between sites n and m in dependence of the normal mode distortion. In some formulations the Hamiltonian is then decomposed into strain and phononic contributions [67, 83] (like our CJTN does for the decomposition of different cooperative distortions) to introduce different vibronic and harmonic constants for vibrational and elastic deformations. The integration of the intersite coupling K is usually solved by a *mean field* approach [84], but becomes rather complex. However, the main result is that in the static picture the deviations of the local distortion from the isolated case to the

cooperative one and the stabilized ground state cooperative distortion stem from the intersite coupling [62, 64, 83, 85]. The orbital ordering is in this picture a secondary consequence of the harmonical intersite interaction.

5.3.2 The Kugel-Khomskii Model: Orbital Order induced by Superexchange

Kliment Kugel and *Daniel Khomskii* emphasized that the neighboring of octahedra with Jahn-Teller active ions leads not only to an harmonic interaction of local distortions but additionally to a purely electronic interaction mediated by superexchange independent of the local Jahn-Teller distortions [57, 86]. By starting from a Hubbard model containing two degenerate orbital states per site with an added intrasite Hund's coupling between the degenerate states, they showed that the superexchange directly couples the spin order to the orbital occupation order. In the case of a perovskite with twofold degenerate e_g states the electronic Hamiltonian in the cubic phase becomes then highly anisotropic due to the directional character of the $d_{z^2-r^2}$ and $d_{x^2-y^2}$ states, which lead to anisotropic hopping integrals $\gamma^{i,j}_{\alpha,\beta}$[1]. The electronic ground state for a cubic perovskite is then an AFM-A magnetic ordering with checkerboard type or columnar orbital ordering of $d_{z^2-r^2}$ orbitals for electrons or $d_{x^2-y^2}$ orbitals for holes (like in $KCuF_3$ with a d^9 configuration the main case study put forward by *Kugel* and *Khomskii*). This orbital ordering is compatible with the actual orbital ordering deduced from the apparent lattice distortions in $KCuF_3$. Hence, the superexchange mechanism and the CJTE are working alongside in $KCuF_3$. One interpretation is that lattice distortions are a secondary effect that follow the orbital ordering that is already engraved in the undistorted phase. In practice, however, such a distinction is difficult to prove as both effects should appear dynamically coupled since a lattice distortion will affect the superexchange strength through the hopping integrals γ and a specific electronic state will activate a specific vibronic coupling. From an ab initio point of view it has been shown by *Pavarini* and coworkers using material specific DFT+DMFT calculations that the super-exchange mechanism is not strong enough to explain the high transition temperatures in $LaMnO_3$ [87] and $KCuF_3$ [88]. From static DFT calculations the orbital ordering appears spontaneously without distortions in the fluorine perovskites $KCuF_3$ and $KCrF_3$ but not in $LaMnO_3$ [89].

1: Here, α and β denote the two degenerate orbital states on lattice sites i and j.

5.3.3 The Peierls Distortion as a Metal To Insulator Transition Mechanism

Rudolf Peierls explained the MIT in solids from a different angle. Instead of *local* orbitals and *local* distortions, he emphasized electronic bands in the periodic solid interacting with *cooperative* distortions [90]. His analysis of the monoatomic chain with one electron in a s-orbital per site is illustrated in Fig. 5.1. In the regularly spaced chain with a lattice parameter a the band dispersion with respect to the momentum k of the s band is within the tight-binding approximation a cosine with the minimum at 0 and the maximum at the Brillouin zone boundary $\pm\frac{\pi}{a}$. For

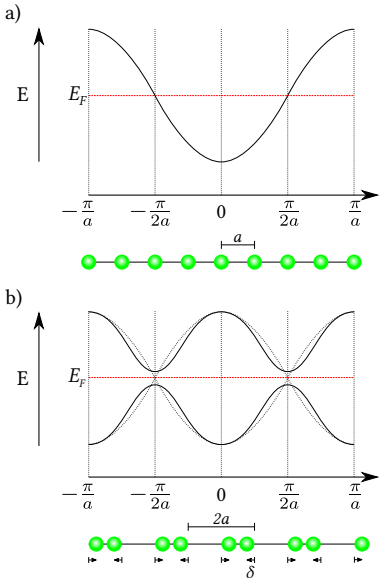

Figure 5.1: Peierls Transition in linear atomic chain with one electron and one s orbital per lattice site. a) Electronic bands in a regular distanced chain with unit-cell lattice parameter a. The Fermi surface at the energy E_F consists of two points at $\pm\frac{\pi}{2a}$. b) A distortion that doubles the periodicity of the unit cell will open a band gap at the Brillouin-zone boundary that was the Fermi surface of the initially undistorted linear chain. The electronic bands of the distorted chain are drawn in black solid lines, the bands of the initially undistorted cell in the dotted line.

the case of one electron per atom the band is half-filled. The Fermi energy is thus exactly at half the band-width and the Fermi surface consist of two points at $\pm\frac{\pi}{2a}$. The chain is thus metallic. A collective distortion that will double the periodicity of the atomic chain will divide the Brillouin zone size in half such that the new zone boundary is at $\pm\frac{\pi}{2a}$. The new unit cell will then contain two atoms and the new brillouin zone respectively two bands. The periodicity of the potential will finally open a band gap at the new zone boundary, which was initially the Fermi level. The Fermi level is thus lying within in the band gap and all states below are occupied and all above are empty. *Peierls* showed that the total band energy is lowered through the band opening by integrating over the states close to the Fermi level. The energy difference of the band energy of the distorted to the undistorted chain in dependence of the amplitude of the displacement δ is given by

$$\Delta E_{band} \propto -\delta^2 \log \delta. \tag{5.2}$$

This energy gain will favor a dimerization of the atomic chain. Chemically this might be interpreted as the formation of a *bonding* and *anti-bonding* band [91]. Different band fillings would induce different periodicities of distortion that would lower the total energy. E.g. if the band of the monoatomic chain would be quarter filled the system would gain energy by a distortion that quadruples the periodicity and so on. The extension of the Peierls effect to a three-dimensional solid is often called Fermi-Surface-Nesting [92, 93]. *John Slater* proposed the same mechanism but with spin ordering that would double the periodicity [94]. In the *Slater* and *Peierls* picture there is no statement about the driving mechanism. Quite oppositely the main statement is that lattice/spin and orbital ordering forcefully appear together at the transition. Important scientists representing the Kugel-Khomskii approach and the CJTE recognized the Peierls transition as an alternative concept delivering the same results and that all three concepts should be hardly distinguishable [62, 64, 95, 96]. *Roald Hoffmann*, a chemist, called the Peierls transition in the solid state the equivalent to the Jahn-Teller effect in molecules [91].

Part III

Calculation Results

First Principles Studies of $LaMnO_3$

6

Since the discovery of the colossal magnetoresistance effect in $R_x^{3+}A_{1-x}^{2+}MnO_3$ manganese perovskites solid solutions about 25 years ago [97] there has been a continuous research effort to understand the physical behavior of the end-members as well as intermediate compounds. Nonetheless, for the rare earth manganite perovskite side, $RMnO_3$, no fully consistent picture has emerged yet that explains the interplay between structural, magnetic, and electronic degrees of a freedom. Hence, the prototypical member of this series, $LaMnO_3$, still attracts an extensive research interest.

$LaMnO_3$ belongs to a large class of perovskite materials with a Goldschmidt [2] tolerance factor $t < 1$. As such its lattice structure deviates from the ideal cubic perovskite $Pm\bar{3}m$ reference phase by the appearance of cooperative rotations of the MnO_6 oxygen octahedra. Above 1200K, $LaMnO_3$ shows a rhombohedral space group $R\bar{3}c$ [98, 99], with rotations of the connected oxygen octahedra according to a $a^-a^-a^-$ rotation pattern (in Glazer's notations [3]). At 1200 K, $LaMnO_3$ undergoes a structural phase transition to a *Pbnm* phase with $a^-a^-c^+$ rotation pattern, the most common one among the perovskites [4].

In both of these phases, oxygen octahedra rotate in a nearly rigid way. This rigid rotation preserves the cubic symmetry (O_h in Schönflies notation) around the Mn atom if only the octahedron is considered. In such a regular octahedron, the five-fold degenerated Mn *d*- states are split into three degenerate lower energy t_{2g} and two degenerate higher energy e_g states. In the 3+ oxidation state of Mn, four electrons formally occupy the Mn-*d* states. Due to strong intra-site Hund's coupling in the 3*d* shell, Mn adopts a high-spin configuration, where three electrons occupy the t_{2g} and one the e_g states. As the Mn-3*d* states constitute the highest occupied states in $LaMnO_3$, it is consequently metallic in the $R\bar{3}c$ and $Pbnm$ phases at high temperatures.

At 750K and ambient pressure, or lower temperatures and higher pressure ($\approx$ 32GPa), a second structural transition occurs, accompanied by a metal-insulator transition (MIT). This transition is called Jahn-Teller (JT) or Orbital Ordering (OO) transition at the temperature T_{JT} or T_{OO} [100]. At this transition, a sudden increase of volume is observed. The initially nearly cubic unit cell shows a strong tetragonal compression and orthorhombic deformation [101–103]. The oxygen octahedra experience strong cooperative deformations lowering their symmetry from cubic to orthorhombic (O_h to D_{2h}). These are the so-called *Jahn-Teller distortions*. However, no further symmetry reduction occurs and the structure preserves the *Pbnm* space group [104]. Hence, the structures are called O'($T < T_{JT}$) and O ($T > T_{JT}$) [99, 105]. A peculiarity of such isosymmetrical transitions is that the structural order parameter - the Jahn-Teller distortions - are not restricted to zero amplitude before the transition. Consequently in the O phase local Jahn-Teller distortions are

reported and short-range ordered clusters with the diameter of 4 MnO_6 octahedra have been found [82, 99, 105].

In all of the above described phases, the unpaired magnetic moments in the $3d$ shell of manganese are disordered and $LaMnO_3$ is paramagnetic (PM). At $T_N = 140K$ [106], $LaMnO_3$ undergoes a magnetic transition without any structural changes to an antiferromagntic phase with A-type pattern (AFM-A).

There is a long standing debate about the origin of the MIT at T_{JT} in $LaMnO_3$ [100, 107–111]. Broadly, this debate can be summarized into two distinct views: the *cooperative Jahn-Teller Effect* [56, 84, 112, 113] (C-JTE) on the one hand and the spontaneous orbital ordering proposed by the *Kugel-Khomskii* [57] (KK) model on the other hand.

The C-JTE approach extents the Jahn-Teller Effect [55] from an isolated Jahn-Teller center to a solid of coupled centers. In the case of $LaMnO_3$, these are the corner shared oxygen octahedra. The origin of the transition is the *local* degeneracy of the e_g orbitals, which induces a *local* octahedral distortion removing the degeneracy. The coupled octahedra only interact harmonically through their individual deformation. The cooperative ordering of the octahedra results of the minimization of the lattice harmonic energy and creates an orbital ordering.

The KK approach (based on the Mott-Hubbard model [54]) emphasizes instead the roles of the *inter site* super-exchange electronic interactions and dynamical correlations between e_g electrons. It postulates spontaneous orbital and magnetic orderings in the undistorted cubic perovskite phase for a certain ratio of hopping and exchange parameters. The appearance of the cooperative deformation of the oxygen octahedra is here a secondary effect induced by the orbital ordering. From DFT+DMFT calculations, it has been shown that the KK mechanism alone cannot account for the orbital ordering in $LaMnO_3$ [87] and that electron-lattice coupling is crucial in promoting the high orbital ordering transition-temperature. Moreover a recent first-principles study [89] claims that dynamical correlations are not necessary to account for orbital ordering in perovskites. $LaMnO_3$ thereby appears as a special case, where the principal orthorhombic Jahn-Teller distortion is only unstable in the presence of octahedral rotations.

In the present work, we reinvestigate $LaMnO_3$ from first-principles calculations. First, we show that our calculation method properly reproduces a range of measured ground-state properties of $LaMnO_3$. Then, we sample the Born-Oppenheimer potential energy surfaces (PES) of the close competing AFM-A and ferromagnetic (FM) orders and characterize the inherent electronic instabilities, couplings between phonon modes, strains, insulating and metallic states. By a simple Monte-Carlo (MC) simulation we show that these PESs qualitatively reproduce the orbital ordering transition at 750K. Finally, we unveil that $LaMnO_3$ shows an inherent subtle competition between charge-ordering and orbital ordering, which was suspected before [114]. As a support to our analysis, we use the canonical Jahn-Teller distortion notations introduced in section 5.1.

The analysis of the PESs computed from DFT shows that the large electron-lattice coupling, necessary to explain the transition, lies in a Peierls effect [90]. The large coupling is only enabled once the spin

symmetry between neighbouring sites is broken. At elevated temperature this symmetry breaking is produced by dynamical fluctuations of orbital occupations and spin orientations in the PM state, so questioning the ability of DFT to describe such a phenomenon. From MC simulation relying on PESs calculated with DFT and reproducing the MIT, we show that, in line with Ref. [115], the key ingredient of the MIT transition is more the *instantaneous* symmetry breaking, that can be statically treated in DFT, than the *dynamical* nature of the fluctuations. Hence, we assign an important part of the stabilising energy at the MIT transition to *spin symmetry breaking*. This does not mean that dynamical electron correlations do not play any role in stabilising the insulating phase. The use of an appropriate U-correction remains important in treating materials like $LaMnO_3$ from DFT. Nevertheless, together with the recent explanation of charge-ordering in e_g^1 alkaline earth ferrites $AFeO_3$ [116] and rare earth $RNiO_3$ [77] as a Peierls transition, it seems that the cooperative Jahn-Teller/orbital ordering and charge-ordering transitions are simply different coordinates for translational symmetry breaking and therefore they might always compete in perovskites with degenerate e_g states. Finally, we emphasize that for gaining more insights in the dynamical properties of the MIT, new model descriptions are needed that can treat the electrons and nuclei dynamically coupled in large supercells.

On a less academic level our results show the close interconnection between magnetic/electronic- and lattice degrees of freedom in $LaMnO_3$. Hence, $LaMnO_3$ and similar perovskites are inherently interesting for structural engineering of magnetic and electronic properties, which has been realized in the FM phase of thin film $LaMnO_3$ [117–123]. In a second part we study this $LaMnO_3$ thin films be applying varying epitaxial constraints and show that this highly debated FM insulating phase can be favored by the strain condition alone. Effects of the film/substrate interface seem hence only to be relevant to ultra-thin films (a few unit cells). The decisive parameter monitoring the competition between AFM-A and FM phases is the tetragonal strain. Thus, we rationalize the appearance of FM $LaMnO_3$ by the orientation of the epitaxial thin film with respect to the substrate surface that determines the tetragonal strain state responsible for the resulting magnetic order.

6.1 Calculation Parameters and Methods Deployed

Density functional theory (DFT) calculations were performed using the generalized gradient approximation (GGA) with the revised Perdew-Burke-Enzerhof parameterisation for solids (PBEsol) [124] as implemented in the Vienna ab initio simulation package (VASP) [125]. A Liechtenstein $(U|J)$ correction was applied. $(U|J)$ = (5|1.5) were determined by comparing structural, electronic, and magnetic parameters to experimental results. For comparison, we reproduced also the results of *Mellan et al.* using $(U|J)$ = (8|2) [126]. The PAW method [15] was used, with a high plane-wave cutoff energy of 600 eV and a dense 14x14x14 Monkhorst-Pack k-point mesh [127] with respect to the five-atoms cubic perovskite unit cell. Supercells up to 40-atoms were used to treat various

magnetic orderings. The density of the k-point mesh in the supercells was reduced according to the multiplicity of the supercell. During the structural optimizations, the lattice parameters and internal coordinates of atoms were fully relaxed until the Hellmann-Feynman forces on each atom were less than 10^{-5}eV/Å and stresses are less than $4 \cdot 10^{-4}$ eV/Å^3.

We used ISODISTORT [128] to analyze symmetry-adapted modes and symmetry-adapted strains of experimental and optimized structures. In all cases, we used the aristotype $Pm\bar{3}m$ structure of $LaMnO_3$ as reference, with a lattice constant of $a_0 = 3.935$Å that preserves the same volume per formula unit as in the experimental *Pbnm* phase at low temperatures. Then, we used the software INVARIANTS [129] to create invariant coupling terms including symmetry adapted modes and strains. We use the BANDUP utility [130, 131] to unfold electronic band-structures of magnetically or structurally distorted structures back to the Brillouin-zone of the cubic 5-atoms perovskite unit-cell. Finally, we used an in-house tool to approximate PESs from DFT data with a polynomial expansion and to run Monte-Carlo simulations on the determined polynomial.

6.2 Ground State Properties from DFT+U Calculations

In this section we review the structural, magnetic, and dielectric properties of the $LaMnO_3$ bulk ground-state phase. We compare the results of our DFT+$(U|J)$ calculations to experimental values in order to assess the validity of our calculation method (See Table 6.1).

The ground-state *Pbnm* phase can be described in terms of its atomic distortion with respect to the aristotype cubic perovskite structure, taken as reference. This distortion can be decomposed according to the orthorgonal symmetry-adapted phonon modes and lattice strains defined by the irreducible representations of the cubic reference structure. The modes with the largest amplitudes are (i) one in-phase rotation of the oxygen octahedra (ϕ_z^+ irrep: M_2^+) and (ii) two anti-phase rotations ($\phi_x^- + \phi_y^- = \phi_{xy}^-$ irrep: R_5^-), leading together to the $a^-a^-c^+$ rotation pattern [3] and reducing the symmetry to the *Pbnm* space group. This rotation pattern further induces two antipolar motions of the La cations [132–134]. Firstly, an antipolar motion of the La atoms (and also oxygens) of consecutive (001)-planes along the pseudocubic xy-direction (A_X irrep: X_5^-). Secondly, an antipolar motion of La atoms of consecutive (111)-planes equally along the pseudocubic xy-direction (A_R irrep: R_4^-). This latter antipolar motion possesses the same irrep as the Jahn-Teller modes $Q_{4\alpha}^R$ defined in Table 5.1. The respective oxygen motions $Q_{4x}^{\mathbf{R}}$ and $Q_{4y}^{\mathbf{R}}$ do appear also but with an amplitude one order of magnitude smaller than the already small amplitude of the A_R cation motions so that they are not reported in Table 6.1. Finally, the ground-state structure also shows a significant Jahn-Teller distortion $Q_{2z}^{\mathbf{M}}$, and sizable tetragonal (compressive along z-axis) and shear strains $Q_{3z}^{\mathbf{\Gamma}}$ and $Q_{4z}^{\mathbf{\Gamma}}$, all compatible with the *Pbnm* symmetry. The atomic displacement patterns associated to these modes (excluding the strains and Jahn-Teller modes, already sketched in Table 5.1) are shown in Fig. 6.1.

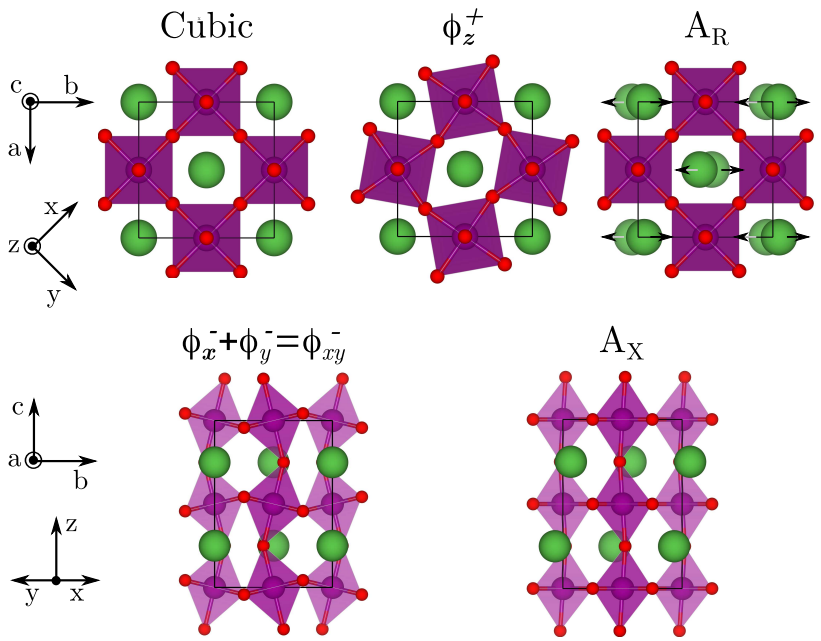

Figure 6.1: Displacement patterns of condensed symmetry adapted modes in the $LaMnO_3$ *Pbnm*-phase (excluding Jahn-Teller distortions). The cubic *xyz*- and orthorhombic *abc*-coordinate system used throughout the paper are indicated. The *Pbnm*-unit cell is shown by the black continuous line. a) Cubic Positions, b) in-phase rotation Irrep: M_3^+, c) antipolar motion at the R-point of the cubic Brillouin zone Irrep: R_4^-, d) anti-phase rotation Irrep: R_5^-, e) antipolar motion at the X-point of the cubic Brillouin zone Irrep: X_5^-.

In the following we refer to calculated physical quantities using the $(U|J)$ parameters of *Mellan et al* [126] as (8eV|2eV) and our new optimized values as (5eV|1.5eV) and compare them to experimental values. In the top part of Table 6.1, we report the relaxed amplitudes of all the modes and strains with imposed AFM-A order. Both tested $(U|J)$ combinations deliver similar strain and mode amplitudes in good agreement with the measured values (maximum deviation for $\phi_{xy}^-(R_5^-) \approx 5\%$).

In the center part of Table 6.1, we compare the Kohn-Sham band gap and the optical dielectric constant ϵ^∞ obtained with the two GGA+U functionals to experimental data. Both calculated band gaps lie well in the range of experimentally measured values [106, 136–141].

The optical dielectric tensor gives a second good measure besides the band gap to test the calculated electronic density. Refs [107, 109] provide directionally resolved measurements of the optical dielectric tensor at low temperature along the *Pbnm*-c axis and the pseudocubic x-direction to compare with our calculations ($\approx 45°$ to the orthorhombic a - and b - directions). In Table 6.1 we report the dielectric tensor in the orthorhombic axis as well as rotated to the same crystallographic orientation as in [107, 109], where $\epsilon_{xx}^\infty = \epsilon_{yy}^\infty$, while in the orthorhombic coordinate systems it holds $\epsilon_{aa}^\infty \neq \epsilon_{bb}^\infty$. In the pseudocubic *x,y,z*-system x and y are not orthogonal, for which reason the off diagonal element $\epsilon_{xy}^\infty \neq 0$. However, since ϵ_{xy}^∞ is one magnitude smaller (< 0.5) than the diagonal terms and as it has not been reported in experiments, we did not note it in Table 6.1.

PBEsol + (8eV|2eV) and PBEsol + (5eV|1.5eV) yield electronic band gaps, which lie well in the range of the experimentally measured ones, although increasing with U. Regarding the optical dielectric constant, PBEsol + (5eV|1.5eV) yields values in better agreement with experiment, which also reproduce the optical anisotropy absent with PBEsol + (8eV|2eV).

In the bottom part of Table 6.1 we compare the calculated magnetic properties with experimental values. We made a two J exchange constant

mean field model, which is sufficient to justify the AFM-A order and can be found in several publications in recent literature [106, 126, 142]. In our definition a negative value of J indicates FM exchange. To calculate the exchange constants, we used the energy differences of the relaxed AFM-A, AFM-G and FM phases and assumed a total spin of $4\mu_B$ per Mn site. In this way the calculated exchange constants contain implicitly spin-phonon coupling, which is however small as the relaxed phases for the different magnetic order are structurally close. Our experimental reference is [106], where the magnetic exchange constants were derived from magnon dispersion measurements. It is noteworthy, that T_N calculated with the measured exchange constants lies 67 K above the measured T_N because of the neglect of spin-fluctuations. Hence, the best benchmark is to compare measured and calculated exchange constants. PBEsol + (8eV|2eV) underestimates both exchange constants by an approximate factor of three. In contrast PBEsol + (5eV|1.5eV) underestimates less the exchange constants with respect to the experiment and finds a Neel-Temperature from mean field theory comparable to the experimental one.

	(5|1.5)	(8|2)	Exp.
Structure			
$Q^{\mathbf{\Gamma}}_{4z}$ $\Gamma^+_5\ (a,0,0)$	-0.036	-0.039	-0.027[b] / -0.027[c]
$Q^{\mathbf{\Gamma}}_{3z}$ $\Gamma^+_3\ (a,0)$	-0.040	-0.040	-0.032[b] / -0.032[c]
A_X $X^-_5\ (0,0,0,0,a,-a)$	0.33	0.34	0.30[b] / 0.29[c]
ϕ^+_z $M^+_2\ (a,0,0)$	0.49	0.51	0.48[b] / 0.48[c]
$Q^{\mathbf{M}}_{2z}$ $M^+_3\ (a,0,0)$	0.19	0.19	0.18[b] / 0.19[c]
ϕ^-_{xy} $R^-_5\ (0,a,-a)$	0.65	0.67	0.63[b] / 0.59[c]
A_R $R^-_4(0,a,a)$	0.06	0.06	0.06[b] / 0.06[c]
Optical Properties			
ϵ^∞_{aa}	7.03	6.02	-
ϵ^∞_{bb}	6.52	5.5	-
ϵ^∞_{xx}	6.77	5.75	$\approx$ 7.3[d,e]
ϵ^∞_{cc}	6.15	5.76	$\approx$ 6[d,e]
E_{Gap}	1.15	1.77	1.1 - 1.9[f]
Magnetic Properties			
μ	3.68	3.75	3.8
$J_{xx} = J_{yy}$	-0.59	-0.25	-0.83[b]
J_z	0.34	0.18	0.58[b]
T_N	42	64	$\sim$ 140 (Calc: 207[b,g])

Table 6.1: Comparison of quantities calculated from DFT with PBEsol+(5|1.5) and PBEsol+(8|2) with experimental values. Top: amplitudes of the symmetry-adapted modes (Å) extracted with ISODISTORT[a] of relaxed $LaMnO_3$ with imposed AFM-A magnetic order. Center: optical dielectric permittivity tensor ϵ^∞ and electronic band gap E_{Gap} (eV). Bottom: magnetic moment μ (μ_B), magnetic exchange constants J (meV) and Neel-Temperature T_N (K).

[a] Normalized with respect to the reference phase (Cubic $Pm\bar{3}m$).
[b] Ref. [106]
[c] Ref. [135]
[d] Ref. [109]
[e] ϵ^∞_{xx} and ϵ^∞_{bb} correspond to ϵ_{1b} and ϵ_{1c} in the lower frequency range below the first optical transition in [109].
[f] Refs. [106, 136–141]
[g] Calculated in Ref. [106] with a two J mean-field approach using the measured exchange constants.

6.3 Inspection of $Q_{2z}^{\mathbf{M}}$ Potential Energy Surfaces

In this section we discuss the shape of the Born-Oppenheimer potential energy surface (PES) around the cubic phase with respect to the key Jahn-Teller distortion in $LaMnO_3$, $Q_{2z}^{\mathbf{M}}$ (See Table 5.1 and 6.1). We quantify mode-mode, mode-strain couplings, and vibronic Jahn-Teller couplings by successively adding one by one the main lattice distortions found in the *Pbnm* ground state. To do so, we fit the free energy surface by potentials of the type:

$$\mathscr{F} = E_0 + \alpha_{JT}\left|Q_{2z}^{\mathbf{M}}\right| + \alpha Q_{2z}^{\mathbf{M}} + \beta(Q_{2z}^{\mathbf{M}})^2 + \gamma(Q_{2z}^{\mathbf{M}})^4, \tag{6.1}$$

where E_0 is the energy at $Q_{2z}^{\mathbf{M}} = 0$, α_{JT} describes the vibronic-coupling terms, α quantifies other linear lattice terms, β quadratic lattice terms, and γ fourth order terms. In the fit, all modes have been normalized such that 1 corresponds to their ground-state amplitude, which can be found in Table 6.1. This approach allows to deduce *how* the magnetic and structural ground state is reached. The introduction of the absolute function in (6.1) allows to distinguish the vibronic coupling term and linear lattice couplings in the $Q_{2z}^{\mathbf{M}}$ coordinate. The cubic reference lattice parameter is $a_0 \approx 3.935$Å, which preserves the same volume per formula unit as the bulk ground-state phase. The sign and strength of the parameters will be qualitatively discussed in the following sections. A description of the fitting procedure and the whole free-energy expansion are given in appendix A.1. Table 6.3 shows fitted values of the coefficients.

Table 6.2: Energy comparison per formula unit of different Magnetic Orderings in the cubic phase of $LaMnO_3$.

Magnetic Ordering	$\frac{\Delta E}{fu}$ (meV)
FM	-126.5
AFM-A	0.00
AFM-C	+175.5
AFM-G	+367.9

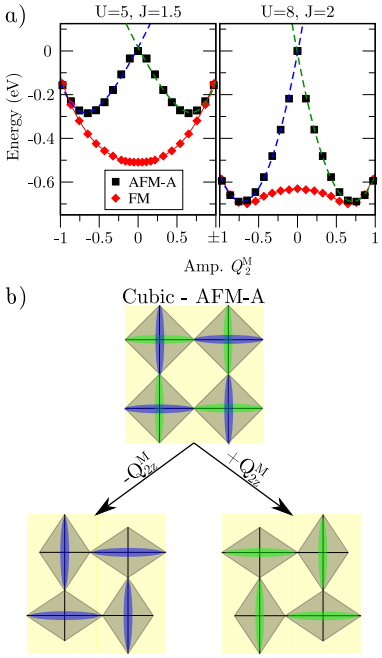

Figure 6.2: a) Comparison of the PES of the $Q_{2z}^{\mathbf{M}}$ Jahn-Teller distortion for different DFT calculation methods used throughout this publication. b) Schematic illustration of orbital orderings, which are degenerate in the cubic structure with AFM-A ordering leading to a metallic phase. A condensation of a $Q_{2z}^{\mathbf{M}}$ distortion with positive or negative amplitude will stabilize one or the other state. Green and blue colors refer to the dashed lines in Fig. 6.2a.

6.4 $Q_{2\alpha}^{\mathbf{M}}$ PES in the cubic Phase

In this section we analyze the relative stability of different magnetic orderings and the stability of $Q_{2z}^{\mathbf{M}}$ distortion in the cubic phase. Inspecting the $Q_{2z}^{\mathbf{M}}$ coordinate is a random choice at this point. Due to the cubic symmetry, the following results would be exactly the same for $Q_{2x}^{\mathbf{M}}$ and $Q_{2y}^{\mathbf{M}}$. Following KK-approach [57], we expect an AFM-A magnetic and orbital ordered insulating ground-state with an instability of $Q_{2z}^{\mathbf{M}}$. Following the C-JTE approach we expect an instability of $Q_{2z}^{\mathbf{M}}$ independent of the magnetic order.

Table 6.2 shows the energy differences per formula unit for different simple magnetic orderings in the cubic phase of $LaMnO_3$. Here our calculations show that the FM ordering is by far the ground state and that large energy differences exists between the different magnetic orders.

Fig. 6.2a shows the PES of the $Q_{2z}^{\mathbf{M}}$ mode around the cubic $Pm\bar{3}m$ phase and its dependence in terms of the $(U|J)$ parameters. The energy of the cubic AFM-A structure has been set to zero. The amplitude of the $Q_{2z}^{\mathbf{M}}$ distortion has been normalized to the bulk ground-state value. While the differences of the relaxed bulk ground state with respect to the $(U|J)$ parameters are subtle (shown in section 6.2), the differences in Fig. 6.2a are rather significant. On the FM surface the $Q_{2z}^{\mathbf{M}}$ distortions changes its character from dynamically stable to unstable for higher U and J values. Similarly, on the AFM-A surface the energy gain of the $Q_{2z}^{\mathbf{M}}$ distortion with respect to the cubic structure is more than twice larger for the larger

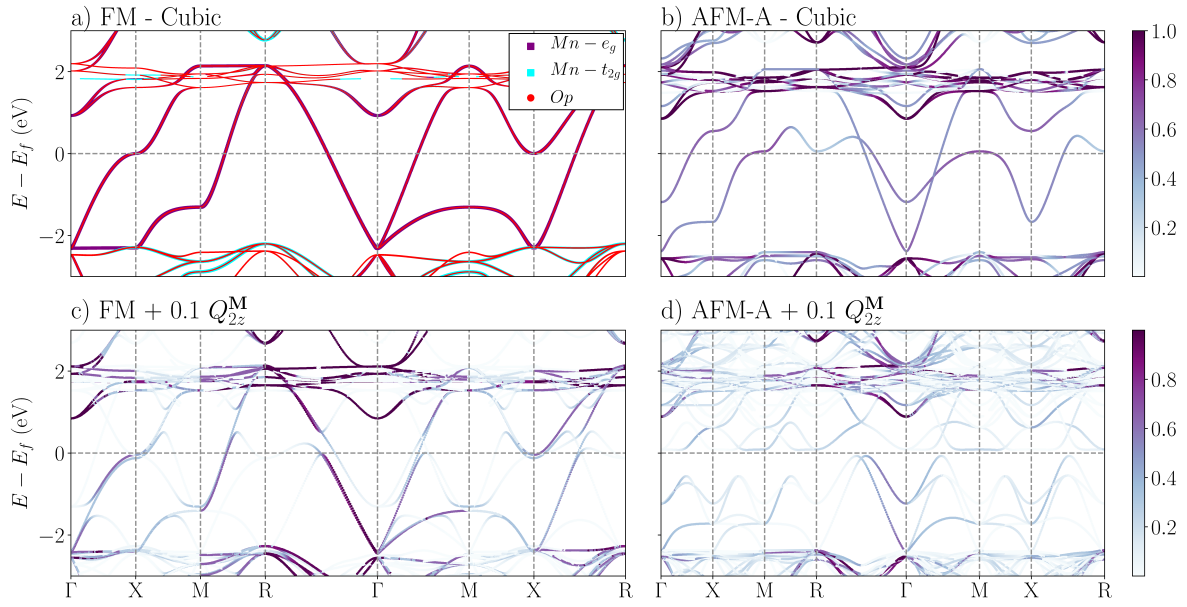

Figure 6.3: Electronic Band Structures of $LaMnO_3$ in the range of ±3eV. a) Projection of electronic bands onto Mn-e_g, Mn-t_{2g}, and O-p orbitals in FM-cubic phase. The size of the dots indicate the orbital character of the bands. b-d) unfolded band structure to cubic Brillouin-zone. The color of the lines indicate the overlap between the supercell and primitive cell k-point. b) AFM-A ordering with cubic atomic positions. c) FM ordering with 10% $Q^{\mathbf{M}}_{2\alpha}$ distortion. d) AFM-A ordering with 10% $Q^{\mathbf{M}}_{2\alpha}$ distortion, where α is one the cubic lattice directions. In the FM cases the majority spin is shown. In the AFM-A cases one of the two equivalent spin channels are shown.

U and J values. At the opposite, the FM ground state and the finite value of α_{JT} on the AFM-A surface are independent of $(U|J)$. Fig. 6.2a shows that the extraction of *quantitative* parameters from DFT calculations is a difficult task as the numerical value can significantly change with the DFT-approach, while the relaxed ground-state structure might be very similar. However, our results are *qualitatively* the same as the ones of a recent study using a U-value of 3.5 eV [89]. In appendix A.2 we show furthermore that the qualitative features shown here with $(U|J)$ = (5eV|1.5eV) do not change when applying $(U|J)$ = (8eV|2eV).

The AFM-C and AFM-G surfaces are significantly higher in energy and not shown here, but they also exhibit a vibronic coupling, which is even stronger than in AFM-A.

To rationalize the shape of the PES, we can inspect the electronic band-structure (Fig. 6.3) in the reference cubic and a distorted structure including 10% $Q^{\mathbf{M}}_{2z}$ (with respect to the ground-state amplitude) distortion in both the FM and AFM-A magnetic orderings. The band structures are unfolded to the cubic Brillouin zone for easy comparison. Fig 6.3a shows the projection of the band-structures in the cubic phase with FM ordering onto $Mn - e_g$, $Mn - t_{2g}$, and $O - p$ states. In line with other works [143–147], the band-structure shows that the e_g states are dispersed symmetrically around the Fermi-level, E_F, in a range of about ±2eV. E_F is crossed at the points X and halfway along M - R, Γ - R, Γ - M and X - R.

If the AFM-A magnetic ordering is imposed (see Fig. 6.3b), the local degeneracy at Γ of the e_g bands is lifted, showing the symmetry breaking produced by the magnetic order. E_F crosses the e_g bands at M and halfway along Γ - X, Γ - M, Γ - R, X - M and X - R. The increase of many

of the occupied valence states in the AFM-A cubic case with respect to the FM ordering (e.g. compare the section from Γ over M to X of Fig. 6.3a and b) leads to the large increase of the total-energy from FM to AFM-A in the cubic phase (See Table 6.2 and Fig. 6.2). The metallicity of the AFM-A cubic phase, despite the local non-degeneracy of the e_g states, can be explained by the degeneracy of two types of orbital orderings within this phase, as schematically drawn in Fig. 6.2b.

If the $Q_{2z}^{\mathbf{M}}$ distortion is added, the electronic bands are split halfway along all the high-symmetry points (Compare Fig. 6.3c and d). The system will gain electronic energy if the e_g bands are crossing the Fermi level at these points as virtual states are shifted to higher energies and occupied ones to lower energies. Moreover, an insulating state can only be created by the application of the $Q_{2z}^{\mathbf{M}}$ distortion if the e_g bands cross the Fermi-level at all the splitting points. In the FM case only four splitting-points and crossings with the Fermi-level coincide: At X and halfway between Γ - M, Γ - R, X - R, and M - R. At the other splitting points halfway between Γ - X, and X - M the e_g bands are deep in the valence states at about -1.5 eV (or one quarter of the e_g bandwidth). The absence of the vibronic coupling can then be explained by

$$\alpha_{JT} = \int_{BZ} \sum_{n=1}^{n_{e^-}} \frac{\partial E_n(\vec{k})}{\partial Q_{2z}^{\mathbf{M}}}\bigg|_{Q_{2z}^{\mathbf{M}}=0} = 0, \tag{6.2}$$

where $E_n(\vec{k})$ is the energy of band n at $\vec{k}$ and its derivatives with respect to $Q_{2z}^{\mathbf{M}}$ are summed over all occupied states, which are the number of electrons contained in the calculation n_{e^-}. Eq. (6.2) means that, overall, for each k-point at which the total electronic energy is decreased by a variation of $Q_{2z}^{\mathbf{M}}$ there is another one at which it is increased by the same amount. Finally, in the FM case there is one direction that is unaffected by the $Q_{2z}^{\mathbf{M}}$ distortion, which can be identified by one band that follows the original e_g paths. Most clearly to be seen at the start of the path from Γ over X to M (Compare Fig. 6.3a and c). This band accounts for the z-direction in real-space that is not affected by the $Q_{2z}^{\mathbf{M}}$ distortion. In the AFM-A case the points at which the condensation of the $Q_{2z}^{\mathbf{M}}$ distortion splits the e_g bands and their crossing with E_F in the cubic Brillouin zone coincide, such that the $Q_{2z}^{\mathbf{M}}$ distortion leads to a lowering of the electronic energy and Eq. (6.2) becomes non zero. Hence the origin of the finite vibronic coupling is a Peierls like effect where the destruction of the translational symmetry leads to an energy gain. The doubling of the periodicity can be seen most clearly in the oscillations from Γ to X and M to R. Here magnetic order and $Q_{2z}^{\mathbf{M}}$ distortion work together in an intriguing way to result in a finite vibronic coupling. Our result shows that future works should focus on the generalization of the spin-structural Peierls-effect in corner shared octahedra networks.

In real space, the condensation of $Q_{2z}^{\mathbf{M}}$ with positive or negative amplitude corresponds to the stabilization of one orbital order, which will represent an non-degenerate electronic ground state in the distorted phase (See Fig. 6.3d) and Fig. 6.2b). The combination of spin and $Q_{2z}^{\mathbf{M}}$ distortion corresponds to the doubling of the periodicity in the three space directions, which stabilizes one distinct orbital order. In the cubic phase both orbital orders are degenerate and explain the metallicity.

Finally, we want to summarize the major result of this section.

(i) The origin of the vibronic coupling on the AFM-A surface appears to be a Peierls like effect, where AFM-A order and $Q_{2z}^{\mathbf{M}}$ distortion combine to break the translational symmetry. The conceptual similarity of Peierls effect, CJTE and also KK induced orbital order has already been noted by *Polinger* [96], *Polinger* and *Bersuker* [64], and recently by *Streltsov* and *Khomskii* [95]. (ii) The absence of spontaneous orbital order and the FM ground state in the cubic phase hint that the KK mechanism might not apply to the cubic phase of $LaMnO_3$ and that a renormalization of the intersite electronic parameters might be key to activate it.

6.5 $Q_{2z}^{\mathbf{M}}$ PES in Presence of other Lattice Distortions

In order to investigate under which structural conditions the AFM-A magnetic order is stabilized, we condensed the principal lattice distortions and strains, and sampled the PES in terms of $Q_{2z}^{\mathbf{M}}$ on top of these already distorted structures. The results are shown in Fig. 6.4.

In Fig. 6.4a, we used the cubic lattice constant $a_0 = 3.935$Å and sampled the PES surface along the $Q_{2z}^{\mathbf{M}}$ line successively when appearing (i) alone, (ii) on top of the octahedral rotations ϕ_z^+ and ϕ_{xy}^- with the bulk ground state amplitude, and finally (iii) on top of the rotations plus the A_X motion with their corresponding ground state amplitudes. In Fig. 6.4b we followed the same procedure for ϕ_z^+ and ϕ_{xy}^- rotations and A_X distortion in the three subpanels, but condensed on top the tetragonal strain $Q_{3z}^{\mathbf{\Gamma}}$ which leads to lattice constants of $a = b = 5.66$Å and $c = 7.61$Å. Finally, in 6.4c we additionally condensed the shear strain $Q_{4z}^{\mathbf{\Gamma}}$. It leads together with $Q_{3z}^{\mathbf{\Gamma}}$ to the ground state orthorhombic lattice constants. Energies in all graphs are expressed with respect to the same energy reference (cubic AFM-A), allowing the reader to easily find the global ground state under certain conditions.

Calculations are reported for FM and AFM-A orders. Additionally, we note in Fig. 6.4 if the relaxed electronic wave function represents a metallic (open symbols) or insulating state (filled symbols). In this section we limit ourselves to a qualitative discussion of the interplay of lattice and electronic band-structure, without an explicit demonstration of unfolded band-structures. The complete set of fitted coefficients is reported in Table 6.3.

6.5.1 Cubic unit cell

Let us first focus on Fig. 6.4a. The left panel corresponds to the pure cubic lattice and hence to the left panel in Fig 6.2a. Going from no rotations (left panel) to the structure with rotations (middle panel) in the cubic lattice, the global energy is lowered since the rotations are unstable ($E_0^{\phi} < 0$ in Table 6.3) . Moreover, $Q_{2z}^{\mathbf{M}}$ changes from dynamically stable to unstable on the FM surface. Also, the shifted single wells of the AFM-A surface becomes deeper.

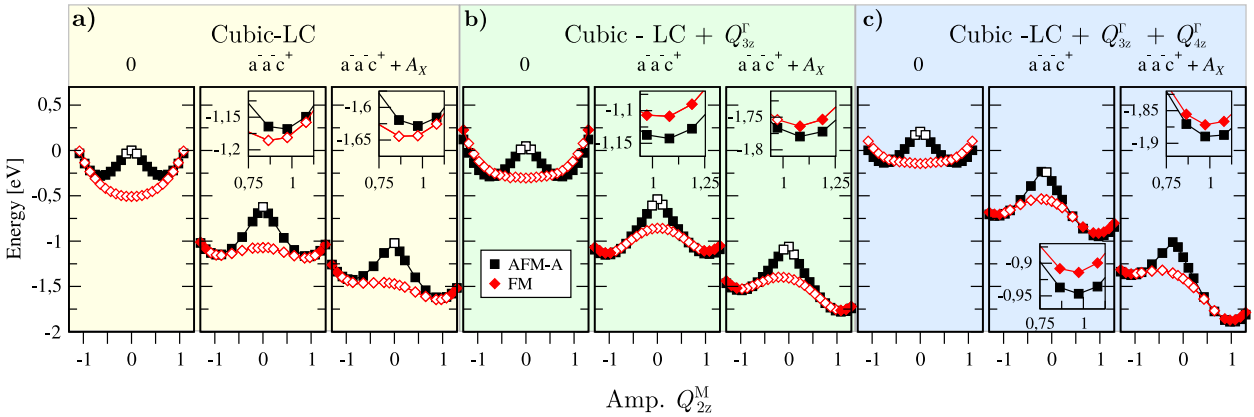

Figure 6.4: Comparison of the PESs of the $Q^{\mathbf{M}}_{2z}$ mode within different distorted structures. The three main panels refer to distinct unit cells : a) cubic lattice constants $a = b = c = 3.935$Å. b) cubic lattice constant and added tetragonal strain Q^{Γ}_{3z} (as in the ground state). c) cubic lattice constant and added tetragonal Q^{Γ}_{3z} and shear Q^{Γ}_{4z} strains, leading to the ground state orthorhombic lattice constants. Within a),b) and c), the three sub-panels refer from left to right to the condensation of $Q^{\mathbf{M}}_{2z}$ mode (i) alone (0), (ii) in presence of octahedral rotations condensed with their ground state amplitudes ($a^-a^-c^+$) and (iii) in presence of octahedral rotations and antipolar motion A_X condensed with their ground state amplitudes ($a^-a^-c^+ + A_X$). All energies refer to the cubic $Pm\bar{3}m$ structure with AFM-A magnetic ordering, which is set to zero. Open (resp. filled) symbols denote metallic (resp. insulating) states.

For the FM-surface this behavior can be attributed to bi-quadratic couplings terms in the free energy expansion between the rotations and the $Q^{\mathbf{M}}_{2z}$ mode

$$\mathscr{F} \propto \beta_2(\phi)^2(Q^{\mathbf{M}}_{2z})^2, \tag{6.3}$$

where the coupling constant β_2 is largely negative and ϕ represents a global rotation amplitude that implies that ϕ^+_z and ϕ^-_{xy} keep the same ratio as in the ground-state (see Table 6.3).

For the AFM-A surface, β_2 is close to zero. The shift of the single wells has to be attributed to a strong enhancement of the vibronic coupling α_{JT} expressed by the parameter $\lambda_\phi < 0$ in Table 6.3. Nonetheless, the ground state is FM and metallic until the largest amplitudes. On the AFM-A surface a band gap opens instantaneously by applying $Q^{\mathbf{M}}_{2z}$. Both effects ($\lambda_\phi < 0$ and $\beta_2 < 0$) should be attributed to the strong reduction of the e_g bandwidth (from about 4eV to 3 eV - not shown here).

On both magnetic surfaces, the rotations alone induce a $Q^{\mathbf{M}}_{2z}$ amplitude close to the experimental one. We emphasize that this strong coupling is related to the specific electronic structure of $LaMnO_3$, as other $Pbnm$ perovskites with significant octahedral rotations show only negligible $Q^{\mathbf{M}}_{2z}$ amplitudes (e.g. $CaMnO_3$ [148]). Additionally to Eq. 6.3, there is a fourth-order term coupling linearly the $Q^{\mathbf{M}}_{2z}$ mode with the rotations:

$$\mathscr{F} \propto \alpha_1[(\phi^-_{xy})^2\phi^+_z]Q^{\mathbf{M}}_{2z}. \tag{6.4}$$

The effect of this term appears however negligible since the symmetry of the potential well is (almost completely) maintained when the rotations are condensed. Although A_X is intrinsically stable in the cubic phase, its presence is naturally driven in presence of ϕ^-_{xy} and ϕ^+_z due to a trilinear coupling term,

$$\mathscr{F} \propto \alpha(\phi^-_{xy}\phi^+_z)A_X, \tag{6.5}$$

which, in another context, is known to be related to the appearance of hybrid improper ferroelectricity [149] in some cation ordered perovskite superlattices. Consequently, as in other $Pnma$ perovskites [134], the

Table 6.3: Table of fitted constants to reproduce the PES in Fig. 6.4. From up to down. Zero point Energies E_0, gathering energy gains or losses of condensing individual modes and strains without $Q^{\mathbf{M}}_{2z}$ distortion. First and-second order parameters $\alpha\&\beta$ gathering linear and quadratic lattice couplings in $Q^{\mathbf{M}}_{2z}$. Electronic Parameter α_{JT} gathering the variation of the electronic instability in dependence of the condensed lattice modes.

					Zero Point Energies E_0					
MO	E_0^{FM}	$E_0^{Q^{\Gamma}_{3z}}$	$E_0^{Q^{\Gamma}_{3z}Q^{\Gamma}_{4z}}$	E_0^{ϕ}	$E_0^{\phi,Q^{\Gamma}_{3z}}$	$E_0^{\phi,Q^{\Gamma}_{3z},Q^{\Gamma}_{4z}}$	E_0^{ϕ,A_X}	$E_0^{\phi,A_X,Q^{\Gamma}_{3z}}$	$E_0^{\phi,A_X,Q^{\Gamma}_{3z},Q^{\Gamma}_{4z}}$	
FM [eV]	-0.51	0.21	0.16	-0.56	0	0.16	-0.40	-0.15	-0.27	
AFM-A [eV]	-	0.05	0.15	-0.63	0.05	0.18	-0.39	-0.12	-0.29	
					First- and Second Order Parameters $\alpha\&\beta$					
MO	α_1	α_2	α_3	α_4	α_5	β_1	β_2	β_3	β_4	β_5	β_6
FM [eV]	-0.02	-0.09	-0.03	-0.11	-0.01	0.26	-0.53	0.04	-0.22	-0.01	0.003
AFM-A [eV]	-0.01	-0.10	-0.02	-0.11	-0.02	0.29	-0.04	0.02	0.08	-0.01	-0.20
					Electronic Parameter α_{JT}					
		λ-Cubic			$\lambda_{Q^{\Gamma}_{3z}}$			$\lambda_{Q^{\Gamma}_{3z}+Q^{\Gamma}_{4z}}$		
	α^0_{JT}	$+\phi$	$+\phi + A_X$	0	$+\phi$	$+\phi + A_X$	0	$+\phi$	$+\phi + A_X$	
AFM-A [eV]		-0.74	-0.20	0.01	-0.09	0.15	-0.03	0.10	-0.18	0.04	

condensation of A_x globally decreases the energy through this term (part of E_0^{ϕ,A_X} in Eq. A.4), producing a rigid down-shift of the energy wells in Fig. 6.4. In a similar way there exist a trilinear term

$$\mathscr{F} \propto \alpha_2 (A_X \phi^{-}_{xy}) Q^{\mathbf{M}}_{2z}. \tag{6.6}$$

This term does significantly break the symmetry of the $Q^{\mathbf{M}}_{2z}$ surface on the contrary to term in Eq. (6.4). The asymmetry created by the crystal field, induced by the combination of ϕ^{-}_{xy} and A_X, is independent of the magnetic order since the fitted coefficient α_2 takes close values for AFM-A and FM ordering (See Table 6.3). That being said, the ground state surface is FM for all structures with cubic lattice constants. Only the AFM-A surface shows insulating behavior around its minima. The coupling terms above are obviously equally valid in the strain distorted unit-cells and similar trends can be seen in the energy surfaces of all three examined cases.

To summarize, we have found (i) that octahedral rotations trigger $Q^{\mathbf{M}}_{2z}$ by e_g bandwidth reduction and (ii) that octahedral rotations combined with the antipolar motion A_X induce a significant crystal field that breaks the symmetry of the $Q^{\mathbf{M}}_{2z}$ PES.

6.5.2 Tetragonally compressed unit cell

Let us now focus on Fig. 6.4b in which the compressive tetragonal strain $Q^{\mathbf{\Gamma}}_{3z}$ has been added to the cubic lattice. Again, the PES in terms of $Q^{\mathbf{M}}_{2z}$ is shown when condensing or not the other lattice distortions. Adding $Q^{\mathbf{\Gamma}}_{3z}$ increases energy independently of the magnetic order, but decreases

their distance at $Q_{2z}^{\mathbf{M}} = 0$ as

$$E_0^{Q_{3z}^{\mathbf{\Gamma}}}(\text{AFM} - \text{A}) < E_0^{Q_{3z}^{\mathbf{\Gamma}}}(\text{FM}). \tag{6.7}$$

On the FM surface the $Q_{2z}^{\mathbf{M}}$ mode gets significantly softened. The softening can be associated to linear-quadratic and biquadratic strain-phonon coupling terms

$$\mathscr{F} \propto \beta_4 Q_{3z}^{\mathbf{\Gamma}}(Q_{2z}^{\mathbf{M}})^2 + \beta_5 (Q_{3z}^{\mathbf{\Gamma}})^2 (Q_{2z}^{\mathbf{M}})^2. \tag{6.8}$$

Here the linear-quadratic term is dominating since $\beta_4 > \beta_5$ (see Table 6.3). This implies directly that the appearance of $Q_{2z}^{\mathbf{M}^2}$ favors a compressive over an elongating tetragonal strain $Q_{3z}^{\mathbf{\Gamma}}$ and vice versa.

On the AFM-A surface it is mainly the electronic instability α_{JT} that is affected by $Q_{3z}^{\mathbf{\Gamma}}$ ($\lambda_{Q_{3z}^{\mathbf{\Gamma}}} < 0$, see Table 6.3) and shifts the amplitude of $Q_{2z}^{\mathbf{M}}$ close to the experimental bulk value. Most interestingly, the ground state surface is no longer the FM one: if the $Q_{3z}^{\mathbf{\Gamma}}$ strain and $Q_{2z}^{\mathbf{M}}$ distortion are condensed together, the AFM-A energy becomes lower than the FM energy at about 100% $Q_{3z}^{\mathbf{\Gamma}}$ + 50% $Q_{2z}^{\mathbf{M}}$. The linear-quadratic and biquadratic strain-phonon coupling terms do exist between the tetragonal strain and all symmetry adapted modes condensed in the *Pbnm* phase.

Octahedral rotations (ϕ) and $Q_{3z}^{\mathbf{\Gamma}}$ shift the energy minima on both magnetic surfaces to values well above 1, which can be explained by the phonon-phonon couplings highlighted in Eq. (6.3)-(6.6). Nonetheless, the "cubic plus rotations" surfaces stay lower in energy than tetragonal strained ones. Interestingly, at this point, the minima on the FM surface become insulating states. We can attribute this to the combined translational symmetry breaking of the anti-phase rotation ϕ_{xy}^{-} and the tetragonal compression of $Q_{3z}^{\mathbf{\Gamma}}$, which together break the translational symmetry just like the AFM-A order.

Adding A_X breaks the symmetry of the energy surface. The difference of energy between the minima along the positive and negative paths of $Q_{2z}^{\mathbf{M}}$ is increased, due to a quadri-linear strain-phonon term,

$$\mathscr{F} \propto \alpha_3 (Q_{3z}^{\mathbf{\Gamma}} \phi_{xy}^{-} A_X) Q_{2z}^{\mathbf{M}}. \tag{6.9}$$

We note that the same term exists replacing $Q_{2z}^{\mathbf{M}}$ with the in-phase octahedral rotation ϕ_z^+. It is because of those two terms that eventually the tetragonal phase gets slightly stabilized over the cubic one.

To summarize, we have additionally found (i) that the tetragonal compressive strain $Q_{3z}^{\mathbf{\Gamma}}$ combined with $Q_{2z}^{\mathbf{M}}$ stabilizes the AFM-A against the FM ordering , and (ii) that $Q_{3z}^{\mathbf{\Gamma}}$ combined with the anti-phase rotation ϕ_{xy}^{-} induces the opening of a band gap on the FM surface around the $Q_{2z}^{\mathbf{M}}$ minima.

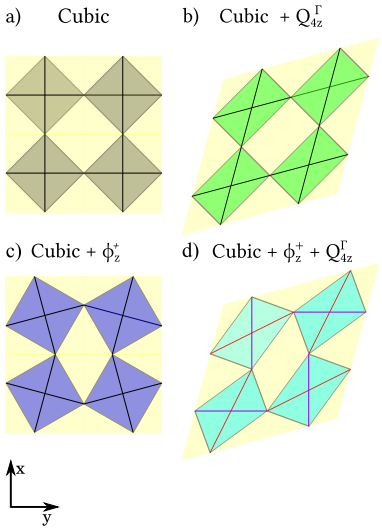

Figure 6.5: Schematic illustration of octahedral rotation ϕ_z^+ and shear strain $Q_{4z}^{\mathbf{\Gamma}}$ acting together as a $Q_{2z}^{\mathbf{M}}$ Jahn-Teller distortion of the oxygen octahedra. a) cubic phase, b) phase with shear strain $Q_{4z}^{\mathbf{\Gamma}}$, c) phase with rotation of the octahedra ϕ_z^+, and d) phase combining shear strain $Q_{4z}^{\mathbf{\Gamma}}$ and rotation ϕ_z^+. The combination of $Q_{4z}^{\mathbf{\Gamma}}$ and ϕ_z^+ acts as an effective $Q_{2z}^{\mathbf{M}}$ distortion : while all octahedral axis are equivalent (black lines) in (a), (b) and (c), the combination of $Q_{4z}^{\mathbf{\Gamma}}$ and ϕ_z^+ in (d) gives rise to shortened (purple) and elongated (red) octahedral axis in a way similar to $Q_{2z}^{\mathbf{M}}$.

6.5.3 Orthorhombic ground sate unit cell

Let us finally focus on Fig. 6.4c, adding together the compressive tetragonal strain $Q_{3z}^{\mathbf{\Gamma}}$ and the orthorhombic shear strain $Q_{4z}^{\mathbf{\Gamma}}$ with their ground state values in the cubic lattice. The strained unit cell has then the lattice parameter of the relaxed ground state cell. Adding the shear strain $Q_{4z}^{\mathbf{\Gamma}}$

on top of $Q_{3z}^{\mathbf{\Gamma}}$ further increases the global energy, if no other modes are condensed. The distance between the magnetic surfaces is approximately unaltered. On the contrary to the cubic and tetragonal cases, the symmetry of the $Q_{2z}^{\mathbf{M}}$ PES is broken when octahedral rotations are condensed. This is due to a trilinear term :

$$\mathscr{F} \propto \alpha_4 (Q_{4z}^{\mathbf{\Gamma}} \phi_z^+) Q_{2z}^{\mathbf{M}}. \tag{6.10}$$

Fig. 6.5 provides a sketch highlighting the physical meaning of Eq. (6.10). Neither an octahedral rotation nor a shear strain alone can lift the degeneracy of the octahedral bond lenghts. However, when the rotation axis and the axis normal to the shear plane coincide, they act together as an effective Q_2 motion and split the bond lengths. If the rotation is anti-phase (ϕ^-) the effective motion is $Q_2^{\mathbf{R}}$, if it is in-phase (ϕ^+) it becomes $Q_2^{\mathbf{M}}$. Hence in $LaMnO_3$ ϕ_z^+ and $Q_{4z}^{\mathbf{\Gamma}}$ build an effective $Q_{2z}^{\mathbf{M}}$ motion. This effective $Q_{2z}^{\mathbf{M}}$ motion explains that once ϕ_z^+ and $Q_{4z}^{\mathbf{\Gamma}}$ are condensed, the metal-insulator transition is reached for smaller $Q_{2z}^{\mathbf{M}}$ amplitudes compared to the previously discussed surfaces. Finally, it also explains, why the gradient discontinuity does not appear at $Q_{2z}^{\mathbf{M}} = 0$. To fit the PES with $Q_{4z}^{\mathbf{\Gamma}}$ and ϕ_z^+ condensed together, we had to introduce a shift of the zero coordinate of $Q_{2z}^{\mathbf{M}}$, which extracts the amplitude of their effective $Q_{2z}^{\mathbf{M}}$ distortion. When $Q_{4z}^{\mathbf{\Gamma}}$ and ϕ_z^+ are condensed with their ground-state amplitudes, $Q_{2z}^{\mathbf{M}}$ takes already $\approxeq$ 15% of its ground-state amplitude (i.e. 0.06Å). It can be extracted in Fig. 6.4c at the position of the gradient discontinuity on the AFM-A surface. Despite the trilinear term in Eq. (6.10), tetragonally and sheared distorted unit cell stay higher in energy compared to the cubic case if only the octahedral rotations are present. It is eventually A_X that induces an orthorhombic ground state through a quartic term, linear in $Q_{2z}^{\mathbf{M}}$ and similar to Eq. (6.9) :

$$\mathscr{F} = \alpha_5 (Q_{4z}^{\mathbf{\Gamma}} A_X \phi_{xy}^-) Q_{2z}^{\mathbf{M}}. \tag{6.11}$$

The FM surface is also insulating around its $Q_{2z}^{\mathbf{M}}$ minima and the AFM-A surface is the global ground state in all $Q_{3z}^{\mathbf{\Gamma}} + Q_{4z}^{\mathbf{\Gamma}}$ distorted cases.

To summarize, we have found (i) that ϕ_z^+ and $Q_{4z}^{\mathbf{\Gamma}}$ act as an effective $Q_{2z}^{\mathbf{M}}$ motion and (ii) a quartic term that stabilizes the ground state unit cell shape.

6.5.4 Summary of Results of PES Analysis

From the discussion of the PESs, we can reach the following conclusions.

(i) Octahedral rotations trigger $Q_{2z}^{\mathbf{M}}$ by a negative bi-quadractic coupling on the FM surface and by an enhanced vibronic coupling on the AFM-A surface. This is attributed to a reduced e_g bandwidth.

(ii) Tetragonal strain $Q_{3z}^{\mathbf{\Gamma}}$ is responsible for the magnetic FM - AFM-A transition, by reducing the energy-difference between the AFM-A and FM surface. We note that this is in line with recent ab initio studies [118, 150, 151] and an experimental study of FM $LaMnO_3$ thin films grown on $SrTiO_3$ [122]. Here, the canonical Jahn-Teller distortion notations allowed us to extract $Q_{3z}^{\mathbf{\Gamma}}$ as the key structural parameter.

(iii) On the FM-surface, a band gap can only be opened by $Q_{2z}^{\mathbf{M}}$ in the presence of compressive tetragonal strain Q_{3z}^{Γ} and the anti-phase rotation ϕ_{xy}^{-}. This is assigned to the combined strong symmetry breaking of Q_{3z}^{Γ} and ϕ_{xy}^{-} along the *Pbnm*-c axis equivalent to the symmetry breaking of AFM-A order.

(iv) In none of the tested structures we found a finite value of α_{JT} on the FM surface. There is no vibronic coupling in the FM surface with respect to $Q_{2z}^{\mathbf{M}}$.

(v) Various lattice couplings lead to almost identical ground-state structures for FM and AFM-A orderings. This explains the absence of a structural distortion at the magnetic transition $T_N \approx 140K$.

(vi) Shear strain Q_{4z}^{Γ} and in-phase octahedral rotation ϕ_z^{+} act as an effective $Q_{2z}^{\mathbf{M}}$ distortion.

6.6 $Q_{2z}^{\mathbf{M}}$ and other Lattice Distortions around the T_{JT} transition

In this section we analyze the temperature evolution of the amplitudes of all relevant strains and phonon modes around the orbital ordering transition at $T_{JT} \approx 750$K, as measured experimentally. We discuss the variation of the amplitudes of lattice modes and strains in connection with the coupling terms defined before. We recalculate the $Q_{2z}^{\mathbf{M}}$ PES within the measured experimental structures around the transition. We show by a simple Monte-Carlo (MC) simulation of the evolution of $Q_{2z}^{\mathbf{M}}$ amplitude with temperature that those PESs qualitatively reproduce the phase transition. Our approach highlights that an important contribution to the stabilizing energy of the insulating phase is the spin symmetry breaking, which appears dynamically in the PM phases around the MIT but can be properly extracted from static DFT calculations.

Our experimental source is the recent study of *Thygesen et al.* [82], in which the authors measured the lattice structure over T_{JT} between 300 K and 1000 K. The aim of their study was to identify the differences in the local structure of the orbital ordered O' and disordered O phases in order to derive a better understanding of the O phase (sometimes

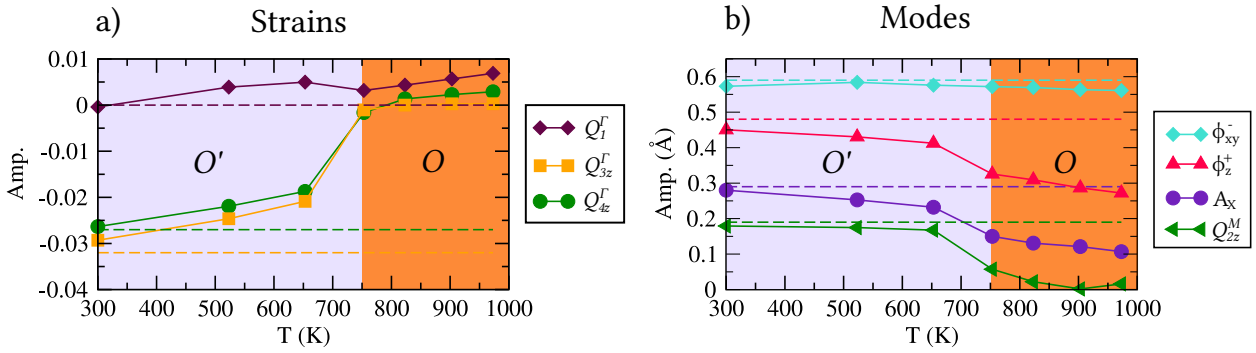

Figure 6.6: Experimental lattice modes and strain amplitudes across the O'/O-transition at $T_{JT} \approx 750K$. Structures extracted from Ref. [82] and analyzed with *ISODISTORT*. Dashed lines show low temperature amplitudes.

also called orbital-liquid phase and the transition has been described as orbital melting [101, 152]).

In Fig. 6.6a we show the symmetry adapted strain and in Fig. 6.6b the symmetry adapted phonon mode analysis of the experimental data around T_{JT}. The low temperature amplitudes noted in Table 6.1 are shown as dashed lines. Additionally, we show the variation of the unit-cell volume through the volume strain $Q_1^{\mathbf{\Gamma}}$, which points out the well-known volume collapse at T_{JT} [82, 101–103]. The tetragonal strain $Q_{3z}^{\mathbf{\Gamma}}$ and shear strain $Q_{4z}^{\mathbf{\Gamma}}$ show a linear decrease in amplitude for temperatures lower than T_{JT}. At T_{JT} they abruptly disappear almost completely and have only small amplitudes in the orbital disordered O phase. From the inspection of symmetry strains in Fig. 6.6a, it is obvious that the disappearance of $Q_{3z}^{\mathbf{\Gamma}}$ and $Q_{4z}^{\mathbf{\Gamma}}$ are much more severe at T_{JT} than the volume collapse of $Q_1^{\mathbf{\Gamma}}$. Although this has been previously pointed out by *Carpenter and Howard* [73], recent studies continue to emphasize the volume collapse [82]. The amplitudes of the modes at 300 K are close to their low temperature values. The amplitude of the anti-phase rotations ϕ_{xy}^- stays approximately constant and close to the low temperature value across the whole temperature range from 300 K to 1000 K. The amplitudes of the in-phase rotation ϕ_z^+ and the antipolar motion A_X decrease linearly between 300 K and T_{JT}. The Jahn - Teller distortion $Q_{2z}^{\mathbf{M}}$ keeps an almost constant amplitude between 300 K and T_{JT}. At T_{JT} there is a discontinuity for ϕ_z^+, A_X, and $Q_{2z}^{\mathbf{M}}$ with a sudden reduction in their amplitude. However, $Q_{2z}^{\mathbf{M}}$ does not completely disappear directly at T_{JT} as it could be expected. Above T_{JT}, ϕ_z^+, A_X, and $Q_{2z}^{\mathbf{M}}$ continue to decrease linearly ($Q_{2z}^{\mathbf{M}}$ until it reaches approximately zero amplitude at $\approx$ 900 K).

The similar linear temperature dependence of ϕ_z^+, A_X, $Q_{2z}^{\mathbf{M}}$ in the O' and O phases can be easily explained by Eq. (6.5) and (6.6). The amplitude change of ϕ_z^+ should be associated as the driving force as A_X is stable by itself and the amplitude of ϕ_{xy}^- is nearly constant . Then A_X follows simply the amplitude of ϕ_z^+ through the trilinear coupling in Eq. (6.5). Consistently, $Q_{2z}^{\mathbf{M}}$ follows the amplitude of ϕ_z^+ through the trilinear coupling in Eq. (6.6).

The small but non-zero amplitude of $Q_{2z}^{\mathbf{M}}$ just before the transition might suggest that the variation of ϕ_z^+ with temperature induces the transition by the trilinear *improper* mechanism of Eq. (6.6).

To get a more detailed insight, we recalculated the PESs of $Q_{2z}^{\mathbf{M}}$ in the experimental structures extracted from Ref. [82] between 523K and 973K and then executed a simple MC simulation on this surfaces to find the mean amplitude of $Q_{2z}^{\mathbf{M}}$ at a given temperature. To account for the PM state at the transition, we calculated the PESs in four distinct simple magnetic orders (FM, AFM-A, AFM-C and AFM-G, see Fig. 6.7a-d). Then we execute a MC simulation of the $Q_{2z}^{\mathbf{M}}$ amplitude on each magnetic surface individually. We perform a 100 times 10 million MC steps from which we extract the mean $Q_{2z}^{\mathbf{M}}$ amplitude and the standard deviation of the amplitude. Finally, we find the overall mean amplitude as the mean of the four surfaces. The resulting mean amplitude is shown alongside the measured one in Fig. 6.7e. Error bars show the standard deviation of the $Q_{2z}^{\mathbf{M}}$ amplitude, which gives a measure on how much $Q_{2z}^{\mathbf{M}}$ fluctuate at a given temperature. The approach of mixing

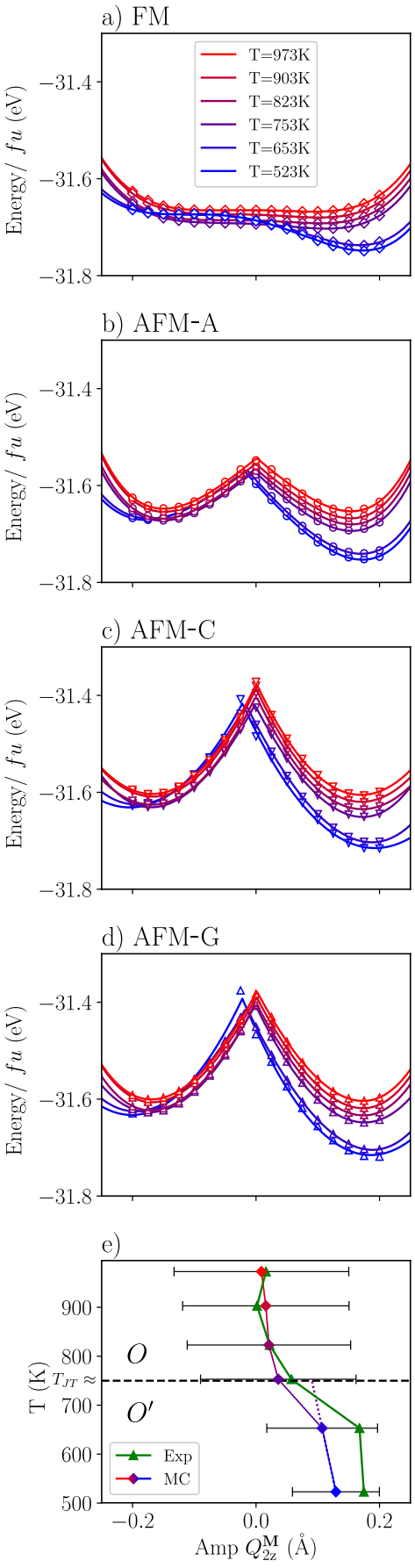

Figure 6.7: a)-d) $Q^{\mathbf{M}}_{2z}$ Born Oppenheimer potential energy surfaces (PESs) as calculated from DFT within the lattice structures measured by *Thygesen et al.* at the indicated temperatures and magnetic orders. Markers show the DFT energies, continuous lines a polynomial fit. e) Experimental amplitudes of $Q^{\mathbf{M}}_{2z}$ and mean amplitudes resulting a Monte-Carlo (MC) simulation of the above PESs with $T_{sim}/T_{exp} = 0.625$. Error Bars show the standard deviation of the MC simulation.

together the simulation of various magnetic orderings can be seen as a simplified account for the multi Slater-determinant character of a PM electronic wavefunction that is more rigorously treated by advanced material specific many-body methods like DFT+DMFT. On the other hand DFT+DMFT calculations typically exclude the influence of the lattice by parameterizing an Anderson impurity model on a given lattice configuration.

Although a renormalization of the temperature is needed ($T_{sim}/T_{exp} = 0.625$), it can be seen that the qualitative features of the $Q_{2z}^{\mathbf{M}}$ amplitude with reducing temperatures are well reproduced by our simple simulation approach: in particular, a small linear increase of $Q_{2z}^{\mathbf{M}}$ before the transition and a sudden jump to larger amplitudes below. The error bars show a huge distribution above T_{JT}, which is consistent with the experimentally described *liquidish* behavior, and a strong reduction of the distribution below.

Through the PESs, we can examine the origin of this transition. The FM surface shows that the rotation amplitudes of ϕ_{xy}^{-} and ϕ_{z}^{+} are large enough even at the highest temperature to produce a weak instability through the bi-quadratic coupling in Eq. (6.3). Then through the trilinear coupling of Eq. (6.6), a weak asymmetry of the surface is induced which increases before the transition. After the transition this asymmetry is significantly amplified such that he minimum on the negative side of $Q_{2z}^{\mathbf{M}}$ disappears. This change can be mainly attributed to the relaxation of the strains $Q_{3z}^{\mathbf{\Gamma}}$ and $Q_{4z}^{\mathbf{\Gamma}}$ and the associated couplings in Eq. (6.8),(6.9),(6.10),(6.11), which are linear in $Q_{2z}^{\mathbf{M}}$. Only taking into account the FM surface a lattice triggered picture would be convincing. However, the minima on this surface are much too shallow to explain the transition at such a high temperature.

The shallow minima are corrected by taking into account the AFM PESs to mimic the PM phase. On the AFM PESs, deep minima exist due to the Peierls condition that is met in all AFM orderings. This translates into a finite vibronic coupling, whose strength is increased going from AFM-A over AFM-C to AFM-G as the e_g bandwidth is decreased. Taking the AFM PESs into account in the MC-simulation instead of relying only on the FM surface increases the transition temperature strongly. This underlines the importance of *spin symmetry breaking* to activate the strong electron-lattice coupling stabilizing the insulating phase. Also, it shows that the importance of the dynamical fluctuations of the spin in the PM phase for stabilizing the insulating phase lies only partly in the activation of dynamical correlations, but equally in the *instantaneous* symmetry breaking it produces. The effect of spin symmetry breaking, although experimentally dynamical, can be properly extracted by static DFT calculations as shown from our simplistic approach.

Finally, a multifaceted image about the origin of the transition emerges. On one hand it is "improperly" induced by the lattice, favoring one side of the $Q_{2z}^{\mathbf{M}}$ well over the other. On the other hand, it incorporates also the characteristics of an order-disorder transition as deep minima for $Q_{2z}^{\mathbf{M}}$ persist in the high temperature *O*-phase, which is magnetically and structurally disordered. The origin of these deep minima is the *dynamic symmetry breaking* of the spin-order in the PM phase.

However, our MC approach does not allow us to comment on the persistent debate of the importance of *dynamic correlations* over *dynamic spin symmetry breaking* and lattice symmetry breaking [115]. Nonetheless, the least we can deduce is that *instantaneous electronic symmetry breaking* contributes to a large part of the stabilization energy that drives the MIT by inducing a large electron-phonon coupling. It has been noted before that such a large electron-phonon coupling is necessary to explain the high MIT transition temperatures and the dynamic Jahn-Teller deformations in the high-temperature phase in $KCuF_3$ [88] and $LaMnO_3$ [87].

Finally, we note that it would be possible to optimize $(U|J)$ values that bring the MC simulation transition temperature to the experimental transition temperature. This would however not lead to any additional insights as it would merely mean to tune a parameter in a reduced model description.

To gain more microscopic insight into the transition mechanism and the dynamical properties of the high temperature metallic *O*-phase, nucleic and electronic subsystems have to be treated *dynamically coupled* in large supercells at finite temperature. An approach to realize such a dynamic coupling are so-called second principles models [44–46].

6.7 Charge vs. Orbital Ordering in $LaMnO_3$

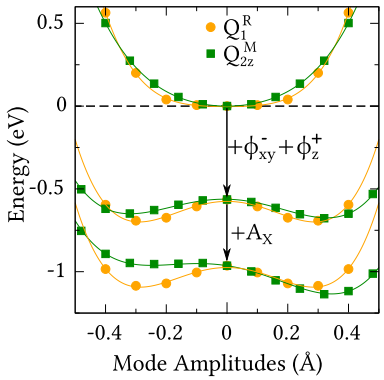

Figure 6.8: PES of $Q_1^{\mathbf{R}}$ and $Q_{2z}^{\mathbf{M}}$ distortions within FM ordering in cubic-structure (top curves), with condensed octahedral rotations ϕ_{xy}^- and ϕ_z^+ - (middle curves), and with additionally condensed antipolar motion A_X (bottom curves).

Until this point, we investigated the relevant *statically appearing* distortions in the single-crystal ground state phase of $LaMnO_3$. However, at few occasions, a charge ordering instability has been discussed as an alternative and competing mechanism to orbital ordering [153, 154] or as the origin of the transition in the high-temperature orbital liquid phase, which has been, in that picture, described as an electron-hole liquid phase [114, 155]. Such a charge-ordering instability in the high-temperature phase should be accompanied by the instability of a *breathing type distortion* $Q_1^{\mathbf{R}}$ (see Table 5.1). Recent works showed that the charge-ordering transition in $RNiO_3$ (a e_g^1 perovskite with doubly occupied t_{2g} states) can be understood as a Peierls transition [77] triggered by the appearance of octahedral rotations. Moreover, the same picture applies to alkaline-earth ferrites, $AFeO_3$ [116], with the same formal occupation of Fe *d*-states as Mn *d*-states ($d^4 = t_{2g}^3 e_g^1$). In those ferrites, the instabilities of $Q_1^{\mathbf{R}}$ and $Q_{2z}^{\mathbf{M}}$ compete and can be tuned by epitaxial strain. A similar behavior has been found in $HoNiO_3$ [156].

In Fig. 6.8, we show that the same competition exists for the $RMnO_3$ series with the example of $LaMnO_3$. Here, we limit ourselves to calculations within the FM ordering. In the top of Fig. 6.8, the PESs of $Q_1^{\mathbf{R}}$ and $Q_{2z}^{\mathbf{M}}$ within cubic $LaMnO_3$ can be seen. Both of them show stable single wells, with comparable harmonic and higher-order dependencies. If the octahedral rotations are condensed, the total energy of the system is significantly reduced and both distortions become dynamically unstable, with $Q_1^{\mathbf{R}}$ slightly favored. This result shows that the approach of a Peierls transition in the $Q_1^{\mathbf{R}}$ coordinate triggered by octahedral rotations [77] is equally valid in $RMnO_3$. The argument is point-by-point similar to that in $AFeO_3$ and $RNiO_3$ compounds, as can be found in [77, 116]. We note also that, on the AFM surfaces, we find the same vibronic coupling for $Q_1^{\mathbf{R}}$ as

for $Q_{2z}^{\mathbf{M}}$, which we do not show for simplicity. Finally, the competition between $Q_1^{\mathbf{R}}$ as for $Q_{2z}^{\mathbf{M}}$ is decided in favor of $Q_{2z}^{\mathbf{M}}$ by the trilinear coupling with the anti-phase rotation ϕ_{xy}^{-} and the antipolar motion A_X (Eq. (6.6)), since there is no such coupling incorporating $Q_1^{\mathbf{R}}$. If the tetragonal and shear strain $Q_{3z}^{\mathbf{\Gamma}}$ and $Q_{4z}^{\mathbf{\Gamma}}$ are relaxed, $Q_1^{\mathbf{R}}$ and $Q_{2z}^{\mathbf{M}}$ get strongly separated (not shown). These results are consistent with the proposed self-trapping of the charge-disproportionated phase [114] and the observation of the coexistence of different phases depending on heat treatments and the history of samples [157].

6.8 $LaMnO_3$ Thin Films

$LaMnO_3$ thin films have been mainly studied grown on the [100] surface of a cubic perovskite $SrTiO_3$ substrate. This is on one hand surely due to the fact that $SrTiO_3$ is the standard high quality substrate that any laboratory working on perovskite thin films has in its drawer, but on the other hand due to the finding of an unusual FM insulating phase for $LaMnO_3$ films grown on $SrTiO_3$. *Roqueta et. al* [122] produced $LaMnO_3$ epitaxial thin films on $SrTiO_3$ [100] surfaces under varying partial oxygen pressure with thicknesses of about 100 - 120 cubic perovskite unit cells (35-45 nm). They found that for the highest partial oxygen pressure their films are fully strained to the substrate, are almost exactly stoichiometric, and the *Pnma* c-axis around which the oxygen octahedron in-phase rotations take place is orientated parallel to the substrate's surface. For lower oxygen pressures they found oxygen vacancies incorporated in their films. All films showed FM insulating behavior, where the stoichiometric films showed the highest saturation magnetization ($\approx 3.5\ \mu_B/Mn$). By means of X-ray absorption measurements they found no evidence for a change in the oxidation state of the manganese ions (for any partial oxygen pressure). *Marton et al.* produced epitaxial $LaMnO_3$ thin films on $SrTiO_3$ [100] surfaces of about 30nm thickness [119, 120]. They found a strongly reduced optical band gap [119] and FM behavior in the as-grown films. Through annealing above 700°C in a reduced oxygen atmosphere they could recover a more insulating AFM phase. They assigned the origin of the FM phase to the accommodation of oxygen vacancies inducing some fraction of Mn^{4+} [119] in the thin film, which then promotes FM behaviour through double exchange as in $R_x^{3+}A_{1-x}^{2+}MnO_3$ solid solutions or to La deficiency [120]. *Wang et al.* [123] produced much thinner $LaMnO_3$ films on $SrTiO_3$ [100] surfaces with thicknesses varying between 1-24 cubic unit cells. They showed that all films are completely strained to the $SrTiO_3$ constants independently of the thickness. Intriguingly they found a sharp transition from an AFM insulating to a FM insulating behavior between 5 and 6 unit cell thick films. In the FM state they found a saturation magnetization about 1.6 μ_B/Mn (for films thicker than 7 unit cells). As they didn't find any structural changes between the 5 and 6 unit cell thick films they assigned the transition to a polar-catastrophe scenario similar to the one in the conducting $LaAlO_3/SrTiO_3$ interface. However, they did not find conductivity at the interface. All studies find an out of plane lattice constants between 3.92 - 3.95 Å, where *Wang et al.* [123]do mention a slight thickness dependent variation in the supplementary material[c]. Neither study does specifically report the space group of the thin film. However, *Roqueta et al.* [122] deduced the existence of octahedral rotations

by XRD, while *Wang et al.* [123] deduce from their RHEED patterns the absence of those.

In this section we first reproduce the FM insulating thin film phase of $LaMnO_3$ on $SrTiO_3$ by imposing a simple constraint to the lattice and using the DFT+(5.5|1.5) method introduced above. Then we show that the origin of that FM insulating phase lies in the reduction of the tetragonal strain Q^{Γ}_{3z} of the thin film with respect to the bulk phase and the appearance of the alternate $Q^{\mathbf{R}}_{3z}$ mode. From a band-structure analysis the appearance of this $Q^{\mathbf{R}}_{3z}$ mode can be equally understood as a Peierls effect and is linked to the opening of the electronic-band gap in the FM phase. Finally, we investigate the epitaxial strain phase diagram and show that there is a phase transition from the FM to AFM-A phase for larger cubic substrate lattice parameters compatible with the earlier work of *Hou et al.* [118]. This transition is related to the orientation of the rotation pattern with respect to the substrate and the tetragonal strain relaxation.

6.8.1 $LaMnO_3$ on $SrTiO_3$ from DFT+U

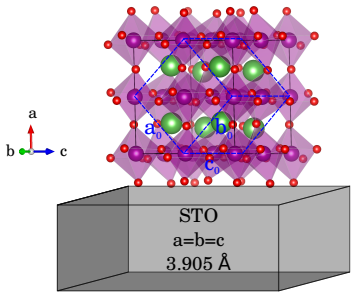

Figure 6.9: Schematic draw of the 40 atoms unit cell (black solid line) used for the constraint thin-films calculations. Lattice parameters b and c were fixed to $2 \cdot a_{STO}$ = 7.81Å while a was free to relax. The blue line shows unit cell of the $P-1$ phase is drawn.

In this section we present the results of first-principles calculations with epitaxial thin-film constraints for $LaMnO_3$ grown on $SrTiO_3$. To impose the constraint of the epitaxial growth we used a $2 \times 2 \times 2$, 40-atoms supercell - with respect to the 5-atoms cubic perovskite structure (see Fig. 6.9). In the geometrical relaxation we fixed the supercell axis b and c to $2 \cdot a_{STO}$=7.81 Å and let the a-lattice parameter, it's angle to the surface, as well as the atomic positions relax. The use of the large supercell allows to relax the orientation of the octahedral rotation pattern in any direction with respect to the fixed lattice parameters. We did not impose any symmetry restrictions during relaxation. The results are collected in Table 6.4. The magnetic ground state is FM in accordance with the experimental results. Interestingly the second most stable state is AFM-C instead of AFM-A. We find 3.95 Å as the pseudocubic out of plane lattice constant, which compares well to the experimental ones. The symmetry analysis with the *FINDSYM*-software [158] showed that our relaxed state is in close proximity to the *P-1* triclinic space group only keeping a center of inversion as the sole symmetry element. As the $Pnma$ unit cell, the *P-1* unit cell possesses 20 atoms. The lattice parameters of the *P-1* unit-cell are parallel to those of $Pnma$ with the sole difference of incorporating angles slightly different from 90° between the lattice vectors. Its orientation within the 40 atoms supercell is drawn in Fig. 6.9 (blue line), which shows that the *Pnma* - c axis lies parallel to the substrate's surface as it is observed in experimentally grown films [122]. The symmetry of the space group appears to be opposed to the $P2_1/n$ symmetry found in first-principles calculations by *Hou et al.* [118]. However, if we increase the tolerance on the lattice parameters and atomic positions in the *FINDSYM* software we find the same $P2_1/n$ space group as *Hou et al.*, which makes us believe that the structure of *Hou et al.* and ours are in close proximity[1]. Our calculations provide a band gap of of 0.49 eV for the FM ground-state, which lies in proximity to the experimentally reported one by *Marton et al.* [119]. The analysis of lattice strains with *ISODISTORT* shows that the large shear strain Q^{Γ}_{4z} and tetragonal strain Q^{Γ}_{3z} are significantly reduced with respect to the

1: However, an explicit comparison is not possible since *Hou et al.* did not provide complete structural information [118].

Table 6.4: Calculated thin film properties with PBEsol + (5eV|1.5eV) for thin film constraints of epitaxial grown $LaMnO_3$ on $SrTiO_3$ (STO) with fixed in plane lattice parameter of a_{STO} = 3.905Å. Energy difference per Formula Unit for various magnetic orders with respect to AFM-A. Cubic lattice constant perpendicular to $SrTiO_3$ surface. Lattice Parameters in the 20-atoms triclinic *P-1* with axis parallel to the *Pnma* one. Amplitudes of symmetry adapted modes and symmetry adapted strains. And electronic band gap. Besides the magnetic energies all values refer to the FM ground state.

	$\Delta E/fu$ (meV)	a (Å)		*P-1*			Strains & Modes (Å)	
AFM-A	0	Calc	3.95	a_0 (Å)	b_0 (Å)	c_0 (Å)	Q^{Γ}_{3z}	-0.005
AFM-C	-2	Exp[a]	3.92 ± 2	5.483	5.624	7.810	Q^{Γ}_{4z}	-0.018
AFM-G	+11	Exp[b,c]	3.92-94	$\alpha = \beta$ (°)	89.68		$Q^{\Gamma}_{4x} = Q^{\Gamma}_{4y}$	-0.004
FM	-20	Exp.[d,e]	3.94	γ (°)	89.34		A_X	0.260
	E_{Gap}[eV]						ϕ^{+}_{z}	0.434
	Calc.	0.49					$Q^{\mathbf{M}}_{2z}$	0.117
	Exp.	0.33					$Q^{\mathbf{R}}_{3z}$	0.077
							ϕ^{-}_{xy}	0.623

[a] Ref. [122]
[b] Ref. [123]
[c] 3.92 Å for 5 unit cells, 3.93 Å for 7 unit cells and 3.94 Å for 20 unit cells (supplementary material of [123])
[d] Ref. [119]
[e] as grown.

bulk ground state. The reduction of Q^{Γ}_{3z} stems from the constraint of the c_0-lattice parameter, which is fixed to $2 \cdot a_{STO}$. The reduction of Q^{Γ}_{4z} stems from the constraint of the a_0 and b_0 lattice parameters to $a_0 - b_0 = 2 \cdot a_{STO}$ [159]. Turning our attention to the symmetry adapted modes, we find that the $Q^{\mathbf{M}}_{2z}$ distortion is reduced to approximately half of the bulk value. Additionally, a $Q^{\mathbf{R}}_{3z}$ Jahn-Teller distortion appears which is absent in the bulk. The other distortions are less influenced by the epitaxial thin film strain constraint but generally reduced (A_X by 21%, ϕ^{+}_{z} by 11%, and ϕ^{-}_{xy} by 4%). In conclusion, we have shown in this section that the $(U|J)$ parameters we deduced in section 6.2 are also suited to describe the epitaxial thin film phase. In the thin film the anti-phase $Q^{\mathbf{R}}_{3z}$ mode appears which imposes a $d_{x^2-y^2}/d_{z^2-r^2}$ orbital ordering compatible with ferromagnetism according to the *Goodenough-Kanamori* rules [160–162]. Hence, although we did not perform calculations incorporating oxygen vacancies, our calculations support the possibility of existence of intrinsic insulating ferromagnetism in stoichiometric $LaMnO_3$ thin films. In the next section we will however examine in depth the conditions under which this intrinsic insulating FM thin film phase can exist.

6.8.2 PES of $Q^{\mathbf{R}}_{3z}$ - Stabilization of Insulating Thin Film FM State

The intriguing structural difference between the thin-film constrained FM insulating and the bulk ground state AFM-A phase is the appearance of the $Q^{\mathbf{R}}_{3z}$ mode. In this section we analyze the dependence of the PES of the $Q^{\mathbf{R}}_{3z}$ mode with respect to the octahedral rotations and the $Q^{\mathbf{M}}_{2z}$ modes as they appear in the relaxed thin film phase in a similar way as we did for the $Q^{\mathbf{M}}_{2z}$ mode in the bulk ground state. Secondly, we investigate the possible connection of the $Q^{\mathbf{R}}_{3z}$ mode to the opening of an electronic band gap within the FM phase. As the lattice strains are greatly reduced in

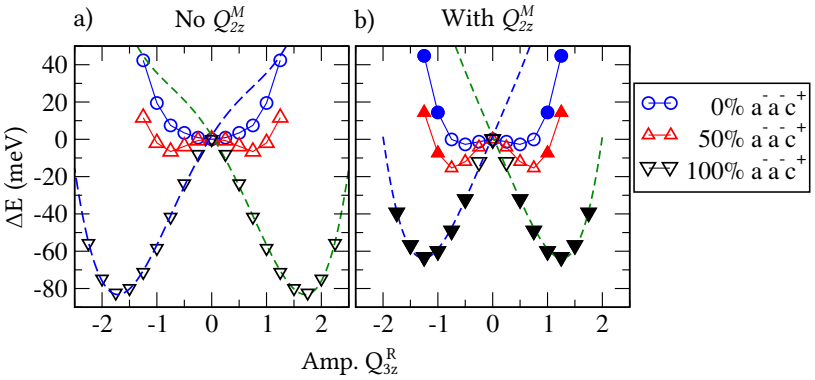

Figure 6.10: PES of $Q^{\mathbf{R}}_{3z}$ Jahn-Teller distortion in a cubic lattice. a) Sampling of $Q^{\mathbf{R}}_{3z}$ surface with three different rotation amplitudes. 100% rotations refers to the rotation amplitude in the relaxed $LaMnO_3$ on $SrTiO_3$ phase. b) The same but with the $Q^{\mathbf{M}}_{2z}$ mode condensed as it appears in the relaxed $LaMnO_3$ on $SrTiO_3$ thin film. Open symbols represent metallic and filled ones insulating structures.

the thin film phase we do not investigate the couplings of $Q^{\mathbf{R}}_{3z}$ with the strains but use only a cubic cell with a lattice constant of $a_0 = 3.935$Å. As we are interested in the FM phase we only show the $Q^{\mathbf{R}}_{3z}$ FM PES. We fit polynomials of the form

$$\mathscr{F} = \alpha_{JT}\left|Q^{\mathbf{R}}_{3z}\right| + \beta(Q^{\mathbf{R}}_{3z})^2 + \gamma(Q^{\mathbf{R}}_{3z})^4 \tag{6.12}$$

to rationalize the shape of the surface. The resulting PESs are shown in Fig. 6.10. In Fig. 6.10 a) we show the $Q^{\mathbf{R}}_{3z}$ PESs for three different amplitudes of octahedral rotations (0%,50%,and 100% of their amplitude in the relaxed thin film). In Fig. 6.10 b) we show the same three $Q^{\mathbf{R}}_{3z}$ PESs, but with the $Q^{\mathbf{M}}_{2z}$ mode already condensed with it's relaxed thin film amplitude. Each PES is set to zero energy at $Q^{\mathbf{R}}_{3z} = 0$. We emphasize that only energy differences by condensing the $Q^{\mathbf{R}}_{3z}$ can be extracted, but not the global ground state[2].Open symbols in Fig. 6.10 refer to a metallic ground state at the given structure, filled ones to an insulating.

Let's turn our attention to Figure 6.10 a). Without rotations (in the purely cubic phase) the $Q^{\mathbf{R}}_{3z}$ is stable. Increasing the rotations destabilize it. Interestingly, the destabilization stems from an increased value of α_{JT} *and* a negative value of β. However, for neither amplitude of the octahedral rotations an electronic band gap is opened. For the case of 100% rotations the minima lie well above 1.

Now let's turn our attention to Figure 6.10 b). If the $Q^{\mathbf{M}}_{2z}$ mode is condensed the $Q^{\mathbf{R}}_{3z}$ modes shows a weak instability even in the absence of rotations due to $\alpha_{JT} < 0$ (Compare Fig. 6.10 b)). Condensing the rotations increases α_{JT} and the stabilization energy of $Q^{\mathbf{R}}_{3z}$ is significantly increased. At 100% rotations β is positive, the minima are insulating and are lying close to 1. The total energy gain of condensing $Q^{\mathbf{R}}_{3z}$ is reduced in the presence of $Q^{\mathbf{M}}_{2z}$, which means that the biquadratic coupling between $Q^{\mathbf{R}}_{3z}$ and $Q^{\mathbf{M}}_{2z}$ is positiv. Consequently, the appearance of one disfavors the appearance of the other, which explains the absence of $Q^{\mathbf{R}}_{3z}$ in the bulk phase. However, we emphasize that under the thin film constraint and the reduction of the tetragonal strain Q^{Γ}_{3z}, the combination of $Q^{\mathbf{M}}_{2z}$ and $Q^{\mathbf{R}}_{3z}$ under the presence of the rotations is the lowest energy structure.

To understand how the octahedral rotations destabilize the $Q^{\mathbf{R}}_{3z}$ Jahn-Teller mode from an electronic point of view, we show in Fig. 6.11 the electronic band structure for selected distorted structures in the first Brillouin zone of the orthorhombic unit cell with uniform (pseudocubic) lattice constants $\frac{a}{\sqrt{2}} = \frac{b}{\sqrt{2}} = \frac{c}{2} = 3.935$Å. We show the majority spin

2: We decided to do so, since the energy gain of condensing the octahedral rotations is a magnitude larger than the one of condensing the $Q^{\mathbf{R}}_{3z}$. If we applied the same procedure as in the results of Fig. 6.4, the instabilities in Fig.6.10 would be hardly visible.

Table 6.5: Fitted coefficients of $Q^{\mathbf{R}}_{3z}$ PES from Fig. 6.10.

Rot.Amp (%)	α_{JT}	β	γ
	No $Q^{\mathbf{M}}_{2z}$		
0	4.73	-0.92	15.57
50	-0.38	-20.55	18.05
100	-49.53	-15.73	5.18
	With $Q^{\mathbf{M}}_{2z}$		
0	-7.75	-2.73	23.97
50	-21.80	-11.85	24.42
100	-72.90	2.75	8.27

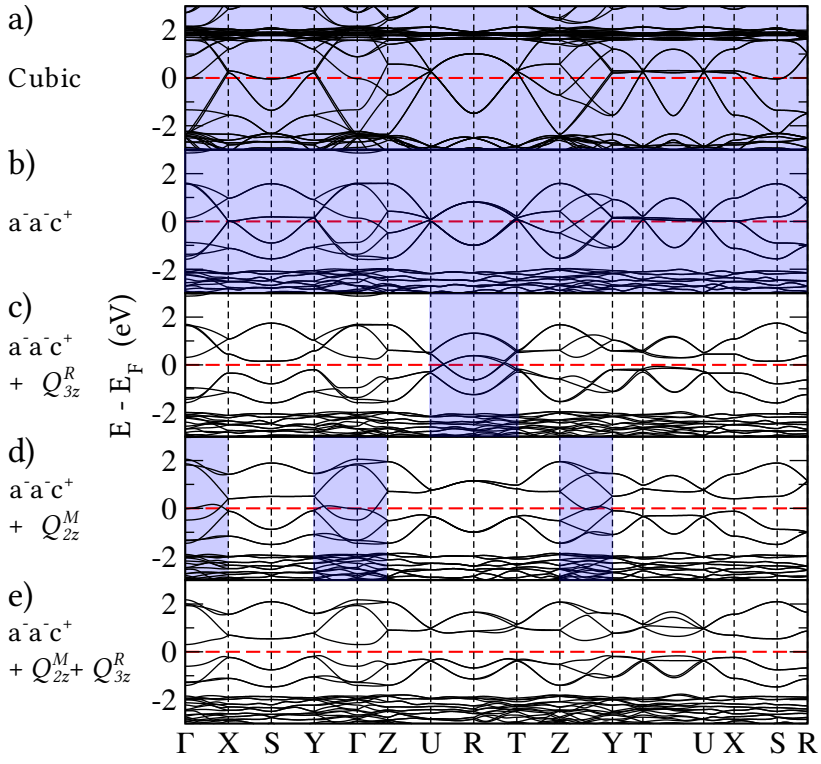

Figure 6.11: Electronic majority band structure in FM $LaMnO_3$ with different condensed modes in the first Brillouin-zone of the regular orthorhombic unit cell. a) Cubic band structure folded to orthorhombic unit cell. b) Added $a^-a^-c^+$ Rotations. c) Rotations plus $Q^{\mathbf{R}}_{3z}$ Jahn-Teller distortion. d) Rotations plus $Q^{\mathbf{M}}_{2z}$ Jahn-Teller distortion. d) Rotations and both Jahn-Teller distortions. Metallic parts of the Brillouin zone are highlighted in blue. The Fermi level is emphasized in a dashed red line.

channel of the FM calculations in a window of ±3eV around the Fermi-level[3]. In Fig. 6.11 a) we show the electronic structure of the cubic phase (this is the folded band structure of Fig. 6.3 a) in section 6.4). The largely dispersed bands with a bandwidth of approximately 4.5 eV around the Fermi level are Mn e_g/O-p hybrid bands . In the metallic cubic structure at almost each high symmetry point there is a double crossing of the e_g-bands compatible with a Peierls condition. We highlight parts of the Brillouin zone where bands cross the Fermi level in blue. If the rotations are condensed, the metallicity persists ,but the bandwidth is significantly reduced to ≈ 3eV due to the decreased overlap of the e_g orbitals with the neighboring oxygen states. Due to the reduced bandwidth, the e_g bands are well separated from the bands above and below (Compare Fig. 6.11 b)). If the $Q^{\mathbf{R}}_{3z}$ Jahn-Teller distortion is condensed on top of the rotations, a band gap is opened in the whole Brillouin-zones besides the path U-R-T, which explains the metallic behavior found in Fig. 6.10 a) (Compare Fig. 6.11 c)). On the other hand if only the $Q^{\mathbf{M}}_{2z}$ Jahn-Teller distortion is condensed on top of the rotations a band gap is opened in the section U-R-T, but not in the sections $\Gamma - X$,$\Gamma - Y$, $\Gamma - Z$, and $Z - Y$ (Compare Fig. 6.11 d)). Hence, if $Q^{\mathbf{M}}_{2z}$ and $Q^{\mathbf{R}}_{3z}$ are condensed together the band gap is opened in the whole Brillouin-zone at the FM state becomes insulating ($E_g \approx 0.5eV$). We emphasize, that a similar mechanism is apparent on the bulk FM PES but replacing $Q^{\mathbf{R}}_{3z}$ by the tetragonal strain $Q^{\mathbf{\Gamma}}_{3z}$ which leads to larger energy gains. If the $Q^{\mathbf{R}}_{3z}$ mode is condensed without rotations the section X-S-R and T-U are not opened which leads to a total energy cost, since more occupied states are moved up than down. This results in a stabilization of the mode (not shown). The $Q^{\mathbf{M}}_{2z}$ distortion on the FM surface, however seems to be solely, introduced by the biquadratic and trilinear coupling terms we described earlier, since we did not find any gradient discontinuity in the FM $Q^{\mathbf{M}}_{2z}$ PESs in Fig. 6.4 a). Nonetheless, similarly the negative biquadratic coupling can

3: The minority spin channel possesses a band gap of ≈ 3.5 − 4eV

be explained by the reduced bandwidth similarly as it has been done recently in an ab initio study of rare earth nickelates and the breathing type distortion $Q_1^{\mathbf{R}}$ [77].

Finally, we can summarize the mechanism producing the insulating FM state in the LMO-$SrTiO_3$ thin film.
(i) The reduction of the strain $Q_{3z}^{\mathbf{\Gamma}}$ due to the alignment of the *Pnma* c-axis induces a change of the magnetic PES from AFM-A to FM.
(ii) The persistence of the rotations induces the $Q_{2z}^{\mathbf{M}}$ mode by reducing the bandwidth of the e_g electrons expressed in biquadratic couplings.
(iii) Also due to the e_g bandwidth the $Q_{3z}^{\mathbf{R}}$ mode is destabilized through an increase of α_{JT}.
(iv) Together, $Q_{2z}^{\mathbf{M}}$ and $Q_{3z}^{\mathbf{R}}$ open a band gap in the whole brillouin-zone keeping the FM order .

6.8.3 Epitaxial Strain Phase Diagram of $LaMnO_3$

In this section we revisit the epitaxial strain phase diagram of $LaMnO_3$. We apply the analysis of symmetry adapted modes and strains, in order to generate a complete picture of the development of properties and the structure of thin films under varying epitaxial strain conditions. We relaxed $LaMnO_3$ without symmetry restrictions keeping a and b parameters fixed to a range $a_0 = 3.935 \pm 1.5\%$ using the 40-atoms unit cell from Section 6.8. The results are gathered in Fig. 6.12 a) - g). For strains between -1.5 % and 0.5 % we find that the *P-1* phase with the c-axis parallel to the substrate surface is the most stable one, like in the case of $LaMnO_3$ on $SrTiO_3$. The magnetic ground state in this phase is FM and the distance in energy to the AFM-A state is constantly about 20 meV/fu (Compare Fig 6.12 a)). At about +0.5 % strain a phase-transition to the *Pnma* phase appears, where the orientation of the c-axis changes form parallel to orthogonal and at the same time the magnetic ground state changes from FM to AFM-A. In this phase the energy difference between the two magnetic orders is greatly reduced to some meV/fu like in the bulk.

The structural information of $LaMnO_3$ under varying epitaxial strain are shown in Fig. 6.12 b) - g). Fig. 6.12 b) and c) show the pseudocubic lattice constants and the crystallographic angles[4] contained in the thin film. Fig. 6.12 d) and e) contain the same information, but expressed in symmetry adapted normal and shear strains. Fig. 6.12 f) shows the amplitude of the antipolar motion A_X as well as the in and out-of phase octahedral rotations ϕ_{xy}^{-}/ϕ_z^{+}. Finally, Fig. 6.12 g) contains the development of the Jahn-Teller distortions $Q_{3z}^{\mathbf{R}}$ and $Q_{2z}^{\mathbf{M}}$ in dependence of epitaxial strain. Looking at the pseudocubic lattice constants in Fig. 6.12 b) in the *P-1* phase we note that c_{pc} is equal to the imposed lattice constant, since it is oriented parallel to the surface. a_{pc} and b_{pc} do not vary with epitaxial strain in this phase. The accommodation of the epitaxial lattice strain within the a_{pc} and b_{pc} plane is achieved by varying the lattice angle γ as it can be extracted from 6.12 c). The same information is reflected in the analysis of symmetry adapted strains in Fig. 6.12 d) and e). For the tetragonal strain $Q_{3z}^{\mathbf{\Gamma}}$ is altered between -0.01 and 0.01 in the *P-1* phase due to the change of the epitaxial lattice parameter. It is relatively small compared to the bulk (≈ -0.04). The variation of the lattice angle γ is

4: Angles and pseudocubic lattice constants are deduced from the 20 atoms unit cell as $a_{pc} = \frac{a_0}{\sqrt{2}}$, $b_{pc} = \frac{b_0}{\sqrt{2}}$, and $c_{pc} = \frac{c_0}{2}$ (Compare Fig. 6.9).

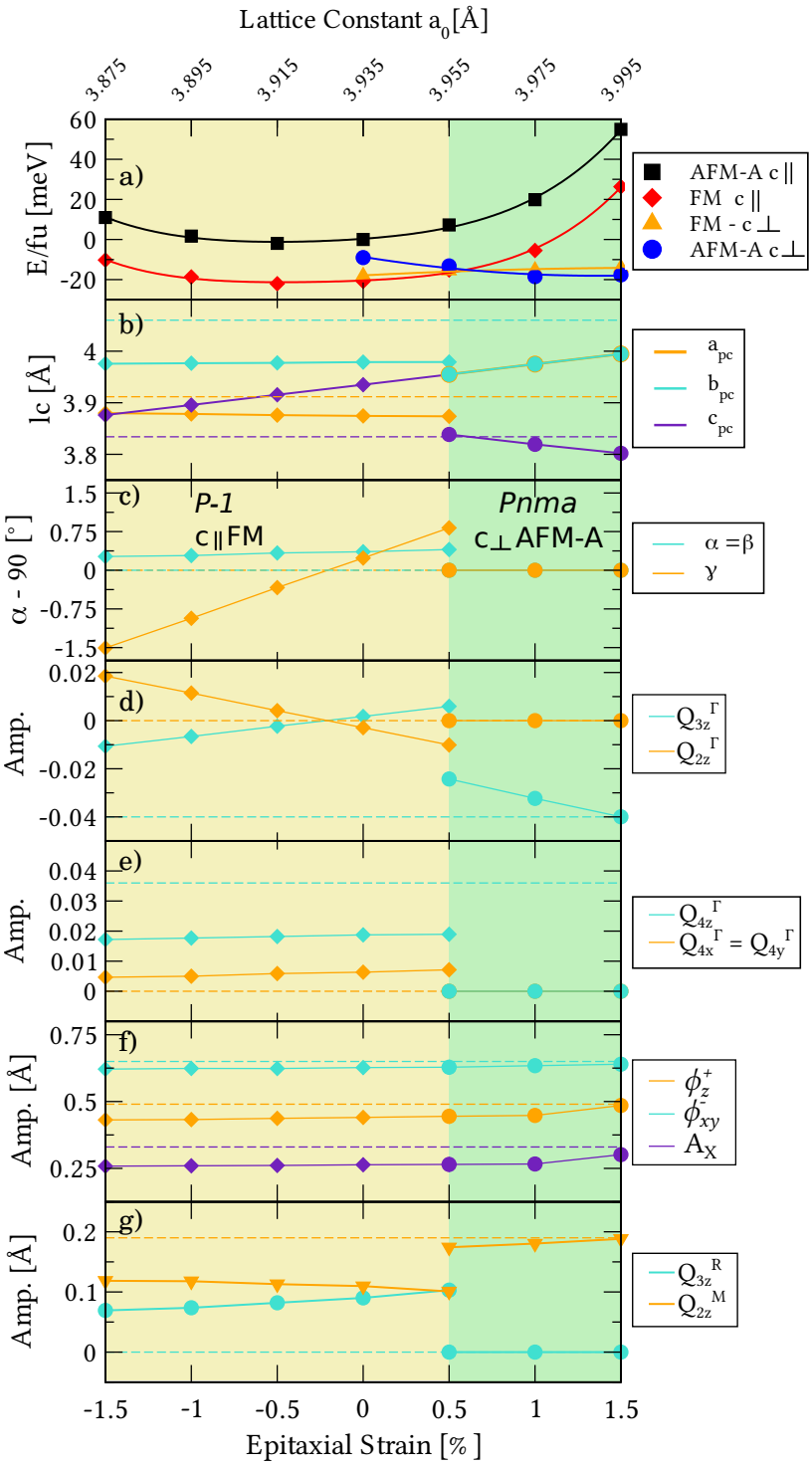

Figure 6.12: Epitaxial strain phase diagram of $LaMnO_3$ on [100] cubic perovskite substrates from constraint DFT calculations. a) Total Energy/fu referenced to zero strain *P-1* AFM-A phase, b) pseudocubic lattice constants, c) crystallographic angles, d) normal strains Q_{2z}^{Γ} and Q_{3z}^{Γ}, e) shear strains $Q_{4x,y,z}^{\Gamma}$, f) amplitude of octahedral rotations ϕ_{xy}^-/ϕ_z^+ and antipolar motion A_X, and g) amplitudes of Jahn-Teller distortions $Q_{3z}^{\mathbf{R}}$ and $Q_2^{\mathbf{M}}$ contained in the film depending of applied epitaxial strain. Corresponding bulk values are shown in dashed lines.

expressed in the lattice strain Q_{2z}^{Γ}. It appears as a normal strain in the analysis of the symmetry adapted strains with respect to the $Pm\bar{3}m$ phase, but changes the angle γ in the 20-atoms orthorhombic unit cell which is rotated 45° to the cubic one. The shear strain Q_{4z}^{Γ} tunes the inequality of a_{pc}/b_{pc} and is quasi-constant in the *P-1* phase. The Jahn-Teller phonon like modes $Q_{3z}^{\mathbf{R}}$ and $Q_{2z}^{\mathbf{M}}$ stay fairly constant within the *P-1* phase. At the transition to the $Pnma$ phase the following structural changes occur. The c_0 axis changes orientation to be orthogonal to the substrate's surface and relaxes greatly also expressed in a great jump of

the $Q^{\mathbf{\Gamma}}_{3z}$ strain. The a_0/b_0 plane is parallel to the substrate's surface. Hence $a_{pc} = b_{pc}$, expressed in the fact that the shear strain $Q^{\mathbf{\Gamma}}_{4z}$ becomes strictly zero. All lattice angles fall to 90°, hence also the amplitude of strain $Q^{\mathbf{\Gamma}}_{2z}$ is strictly zero. In conclusion the epitaxial strain accommodation in the *Pnma* phase is achieved solely by the variation of a_{pc} and b_{pc}. Figure. 6.12 f) shows that the amplitudes of the antipolar motion and the octahedral rotations are unchanged through the transition. Only the amplitude of the Jahn-Teller modes change significantly. The $Q^{\mathbf{R}}_{3z}$ amplitude falls to strictly zero in the *Pnma* phase since it is not allowed by symmetry. The $Q^{\mathbf{M}}_{2z}$ mode is greatly amplified to a value close to the bulk ground state across the transition to the *Pnma* phase. We remark that the epitaxial strain-phase diagram that we presented here, is principally equivalent to the one presented by *Hou et. al* [118], who found equally a phase transition from FM to AFM-A with similar distortions of the oxygen octahedra as presented here. We assign the slight change for the absolute value of the epitaxial lattice parameter at which the transition occurs to the different calculation parameters (notable different $(U|J)$ corrections). However, as in the case for the $LaMnO_3$ on $SrTiO_3$ thin film we assign the phase *P-1* in the regime between -1.5 % and 0.5 % epitaxial strain in contrast to $P2_1/n$ assigned by *Hou et. al*. We believe the major differences between our and their phases are the lattice angles $\alpha = \beta \approx 0.35°$ in our case, which in their case were zero or have been disregarded for simplicity.

In the following we examine *why* the film is preferring one orientation of the c-axis over another for certain values of the imposed epitaxial lattice constant. To do so, we sample the FM and AFM-A PESs of the lattice strains $Q^{\mathbf{\Gamma}}_{3z}$ and $Q^{\mathbf{\Gamma}}_{4z}$ in the *P-1* and $Pnma$ phase, since $Q^{\mathbf{\Gamma}}_{3z}$ is the strain that can relax in the c_0-orthogonal ($Pnma$) and $Q^{\mathbf{\Gamma}}_{4z}$ in the c_0-parallel (*P-1*) configuration. The *P-1* and *Pnma* phases are constructed by condensing symmetry adapted modes (A_X, ϕ^+_z, ϕ^-_{xy},$Q^{\mathbf{M}}_{2z}$, and $Q^{\mathbf{R}}_{3z}$) as we found them at 0% epitaxial strain. Then, we sample the strain PESs starting from an unstrained unit cell with the pseudo-cubic lattice constant $a_{pc} = 3.935$Å keeping the amplitudes of the modes fixed. The amplitudes of the modes in the *P-1* and *Pnma* phases are shown in Table 6.6. Fig. 6.13 a) and b) show the PESs. All energies in both graphs have been referenced to the energy of the unstrained AFM-A *Pnma* phase. Firstly, we discuss the energies at zero strain in both phases. In the *Pnma* phase there is a weak stabilization of about 5 meV/fu of the FM over the AFM-A order (See 6.13 b). We could expect this result, from Sec. 6.3 where we showed that the FM to AFM-A transition is linked to the condensation of $Q^{\mathbf{\Gamma}}_{3z}$. On the contrary in the *P-1* AFM-A and FM order are separated by an energy difference of about 25 meV/fu, which fairly reproduces the energy difference between the two magnetic orders in the epitaxial strain phase diagram Fig. 6.12 a). The origin of the stabilization of the FM state can be clearly assigned to the change of the amplitude of the Jahn-Teller modes $Q^{\mathbf{M}}_{2z}$ and $Q^{\mathbf{R}}_{3z}$ with respect to the *Pnma* phase. The electronic instability of the $Q^{\mathbf{R}}_{3z}$ mode - highlighted in Sec. 6.3 Fig. 6.10 - only exist in the FM phase. However, in the AFM-A phase the electronic instability doesn't exist and the condensation of mode $Q^{\mathbf{R}}_{3z}$ increases the total energy. Now, we discuss the PES of the tetragonal strain $Q^{\mathbf{\Gamma}}_{3z}$ in both structural phases. In the *P-1* phase this strain is almost stable, while in the *Pnma* phase the strain becomes strongly unstable as we expect from sec. 6.3 through the various strain mode couplings. At about $Q^{\mathbf{\Gamma}}_{3z} = -0.015$Å the magnetic transition appears and the AFM-A magnetic order becomes stabilized over the

Phase	A_X(Å)	ϕ_z^+(Å)	ϕ_{xy}^-(Å)	$Q_{2z}^{\mathbf{M}}$(Å)	$Q_{3z}^{\mathbf{R}}$(Å)	E/fu(eV)
P-1	0.20	0.40	0.64	0.11	0.09	-31.744
Pnma	0.20	0.40	0.64	0.17	0	-31.728

Table 6.6: Amplitudes of symmetry adapted modes used for a model structures to investigate the strain energy dependence across the epitaxial strain transition.

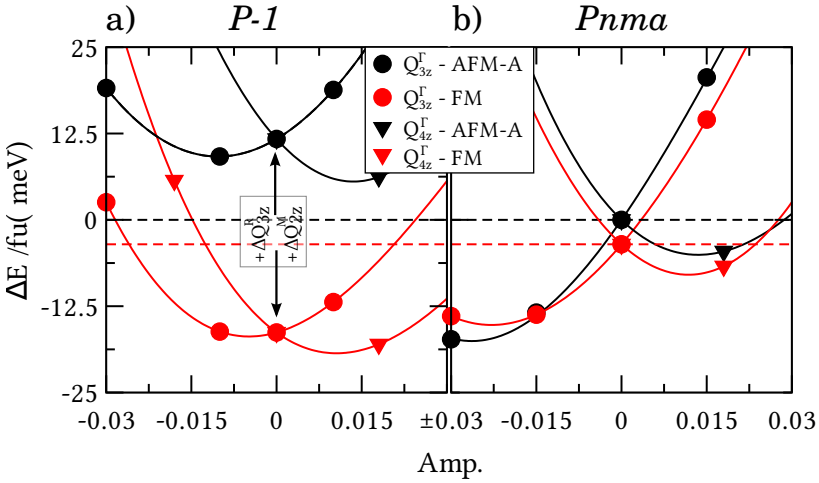

Figure 6.13: PES of symmetry adapted strains Q_{3z}^{Γ} and Q_{4z}^{Γ} for different structures and magnetic orderings. a) Structure *P-1* and b) structure *Pnma* as described in Tab. 6.6. Common reference for all energies in all graphs zero coordinate of the *Pnma* structure with AFM-A ordering.

FM one. In contrast to the tetragonal strain Q_{3z}^{Γ} the shear strain Q_{4z}^{Γ} is unstable in both structural and magnetic configurations. Condensing this strain gives the possibility to gain a few meV/fu with respect to the zero strain reference.

With this information we can draw the following picture for the phase transition starting from large lattice constants in the *Pnma*-phase.
(i) The c-axis orientates orthogonal to the substrate's 100 surface in the *Pnma*-phase and relaxes to a value close to the bulk ground state. The magnetic ground state is AFM-A.
(ii) Going to smaller substrate lattice constants, the amplitude of Q_{3z}^{Γ} is increased (i.e. the tetragonal compression is reduced).
(iii) At approximately $Q_{3z}^{\Gamma} = 0.015$ the magnetic phase transition from AFM-A to FM occurs.
(vi) On the FM PES the $Q_{3z}^{\mathbf{R}}$ mode is unstable and condensed in the structure.
(v) As a result, it becomes favorable to relax the Q_{4z}^{Γ} strain for which the orientation of the crystallographic lattice parameters has to change from c_o-orthogonal to c_0-parallel.

Finally, we show in Fig. 6.14 the electronic band gap and optical dielectric constant of the c_0-parallel *P-1* and c_0-orthogonal *Pnma* phases in dependence of epitaxial strain. Within the epitaxially strained *Pnma* phase both properties are similar to the bulk values, which we could expect, since in this phase the magnetic order as well as the amplitudes of the strain Q_{3z}^{Γ} and the mode $Q_{2z}^{\mathbf{M}}$ are equal, respectively similar, to the bulk. On the contrary the properties of the *P-1* phase are significantly different. The optical dielectric constant is increased approximately by a factor of 3 and becomes almost isotropic since the tetragonal strain is greatly reduced. At the same time the electronic band gap is reduced about 0.3 ~ 0.4eV at the transition. These changes of properties might be technologically exploited by growing $LaMnO_3$ thin films on piezoelectric substrates with a lattice constant matching the transition lattice constant

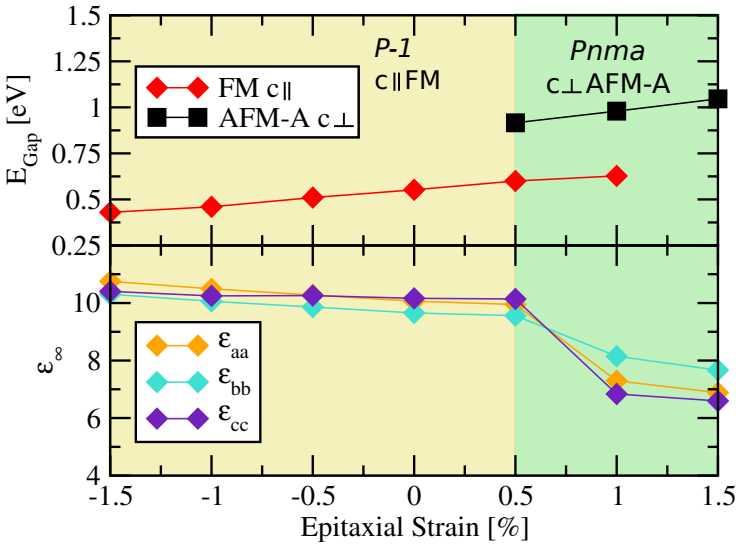

Figure 6.14: Kohn-Sham independent particle system band- gap and optical dielectric constant ϵ_∞ from DFPT in $LaMnO_3$ thin films dependence of epitaxial strain.

value, hoping to be able to drive the film back and forth between the two phases by an electric field exploiting the converse piezoelectric effect of the substrate. On the contrary the hope to achieve a large effect by this approach could be limited, since the rotation pattern has to be changed through transition, which implies surpassing a large energy barrier. If this is the case one would rather expect, that a change of strain by using the converse-piezoelectric effect will only slightly vary the properties of the thin film *within* one phase. However, the phase diagram of Fig. 6.12 also predicts a change from AFM-A to FM in this scenario. This approach has been experimentally investigated in two studies by *Zheng et al.* [163, 164]. They investigated thin films of $LaMnO_3$, $CaMnO_3$ and $LaMnO_{3+\delta}$ incorporating some degree of oxygen vacancies on PMN-PT substrates. While they did find a substantial effect on the electric conductivity of $LaMnO_3$ thin films caused by the strain-change induced by an electrical field exploiting the converse piezoelectric effect of the substrate, the mechanism causing the change of conductivity in the film stayed rather unclear. Our results show a paradigm that it could simply be related to a - partly - phase transition of the film caused by the epitaxial strain. However,the limited characterization of the $LaMnO_3$ thin films and the complete absence of a characterization of the substrate/film interface in the studies of *Zheng et al.* are insufficient to unambiguously claim that the reduction of conductivity is simply and only caused by the strain effects we present in this work.

6.9 Conclusions

In conclusion we presented first-principles calculations able to consistently reproduce the bulk ground state properties of $LaMnO_3$. We systematically investigated the PESs of $LaMnO_3$ around its aristotype cubic reference structure. To do so, we used the decomposition of lattice distortions into orthonormal symmetry adapted strains and phonon like modes using ISODISTORT [128] and the canonical Jahn-Teller distortion notation that we introduced in section 5.1. This approach provides us an orthonormal basis to study the interplay between lattice distortions and the electronic and magnetic structure.

The investigation of the $Q_{2z}^{\mathbf{M}}$ PES in the cubic phase by our first principles calculations showed that the origin of the vibronic coupling in the $Q_{2z}^{\mathbf{M}}$ coordinate lies in a Peierls effect. The Peierls condition is met in the AFM-A phase when the spin symmetry broken along the cubic z-direction. Then $Q_{2z}^{\mathbf{M}}$ distortion and AFM-A order break all thee translational symmetries and open a band gap.

Through the analysis of the PESs under the presence of other significant lattice distortions that appear in the *Pbnm* phase of $LaMnO_3$ we were able to explain a number of interlocking mechanisms between strain/phonon like distortions, magnetic ordering and the opening of an electronic band gap. Of these the most important are:
(i) Octahedral rotations trigger the $Q_{2z}^{\mathbf{M}}$ mode on the FM surface by a negative biquadratic coupling and the AFM surfaces by an increase of the vibronic coupling. The origin of both is the reduced e_g - bandwidth.

(ii) The most important parameter for stabilizing FM over AFM-A magnetic ordering is the tetragonal strain $Q_{3z}^{\mathbf{\Gamma}}$. Reducing this strain will favor the FM state serving as paradigm for engineering FM phases in rare-earth manganites.

(iii) The minimum of FM and AFM-A surfaces have the same structural distortion. This explains the absence of any structural transformations at the AFM to PM transition at $T_N = 140K$.

Then, we went further and showed from a MC simulation that the orbital ordering transition at $T_{JT} = 750K$ can be qualitatively reproduced by the PESs provided by our DFT calculations. The analysis of this transition showed mixed characteristics of order-disorder, lattice improper, and electronically induced, transitions. In this view the electronic driving force of the MIT can be attributed to *spin symmetry breaking* in the PM metallic phase. It enables the large electron-phonon coupling to explain the high MIT in $LaMnO_3$. Although the spin symmetry breaking appears *dynamically* in the PM phase, its importance lies more in the instantaneous symmetry breaking, which can hence be extracted from *static* DFT calculations, than in its dynamical nature. Nonetheless, this does not rule out any contribution from dynamical electron correlations in stabilising the insulating phase since appropriate U correction to DFT remains important for treating properly $LaMnO_3$.

Further, we showed from first-principles that a subtle competition between charge-ordering and orbital ordering exists in $LaMnO_3$, which further enriches its behavior.

Finally, we turned our attention to the FM thin film phase of $LaMnO_3$ grown on $SrTiO_3$. Our calculations showed that an intrinsic FM phase in stoichiometric $LaMnO_3$ is possible. Oxygen vacancies, that have sometimes been claimed to be the origin of the FM thin film phase, are not necessary to stabilize the FM order. With the help of the canonical Jahn-Teller distortion notations we could extract that the tetragonal strain is the detrimental distortion that selects the stability between AFM-A and FM orders, which we could expect from the analysis of the bulk PESs. If the tetragonal strain is reduced by the thin film constraint, the FM order is preferred.

While we believe that our work will serve as a sound basis for general lattice-electronic dependencies in $LaMnO_3$ and related compounds, we

are aware that not all questions in this compound are resolved. Especially the dynamic nature of *O* phase and the precise mechanism of the orbital ordering transition will remain highly debated and we emphasize the need for new general predictive model descriptions. Our work highlights that such model needs to include properly the *self-consistent interplay* between lattice, strain and electronic degrees of freedom. A promising tool to achieve such a model description is the generation of so-called second-principles model transferring first-principle results into local lattice and electronic effective potentials. Such second principle models would then give rise to large scale simulations at finite temperature with access to complete local information and allow for local lattice as well as electronic fluctuations needed to study the cooperative Jahn-Teller effect in its comprehensive dynamical complexity.

First-Principles study of Alkaline Earth Ferrites

7

ABO_3 perovskite oxides, with a transition metal at the B-site, form a vast class of functional materials, fascinating by the diversity of their unusual properties [92, 165, 166]. Amongst them, different families of compounds with a formal e_g^1 occupation of the d orbitals at the B-site, like rare-earth manganites ($d^4 = t_{2g}^3 e_g^1$ in $R^{3+}Mn^{3+}O_3$, with R a rare-earth element), rare-earth nickelates ($d^7 = t_{2g}^6 e_g^1$ in $R^{3+}Ni^{3+}O_3$), or alkaline earth ferrites ($d^4 = t_{2g}^3 e_g^1$ in $A^{2+}Fe^{4+}O_3$, with A = Ca, Sr or Ba) are similarly prone to show metal-insulator transitions (MIT). However, the mechanism behind such a transition can be intriguingly different from one family to the other.

$RNiO_3$ (except R=La) and $RMnO_3$ compounds crystallize in the same metallic $Pbnm$ $GdFeO_3$-type phase at sufficiently high-temperature. This phase is compatible with their small tolerance factor and labeled ($a^-a^-c^+$) in Glazer's notation [3]. It differs from the aristotype cubic perovskite structure, only expected at very high temperature and not experimentally observed, by the coexistence of two types of atomic distortions: (i) in-phase rotation of the oxygen octahedra along z direction (ϕ_z^+) and (ii) anti-phase rotations of the same oxygen octahedra with identical amplitude around x and y directions (ϕ_{xy}^-). On the one hand, $RNiO_3$ compounds show on cooling a MIT ($T_{MIT} = 0 - 600K$) concomitant with a structural transition from $Pbnm$ to $P2_1/n$ [167]. This lowering of symmetry arises from the appearance of a breathing distortion of the oxygen octahedra ($Q_1^{\mathbf{R}}$), recently assigned to a structurally triggered mechanism [77] and producing a kind of charge ordering (CO) [154, 168–171]. On the other hand, $RMnO_3$ compounds also exhibit on cooling a MIT ($T_{MIT} \approx 750K$) but associated to orbital ordering (OO) and linked to the appearance of Jahn-Teller distortions ($Q_{2z}^{\mathbf{M}}$) compatible with the $Pbnm$ symmetry [105, 172].

In comparison, $AFeO_3$ compounds do not behave so systemically and adopt seemingly different behaviors. While $SrFeO_3$ and $BaFeO_3$ keep the ideal cubic perovskite structure and show metallic behavior at all temperatures [7, 173], $CaFeO_3$, which crystallizes above room temperature in a $Pbnm$ $GdFeO_3$-type phase, exhibits a behavior similar to nickelates. At 290K, a MIT takes place at the same time as its symmetry is lowered to $P2_1/n$ due to the appearance of a breathing distortion [174, 175]. A variety of explanations have been previously proposed to elucidate the MIT in $CaFeO_3$, including orbital hybridization [176], electron-lattice interactions [177, 178], and ferromagnetic coupling [179]. However, no net picture has emerged yet to rationalize its behavior and that of other ferrites.

Here, we show from first-principles calculations that the CO-type MIT in bulk $CaFeO_3$ arises from the same microscopic mechanism as in the nickelates and must be assigned to a progressive triggering of $Q_1^{\mathbf{R}}$ atomic distortions by ϕ_z^+ and ϕ_{xy}^- atomic motions. We demonstrate that this triggered mechanism is universal amongst the ferrite family and that an

insulating phase can be induced in metallic $SrFeO_3$ from appropriate tuning of oxygen rotations. Going further, we reveal that CO and OO compete in $AFeO_3$ compounds and we unveil the possibility to switch from CO-type to OO-type MIT in $CaFeO_3$ thin films under appropriate strain conditions. This offers a convincing explanation for the enormous resistivity at room-temperature recently found in $CaFeO_3$ films grown on $SrTiO_3$ [180].

7.1 Calculation Details

Our first-principles calculations relied on density functional theory (DFT) as implemented in VASP [15, 181]. We worked with the PBEsol [124] exchange-correlation functional including U and J corrections as proposed by Liechtenstein [19]. We used $(U|J) = (7.2|2.0)$ eV, a plane-wave energy cutoff of 600 eV and Monkhorst-Pack [127] k-point samplings equivalent to $12 \times 12 \times 12$ for a 5-atoms cubic perovskite cell. The lattice parameters and internal atomic coordinates were relaxed until atomic forces are less than 10^{-5}eV/Å. The phonon dispersion curves were calculated with $2 \times 2 \times 2$ supercells using finite displacement method. A special care was devoted to the determination of appropriate U and J parameters, which is discussed in detail in appendix B. We found that $(U|J) = (7.2|2.0)$ eV provides good simultaneous description of the structural (lattice constant and distortion amplitudes), electronic (insulating ground- state) and magnetic (AFM spiral-type ground state very close in energy to the FM configuration) properties of $CaFeO_3$.

7.2 Bulk $CaFeO_3$

In order to clarify the mechanism behind the $P2_1/n$ insulating ground state of $CaFeO_3$, we first focus on the phonon dispersion curves of its parent cubic phase (Fig. 7.1a). Calculations are reported in a ferromagnetic configuration, which is representative to unravel the essential physics. On the one hand, Fig. 7.1a) shows expected unstable phonon modes at M point (M_2^+, $\omega_M = 181i\text{cm}^{-1}$) and R point ($R_5^-$, $\omega_R = 197i\text{cm}^{-1}$) of the Brillouin zone, related respectively to the ϕ_z^+ and ϕ_{xy}^- distortions yielding the *Pbnm* phase. On the other hand, it attests that the R_2^- mode related to the $Q_1^{\mathbf{R}}$ distortion is significantly stable ($\omega_B^2 = 343\text{cm}^{-1}$), so questioning the origin of its appearance in the $P2_1/n$ phase. The answer is provided in Fig. 7.1 d), reporting the evolution of the energy with the amplitude of $Q_1^{\mathbf{R}}$ at fixed amplitudes of ϕ_z^+ and ϕ_{xy}^-. It demonstrates that, although initially stable (single well – SW – with a positive curvature at the origin $\alpha_B \propto \omega_B^2 > 0$) in the cubic phase, $Q_1^{\mathbf{R}}$ will be progressively destabilized (double well – DW – with a renormalized negative curvature at the origin $\tilde{\alpha}_B < 0$) as ϕ_z^+ and ϕ_{xy}^- develop in the *Pbnm* phase. The curvature $\tilde{\alpha}_B$ changes linearly with $(\phi_z^+)^2$ and $(\phi_{xy}^-)^2$ ($\tilde{\alpha}_B = \alpha_B + \lambda_{BM}(\phi_z^+)^2 + \lambda_{BR}(\phi_{xy}^-)^2$) so that its evolution must be assigned to a *cooperative* biquadratic coupling ($\lambda_{BM}, \lambda_{BR} < 0$) of $Q_1^{\mathbf{R}}$ with ϕ_z^+ and ϕ_{xy}^- as highlighted by the following terms in the Landau-type energy expansion around the cubic phase:

$$E \propto \alpha_B (Q_1^{\mathbf{R}})^2 + \lambda_{BM}(\phi_z^+)^2 (Q_1^{\mathbf{R}})^2 + \lambda_{BR}(\phi_{xy}^-)^2 (Q_1^{\mathbf{R}})^2 \qquad (7.1)$$

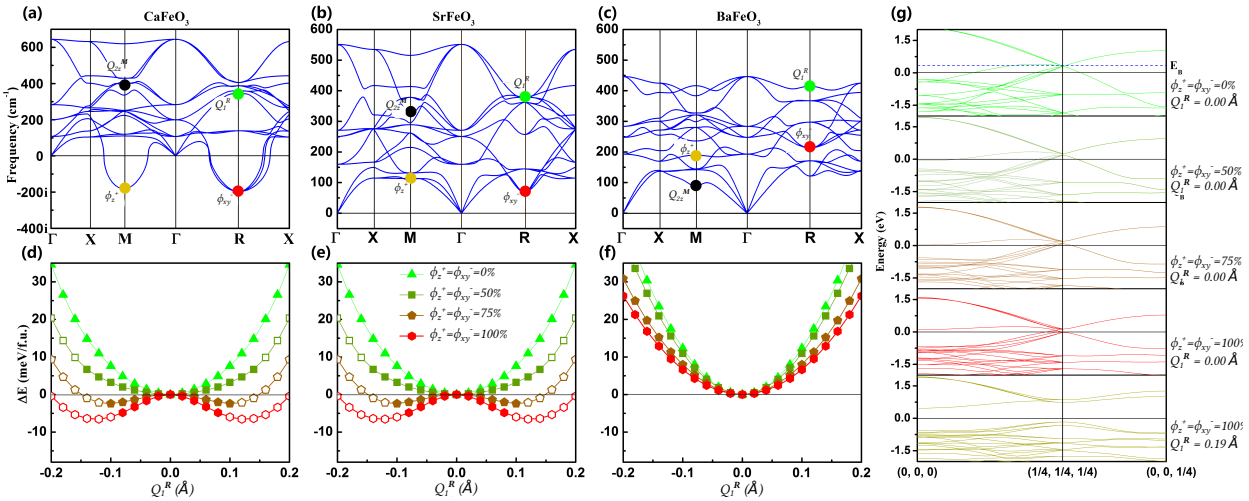

Figure 7.1: (a-c) Phonon dispersion curves of cubic $CaFeO_3$ (a), $SrFeO_3$ (b), and BaFeO3 (c) on which most relevant modes are pointed. (d-f) Evolution of the energy with respect to the breathing distortion amplitude ($Q_1^{\mathbf{R}}$) at fixed rotation (ϕ_z^+) and (ϕ_{xy}^-) amplitudes in $CaFeO_3$ (d), $SrFeO_3$ (e), and $BaFeO_3$ (f). Opened (resp. filled) symbols denote insulating (resp. metallic) states. (g) Electronic band structure of $CaFeO_3$ along selected lines of the $Pbnm$ or $P2_1/n$ Brillouin zone (**k** in reduced pseudocubic coordinates) for different amplitude of disortions. All results were calculated with FM spin order and using a fixed cubic cell with the same volume as the ground state. Distortion amplitudes are normalized to those calculated by *ISODISTORT* [128] in the $CaFeO_3$ AFM ground state.

For large enough amplitudes of ϕ_z^+ and ϕ_{xy}^-, $Q_1^{\mathbf{R}}$ becomes unstable and will spontaneously appear in the structure. In Fig. 7.1b) we further notice that the amplitude of $Q_1^{\mathbf{R}}$ required for making the system insulating decreases for increasing ϕ_z^+ and ϕ_{xy}^-, yielding therefore an insulating $P2_1/n$ ground state.

This behavior is point by point similar to that reported recently in rare-earth nickelates by Mercy *et al.* [77] who subsequently assigned the MIT to a structurally triggered phase transition, in the sense originally defined by Holakovský [182]. In Ref. [77], the unusual cooperative coupling of $Q_1^{\mathbf{R}}$ with ϕ_z^+ and ϕ_{xy}^- at the origin of this triggered mechanism was moreover traced back in the electronic properties of nickelates and further related to a type of structurally triggered Peierls instability.

Fig 7.1g) shows that this explanation still hands for ferrites. In the cubic phase of $CaFeO_3$ (Fe^{4+} with formal occupation $d^4 = t_{2g}^3 e_g^1$), the Fermi energy, E_F, crosses anti-bonding Fe $3d$ – O $2p$ states with a dominant e_g character. Activation of $Q_1^{\mathbf{R}}$ can open a gap in these partly occupied e_g bands at $q_B = (1/4, 1/4, 1/4)$, but around an energy E_B initially above E_F. The role of ϕ_{xy}^- and ϕ_z^+ is to tune Fe $3d$ – O $2p$ hybridizations in such a way that E_B is progressively lowered towards E_F. As they develop into the structure, activating $Q_1^{\mathbf{R}}$ affects more and more substantially energy states around E_F and yields an increasing gain of electronic energy explaining the progressive softening of ω_B. The e_g bandwidth in $CaFeO_3$ being smaller than in the nickelates, E_B is initially closer to E_F consistently with a softer ω_B and the smaller amplitude of ϕ_{xy}^- and ϕ_z^+ required to destabilize $Q_1^{\mathbf{R}}$.

7.3 Bulk $SrFeO_3$ and $BaFeO_3$

The triggered mechanism highlighted above further straightforwardly explains the absence of MIT in other alkaline-earth ferrites. Because

of their larger tolerance factors and as confirmed from the absence of unstable mode in their phonon dispersion curves (Fig. 7.1b) and c)) $SrFeO_3$ and $BaFeO_3$ preserve their cubic structure down to zero Kelvin [7, 173] and so do not spontaneously develop the oxygen rotations mandatory to trigger the MIT. The cooperative coupling of $Q_1^{\mathbf{R}}$ with ϕ_z^+ and ϕ_{xy}^- remains however a generic features of all ferrite compounds.

As illustrated in Fig. 7.1e) and 7.1f), $Q_1^{\mathbf{R}}$ is progressively destabilized when increasing artificially the amplitudes of ϕ_z^+ and ϕ_{xy}^- distortions in $SrFeO_3$ and $BaFeO_3$. Since, in the cubic phase of these compounds, ω_B is originally at frequencies slightly larger than in $CaFeO_3$ ($\omega_B = 362\text{cm}^{-1}$ in $SrFeO_3$ and $\omega_B = 415\text{cm}^{-1}$ in $BaFeO_3$), larger distortions are required to induce the MIT. In $SrFeO_3$, amplitudes of ϕ_z^+ and ϕ_{xy}^- corresponding to 75% of their ground-state values in $CaFeO_3$ are nevertheless enough to force an insulating ground state. In $BaFeO_3$, the cooperative coupling is less efficient and much larger amplitudes would be required.

This highlights the possibility of inducing a MIT in $SrFeO_3$ thin films or heterostructures under appropriate engineering of ϕ_{xy}^- and ϕ_z^+. Moreover, it provides a vivid explanation to the decrease of T_{MIT} experimentally observed in $Ca_{1-x}Sr_xFeO_3$ solid solutions as x increases [183]. For increasing Sr concentrations, the average tolerance factor increases and the mean amplitudes of ϕ_z^+ and ϕ_{xy}^- decrease. This analysis is supported by DFT calculation at 50/50 Ca/Sr composition using an ordered supercell (see appendix B.3).

Charge versus orbital ordering – It remains intriguing why $CaFeO_3$ ($t_{2g}^3 e_g^1$) prefers to exhibit a breathing distortion ($Q_1^{\mathbf{R}}$) and CO as $RNiO_3$ compounds ($t_{2g}^6 e_g^1$) rather than a Jahn-Teller distortion ($Q_{2z}^{\mathbf{M}}$) and OO as $RMnO_3$ compounds ($t_{2g}^3 e_g^1$). In Ref. [153] Whangbo *et al.* argue that $Q_1^{\mathbf{R}}$ is favored in $CaFeO_3$ by the relatively strong covalent character of the Fe-O bond while the $Q_{2z}^{\mathbf{M}}$ distortion is preferred in $LaMnO_3$ by the weak covalent character of the Mn-O bond. So, we anticipate that weakening the covalence by increasing the Fe-O distance might favor $Q_{2z}^{\mathbf{M}}$ and OO in $CaFeO_3$. To realize practically this idea, we investigated the role of tensile epitaxial strain on the ground state of $CaFeO_3$ thin films.

7.4 $CaFeO_3$ Thin Films

The phase diagram of $CaFeO_3$ films epitaxially grown on a cubic perovskite (001)-substrate is reported Fig. 7.2a). The evolution of the energy with the lattice constant of the substrate is shown for FM and A-type AFM orders with either charge or orbital ordering. Although S- and T-type spiral magnetic orders (not shown here) possess a slightly lower energy at the bulk level, the FM order becomes quickly the GS under small tensile strain; C-type and G-type AFM order are much higher in energy and not shown. Both possible orientations of the orthorhombic ($a^-a^-c^+$) oxygen rotation pattern, with the long c-axis either in-plane or out-of-plane were also considered: while c-axis in-plane is favored at zero strain, c-axis out-of-plane becomes more stable under tensile strains.

Fig. 7.2a) demonstrates the possibility of switching from a CO to an OO ground state in $CaFeO_3$ using strain engineering: under increasing tensile strain, the ground state of the film changes from an insulating

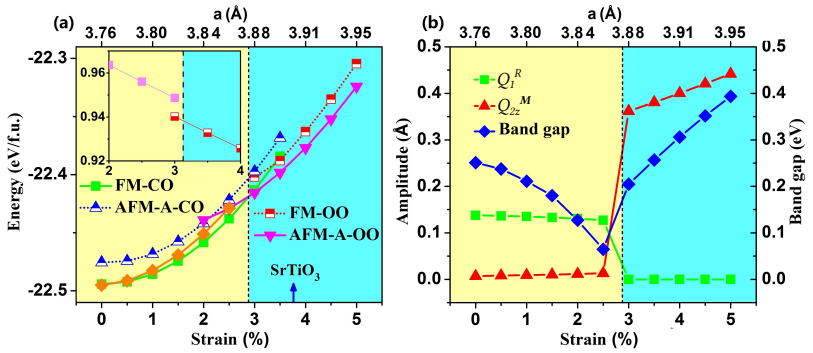

Figure 7.2: (a) Total energy as a function of tensile strain (or in-plane lattice constant) for $CaFeO_3$ epitaxial films with c-axis out-of-plane, in CO and OO states with either FM or A-type AFM spin ordering; FM CO state with the long c-axis in-plane is plot in orange for comparison. A change of ground state from FM-CO phase (yellow area) to A-type AFM-OO phase (blue area) is observed. Inset: c/a ratio of the ground state structure as a function of strain. (b) Evolution of $Q_1^{\mathbf{R}}$ (green), $Q_{2z}^{\mathbf{M}}$ (red) and band gap (blue) as a function of strain (or in-plane lattice constant).

Amplitudes (Å)	$Q_{2z}^{\mathbf{M}}$	$Q_1^{\mathbf{R}}$	ϕ_z^+	ϕ_{xy}^-	A_X
a = 3.76Å-CO	0.007	0.137	0.788	1.111	0.440
a = 3.76Å-OO	0.256	0.000	0.717	1.194	0.457
a = 3.91Å-OO	0.400	0.000	0.676	1.309	0.552
Energies (meV/fu)	$\Delta E_{JT}^{(1)}$	$\Delta E_{JT}^{(2)}$	$\Delta E_{JT}^{(3)}$	ΔE_{JT}	ΔE_{AFM-A}
a = 3.76Å-OO	4.4	-43.6	-15.8	-55.0	74.5
a = 3.91Å-OO	-104.3	-80.9	-31.0	-216.2	49.3

Table 7.1: Top: Amplitudes of dominant distortions [128] in the relaxed CO (FM) and OO (AFM-A) phases of $CaFeO_3$ epitaxial films under 0% (a = 3.76Å) and 4% (a = 3.91Å) tensile strain. Bottom : Energy contributions associated to the different terms in Eq.(7.2), obtained from the amplitudes of distortion reported above.

FM-CO $P2_1/n$ configuration at small strain to an insulating A-type AFM-OO *Pbnm* configuration above 3% tensile strain (a=3.88Å). Fig. 7.2b) highlights the strain evolution of $Q_1^{\mathbf{R}}$ and $Q_{2z}^{\mathbf{M}}$ distortions together with the change of band gap. Under increasing tensile strain, $Q_1^{\mathbf{R}}$ – and, with it, the difference of magnetic moments of neighboring Fe sites – slightly decreases and is abruptly suppressed at the phase transition; at the same time, the band gap – already reduced in this FM phase – decreases and closes precisely at the phase boundary. The origin of the closing of the band gap is the tetragonal strain induced by the epitaxial strain condition (see section B.2 in the appendix) Conversely, $Q_{2z}^{\mathbf{M}}$ is nearly zero below 3% tensile strain while it suddenly appears at the transition and then continuously increases. In this phase all Fe sites carry the same charge and net magnetic moment of 3.57 μ_B, which is insensitive to epitaxial strain. Amazingly, the amplitude of $Q_{2z}^{\mathbf{M}}$ (0.37 Å) in a $CaFeO_3$ film grown on a $SrTiO_3$ substrate (a = 3.905 Å) is comparable to that of bulk $LaMnO_3$ (0.36 Å). Such similar amplitude suggests that the T_{MIT} associated to the OO state in strained $CaFeO_3$ films might be much larger than the T_{MIT} associated to the CO state in bulk and comparable to the one of $LaMnO_3$ (T_{MIT} = 750K).

Our findings provide a convincing explanation for the insulating character of $CaFeO_3$ films on $SrTiO_3$ at room temperature and for the absence of CO MIT in the 100-300K temperature range as recently pointed out in Ref.[180]. They suggest to probe the presence of OO MIT at higher temperature. A key feature, highlighted in the insert in Fig. 7.2a), is the jump of c/a ratio at the transition boundary, which provides another concrete hint for experimentalists to probe the CO-OO transition.

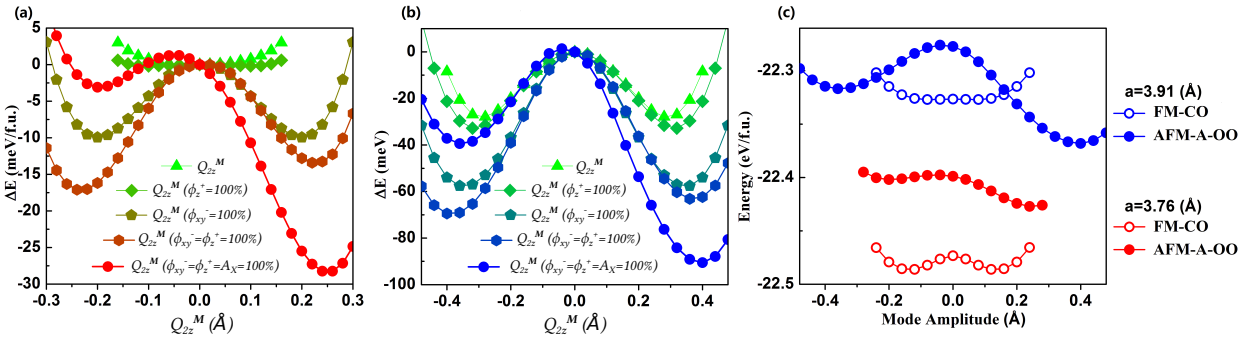

Figure 7.3: Evolution of the energy with Jahn-Teller distortion amplitude $Q_{2z}^{\mathbf{M}}$ in AFM-A magnetic order and at fixed amplitudes of other distortion (see legend) for $CaFeO_3$ epitaxial films under strain of (a) 0% (a = 3.76 Å) and (b) 4% (a = 3.91 Å). (c) Evolution of the total energy as a function of $Q_1^{\mathbf{R}}$ in FM-CO state (open symbol) and $Q_{2z}^{\mathbf{M}}$ in A-type AFM-OO state (filled symbol) for $CaFeO_3$ thin film under 0% (a = 3.76Å, red) and 4% (a = 3.91Å, blue) strains. ϕ_z^+, ϕ_{xy}^- and Q_X are fixed to their amplitudes in the relevant phase (except for the FM-CO state at 4% which cannot be stabilized and for which we kept positions in the A-type AFM-OO phase).

7.5 Tuning the Competition between Charge- and Orbital-Order

To rationalize the emergence of an OO ground state in $CaFeO_3$ films, we quantify the lowest-order couplings of $Q_{2z}^{\mathbf{M}}$ with other distortions in a Landau-type free energy expansion and investigate their sensitivity to magnetic order and epitaxial strain :

$$E \propto \alpha_{JT}(Q_{2z}^{\mathbf{M}})^2 + \lambda_{MJ}(\phi_z^+)^2(Q_{2z}^{\mathbf{M}})^2 + \lambda_{RJ}(\phi_{xy}^-)^2(Q_{2z}^{\mathbf{M}})^2 + \gamma\phi_z^+ A_X Q_{2z}^{\mathbf{M}} \tag{7.2}$$

The first term quantifies the *proper* harmonic energy contribution $\Delta E_{JT}^{(1)}$ associated to the appearance of $Q_{2z}^{\mathbf{M}}$. The second and third terms in Eq. (7.2) account for a change of energy $\Delta E_{JT}^{(2)}$ in presence of ϕ_z^+ and ϕ_{xy}^-, linked to their lowest bi-quadratic coupling with $Q_{2z}^{\mathbf{M}}$. Finally, sizable antipolar motions of the Ca cations and apical oxygens (A_X mode, see Table 7.1), which are driven by ϕ_z^+ and ϕ_{xy}^- [132], couple in a trilinear term with ϕ_{xy}^- and $Q_{2z}^{\mathbf{M}}$ (last term in Eq.(7.2)). This coupling produces an energy lowering $\Delta E_{JT}^{(3)} < 0$, through a so-called *hybrid improper* mechanism yielding an asymmetry in the $Q_{2z}^{\mathbf{M}}$ energy well [1]. Compendiously, appearance of a $Q_{2z}^{\mathbf{M}}$ distortion requires $\Delta E_{JT} = \Delta E_{JT}^{(1)} + \Delta E_{JT}^{(2)} + \Delta E_{JT}^{(3)} < 0$.

1: The coexistence of ϕ_z^+ and ϕ_{xy}^- already produces an asymmetry in the energy well through the term $E \propto \delta(\phi_{xy}^-)^2\phi_z^+ Q_{2z}^{\mathbf{M}}$. However, this asymmetry is in the negligible range of 1 meV (see Fig. 7.3a-b).

In bulk $CaFeO_3$, α_{JT} is large ($\omega_{JT}(FM)$ = 390 cm^{-1}) in the FM cubic phase, which prohibits ΔE_{JT} to become negative for sizable amplitudes of $Q_{2z}^{\mathbf{M}}$. Switching to the A-type AFM spin order tremendously lowers α_{JT} ($\omega_{JT}(AFM-A)$ = 144 cm^{-1}) but simultaneously increases the total energy by ΔE_{AFM-A}. The stabilization of an OO phase with $Q_{2z}^{\mathbf{M}}$ against the CO phase with $Q_1^{\mathbf{R}}$ so depends eventually on the counterbalance between ΔE_{AFM-A} and ΔE_{JT}.

This is quantified for epitaxial thin films in Fig. 7.3 and Table 7.1. Under negligible tensile strain (a= 3.76 Å, Fig. 7.3a), with A-type AFM order, ω_{JT} is even softer than in bulk $CaFeO_3$, yielding $\Delta E_{JT}^{(1)} \approx 0$. Then, similarly to what was discussed for $Q_1^{\mathbf{R}}$ in bulk compounds, ϕ_{xy}^- and ϕ_z^+ trigger $Q_{2z}^{\mathbf{M}}$ ($\lambda_{MJ}, \lambda_{RJ} < 0$), yielding $\Delta E_{JT}^{(2)} < 0$. Finally, the hybrid improper coupling

with A_X and ϕ^-_{xy} provides a further $\Delta E^{(3)}_{JT} < 0$. However, although globally negative, ΔE_{JT} cannot overcome ΔE_{AFM-A}(Fig. 7.3c). Under large tensile strain (a= 3.91 Å, Fig. 7.3b) α_{JT} is significantly reduced by coupling with the epitaxial tetragonal strain $Q^{\mathbf{\Gamma}}_{3z}$ ($\alpha_{JT} \propto \gamma_{JT} Q^{\mathbf{\Gamma}}_{3z} + \lambda_{JT}(Q^{\mathbf{\Gamma}}_{3z})^2$ [75]), yielding a huge negative $\Delta E^{(1)}_{JT}$. Then, although λ_{MJ} and λ_{RJ} are reduced and γ remains unaffected (see section B.4), $\Delta E^{(2)}_{JT}$ and $\Delta E^{(3)}_{JT}$ are increased roughly by a factor of 2, mainly due to the increase of $Q^{\mathbf{M}}_{2z}$. Globally, $|\Delta E_{JT}|$ in A-type AFM order is now much larger than ΔE_{AFM-A}, which moreover has been slightly reduced, and the OO phase with $Q^{\mathbf{M}}_{2z}$ is stabilized against the CO phase with $Q^{\mathbf{R}}_1$ (Fig. 3c). We notice that ϕ^+_z and ϕ^-_{xy} are not strongly affected by strain so that the stabilization of the OO phase must be primarily assigned to the strain renormalization of α_{JT}. $E^{(2)}_{JT}$ and $\Delta E^{(3)}_{JT}$ play however an important complementary role and tuning ϕ^+_z and ϕ^-_{xy} would offer an alternative strategy to stabilize the OO phase.

7.6 Conclusions

We have rationalized the appearance of a CO-type MIT in alkaline-earth ferrites, showing that, in $CaFeO_3$, such a MIT arises from the triggering of $Q^{\mathbf{R}}_1$ by ϕ^+_z and ϕ^-_{xy} and that this mechanism can induce a CO insulating ground state in $SrFeO_3$ under appropriate tuning of ϕ^+_z and ϕ^-_{xy}. Going further, we found that OO is also incipient to $CaFeO_3$ and that an OO-type MIT can be engineered in thin films under moderate tensile strain, which is consistent with a recent theoretical study on $BaFeO_3$ [**Cherair_2018**]. We have shown that the appearance of the OO-type insulating ground state arises from a delicate balance between different energy terms, suggesting different strategies to stabilize it. Interestingly, the emergence of the OO phase in ferrites is the result of a purely structural instability and we did not find any gradient discontinuity in the energy (corner point), fingerprint of the electronic instability usually associated to OO phases [185]. Such a structural stabilization of the OO phase might offer a reasonable explanation to the emergence of an OO phase in other materials like $RNiO_3$ compounds [156].

Second-Principles Study of $CaTiO_3$

8

In this chapter we present the application of the second-principles (SP) approach to construct a lattice model (introduced in section 3.2) for the perovskite $CaTiO_3$.

$CaTiO_3$ is the mineral called perovskite that gave its name to the ABO_3 family of related compounds. As the majority of perovskites, $CaTiO_3$ has a Goldschmidt [2] tolerance factor $t < 1$ and thus exhibits the non-polar $Pnma$ crystal symmetry [4] at low temperatures (room temperature until at least 1350K [186]) with an $a^-a^-a^+$ rotation pattern (in Glazer's notations [3]) and sizable antipolar motions of the Ca atoms (A_X irreducicble representation (irrep): X_5^-). At very low temperatures $CaTiO_3$ shows the characteristics of an incipient ferroelectric with the onset of the divergence of the dielectric constant indicating the approach of a ferroelectric transition that is however suppressed by quantum fluctuations [187, 188]. Additionally, polar distrotions at domain walls of the rotation pattern (also called twinning or ferroelastic domain walls) have been predicted [189, 190] and confirmed experimentally [191].

Moreover, $CaTiO_3$ is used as a structural analog to (Mg,Fe)SiO_3 which constitutes about 85% of the lower earth mantle [192]. For this reason elucidating the high-temperature phase sequence is of particular interest and has been extensively studied [186, 193–199]. The latest consent about the phase transition sequence in $CaTiO_3$ is that it occupies the $Pnma$ space group from low-temperatures until 1512±13K, where it undergoes an orthorhombic to tetragonal phase transition from the $Pnma$ to the $I4/mcm$ space group (rot. pattern $a^0a^0c^-$), to finally go to the ideal perovskite cubic space group $Pm\bar{3}m$ at 1635±12K [186, 199]. There is, however, some debate over a possible intermediate orthorhombic phase between the $Pnma$ and the tetragonal $I4/mcm$ phase. *Kennedy et al.* [198] and *Guyot et al.* [195] propose from XRD and drop-calorimetry measurements an intermediate phase with $Cmcm$ symmetry (rot. pattern $a^0b^-c^+$) in a small temperature range ($\approx 100K$). This has been reproduced by a phenomenological Landau type potential fitted on ab initio data [200]. *Carpenter* proposed instead an intermediate $Imma$ phase (rot. pattern $a^-a^-c^0$) from a theoretial analysis of a Landau type potential [201].

The reference structure around which we develop the SP lattice model is the ideal perovskite cubic $Pm\bar{3}m$ phase. The harmonic part of the model is extracted from DFPT calculations at this cubic structure. The phonon dispersion is shown in Fig. 8.1. Phonons with imaginary frequencies appear at the M-, R-, and Γ-point of the cubic Brillouin zone (BZ). The modes at M and R correspond to the octahedral in-phase (ϕ^+) and anti-phase (ϕ^-) rotations. The instability at the Γ point corresponds to polar distortion that moves the Ti cation out of the center of the oxygen octahedron known from the prototypical ferroelectric perovskite $BaTiO_3$.

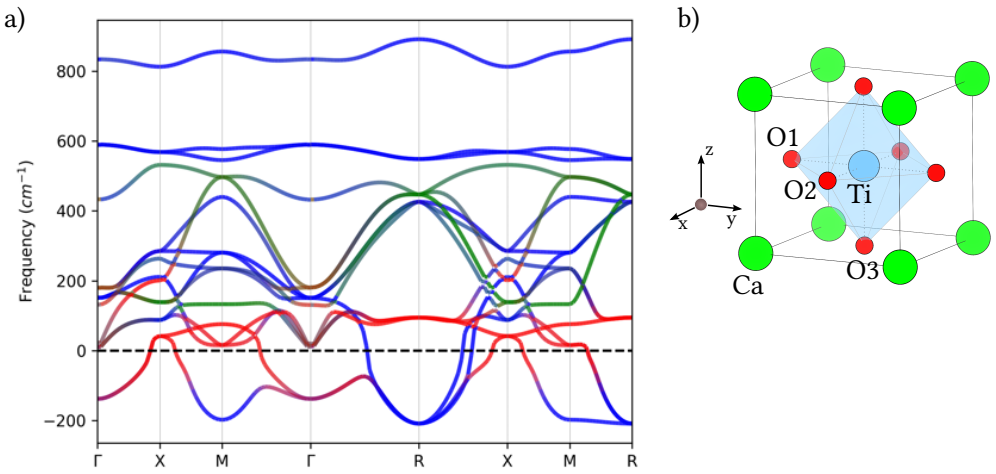

Figure 8.1: a) Phonon dispersion of $CaTiO_3$ in the relaxed ideal perovskite cubic $Pm\bar{3}m$ phase. Imaginary phonon frequencies showing instable phonon modes are drawn on the negative frequency axis. The color code shows the atomic contribution of the phonon mode vector for a given band at a given q-vector. Blue refers to Oxygen, red to Titanium and green to Calcium motions. b) Ideal cubich perovskite reference structure of $CaTiO_3$ with atom labels indicated.

$CaTiO_3$ has attracted considerable research interest due to this hidden ferroelectric instability that is absent in its ground state structure. The common understanding of this absence is that the rotational instabilities and the ferroelectric instability are competing and mutually exclusive [202]. A strategy to introduce ferroelectricity in $CaTiO_3$ is strain engeneering. Thereby, thin films of $CaTiO_3$ are grown on substrates with some degree of lattice mismatch to introduce an external strain. This route has been explored extensively by first-principles calculations imposing strain constraints [200, 203, 204]. These calculations predicted that $CaTiO_3$ grown on [100] surfaces with either tensile strain of about 1.5% or compressive strain of about 3% will reintroduce a ferroelectric instability. These predictions have been confirmed experimentally first on the tensile [205] and recently on the compressive side [206]. However, on the tensile side the ferroelectric-to-paraelectric transition temperature T_C was far below room temperature [205]. On the compressive side T_C can be as high as 800K [206]. From ab initio calculations the polarization amplitude was estimated to be lower than 9 µC cm^{-2} [206].

In this chapter we show the development of the SP lattice model. Frist, we introduce the training set (TS) that we created for selecting and fitting few anharmonic parameters. Then, we show the quality of the slected fit with respect to this TS and impose the boundedness of the model. Next, we validate the model by comparing ab initio total energies of the most important competing phases and comparing the phonon dispersion of the ground-state $Pnma$ structure calculated by DFPT and the SP lattice model. Finally, we make a virtual heating experiment and compare the phase transition sequence of the SP lattice model to the experimentally proposed one. We find that the model reproduces qualitatively well the energy sequence of the relaxed phases and the phonon dispersion of the $Pnma$ structure at 0K. The phase transition sequence at high-temperature is in line with *Carpenter's* propositions, but not with experiment. To this end we conclude that for a refined description at high-temperatures higher order strain-phonon coupling terms would need to be incorparated in the lattice model.

8.1 Calculation Parameters and Methods Deployed

To create the TS, ab initio density functional theory (DFT) calculations were deployed as implemented in the Abinit software package [47, 207–209] using the generalized gradient approximation (GGA) with the Wu-Cohen (WC) parametrization for the exchange-correlation potential [210], which has been recently shown to provide excellent results for $CaTiO_3$ [211]. We used optimized norm-conserving pseudo-potentials [14] created with the WC exchange-correlation functional treating the following orbitals as valence states: for Ca, $3s$,$3p$,$4s$,$3d$, for Ti,$4s$,$4p$,$4d$, and $5s$, and for O, $2s$ and $2p$. Γ centered Monkhorst-Pack k-point meshes [127] with a density of $8 \times 8 \times 8$ with respect to the five atoms cubic perovskite unit cell have been used. Most calculations have been performed in a $2 \times 2 \times 2$ 40-atoms supercell to accommodate various lattice distortions without imposing symmetry restrictions. In this supercell the k-point mesh was reduced to $4 \times 4 \times 4$. The expansion of the electronic wave function by a plane wave basis has been cutoff at 40 Ha. Density Functional Perturbation Theory (DFPT) calculations as implemented in the Abinit package have been used to calculate dynamical charges and lattice dynamical properties at the relaxed cubic $Pm\bar{3}m$ structure of $CaTiO_3$. Dynamical matrices have been calculated on a $2 \times 2 \times 2$ q-point mesh i.e. at the BZ center and boundary, which reveals to be sufficient. The Multibinit software package was used to create the SP lattice model. At the harmonic level interatomic force constants and dipole-dipole interactions were extracted from the dynamical matrices, dynamical charges and dielectric tensor calculated with DFPT. At the anharmonic level, a cutoff radius of one cubic lattice cell parameter was used to create the set of anharmonic symmetry adapted terms (SATs) at third and fourth order incorporting strain-phonon coupling terms, which are linear in the strain coordinate. From this set of anharmonic terms, a few have been automatically selected to qualitatevily reproduce the TS data. The goal function (GF) has been minimized with respect to the forces and stresses provided in the TS. Finite temperature simulations using the lattice SP model have been performed using a Hybrid molecular dynamics Monte-Carlo approach (HMC) [49] using an isothermal/isoenthalpic molecular dynamics algorithm [50] (readily implemented in Abinit) to generate new steps in the Markov Chain. 40 MD steps with a time propagation of 0.48 fs per step were executed between each Metropolis-Hastings Monte-Carlo evaluation. 1000 Metropolis-Hastings Monte-Carlo evaluations were performed at each temperature. The average structure at a given temperature is defined as the average drawn from the last 550 MC steps. To relax phases of interest from ab initio and from the SP lattice model we used the Broyden-Fletcher-Goldfarb-Shanno method as implented in Abinit (which has been linked to Multibinit). To calculate phonon dispersion and phonon density of states using the SP lattice model we used *Phonopy* [212] to create an irreducible set of finite displacements, whose total energy was then evaluated by Multibinit using the SP lattice model. Those energies are then used by *Phonopy* to calculate interatomic force constants and interpolate the phonon band structure.

8.2 Second-Principles Lattice Model for $CaTiO_3$

In this section we present the construction and validation of the SP lattice model for $CaTiO_3$.The generation of a SP lattice model is an iterative procedure that can be devised into three main steps. i) Creation of the TS - ab initio data containing total energies, forces, and stresses evaluated at various lattice configurations -, ii) fitting and bounding a SP lattice model by using the automated tools in Multibinit (introduced in section 3.2), and iii) physically validating the model. Step iii) conists first of relaxing nucleic positions using SP lattice model as well as dynamics at low temperature to find the ground state of the SP model and check its stability. If this first physical test suceeds more advanced tests can follow as calculating the energy of competing phases by imposing lattice symmetries of those phases upon relaxation of the nucleic positions as well as calculating phonon dispersions of the ground state or other phases of interest and compare them to ab initio references. Eventually HMC heating curves were calculated and compared with experimental observations. If step iii) doesn't deliver sufficient physical properties an iteration could restart with steps i) or ii). A restart at step ii) aims to improve the fit by changing the parameters defining the generation of SATs to generate a larger set of SATs from which the automatized fit procedure selects. This can mean increasing the cutoff for SATs, incorporation of additional strain-phonon or anharmonic strain terms, or changing the maximum order of strain multiplicand in strain phonon terms (see section 3.2.3). This can also be done in an extending spirit by keeping the SATs that hat been chosen in an previous observation. Iterating over steps ii) and iii) without achieving satisfying results means that the TS is not complete enough (at least for the trageted physical properties) and going back to step i) becomes necessary. Here, the goal is to add additional configurations to the TS that are qualitatively different.

The outlined iterative procedure has been carried out *"by hand"* with interjectional development steps in which additional capabilities have been added to the Multibinit package. At each iteration the previous experiences were incorporated into the TS generation, development of fitting procedures, and fitting parameters. In the following sections we present the eventual *"working"* TS and SP model that leaves room for improvement. Additionally, we point out findings that we deem essential for a succesful model generation. In the future, generation of semi-automated processes for the iterative fitting and TS creation building on those experiences are desirable to facilitate model creation, which proves chalenging for materials like $CaTiO_3$ and other perovskites.

8.2.1 Training Set

Figure 8.2 shows the total energy of the TS that we used for fitting the SP lattice model for $CaTiO_3$. As indicated in the figure two strategies have been used to create the TS. First, as propsed by *Escorihuela-Sayalero et al.* [45] we used ab initio MD calculations (isothermal/isoenthalpic ensemble [50]) starting from the cubic reference phase with different goal temperatures. The aim thereby is to explore lattice configuration as they would appear at the goal temperature and explore the potential energy landscape in an *unbiased* way. While it is true that this approach

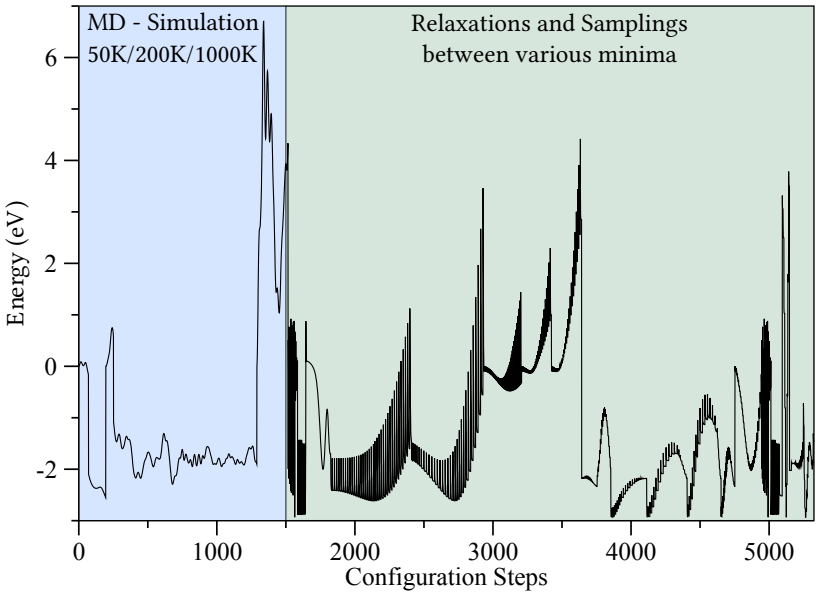

Figure 8.2: Total energy of the training set used to the train the polynomial expansion for the lattice SP model of $CaTiO_3$. The TS contains 5324 different lattice configurations.

is free of *"human biasing"* and indepently explores the energy landscape it has several drawbacks. At low goal temperatures it will generally find a very steep and short path between the starting structure ($Pm\bar{3}m$ in our case) and a minimum in which it gets stuck (might or might not be the ground state phase). The PES around this minimum is then not much explored due to the low thermal energy. This behavior is especially critical for the boundedness of the SP model as exploring the energy barriers around the minimum will favor a bounded fit. Moreover, phases representing other local minima in betweeen the starting structure and the minimum in which the MD run gets stuck are not explored. If the goal temeperature is increased, more of the stable phonons are populated and the coupling between those and the instable phonons is explored. The average amplitude of the instable phonon modes will decrease. Thus, large amplitudes of the instable phonon modes that will favor a bounded model fit are also not explored with increased temperature.

Nonetheless, using only the ab initio MD data from Fig. 8.2 we were able to fit a lattice model that had the expected $Pnma$ structure as its ground state. However, especially the polar instability (instable phonon modes at Γ in Fig. 8.1) was not explored by the ab initio MD run. Unsurprisingly, we realized that the description of the instable polar mode PES by this first model was very poor.

This insight led to the addition of the second part of the TS, where we explored manually all instable phonon modes individually as well as many combinations. To do so, we condensed instable phonon modes (individually or combinations of several) with different amplitudes form zero to well beyond the minimum amplitude. At each amplitude, we performed a relaxation of the unit cell shape with fixed atomic internal coordinates to explore the strain-phonon coupling. Moreover, we added some linear interpolation paths between competing minima e.g. $R\bar{3}c$ ($a^-a^-a^-$ rotation pattern) to $Pnma$ ($a^-a^-c^+$ rotation pattern). Along these paths, essentially the oxygen octahedral rotation pattern is changed from one minimum to another. In perovskites, it is often the rotation pattern that drives cation displacements [132–134, 202]. Thus, we only fixed the internal coordinates of the oxygen atoms and let relax the

cell shape and postitions of the Ca and Ti atoms along this paths to additonally explore the strength of the coupling of cation displacements with octahedral rotations. Eventually, this second part of the TS made up the majority of the configurations included. The final TS contains 5324 lattice configurations.

8.2.2 Automatized Fitting and Selection of Symmetry Adapted Terms

In this section we present the anharmonic SATs that we defined for the anharmonic part of the SP lattice model with the help of the automatized fitting procedure. The automatized fitting process is controled by two aspects. First, the parameters that govern the generation of the anharmonic SATs from which then the fitting and selection algorithm chooses and second, the number of SATs after which we stop the selection algorithm. We tried various combinations of the aforementioned. We eventually let the automatized procedure choose 60 anharmonic SATs. First 30 that take Ca as the central atom and second 30 that take Ti as the central atom. The SATs are listed in Table 8.2. Fig. 8.3 a) shows total energy of the TS (black) alongside the total energy of SP lattice model with 60 SATs (red). The SP model with 60 SATs reproduces nicely the shape of the TS energy surface. However, there is a considerable offset with respect to the energy. This offset stems from the fact that the selection and fitting of the SATs and their coefficients has been excecuted on optimizing the GF on the forces and stresses only, not taking into account the energy. We also tried taking into acount the total energy, which lead to a numerical better description of the total energy, but to a physical worse behavior of the SP lattice model.

Fig. 8.3 b) and c) show the convergence of the GF with respect to the total energy (G_E) and with respect to the forces and stresses (G_{FS}) as a function of the number of selected SATs. G_E reaches quickly its convergence value after about 20 selected SATs. The value of G_{FS} on which the coefficients of the anharmonic SATs are fitted, converges more slowly. After 30 selected terms the switch from Ca to Ti as the central atom is visible by a small gradient discontinuity in the G_{FS} curve. This dicontinuity stems from the change of the set of SATs from which the SAT selection algorithm choses. After about 50 terms the SP model could be said to be converged. The final convergence value of $G_{FS} = 3.45 \cdot 10^{-2} \left(\mathrm{eV^2 \AA^{-2}}\right)$ seems very good taking into account the large and demanding TS and comparing to the less demanding case of $SrTiO_3$ [45]. However, we note that we did not find a strict numerical way of asserting the quality of a model and one should be aware of the problem of *overfitting* [45]. E.g. we tried adding further terms to the 60-terms model using oxygen atom as the central atom in the SATs. While numerically the quality of the model improved, the physical quality worsend (especially the energy difference between some competing phases). The only stringent way to assess the quality of the model that we found so far is through *physical* testing, which we show in the next section.

The 60-terms model generated by the automatic term selection shows a $Pnma$ ground state in a $2 \times 2 \times 2$ simulation box. MD simulations using this model diverge at temperatures larger than 250K in the $2 \times 2 \times 2$

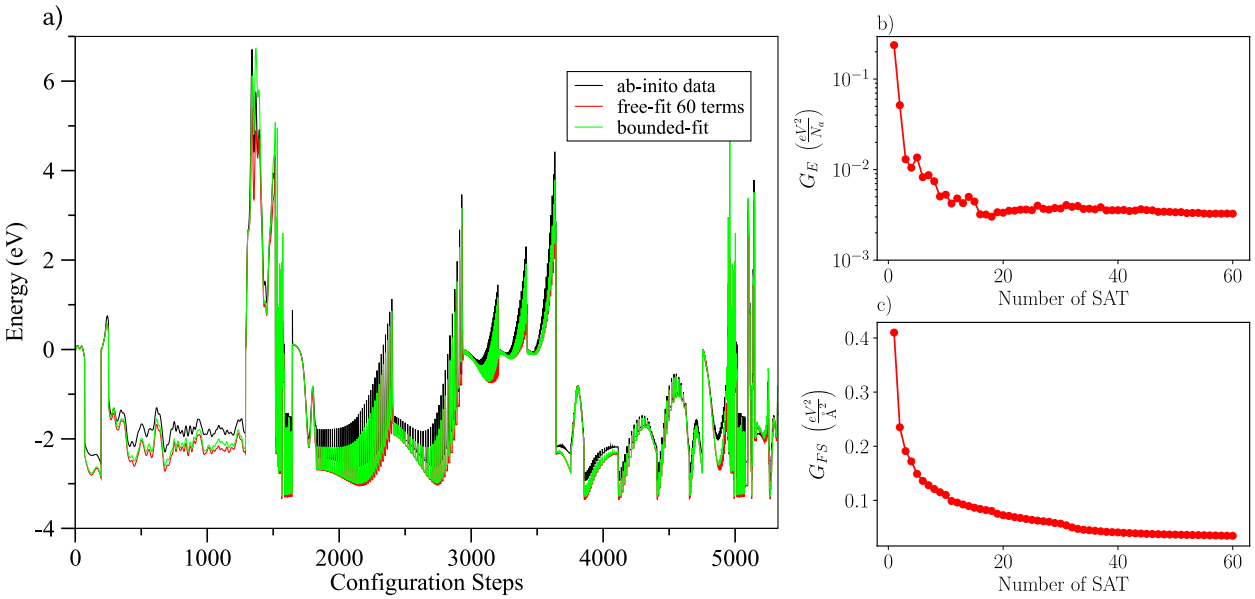

Figure 8.3: a) Ab-initio TS data (black same as in Fig. 8.2), first free fitted lattice model of 60 terms (red), and bounded model (green). b) Convergence of the energy goal function G_E (in eV^2/N_a, where N_a is the number of atoms in the TS supercell) with respect of the number of selected symmetry adapted terms (SAT). c) Convergence of Forces and Stresses goal function G_{FS} with respect to number of selected SAT. The first 30 SATs are selected with Ca as the central atom and the second 30 with Ti (see also Tab. 8.2).

Model	$G_E\left(\text{eV}^2N_{at}^{-1}\right)$	$G_F\left(\text{eV}^2\text{Å}^{-2}\right)$	$G_S\left(\text{eV}^2\text{Å}^{-2}\right)$
Free fit	$3.25 \cdot 10^{-3}$	$1.38 \cdot 10^{-2}$	$2.07 \cdot 10^{-2}$
Bounded	$3.14 \cdot 10^{-3}$	$1.95 \cdot 10^{-2}$	$2.52 \cdot 10^{-2}$

Table 8.1: Goal Function values for the energy (G_E), forces (G_F), and stresses (G_S) before and after bounding.

simulation box or at lower temperatures in larger simulation boxes. To enforce boundedness we used the bounding algorithm (see section 3.2.5) adding additional even SATs with positive coefficients at order 6 and 8. After applying this algorithm the total number of anharmonic SATs is 360. The large number of bounding terms is necessary, since most initally selected SATs are either odd or have a negative coefficient. The bounding algorithm is designed to keep the quality of the initial fit. Fig. 8.3 and Tab. 8.1 shows that this is ensured. In the next section, we explore the physical quality of this bounded model. Although this model does show a number of convincing physical properties, we should keep in mind that due to the nature of the polynomial expansion and the additive bounding algorithm the existence of spurious minima with very large distortions is not excluded.

Table 8.2: 60 first selected symmetry adapted terms (SATs) and their coefficient values. The fist 30 terms have Ca as the cetnral atom and the second 30 Ti. The unit of the coefficient is given in Hartree energy per Bohr radius $\left(\frac{\text{Ha}}{{a_0}^m}\right)$, where m is the order of the atomic displacement in the SAT. Indices in square brackets give the caretesian index of the cell the atom is located in (if it is not in cell [000]).

Index	Order	Name	Value
1	3	$(Ca_x - O1_x)^1(Ca_x - O1_x[-100])^1(\eta_1)^1$	1.848E-02
2	4	$(Ca_x - O1_x)^2(Ca_y - O2_y)^1(Ca_x - O1_x[-100])^1$	6.362E-04
3	4	$(Ca_x - O1_x)^2(Ca_x - O3_x[-1-10])^2$	4.198E-04
4	3	$(Ca_y - O1_y)^2(\eta_2)^1$	-6.528E-02
5	3	$(Ca_x - O1_x)^1(Ca_x - Ti_x[00-1])^1(\eta_1)^1$	2.020E-02
6	4	$(Ca_x - O1_x)^2(Ca_x - O3_x[-1-10])^1(Ca_x - Ti_x[-1-1-1])^1$	-7.043E-05
7	3	$(Ca_x - O1_x)^1(Ca_z - Ti_z[-1-10])^1(\eta_5)^1$	-1.005E-02
8	4	$(Ca_x - O1_x)^1(Ca_x - O2_x)^1(Ca_x - O2_x[0-10])^1(Ca_x - O2_x[0-1-1])^1$	8.816E-04
9	4	$(Ca_x - O1_x)^2(Ca_z - O1_z)^2$	2.228E-03
10	4	$(Ca_x - O1_x)^1(Ca_x - Ti_x)^1(Ca_x - O2_x[0-1-1])^2$	-8.955E-04
11	4	$(Ca_x - O1_x)^1(Ca_x - O2_x)^1(Ca_x - Ti_x[0-1-1])^1(Ca_x - Ti_x[-1-1-1])^1$	1.250E-03
12	3	$(Ca_x - O1_x)^1(Ca_y - O2_y)^1(\eta_1)^1$	-2.303E-02
13	4	$(Ca_x - O1_x)^1(Ca_y - O2_y)^1(Ca_x - O3_x)^1(Ca_x - O1_x[-10-1])^1$	-1.742E-04
14	3	$(Ca_x - O1_x)^1(Ca_z - O1_z)^1(Ca_z - Ti_z[00-1])^1$	1.480E-03
15	4	$(Ca_x - O1_x)^1(Ca_x - O2_x)^1(Ca_x - O2_x[00-1])^1(Ca_x - Ti_x[-1-10])^1$	-1.234E-03
16	4	$(Ca_x - O1_x)^1(Ca_y - O2_y)^1(Ca_y - O3_y)^1(Ca_z - O1_z[00-1])^1$	-3.965E-04
17	4	$(Ca_x - O1_x)^1(Ca_x - Ti_x)^1(Ca_y - Ti_y[-10-1])^1(\eta_1)^1$	-3.810E-02
18	4	$(Ca_x - O1_x)^1(Ca_x - O2_x)^2(Ca_y - O2_y)^1$	1.474E-03
19	4	$(Ca_x - O1_x)^1(Ca_x - Ti_x)^1(Ca_x - O2_x)^1(Ca_y - O2_y)^1$	3.601E-04
20	4	$(Ca_x - O1_x)^1(Ca_y - O2_y)^1(Ca_y - Ti_y)^2$	-1.650E-04
21	4	$(Ca_x - O1_x)^2(Ca_x - O2_x)^1(Ca_y - O2_y)^1$	-1.179E-03
22	3	$(Ca_x - O1_x)^1(Ca_z - O2_z)^1(Ca_y - O3_y)^1$	-1.445E-03
23	3	$(Ca_x - O1_x)^1(Ca_x - O1_x[00-1])^1(\eta_1)^1$	-7.627E-03
24	4	$(Ca_x - O1_x)^1(Ca_y - Ti_y[-100])^1(Ca_x - Ti_x[-1-1-1])^1(\eta_3)^1$	-3.976E-02
25	3	$(Ca_x - O1_x)^2(\eta_1)^1$	-1.444E-02
26	4	$(Ca_x - O1_x)^2(Ca_z - O1_z)^1(Ca_x - O1_x[-10-1])^1$	1.013E-03
27	3	$(Ca_x - O1_x)^1(Ca_y - O3_y)^1(Ca_z - Ti_z)^1$	7.621E-04
28	3	$(Ca_y - O1_y)^2(Ca_y - Ti_y)^1$	2.867E-02
29	3	$(Ca_y - O1_y)^1(Ca_y - Ti_y)^2$	-2.837E-02
30	3	$(Ca_x - Ti_x)^3$	8.851E-03
31	3	$(Ti_x - O1_x)^2(Ti_y - Ti_y[010])^1$	3.698E-03
32	4	$(Ti_x - O1_x)^1(Ti_x - O2_x)^2(Ti_x - O2_x[100])^1$	6.052E-03
33	3	$(Ti_y - O1_y)^2(\eta_2)^1$	-4.456E-01
34	4	$(Ti_x - O1_x)^1(Ti_y - O2_y)^1(Ti_x - O2_x[100])^1(Ti_y - O1_y[010])^1$	1.272E-02
35	3	$(Ti_x - O1_x)^1(Ti_x - Ti_x[010])^1(\eta_1)^1$	-3.528E-02
36	3	$(Ti_x - O1_x)^1(Ti_y - O1_y)^1(Ti_x - Ti_x[100])^1$	-1.086E-03
37	4	$(Ti_x - O1_x)^2(Ti_y - O1_y)^2$	-1.359E-02
38	4	$(Ti_x - O1_x)^3(Ti_y - O2_y)^1$	-1.112E-03
39	4	$(Ti_x - O1_x)^2(Ti_y - O2_y)^1(Ti_y - Ti_y[010])^1$	-3.526E-03
40	3	$(Ti_x - O1_x)^2(Ti_z - O3_z)^1$	2.768E-03
41	3	$(Ti_x - O1_x)^2(Ti_x - O2_x)^1$	2.181E-03
42	4	$(Ti_x - O1_x)^2(Ti_z - O1_z)^1(Ti_y - O3_y)^1$	-8.160E-04
43	3	$(Ca_x - Ti_x)^2(Ca_y - Ti_y)^1$	1.515E-03
44	3	$(Ca_x - Ti_x)^1(Ca_y - Ti_y)^1(Ca_z - Ti_z)^1$	6.217E-03
45	3	$(Ti_x - O1_x)^2(\eta_3)^1$	-2.658E-03
46	3	$(Ti_y - O1_y)^1(Ti_y - O1_y[010])^1(\eta_2)^1$	3.765E-01
47	3	$(Ti_x - O1_x)^1(Ti_z - O1_z)^1(\eta_5)^1$	-3.137E-02
48	3	$(Ti_y - O1_y)^1(Ti_x - O2_x)^1(\eta_1)^1$	-3.176E-01
49	3	$(Ti_x - O1_x)^1(Ti_x - O1_x[010])^1(Ti_y - O1_y[010])^1$	-1.067E-02
50	3	$(Ti_x - O1_x)^1(Ti_x - O3_x)^1(\eta_4)^1$	1.276E-02
51	4	$(Ti_x - O1_x)^1(Ti_z - O2_z)^1(Ti_z - O1_z[010])^1(\eta_1)^1$	1.474E-02
52	4	$(Ti_x - O1_x)^1(Ti_x - O1_x[010])^1(Ti_y - O1_y[010])^2$	4.377E-03
53	4	$(Ti_x - O1_x)^2(Ti_y - O2_y)^1(\eta_3)^1$	1.202E-01
54	3	$(Ti_x - O1_x)^1(Ti_x - O2_x)^1(Ti_y - O2_y)^1$	-3.119E-03
55	3	$(Ti_x - O1_x)^1(Ti_x - O3_x)^1(Ti_z - Ti_z[001])^1$	2.610E-03
56	3	$(Ti_x - O1_x)^1(Ti_x - O3_x)^1(Ti_z - O3_z)^1$	-3.649E-03
57	3	$(Ti_x - O1_x)^2(Ti_y - O3_y)^1$	-1.079E-03
58	4	$(Ti_y - O1_y)^4$	1.550E-02
59	4	$(Ti_x - O1_x)^2(Ti_y - O1_y)^1(Ti_y - O3_y)^1$	2.514E-03
60	4	$(Ti_x - O1_x)^2(Ti_x - O2_x)^1(Ti_x - O1_x[010])^1$	1.253E-03

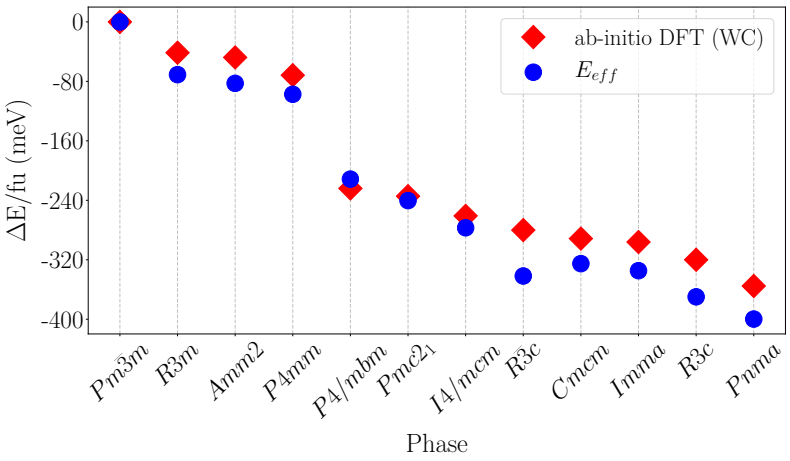

Figure 8.4: Comparision of total energies for selected relaxed phases from ab initio*and the bounded SP model (E_{eff}). Note that the structures at which the energies are evaluated from ab initio an the SP model are not the same, but the relaxed ones for the given phase symmetry from ab initio repsectively the SP model.

8.2.3 Model Validation

In this section we present a physical validation of the SP lattice model whose construction was outlined before. The validation consists of four tests that compare calculated properties of the SP lattice model to ab initio or experimental references. First, we relax all relevant phases of $CaTiO_3$ from ab initio and the SP lattice model and compare their total energies with respect to the cubic reference, second, we compare the ground-state $Pnma$ structure that the SP lattice model provides against ab initio and experimental references, third and last, we compare the phonon dispersion of this ground state phase from the SP lattice model to ab initio calculations. Let us start with the comparison of energies of relevant competing phases. We include two types of phases which are instable with respect to the cubic $Pm\bar{3}m$ reference. First, phases that contain polar displacements with Ti off centering, and second, phases that contain different octahedral rotation patterns. The phases with symmetry $P4mm$, $Amm2$, and $R3m$ belong to the first set with polar displacements in one, two, and respectively three Cartesian directions. To the second category belong the phases of symmetry (rot. pattern in brackets): $P4/mbm$ ($a^0a^0c^+$), $I4/mcm$ ($a^0a^0c^-$), $Cmcm$ ($a^0b^-c^+$), $Imma$ ($a^-a^-c^0$), $R\bar{3}c$ ($a^-a^-a^-$), and $Pnma$ ($a^-a^-c^+$). We note that some antipolar motions of Ca atoms are allowed by symmetry in the phases $Imma$, $Cmcm$, and $Pnma$. Finally, we add the polar phases $Pmc2_1$ and $R3c$ into set of tested structures. The former is derived from the $P4/mbm$ phase with a $a^0a^0c^+$ rotation pattern, but including a planar polar distortion of the Ca cations, and the latter is derived from the $R\bar{3}c$ phase containing a $a^-a^-a^-$ rotation pattern with an additional distortion of the Ca atoms in the [111] direction[1].

Fig. 8.4 shows the energy difference per formula unit of the tested phases to the cubic reference provided by the SP lattice model (E_{eff}: blue dots) and ab initio calculations (DFT: red diamonds). The SP lattice model reproduces well the order of energy of the phases as provide by ab initio calculations. The only exception is the $R\bar{3}c$ phase that is somewhat overstabilized. There exist some considerable energy difference for the

1: We give some additional information about this $R3c$ phase in appendix C.

* Energy of Phases $R3m$, $Amm2$, $P4mm$, $P4/mbm$, $I4/mcm$, and $R\bar{3}c$ have been adapted from Ref. [211], that used the same ab initio calculation approach that we used in this work.

Table 8.3: Unit cell Voulme (V), lattice constants (a,b,c) and normal lattice strains (in CJTD notation) and symmetry adapted mode distortions of the $Pnma$ phase of $CaTiO_3$ calculated by a relaxation of the fitted of the SP lattice model (E_{eff}), a relaxtion using ab initio calculations (DFT), and a experimental reference (powder neutron diffraction) at 7K [213].

	E_{eff}	DFT	Exp.[a]
V (Å^3)	220.454	219.827	222.477
a (Å)	5.343	5.333	5.368
b (Å)	5.434	5.433	5.434
c (Å)	7.594	7.587	7.627
Q_1^{Γ} [b]	-0.010	-0.011	-0.005
Q_{3z}^{Γ} [b]	-0.003	-0.003	-0.001
Q_{4z}^{Γ} [b]	-0.012	-0.013	-0.009
ϕ_{xy}^{-} (Å)[b]	0.635	0.622	0.574
ϕ_{z}^{+} (Å)[b]	0.437	0.444	0.433
A_X (Å)[b]	0.272	0.261	0.225

[a] Structural Values taken from Ref. [213] at 7K.
[b] Mode and Strain amplitudes have been evaluated using ISODISTORT [128] with respect to a cubic 5-atoms $Pm\bar{3}m$ perovskite structure with a cubic lattice constant of $a = 3.827$Å

individual relaxed phases. This could be expected from the construction of the model and the energy deviations found between the SP lattice model and the training set data. The maximum difference is found for the $R\bar{3}c$ phase of about 61 meV/fu. The average energy difference is about 30 meV/fu. From this result we can expect that phase transition temperatures and phase stabilities will be overestimated by the SP lattice model. However, it is adequate to compare the total energy of different structures to test which is the most stable.

Let us now turn our attention to Table 8.3 and the second test comparing the relaxed structure of the $Pnma$ phase provided by the SP lattice model to the ab initio reference and experiment. As can be extracted from Table 8.3 the SP lattice model is reproducing almost exactly the ab initio reference structure althoug the stabilization energy is about 44 meV/fu too low. Both, SP lattice model and ab initio, compare well against the experimental reference measured at low temperature [213]. Generally the lattice distortions are overestimated by the SP lattice model and ab initio calculations, which could be assigned to the absence of zero-point fluctuations in the static relaxations that we performed here.

Fig. 8.5 shows the result of the third test that is the comparison of the phonon dispersion and density of states ofi ground-state phase as obtained from the SP lattice model and ab-intio DFPT calculations. The phonon dispersion of the SP lattice model and DFPT coincide quite well. The general dispersion, band gaps and widths are well reproduced by the SP lattice model. It should be noted that that the phonon dispersion of the SP lattice model around the $Pnma$ phase is dominated by the contribution of the *anharmonic* terms in the polynomial expansion. Main differences can be found in the highest energy band (that corresponds to breathing distortion like modes Q_1), whose width is overestimated and the position is too high, and at the at about 550 cm^{-1}, where the SP lattice model again overestimates the band width. The descirption of those parts of the phonon dispersion could be improved by specifially adding some $Pnma$ structures with this specific high energy phonon modes condensed to the TS.

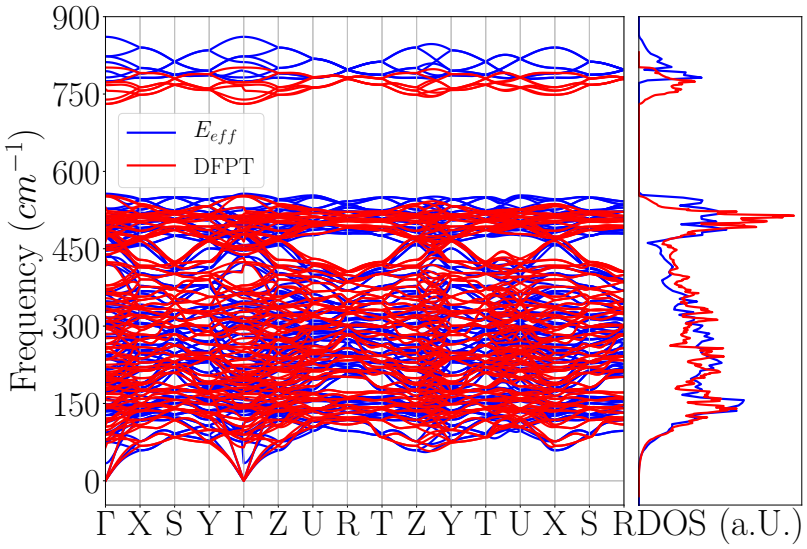

Figure 8.5: Comparison phonon dispersion an density of states at the $Pnma$ ground state structure calculated by DFPT and by finite-displacements evaulated with the SP model (E_{eff}).

8.3 Temperature Phase Diagram of $CaTiO_3$

After the validation the SP lattice model mainly against ab initio data, we use it here in a virtual heating experiment between 50-2150K in steps of 50K utilizing a HMC method. To do so, we use a large $16 \times 16 \times 16$ simulation cell. The first simulation temperature (50K) is started from the relaxed $Pnma$ phase. Then, we restart each increasing temperature step from the average structure of the preceding temperature. The order parameter of the expected phase transitions in $CaTiO_3$ is the octahedral rotation pattern. Here, we trace the evolution of the octahedral rotations by projecting the distortions of the average structure at a given temperature on the rotational phonon modes defined by the phonon eigenvectors of the in-phase rotation mode around the z axis ϕ_z^+ at the M-point of the cubic BZ and the anti-phase rotation modes around all three Cartesian axis $\phi_{x/y/z}^-$ at the R-point of the cubic BZ using the tool Agate [51]. The rotation mode amplitudes of the heating experiment (dots) are shown alongside an experimental result (triangles, neutron diffraction between room temperature and 1720K [199]) in Fig. 8.6. To extract phase transition temperaturesand the nature of the transition (first or second order) we fit function of the form

$$\phi = K \cdot (T_C - T)^c \tag{8.1}$$

to the simulated average rotation mode amplitudes. An exponent c close to one half hints to second order transition. An exponent close to one quarter to a first order one.

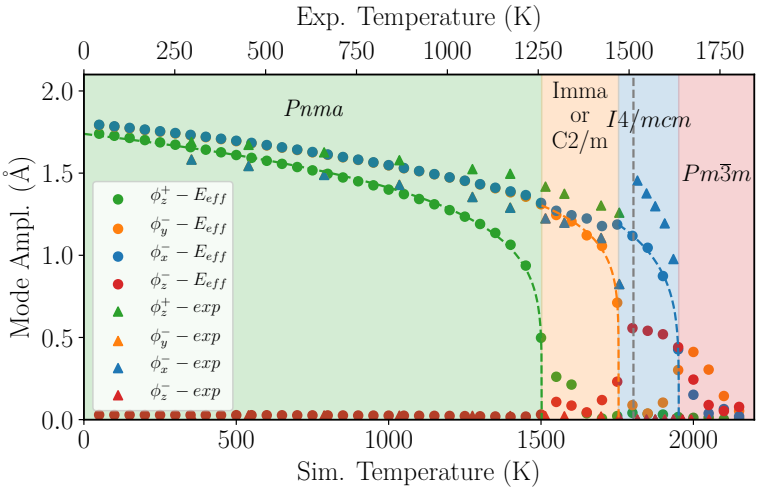

Figure 8.6: Comparison of rotation mode amplitudes extracted with AGATE[51] of experimental structures (triangles, Ref. [199]) with rotation mode amplitudes calculated from SP lattice model by a Hybrid Monte-Carlo simulation in a $16 \times 16 \times 16$ simulation cell (circles). Functions of the form $\phi = K \cdot (T_C - T)^c$ are fitted to extract transition temperatures and critical exponents (dashed lines). Experimental and simulation temperature are rescalled so that the transition to the cubic $Pm\bar{3}m$ phase fall together. The grey dashed line shows the experimentally determined transition temperature from $Pnma$ to $I4/mcm$.

Table 8.4: Fitted coefficients K, transition temperaturs T_C, and exponents c for the three dominant rotation modes upon heating (compare also Fig. 8.6)

	K	T_C (K)	c
ϕ_z^+	0.43	1502	0.19
ϕ_y^-	0.57	1755	0.15
ϕ_x^-	0.37	1951	0.22

Starting from the relaxed $Pnma$ phase at low temperatures the average rotational mode amplitudes continously decrease with increasing simulation temperature. The SP lattice model exhibits a first phase transition at about 1500K at which the in-phase rotation mode ϕ_z^+ dissappears. With an exponant $c \approx 0.19$ the transition is close to a first order one. The anti-phase rotations are almost unchanged at the transition. In the subsequent phase at simulation temperatures larger than 1500K it is then the anti-phase rotation mode ϕ_y^- that quickly declines and dissappears at about 1755K, while the other anti-phase rotation mode ϕ_x^- remains at larger amplitudes. The phase between 1500K or 1755K should hence be assigned either to have $Imma$ symmetry with a $a^-a^-c^0$ rotation pattern or $C2/m$ with a $a^-b^-c^0$ rotation pattern. The exponent of the ϕ_y^- amplitude fitted between 1500K and 1755K does hint to a first-order transition, but with $c \approx 0.15$ the exponent lies somewhat far away from one quarter. A possible origin of this could be insufficent statistics close to the transition. The amplitude of the remaining rotation mode ϕ_x^- is slightly incrased at the transition. Above 1755K the anti-phase rotation mode around the z-axis ϕ_z^- appears additionally. However, closer inspection of the local distortion pattern showed that this ϕ_z^- does not statically appear in the whole simulation box, but just in some unit cells. Otherwise rotation around the z-axis appears disordered, but the average amplitude is not zero. Thus, we assigned the phase $I4/mcm$ with rotation pattern $(a^0a^0c^-)$ to the phase at simulation temperatures higher than 1755K, since there is only one anti-phase rotation that appears coherently ordered in the whole simulation box. This last ordered rotation quickly dissapears when the temperature is further increased and a final transition appears at 1951K. The non-zero rotation mode amplitudes above this temperature stem from disordered octahedral rotations. Hence, we assign the cubic phase $Pm\bar{3}m$ to temperatures above 1951K.

To compare our results to the experimental measurement of *Yashima and Ali* [199], we rescale the simulation to the experimental temperature such that the transition to the cubic $Pm\bar{3}m$ phase fall togeter (exp. 1635K, sim. 1951K). While SP lattice model and experiment compare well in the low temperature range, some differences appear at high-temperature and in the phase transition sequence. While experimentally the anti-phase rotation ϕ_y^- and in-phase rotation mode ϕ_z^+ dissapear at once at 1512K, the

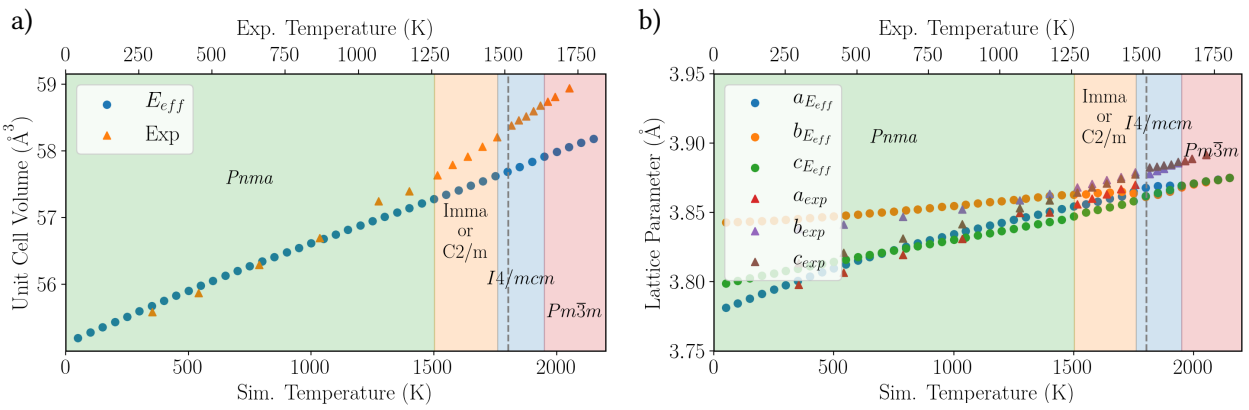

Figure 8.7: Pseudocubic unit cell volume (a) and lattice parameters (b) upon heating from experiment [199] and calculated from the SP lattice model (E_{eff}) by a Hybrid Monte-Carlo Simulation in a $16 \times 16 \times 16$ simulation cell. Experimental and simulation temperature are rescalled so that the transition to the cubic $Pm\bar{3}m$ phase fall together. The grey dashed line shows the experimentally determined $Pnma$ to $I4/mcm$ transition temperature.

model predicts that they dissappear sequentially. Furthermore, the jump of the remaining anti-phase rotation at the transition to the $I4/mcm$ phase appears much smaller in the SP lattice model than from experiment. On the other hand the transition temperaturs and phase stability ranges seem to compare very well in the rescaled temperature between experiment and SP lattice model simulation and the ϕ_x^- mode seems to reproduce correctly the experimental behavior until the $I4/mcm$ transition. Possible origins for the differences could be an overestimation of the stabiliation energy of the anti-phase rotation modes respectively underestimation of the in-phase rotation mode. Furthermore, at very high-temperatures the bounding terms might become activated through large dynamical distortions. Those bounding terms have been extrapolated and are not directly based on ab initio data. Hence, if they have a significant influence at high simulation temperatures they might worsen the behavior of the SP lattice model. However, the prediction of the SP lattice model seems in line with the proposition of *Carpenter* [201].

Finally, we analyze the lattice dilation upon heating. Fig. 8.7 compares the unit cell volume and pseudocubic lattice parameters of the HMC SP lattice model simulation with the experiment of Ref. [199]. The temperature rescaling between experiment and simuation is the same as in Fig. 8.6 and the phase transition temperatures indicated in Fig.8.7 are taken from the analysis of the rotation modes. At the $Pnma$ to $Imma$ transition predicted by the SP lattice model no discontinuity in the lattice parameters is visible. At the $Imma$ to $I4/mcm$ transition predicted by the SP lattice model the pseudocubic lattice parameters become tetragonal, which supports the assignment of the tetragonal $I4/mcm$ phase. Finally, at the $I4/mcm$ to $Pm\bar{3}m$ transition the pseudocubic lattice parameters become equal to each other which supports the assignment of $Pm\bar{3}m$ phase.

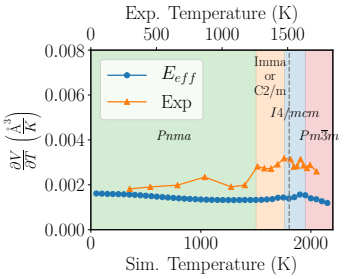

Figure 8.8: Psudocubic unit cell thermal volume expansion as calcluated by step-forward gradients from the data presented in Fig. 8.7. a)

Within the $Pnma$ phase the lattice dilation between SP lattice model and experiment compare well. However, at about 800K a crossing of the pseudocubic *a* and *c* lattice parameter is predicted by the SP lattice model that is not observed in experiments. At higher temperatures (>1500K) experiment and simulation significantly deviate, where the experimentally measured thermal expansion increases, while the simulated one stays essentially constant (see Fig. 8.8). A simple explanation for the

strictly linear behavior of the model might be that we only included strain phonon terms that are linear in the strain part. Thus, the description of the SP lattice model at high-temperatures might be improved by extending the SP lattice model (or refitting it from scratch) with including Strain-Phonon terms that contain quadratic strain multipliers.

8.4 Conclusions

In this section we showed the construction and validation of a SP lattice model for $CaTiO_3$. $CaTiO_3$ proves to be a demanding case due to the large energy difference and significant distortion amplitudes between the cubic reference and the ground state structure, and moreover, due to many competing phases that show only small energy differences. The decision of convergence of the TS and the SP lattice model have been taken by physical inspection. Stringent numerical descriptors that assert the quality of a fitted model other than the GF and the completness of a TS are missing and should be developed in the future. The SP lattice model of $CaTiO_3$ shows however a number of convincing properties. With the exception of the $R\bar{3}c$ phase it predicts correctly the order of energy of competing phases, it reproduces excellently the structure of the $Pnma$ ground state and its phonon dispersion, and the lattice dillation at low and intermediate temperatures are in good agreement with experiment. The main shortcomings are significant energy differences between the ab initio reference and the SP-lattice model for competing relaxed phases (several 10 meV/fu). This energy differences are most likely at the origin of the overestimation of the phase transition temperatures. The prediction of the phase transition sequence at highest temperatures is in line with a proposition of *Carpenter* [201] based on Landau theory, however, in contrast to the experimentally proposed ones [186, 193–199], which has been reproduce by a Landau like potential fitted on ab initio data [200]. However, the disagreement applies to a temperature range of about 100K. The three possible phases in this range ($Pbnm$, $Cmcm$, and $Imma$) are all orthorhombic for which reason they are difficult to resolve experimentally as additionally dynamical mixtures of those phases could exist due to the large thermal energy and close competing free energies. Nonetheless, we remark that in none of the experimental studies the *Imma* phase has been explicitly considered and a reinvestigation could be meaningful. On the other side, the high-temperature behavior of the SP lattice model presented here, could possibly be refined by including additional data in the TS and extending the polynomial expansion with strain-phonon terms that contain quadratic strain multipliers.

We conclude that the presented SP lattice model potential can be used for dynamical studies within the $Pnma$ phase at modest temperatures and to compare statically the relative stability of different structures. Further validations of the model could be reproductions of the epitaxial strain phase diagram as calculated by ab initio methods [200, 203, 204] or testing the SP lattice model's description of ferroelastic domain walls. The local polynomial development of the lattice energy thereby allows for distortion gradients, which is a great advantage over Landau type phenomenological potentials like the one from Ref. [200] that rely on homogenous distortions and strains.

Part IV

Conclusions

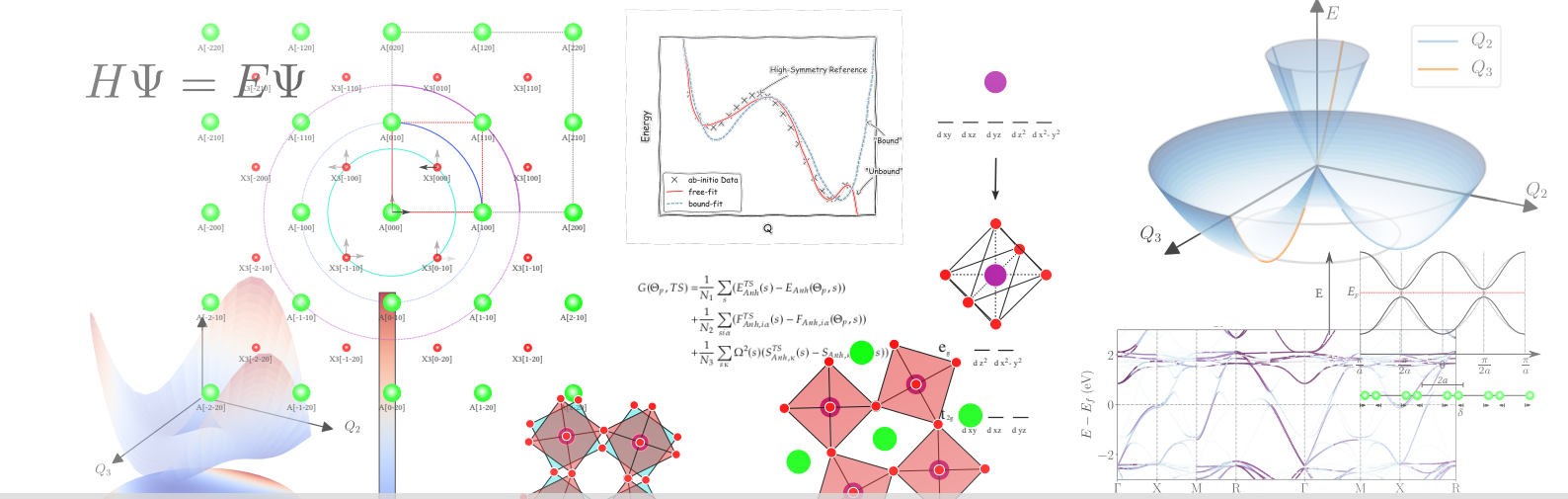

9 Concluding Remarks

In this thesis work we presented first-principles studies of the origin of metal-insulator transitions in $LaMnO_3$ and the alkaline earth ferrites series $AFeO_3$. Secondly, we presented methodological developments for effective potentials using polynomial expansions fitted on first-principles data. Finally, we applied this method to the perovskite $CaTiO_3$.

In chapter 2, we gave a brief introduction to the density functional theory formalism that allows to perform efficient ab initio calculations. The output of such calculations is on one hand the ground state energy for a given atomic arrangement in a given electronic state, on the other hand, properties of this given electronic state like the magnetic order or the existence of a Fermi surface. Sampling the energy eigenvalue for one given electronic state leads to the exploration of the so-called Born-Oppenheimer potential energy surface. Moreover, first and second order derivatives of the energy eigenvalue at a given nuclear configuration can be calculated using density functional perturbation theory. Those derivatives represent relevant physical properties of the solid like vibrational frequencies, elastic constants or the piezoelectric tensor.

In chapter 3, we introduced the so-called second-principles technique and it's implementation in the software package MULTIBINIT. The main idea of this technique is to represent first-principles quantities by a polynomial expansion. In practice this means that a least squares optimization between the polynomial expansion and the data of the fitted quantity is performed. In this work, we focused on expanding the Born-Oppenheimer potential energy surface. This approach leads to a so-called second-principles lattice model, which integrates out the explicit treatment of electrons. The advantage of such a model is the lightweight evaluation of the polynomial expansion at a given nuclear configuration compared to a first-principles calculation. This facilitation enables a scale transfer to include more atoms into statistical calculations while keeping the first-principles information.

The major challenge of this technique is to find the right polynomial expansion. In section 3.2.3 we showed that the complete polynomial expansion until order four contains by far too many independent coefficients so that all could be included in the expansion. Therefore, a numerical procedure proposed by *Escorihuela-Sayalero et al.* [45] has been used to select the most important terms from the complete polynomial

expansion. Those automatically generated expansions are very often unbounded from below. Therefore, we introduced an algorithm that starting from an already defined expansion (usually until order four), generates and adds equivalent higher order terms (usually order six and/or eight) and optimizes their coefficients of those terms to impose boundedness.

In chapter 4, we gave an introduction to the theory of the Jahn-Teller effect that describes how degenerate electronic states in molecules induce nuclear displacements that remove the degeneracy of the initial state. We put a special emphasize on degenerate electronic states with e_g symmetry located on a transition metal centered inside an octahedron. We introduced *Van Vleck's* notation of normal vibrational modes of the transition metal octahedron relevant to the Jahn-Teller effect. This recapitulation was relevant for the discussion of metal-insulator transitions in perovskites, where each neighboring octahedron contains a transition metal ion with a formally degenerate electronic state.

In chapter 5, we introduced a canonical notation for *cooperative* Jahn-Teller distortions in the perovskite structure, where each neighboring octahedron contains an transition metal ion with a formally degenerate state. This canonical notation is on one hand based on *Van Vleck's* notation molecular normal modes, and on the other hand on labels of q-points of the cubic Brillouin zone of the ideal perovskite structure. This q-point labels indicate the cooperative arrangement of the local distortion indicated by *Van Vleck's* label. We felt the need to introduce this notation, as various notations exist in the literature whose connection is often not clear. Furthermore, our notation defines a *unique* symbol for each possible distortion. We hope that this notation facilitates the comparison of different perovskite showing metal-insulator transitions accompanied by cooperative distortions of anion octahedra. Moreover, in section 5.3, we gave a brief recapitulation of theoretical concepts about the origin of metal-insulator transitions perovskites which are the *cooperative Jahn-Teller effect*, the *Kugel-Khomskii model of superexchange*, and the *Peierls transition* based on translational symmetry breaking. Thereby, it became apparent that a distinction of those three concepts experimentally or from first-principles calculations is challenging as they are all capable of predicting the right ground-state.

In chapter 6, we studied $LaMnO_3$ from first-principles. Our key method was to sample the Born-Oppenheimer potential energy surface for the competing antiferromagnetic type A (AFM-A) and ferromagnetic (FM) surface for all relevant distortions appearing in the *Pnma* ground state. Thereby, we could show interesting cooperative mechanisms. First, that the metal-insulator transition is enabled by the octahedral rotations incorporated in the *Pnma* phase. Second, we could show that the AFM-A ground state magnetic order is stabilized by the strong tetragonal distortion that appears in the ground state. From this point we could show that the reduction of this distortion in the thin film configuration of $LaMnO_3$ grown on $SrTiO_3$ is capable of changing the magnetic ground state from AFM-A to FM, as it is observed experimentally. Furthermore, analyzing closely the electronic band structure in the cubic and slightly $Q_{2z}^{\mathbf{M}}$ Jahn-Teller distorted phase showed that the gap opening mechanism from first-principles is compatible with the Peierls picture. Performing simple Monte-Carlo simulations using the Born-Oppenheimer surface

for different magnetic orderings showed that spin symmetry breaking in the paramagnetic spin disordered phase is at least partly responsible for the high metal-insulator transition temperature of $LaMnO_3$ by activating strong electron-lattice coupling.

In chapter 7, we applied the same approach to the alkaline earth ferrite series $AFeO_3$. Thereby, we could show that similar mechanism that we found in the study of $LaMnO_3$ apply to the $AFeO_3$ series. For instance, the absence of the metal-insulator transition in $SrFeO_3$ and $BaFeO_3$ could be directly linked to the absence of octahedral rotations in this compounds, while the presence of octahedral rotations in $CaFeO_3$ enables the metal-insulator transition. However, here the metal-insulator transition is related to charge ordering and a different distortion coordinate. Nonetheless the analyses of the electronic band structure from a static point of view shows the compatibility of the band gap opening with the Peierls mechanism. Finally, we could show that imposing an external strain can change the metal-insulator mechanism from charge order to orbital order (like in $LaMnO_3$), which might explain the experimentally found high metal-insulator transition temperature of $CaFeO_3$ grown on $SrTiO_3$.

We see our work on the metal-insulator transition in perovskites in line with recent studies of *Alexander Zunger* and coworkers [89, 115, 214, 215]. We expect that in the near future the interpretation differences between researchers performing static DFT(+U) calculations and those performing time averaged dynamic DFT+DMFT (DMFT: for dynamical mean field theory) calculations will be resolved. Our impressions is that there might indeed be no contradiction in the results of both approaches, but rather in the interpreation of those. A key ingredient will be the understanding of the paramagnetic insulating phase below, and the paramagnetic metallic phases above the metal-insulator transition. From our point of view these phases should be seen as correlated spin liquids where the electronic wave function at each point in time breaks the translational symmetry of the crystal enabling strong electron-phonon coupling, which is compatible with our and Zunger's DFT calculations. However, in the time average the symmetry of the crystal lattice is preserved in the electronic wavefunction and the population of up- and down-spin becomes equal, which is compatible with the DMFT results. We think that second-principles models including electron lattice coupling might help to solve this issue.

Finally, in chapter 8, we applied the second-principles technique to $CaTiO_3$. $CaTiO_3$ proved to be a very challenging material due to many instabilities with respect to the ideal cubic reference structure, many competing phases, and large distortions in the ground state phase. Despite these challenges we created an effective second-principles lattice model. To our best knowledge it is the first atomistic lattice model based on first-principles data constructed for $CaTiO_3$. The lattice model predicts the right phase stability sequence, phonon dispersion of the ground state $Pnma$ phase, and lattice dilatation at moderate temperatures (several hundred K) of the $Pnma$ phase. The high temperature phase transition sequence was not in accordance with experimental measurements which are, however, for their part subject of debate. An interesting finding was a strongly polar phase ($\approx 50 \frac{\mu C}{cm^2}$) with $R3c$ symmetry and a $a^-a^-a^-$ rotation pattern. Finding a way to stabilize this phase using the second-principles lattice model is part of ongoing research.

However, it remains to be seen if the approach of using polynomial expansions to create effective models in a well defined automated way proves to be successful. The major challenge of this approach is the diverging number of parameters in the high order polynomial expansion from which few have to be selected. The experience shows that it is very challenging to find those few important terms even in the assistance of algorithmic approaches. Nonetheless, borrowing more advanced algorithms from machine learning communities for feature selection and solving under-determined linear equation systems techniques can help to define more robust expansions, as has been recently demonstrated [216]. A different approach that has been recently demonstrated is to change the type of basis function to expand the potential energy surface. This, so-called, *Gaussian Approximation Potentials* [217–221] seem to be successful in creating effective lattice interaction potentials. Here, the approach is qualitatively the same as in second-principles (least squares optimization of parameters in a basis function space with respect to first-principles data), but the polynomial expansion is replaced by a different type of basis functions relying on less independent parameters.

Appendix

Additional Information to first-principles studies of $LaMnO_3$

A

A.1 Fitting of Q_{2z}^{M} PES

In the following we discuss briefly the parameterisation of the Q_{2z}^{M} surface in a free energy expansion. To do so, we fitted each of the PES in Fig. 6.4 by a polynomial of the shape

$$\mathscr{F} = E_0 + \alpha_{JT}|Q_{2z}^{M}| + \alpha Q_{2z}^{M} + \beta(Q_{2z}^{M})^2 + \gamma(Q_{2z}^{M})^4, \tag{A.1}$$

where the introduction of the absolute function allows to quantify the vibronic couplings independent of linear asymmetries of the whole PES due to the crystal field. By the generation of invariant terms using the *INVARIANTS* [129] tool, we defined the following free energy expansion

$$\begin{aligned}\mathscr{F}(Q_{2z}^{M}) = \quad & E_0 + \alpha_{JT}|Q_{2z}^{M}| + \alpha_1[(\phi_{xy}^{-})^2\phi_z^{+}]Q_{2z}^{M} + \alpha_2(\phi_{xy}^{-}A_X)Q_{2z}^{M} + \alpha_3(Q_{3z}^{\Gamma}\phi_{xy}^{-}A_X)Q_{2z}^{M} + \alpha_4(Q_{4z}^{\Gamma}\phi_z)Q_{2z}^{M} \\ & + \alpha_5(Q_{4z}^{\Gamma}A_X\phi_{xy}^{-})Q_{2z}^{M} + \beta_1(Q_{2z}^{M})^2 + \beta_2\phi^2(Q_{2z}^{M})^2 + \beta_3A_X^2(Q_{2z}^{M})^2 + \beta_4Q_{3z}^{\Gamma}(Q_{2z}^{M})^2 + \beta_5(Q_{3z}^{\Gamma})^2(Q_{2z}^{M})^2 \\ & + \beta_6(Q_{4z}^{\Gamma})^2(Q_{2z}^{M})^2 + \gamma(Q_{2z}^{M})^4\end{aligned} \tag{A.2}$$

where we denote coefficients of terms that are of first-order in Q_{2z}^{M} with α, second with β, and fourth with γ. All modes have been normalized such that 1 represents their ground-state amplitude, which can be found in Table 6.1. Since we are not interested in the fourth-order couplings we wrote only one fourth order term and we will not list the variation of its value. Moreover, we used

$$\phi = \phi_z^{+} = \phi_{xy}^{-} \tag{A.3}$$

in the β_2 term, to define a total rotations amplitude ϕ, as we did not vary the rotations individually. Equation (A.3) implies that β_2 is only valid along a line where the ratio of the amplitudes of the rotations ϕ_z^{+} and ϕ_{xy}^{-} is the same as in the ground-state. E_0, the energy at $Q_{2z}^{M} = 0$, is a function of the applied structural distortions. It can be decomposed in the following way

$$E_0 = E_0^{FM} + E_0^{Q_{3z}^{\Gamma}} + E_0^{Q_{3z}^{\Gamma}Q_{4z}^{\Gamma}} + E_0^{\phi} + E_0^{\phi,Q_{3z}^{\Gamma}} + E_0^{\phi,Q_{3z}^{\Gamma},Q_{4z}^{\Gamma}} + E_0^{\phi,A_X} + E_0^{\phi,A_X,Q_{3z}^{\Gamma}} + E_0^{\phi,A_X,Q_{3z}^{\Gamma},Q_{4z}^{\Gamma}} \tag{A.4}$$

, where each quantity shows the individual energy gains or losses with respect to the cubic AFM-A phase dependent of distortions or magnetic orderings in the superscript. As described in the main text the individual strains and distortions were applied with their amplitude in the ground-state of $LaMnO_3$. The values of E_0 indicate hence the stability or instability

of strains and atomic displacements in the FM and AFM-A phase in the absence of the $Q_{2z}^{\mathbf{M}}$ distortion. Finally, we also investigated the variation of the strength of the electronic instability parameter α_{JT} as a function of the other lattice distortions

$$\begin{aligned}\alpha_{JT} \quad &= \alpha_{JT}^{0}(1 + (\lambda_{\phi} + \lambda_{\phi+A_X} A_X)\,\phi \;+ (\lambda_{Q_{3z}^{\Gamma}} + ((\lambda_{Q_{3z}^{\Gamma}+\phi} + \lambda_{Q_{3z}^{\Gamma}+\phi+A_X} A_X)\,\phi \\ &\quad + (\lambda_{Q_{3z}^{\Gamma}+Q_{4z}^{\Gamma}} + (\lambda_{Q_{3z}^{\Gamma}+Q_{4z}^{\Gamma}+\phi} + \lambda_{Q_{3z}^{\Gamma}+Q_{4z}^{\Gamma}+\phi+A_X}\, A_X\,)\,\phi\,)\,Q_{4z}^{\Gamma}\,)\,Q_{3z}^{\Gamma}\,) \quad \text{(A.5)}\end{aligned}$$

, where we assume a linear dependence of the α_{JT} to the other lattice distortions. Further studies would need to clarify the explicit dependence of α_{JT} to the surrounding lattice. As mentioned in the main text α_{JT} is strictly zero on the FM surface, for which reason only its values for AFM-A ordering has been reported in Table 6.3 below.

A.2 Effect of (U | J) Parameters on the PES

In this section we provide additional information for the connection between the values of $(U|J)$ parameters in DFT+U calculations and the shape of the $Q_{2z}^{\mathbf{M}}$ PES.

Firstly, we explain the different shapes of the PES presented in Fig. 6.2 in Subsection 6.4. For this purpose, we show the electronic band-structures of $LaMnO_3$ in its cubic phase (space group $Pm\bar{3}m$) and in a 10% $Q_{2z}^{\mathbf{M}}$ distorted structure (space group $P4/mbm$) in FM-ordering using one one hand $(U|J)$ = (5eV|1.5eV) and one the other hand $(U|J)$=(8eV|2eV) (see Fig. A.1). All band structures are presented in the Brillouin zone of the 20-atoms supercell, that is the conventional unit-cell for the *Pnma* space-group. The main difference between (5eV|1.5eV) and (8eV|2eV) in Fig. A.1 is the splitting energy at gap-openings at high symmetry k-points. These are emphasized with blue dashed lines for the high symmetry points **U** and **T**. The splitting energy is significantly increased by the larger $(U|J)$ values (from about 0.5eV to 0.8eV). This difference can explain the different curvature of the FM $Q_{2z}^{\mathbf{M}}$ PES in Fig. 6.2 in subsection 6.4. Through the larger splitting a band gap is opened in a larger part of the Brillouin zone for the same $Q_{2z}^{\mathbf{M}}$ amplitude. The path U-T represents an example. While there is a band just at the Fermi-level in the case of using (5eV|1.5eV) which will induce a positive PES curvature, the same band is well below the Fermi level in the case of (8eV|2eV) and will therefore contribute to a negative curvature.

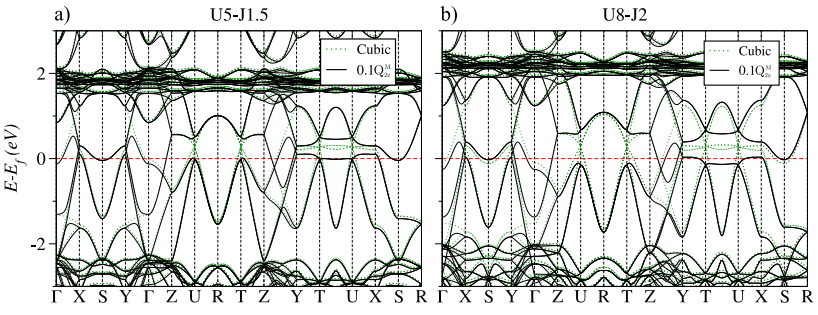

Figure A.1: Electronic Band Structures of the majority spin in FM ordering around the Fermi level. Green dotted lines correspond to the electronic bands in the cubic lattice ($Pm\bar{3}m$) and continuous black lines to the cubic lattice plus 10% $Q_{2z}^{\mathbf{M}}$. The red dashed lines shows the Fermi level. Blue lines indicate the effect of larger U_{eff} onto the band-opening at the high symmetry points U and T. a) $(U|J)$=(5eV|1.5eV), b)$(U|J)$=(8eV|2eV).

Secondly, we address the question if changing the $(U|J)$ parameters would *qualitatively* change the results presented in this work. Notably, would a different choice of $(U|J)$ change the results, that the tetragonal strain $Q^{\mathbf{\Gamma}}_{3z}$ controls the competition between FM and AFM-A? From Fig. 6.2 in Section 6.4 we know that in the cubic phase (space group $Pm\bar{3}m$ applying (8eV|2eV) keeps the FM ground state. Here we additionally show in Fig. A.2 the $Q^{\mathbf{M}}_{2z}$ FM and AFM-A PESs within the cubic lattice *with octahedral rotations* condensed with their corresponding ground-state amplitude first using $(U|J)$ = (5eV|1.5eV) and then $(U|J)$=(8eV|2eV). The first main difference between (5eV|1.5eV) and (8eV|2eV) is the increased stabilization energy between $Q^{\mathbf{M}}_{2z} = 0$ and the minima positions. The minima positions themselves are not shifted and lie close to the GS amplitude of $Q^{\mathbf{M}}_{2z}$ (=1 in Fig. A.2). The second main difference is the insulating electronic GS around the minima on the FM PES when (8eV|2eV) is used. Both these differences can be understood by the analyses of the electronic band structures in dependence of the $(U|J)$ presented in the paragraph above. However, the important common ground between both $(U|J)$ cases are that the FM PES is the lowest in energy. Hence, also in the case of (8eV|2eV) octahedral rotations cannot tune the magnetic ground state. From the analysis in the main text in Section 6.5.1 and in Appendix A.1 we know that the antipolar motion A_X shows an equal trilinear coupling with $Q^{\mathbf{M}}_{2z}$ independent of the magnetic order. Therefore it can not tune the competition between AFM-A and FM. This leaves the tetragonal strain $Q^{\mathbf{\Gamma}}_{3z}$ to be the only structural deformation that can tune competition between AFM-A and FM, which is independent of $(U|J)$.

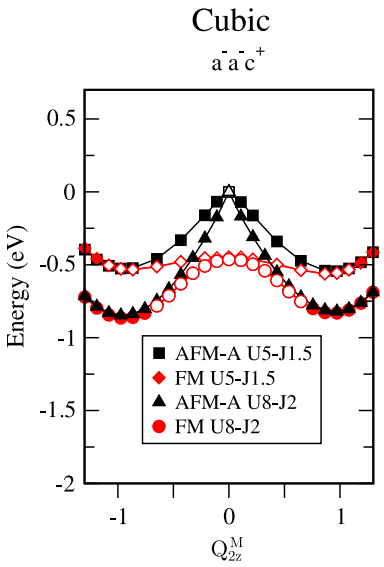

Figure A.2: FM and AFM-A PES of $Q^{\mathbf{M}}_{2z}$ mode within the cubic lattice-parameters and octahedral rotations condensed with their corresponding ground-state amplitude for two $(U|J)$ pairs.

Additional Information to first-principles studies of Alkaline Earth Ferrites $AFeO_3$

B

B.1 Choice of (U|J) Parameters

For our first-principles study of the $AFeO_3$ family we used density functional theory (DFT) as implemented in the *Vienna Ab-Initio Simulation Package* (*VASP*) with the *PBEsol* exchange-correlation functional adding a *Liechtenstein* (U|J) correction of (U|J)=(7.2|2) eV. Those parameters where determined by comparing the magnetic, electronic, and structural ground-state of our calculation to experimental values on which we give additional information in the following two sections.

B.1.1 Magnetic and Electronic Properties

In Fig. B.1 and Table B.1 magnetic and electronic information of our DFT-PBEsol + (U|J) calculations and experimental values are gathered.

Experimentally, $CaFeO_3$ exhibits an antiferromagnetic (AFM) transition at the Néel temperature $T_N = 115$ K. Below, the magnetic state is proposed to be either a spiral spin structure with alternating incommensurate magnetic moments of 2.70 and 3.52 μ_B or a sinusoidal structure with alternating moments of 3.6 and 5.06 μ_B. The helical axis of the spiral structure was proposed to lie along or close to the pseudocubic [111] direction, the sinusoidal axis in or close to the pseudocubic [101] direction. Both spin-waves exhibit periodicity close to $k = \frac{\pi}{3}$. The nearest-neighbor interaction is suggested to be ferromagnetic, the next-nearest anti-ferromagnetic.

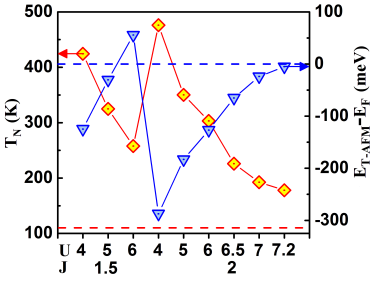

Figure B.1: Effect of U and J value on the Néel temperature T_N (orange curve) and energy difference between T-AFM (or S-AFM) state and FM state (blue curve).

In our calculations, the magnetic ground-state was probed at the collinear level on various magnetic cells up to 16 formula units (ferromagnetic (FM), simple A-type, C-type, and G-type AFM-orders, and more complex E-type, S-type and T-type AFM states as defined in [222]). In the limit of these unit-cells S- and T-type AFM states are the closest to the spiral model of *Woodward et al.* [175] showing ⇑↑↓⇓ sequences along the [111] direction, where ⇑ stands for the larger magnetic moment and ↑ for the smaller ones. For most tested (U|J) values AFM-S or T-type were the ground state, with marginal energy differences in between them. We extracted isotropic spin-exchange parameters until the fourth neighbor and calculated T_N from mean field theory. For U = 7.2 and J = 2 we found the lowest T_N of about 180 K in decent proximity to the experimental one, where T-type AFM is the ground-state. The nearest neighbor exchange is FM ($J_1 = 5.09\text{meV}/fu$), while second and third neighbor interactions are negligible ($J_2 = 0.74\text{meV}/fu$, $J_3 = 0.31\text{meV}/fu$). The fourth nearest-neighbor exchange constant (second nearest along the [001] pseudocubic axis) is strongly AFM ($J_4 = -3.69\text{meV}/fu$), showing the magnetic frustration of the system which would lead to spiral magnetic structures in non-collinear calculations. The corresponding magnetic moments at U = 7.2 and J = 2 of 2.72 and 4.07 μ_B for two nearest-neighboring Fe atoms match sufficiently the experimental results. We further check the band gap with

Table B.1: Comparison of the lattice parameters, amplitudes of relevant atomic distortions (from ISOTROPY [158], Néel temperature T_N and electronic band gap of the $P2_1/n$-phase of $CaFeO_3$ as obtained in the T-AFM state from PBEsol + (7.2|2) method (present), in the FM state from PBEsol + (3.0|0) and experimental results.

$U\|J$ (eV)	a (Å)	b (Å)	c (Å)	Q_1^R (Å)	ϕ_z^+ (Å)	ϕ_{xy}^- (Å)	T_N (K)	E_{Gap} (eV)
7.2|2	5.29	5.34	7.48	0.19	0.81	1.11	180	0.96
3|0[a]	5.29	5.33	7.49	0.08	0.81	1.10	-	0.18
Exp.[b]	5.31	5.35	7.52	0.18	0.83	1.06	115	-

[a] Ref. [179]
[b] Ref. [175]

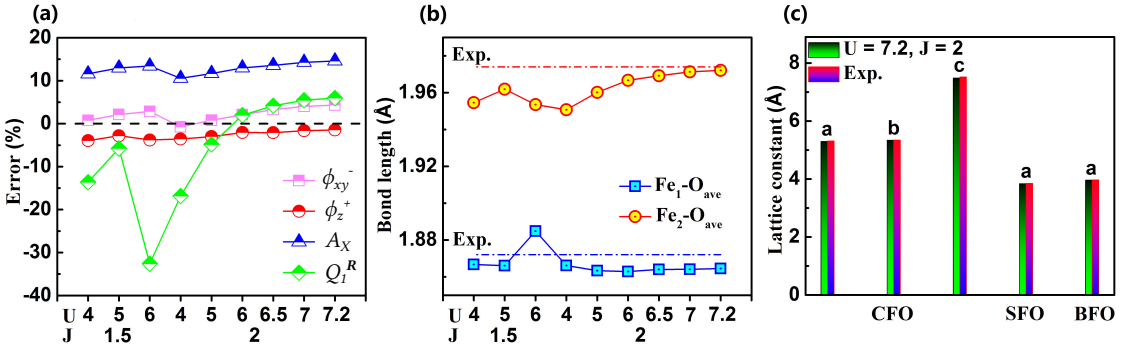

Figure B.2: Effect of U and J value on the (a) Error of the distortions for the lowest energy structure compared to experimental results, (b) average bond length of Fe1 and Fe2 sites in the optimized ground state, (c) lattice constant of T-AFM $CaFeO_3$ and ferromagnetic $SrFeO_3$ and $BaFeO_3$ with U equal to 7.2 and J equal to 2. The ISOTROPY program was used to quantify the distortion modes amplitudes [128]

U = 7.2 and J = 2. The result of 0.96 eV compares well with the previous result of 0.9 eV obtained from Hartree-Fock calculations [153].

B.1.2 Structural Optimization

In Fig. B.2(a), (b), as well as Table B.1 we present structural values in dependency of the (U|J) parameters for $CaFeO_3$. All tested quantities are excellently reproduced by the choice of (U|J)=(7.2|2) eV. In Fig B.2 (c) we additionally show that the experimental cubic lattice parameters of $SrFeO_3$ and $BaFeO_3$ are equally well reproduced by the same calculation approach.

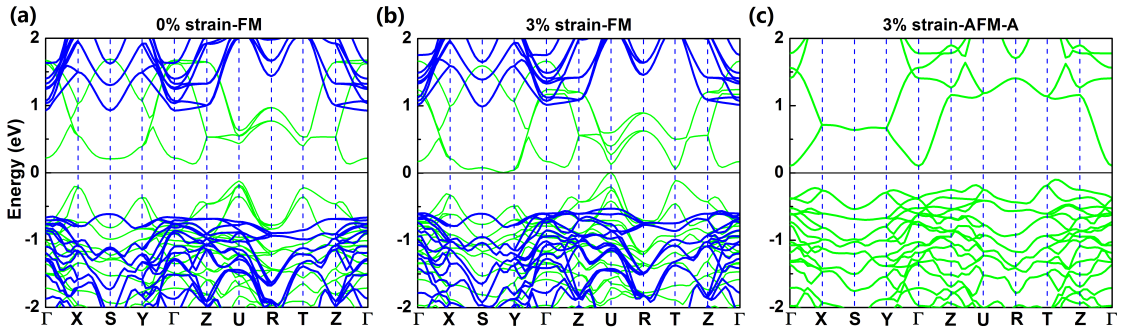

Figure B.3: Electronic Band Structures of (a) FM-CO state under 0% strain, (b) FM-CO state under 3% strain and (c) AFM-A-OO state under 3% strain. Green lines represent the majority, blue lines the minority spin channels.

B.2 Closing of the Band-Gap at the Phase Boundary between Charge- and Orbital-Order under Epitaxial Strain

The transition from charge to orbital ordering takes place precisely, when the band gap is closed at 3% tensile epitaxial strain. At this strain the Charge-Ordered state becomes semimetallic, where the indirect band gap is closed down. A electron pocket is formed along the path $\overline{\mathbf{SY}}$, a complementary hole pocket is formed around the **U** point in the Brillouin zone of the orthorhombic 20-atoms unit cell. These pockets are removed with the appearance of the $Q_{2z}^{\mathbf{M}}$ distortions and the magnetic transition from FM to AFM-A (See Fig. B.3).

Table B.2: Optimized Lattice Constants and distortion mode amplitudes of the breathing distortion $Q_1^{\mathbf{R}}$ and the octahedral rotations ϕ_z^+/ϕ_{xy}^- for $CaFeO_3$, $Ca_{0.5}Sr_{0.5}FeO_3$, and $SrFeO_3$.

	a (Å)	b (Å)	c (Å)	$Q_1^{\mathbf{R}}$(Å)	ϕ_z^+(Å)	ϕ_{xy}^-(Å)
$CaFeO_3$	5.3	5.35	7.5	0.14	0.9	1.11
$Ca_{0.5}Sr_{0.5}FeO_3$	5.39	5.37	7.59	0.11	0.49	0.82
$SrFeO_3$	5.43	5.43	7.68	0	0	0

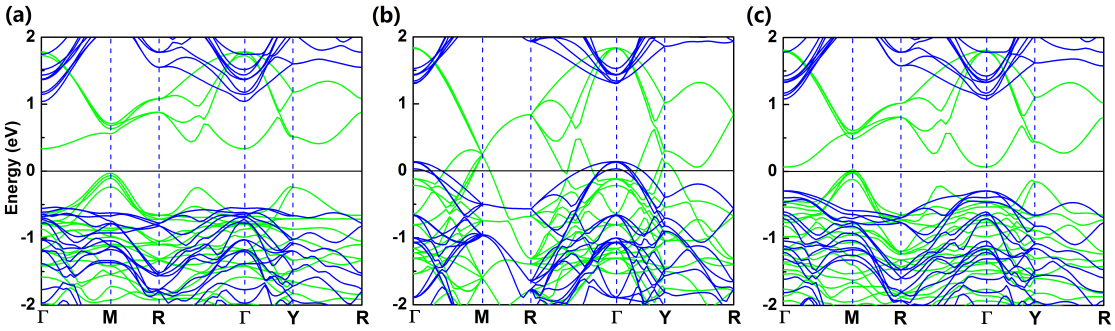

Figure B.4: Band structure of (a) $CaFeO_3$, (b) $SrFeO_3$ and (c) $Ca_{0.5}Sr_{0.5}FeO_3$ ordered along [001] in ferromagnetic state along the high-symmetry path **Γ**(0, 0, 0)-**M** (1/2, 0, 1/2)-**R**(1/2, 1/2, 1/2)-**Γ**(0, 0, 0)-**Y**(0, 1/2, 0)-**R**(1/2, 1/2, 1/2) of the Brillouin zone of orthorhombic lattice. Green lines represent the majority, blue lines the minority spin channels.

B.3 Reduction of MIT Temperature in Ca/$SrFeO_3$ Solid Solutions

In Table B.2 we present the results of structural optimizations of $CaFeO_3$, $SrFeO_3$, and the solid solution $Ca_{0.5}Sr_{0.5}FeO_3$ ordered along the [001] pseudocubic axis. As it is obvious from Table B.2 the triggering mechanism we present in the main manuscript is able to explain the band gap reduction from $CaFeO_3$ to the solid solution and the other way around the opening of it when starting from pure $SrFeO_3$. In Fig. B.4 we provide additionally the calculated electronic band structures of the three materials.

B.4 Coupling Parameters and Decomposition of the Linear Term $\gamma A_X \phi_{xy}^- Q_{2z}^{\mathbf{M}}$

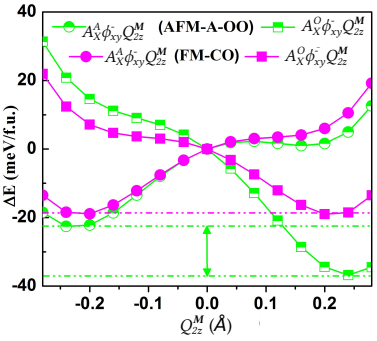

Figure B.5: Decomposition of the trilinear term $\gamma_{RXJT} A_X \phi_{xy}^- Q_{2z}^{\mathbf{M}}$ into the motion of the cations $\gamma_{RXJT}^A A_X^A \phi_{xy}^- Q_{2z}^{\mathbf{M}}$ and oxygens $\gamma_{RXJT}^O A_X^O \phi_{xy}^- Q_{2z}^{\mathbf{M}}$ by fixing A_X^A, A_X^O and ϕ_{xy}^- obtained from AFM-A OO phase (green curve) and FM CO phase (Magenta curve) at 0% strain (a=3.76Å).

Table B.3 represents an extended version of Table 7.1 of the main manuscript. We additionally note the coupling parameters resulting a polynomial fit of the potential energy surfaces presented in Fig. 7.3 (a) and (b) in the main manuscript. The energy contributions to ΔE_{JT} ($\Delta E_{JT} = \sum_i \Delta E_{JT}^i$), where then obtained by simple multiplications of the distortion amplitudes with the coupling parameters according to Eq. (2) of the main manuscript. In Table B.3 we disentangle the oxygen motion A_X^O and cation motion A_X^A appearing in the same irreducible representation X_5^- and investigate the potential energy surface with respect to those displacements. It turns out to be more appropriate to associate individual coupling parameters to A_X^O and A_X^A and write

$$\gamma_{RXJT} A_X \phi_{xy}^- Q_{2z}^{\mathbf{M}} = \gamma_{RXJT}^A A_X^A \phi_{xy}^- Q_{2z}^{\mathbf{M}} + \gamma_{RXJT}^O A_X^O \phi_{xy}^- Q_{2z}^{\mathbf{M}} \qquad \text{(B.1)}$$

Table B.3: Extended Version of Table 7.1 in the main manuscript. Amplitude of distortion modes of $CaFeO_3$ thin film under 0%(=3.76Å) and 4% (=3.91Å) in CO and OO phases, coupling parameters, energy gains ΔE^i_{JT} related to the condensation of $Q^{\mathbf{M}}_{2z}$ mode, and the energy cost related to AFM-A magnetic order. Calculations were executed in FM for the CO-phase and AFM-A for the OO-phases. The units of the coupling parameters are (meV/(Å$^d \cdot$ fu)), where *d* stands for the dimension of the term the parameters is associated to.

Amplitudes (Å)	$Q^{\mathbf{M}}_{2z}$	$Q^{\mathbf{R}}_1$	ϕ^+_z	ϕ^-_{xy}	A_X	A^A_X	A^O_X
a = 3.76Å-CO	0.007	0.137	0.788	1.111	0.440	0.413	-0.149
a = 3.76Å-OO	0.256	0.000	0.717	1.194	0.457	0.371	-0.270
a = 3.91Å-OO	0.400	0.000	0.676	1.309	0.552	0.407	-0.374
Parameters (meV/(Å$^d \cdot$ fu))	α_{JT}	λ_{MJT}	λ_{RJT}	γ_{RXJT}	γ^A_{RXJT}	γ^O_{RXJT}	
a = 3.76Å-CO	102.4	-183.0	-375.8	7.2	-131.5	-389.2	
a = 3.76Å-OO	66.7	-181.1	-401.2	-113.0	-129.7	-372.5	
a = 3.91Å-OO	-651.7	-69.9	-276.3	-107.1	-106.5	-280.0	
Energies (meV/fu)	ΔE^1_{JT}	ΔE^2_{JT}	ΔE^3_{JT}	ΔE_{JT}	ΔE_{AFMA}		
a = 3.76Å-CO	6.7	-37.8	-0.9	-32.0	62.3		
a = 3.76Å-OO	4.4	-43.6	-15.8	-55.0	74.5		
a = 3.91Å-OO	-104.3	-80.9	-31.0	-216.2	49.3		

Comparing the amplitudes A^O_X, A^A_X and the energy well with respect to $Q^{\mathbf{M}}_{2z}$ associated with the above coupling(Fig. B.5) for CO and OO phase at 0% strain, it becomes apparent that the asymmetric energy contribution ΔE^3_{JT} in OO phase stems primarily from the change of the relative amplitudes A^O_X/A^A_X as γ^O_{RXJT} and γ^A_{RXJT} are rather constant in the two phases.

Ferroelectric R3c phase of $CaTiO_3$

C

In the main text we noted that there exists a polar phase of $CaTiO_3$ with $R3c$ symmetry that is second lowest in energy of all the phases that we explored for training the second principles model. To our best knowledge this phase hasn't been explored yet from ab initio calculations and thus a closer investigation using ab initio methods and taking advantage of the SP lattice model seemed desirable to us. The polar phase $R3c$ derives from the $R\bar{3}c$ phase with an $a^-a^-a^-$ rotation pattern (rotation mode ϕ^-_{xyz}, irrep. $R^-_5(a,a,a)$). It additionally incorporates a polar displacement of the Ca and Ti atoms along the body diagonal of the cubic perovskite phase (crystallographic direction [111]) against the oxygen octahedral cage (mode p_{xyz}, irrep. $\Gamma^-_4(a,a,a)$). In the mode vector the Ca displacement is more then twice as large as the Ti displacement (see Fig. C.2). The alignment of the rhombohedral unit cell of the $R3c$ phase within a 2×2×2 supercell of the five atoms cubic perovskite cell is shown in Fig. C.2. It is characterized by one lattice constant a_r and an crystallographic angle α in the vicinity of 60° that is the same between all three lattice vectors. In terms of normal strains with respect to the five atoms cubic perovskite phase the rhombohedral unit cell is described by a volume change Q^Γ_1 and three equal shear strains $Q^\Gamma_{4x} = Q^\Gamma_{4y} = Q^\Gamma_{4z}$.

Table C.1 shows those structural values as well as the stabilization energy ΔE over the cubic $Pm\bar{3}m$ reference and the spontaneous polarization P_S of the $R3c$ phase as relaxed from ab initio calculations (DFT) and from the SP lattice model (E_{eff}). Comparing the $R3c$ phase to the $Pnma$ ground state shows on the one hand significantly smaller normal strains of the $R3c$ phase and on the other hand a larger amplitude of the anti-phase rotational mode. The polar mode amplitude is in the same order of magnitude as the anti-phase rotational mode. Consequently, the spontaneous polarization calculated by the berry phase approach is with $P_S \approx 52\left(\frac{\mu C}{cm^2}\right)$ larger than the one of the prototypical ferroelectric

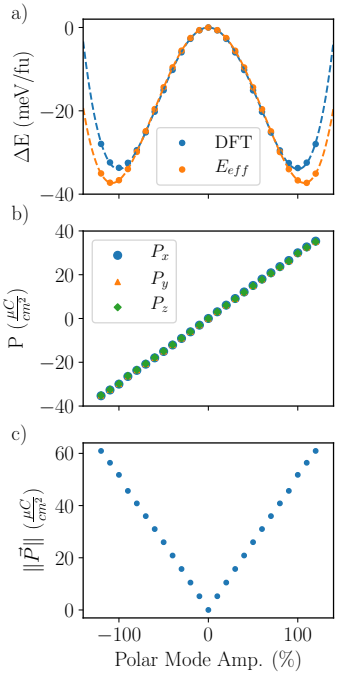

Figure C.1: a) PES of the polar mode p_{xyz} from -120% to 120% of its ground state amplitude calculated from ab initio (DFT) and the SP lattice model (E_{eff}) in steps of 10% . b) Components of the spontaneous polarization P_x, P_y,P_z and c) absolute spontaneous polarization calculated with the berry phase method. a),b), and c) share the same abscissa.

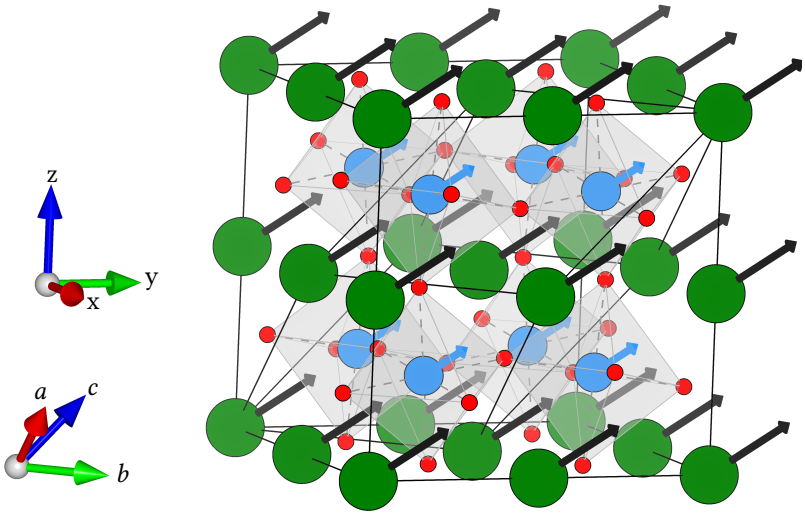

Figure C.2: Illustration of the polar displacements in the $R3c$ phase of $CaTiO_3$ depicted in a $2 \times 2 \times 2$ supercell of the 5 atoms perovskite structure. Ca and Ti displace along the [111] direction of the cubic (xyz) coordinate system illustrated by black respectively light blue arrows. The Ca displacement is approximately two and half times larger than the Ti displacement. Arrows are exaggerated for clarity. Additionally, the orientation of the rhombohedral unit-cell of the $R3c$ phase characterized by one lattice parameter a_r and one angle α within the $2 \times 2 \times 2$ supercell is shown.

Table C.1: Rhombohedral lattice constant a_r, lattice angle (α), normal lattice strains (in CJTD notation) and symmetry adapted mode distortions (symbols of irreducible subspaces in square brackets), and stabilization energy ΔE with respect to the cubic $Pm\bar{3}m$ of the $R3c$ phase of $CaTiO_3$ calculated by a relaxation of the second-principles lattice model (E_{eff}), and by a relaxation using ab initio calculations (DFT). Mode and Strain amplitudes have been evaluated using ISODISTORT [128] with respect to a cubic 5-atoms $Pm\bar{3}m$ perovskite structure with a cubic lattice constant of $a = 3.827$Å.

	a_r (Å)	α (°)	Q_1^{Γ} $[\Gamma_1^+(a)]$	$Q_{4x,y,z}^{\Gamma}$ $[\Gamma_4^+(a,a,a)]$	ϕ_{xyz}^-(Å) $[\ R_5^-(a,a,a)\ ]$	p_{xyz} (Å) $[\ \Gamma_4^-(a,a,a)]$	ΔE (eV/fu)	P_S $\left(\frac{\mu C}{cm^2}\right)$
E_{eff}	5.433	59.513	0.0004	0.009	0.712	0.608	-0.369	61.58
DFT	5.422	59.677	-0.002	0.006	0.675	0.548	-0.320	51.77

$BaTiO_3$ [223]. The SP lattice model reproduces well the relaxed ab initio $R3c$ phase. However, the anti-phase rotation mode amplitude, the polar mode amplitude and the stabilization energy are overestimated. We recalculated the spontaneous polarization of the $R3c$ phase provided by the SP lattice model by multiplying the displacements of the atoms with their Born-Effective Charge tensor calculated in the cubic phase *. In consequence the spontaneous polarization is overestimated by almost 19%, but gives the right order of magnitude.

Fig. C.1 shows the PES and the polarization in dependency of the polar mode amplitude between -120% and 120% of its ground state amplitude in the $R3c$ phase. We calculated the PES from ab initio (DFT) and from the SP lattice model. To compare the PESs we defined the non-polar structure with $R\bar{3}c$ symmetry as the zero energy reference. The reproduction of the ab initio data by the SP lattice model is excellent, especially the stabilization energy is only slightly overestimated. Hence, we can conclude that the greatest part of the overestimation of the stabilization energy of the $R3c$ phase over the cubic reference by the SP lattice model stems from the overestimation of the stabilization energy of the anti-phase rotations. Moreover, the polar mode PES shows that it is a *proper* ferroelectric instability that produces the spontaneous polarization. With $\approx$ 34meV/fu the stabilization energy of the polar mode lies in proximity of the one of $BaTiO_3$ [224]. Thus we can hope that the polarization in the $R3c$ phase is switchable and the transition temperature to a paraelectric phase is considerably high, in the best case above room temperature.

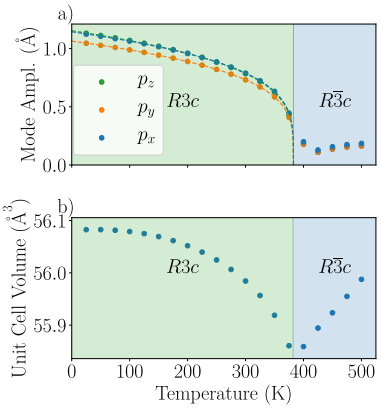

Figure C.3: a) Polar mode amplitude upon a heating simulation of $CaTiO_3$ starting from the relaxed $R3c$ phase in a 10×10×10 supercell. Dashed lines represent fits of the form $p = K \cdot (T_C - T)^c$ b) Pseudocubic unit cell volume resulting the same simulation.

To get an estimate of the transition temperature of a hypothetical homogeneous $R3c$ phase we executed a virtual heating experiment between 25K and 500K using the HMC method in a $10 \times 10 \times 10$ unit cell starting from the relaxed $R3c$ phase at low temperature. Fig. C.3 shows the projection onto the three polar modes p_x, p_y, and p_z and b) the unit cell volume per formula unit upon heating. The ferroelectric to paraelectric transition appears at 382K and is of first-order. Interestingly it is accompanied by a negative thermal expansion. The origin of this negative thermal expansion should lie in a cooperative coupling between the polar distortion and lattice strains as it is typical for perovskite ferroelectrics. As the average polar mode amplitude upon heating decreases the unit cell volume decreases as this coupling seems to overcome the positive thermal expansion originating from populating stable phonons. Inversely this result shows that increasing the unit cell volume will favor the polar

* Using this approach with th $R3c$ phase as relaxed from ab initio calculations delivers $P_S = 52.79 \frac{\mu C}{cm^2}$.

instability.

As the simulated transition temperature is above room temperature we could hope for a strong room temperature ferroelectric, if there is a way to stabilize the $a^-a^-a^-$ rotation pattern over the $a^-a^-c^+$ rotation pattern. However, we note that transition temperatures calculated with effective models come typically with significant uncertainties and can differ a few hundred K from experimentally values.

From a physical and technological perspective it would be highly desirable to find a way to stabilize this $R3c$ phase. From our results we can anticipate that the crucial factor for destabilizing the polar mode is imposing the $a^-a^-a^-$ rotation pattern to $CaTiO_3$, which seems to have been realized before[1]. Unfortunately, perovskites like $CaTiO_3$ with formal charges of 2+ on the A site and 4+ on the B site and Goldschmidt tolerance factors smaller than 1 are known to prefer $a^-a^-c^+$ over the $a^-a^-a^-$ rotation pattern [225] without exception [226]. A popular way of engineering rotation angles and properties of perovskites materials is strain engineering [227]. However, in numerous theoretical and experimental studies of $CaTiO_3$ thin films constrained by [001] surfaces of perovskite substrate the rotation pattern seemed to never have changed to $a^-a^-a^-$ from $a^-a^-c^+$.

1: See remark 32 in Ref. [203]

A different approach that has been explored, is to grow $CaTiO_3$ on the [111] surface of $LaAlO_3$, which has $R\bar{3}c$ symmetry wit ht a $a^-a^-a^-$ rotation pattern [228]. This follows the idea of a recent thin film study of $NdNiO_3$ in a different context that suggested that the rotation pattern of a substrate can be transferred more efficiently to the thin film if the film is grown on the [111] surface of the substrate due to the higher connectivity of the oxygen octahedra between substrate and thin film in the [111] configuration [229].

However, in the experimental study by *Wan* [228] the $CaTiO_3$ turned out to be not ferroelectric and the idea seems to have been dropped afterwards. The SP lattice model of $CaTiO_3$ seems to be predestinated to retake this work as not only strain constraints but also rotational interfaces can be constructed in considerably large unit cells. Preliminary calculations that couldn't be finished before the end of the manuscript confirmed that on the [111] surface of $LaAlO_3$ the $Pnma$ phase of $CaTiO_3$ should be the most stable one. The rule of *Woodward* [225] that perovskite with formal charges of 2+ on the A site and 4+ on the B site do not show $R\bar{3}c$ like phases seems thus fulfilled even under the constrained. The stabilization of the $Pnma$ phase over $R\bar{3}c$ under the constrained is linked to the fact that ferroelastic domain walls at which the rotation pattern changes from $a^-a^-a^-$ to $a^-a^-c^+$ are energetically quite cheap. Nonetheless, the SP lattice model will allow for further explorations e.g. if in a ultra thin film limit the ferroelastic domain wall energy will become to large per formula unit to stabilize the $Pnma$ phase over $R3c$ or imposing different constrains like a [11-2] surface of an $a^-a^-a^-$ rotation pattern to which the polarization in the [111] direction of the $R3c$ phase would be completely orthogonal and the depolarizing field energy could be minimized. Moreover, we remark that in the experimental study by *Wan* [228] et al $CaVO_3$ was used as the back electrode between the $LaAlO_3$ substrate and the $CaTiO_3$ thin film. $CaVO_3$ has itself a $Pnma$ ground state. Therefore, it might be possible that the $CaTiO_3$ film has actually been

grown on the [111] surface of a $Pnma$ material. An interesting alternative back electrode would be $LaNiO_3$ whose ground state is a metallic $R\bar{3}c$ phase.

Bibliography

[1] Felix Bloch. 'Über die Quantenmechanik der Elektronen in Kristallgittern'. In: *Zeitschrift für Physik* 52.7 (July 1929), pp. 555–600 (cited on pages 2, 14).

[2] V. M. Goldschmidt. 'Die Gesetze der Krystallochemie'. In: *Naturwissenschaften* 14.21 (1926), pp. 477–485. DOI: 10.1007/BF01507527 (cited on pages 3, 61, 101).

[3] A. M. Glazer. 'The classification of tilted octahedra in perovskites'. In: *Acta Crystallogr. Sect. B Struct. Crystallogr. Cryst. Chem.* 28.11 (Nov. 1972), pp. 3384–3392. DOI: 10.1107/s0567740872007976 (cited on pages 4, 55, 61, 64, 93, 101).

[4] Michael W. Lufaso and Patrick M. Woodward. 'Prediction of the crystal structures of perovskites using the software program SPuDS'. In: *Acta Crystallogr. Sect. B Struct. Sci.* 57.6 (2001), pp. 725–738. DOI: 10.1107/S0108768101015282 (cited on pages 4, 61, 101).

[5] B. Ravel et al. 'Local structure and the phase transitions of BaTiO3'. In: *Ferroelectrics* 206.1 (1998), pp. 407–430. DOI: 10.1080/00150199808009173 (cited on page 5).

[6] Kousuke Nishimura et al. 'High-pressure synthesis of BaVO3: A new cubic perovskite'. In: *Journal of Physics and Chemistry of Solids* 75.6 (2014), pp. 710–712. DOI: https://doi.org/10.1016/j.jpcs.2014.02.001 (cited on page 5).

[7] Naoaki Hayashi et al. 'BaFeO3: A ferromagnetic iron oxide'. In: *Angew. Chemie - Int. Ed.* 50.52 (2011), pp. 12547–12550. DOI: 10.1002/anie.201105276 (cited on pages 5, 93, 96).

[8] M. Born and R. Oppenheimer. 'Zur Quantentheorie der Molekeln'. In: *Ann. Phys.* 389.20 (1927), pp. 457–484. DOI: 10.1002/andp.19273892002 (cited on page 11).

[9] P. Hohenberg and W. Kohn. 'Inhomogeneous electron gas'. In: *Phys. Rev.* 136.3B (Nov. 1964), B864–B871. DOI: 10.1103/PhysRev.136.B864 (cited on page 12).

[10] W. Kohn and L. J. Sham. 'Self-consistent equations including exchange and correlation effects'. In: *Phys. Rev.* 140.4A (Nov. 1965), A1133–A1138. DOI: 10.1103/PhysRev.140.A1133 (cited on page 12).

[11] S. H. Vosko, L. Wilk, and M. Nusair. 'Accurate spin-dependent electron liquid correlation energies for local spin density calculations: a critical analysis'. In: *Canadian Journal of Physics* 58.8 (1980), pp. 1200–1211. DOI: 10.1139/p80-159 (cited on page 13).

[12] J. P. Perdew and Alex Zunger. 'Self-interaction correction to density-functional approximations for many-electron systems'. In: *Phys. Rev. B* 23 (10 May 1981), pp. 5048–5079. DOI: 10.1103/PhysRevB.23.5048 (cited on page 13).

[13] D. M. Ceperley and B. J. Alder. 'Ground State of the Electron Gas by a Stochastic Method'. In: *Phys. Rev. Lett.* 45 (7 Aug. 1980), pp. 566–569. DOI: 10.1103/PhysRevLett.45.566 (cited on page 13).

[14] D. R. Hamann, M. Schlüter, and C. Chiang. 'Norm-Conserving Pseudopotentials'. In: *Phys. Rev. Lett.* 43 (20 Nov. 1979), pp. 1494–1497. DOI: 10.1103/PhysRevLett.43.1494 (cited on pages 14, 103).

[15] P. E. Blöchl. 'Projector augmented-wave method'. In: *Phys. Rev. B* 50.24 (1994), pp. 17953–17979. DOI: 10.1103/PhysRevB.50.17953 (cited on pages 14, 63, 94).

[16] Fabien Tran et al. 'Hybrid exchange-correlation energy functionals for strongly correlated electrons: Applications to transition-metal monoxides'. In: *Phys. Rev. B* 74 (15 Oct. 2006), p. 155108. DOI: 10.1103/PhysRevB.74.155108 (cited on page 15).

[17] V. I. Anisimov et al. 'Density-functional theory and NiO photoemission spectra'. In: *Phys. Rev. B* 48 (23 Dec. 1993), pp. 16929–16934. DOI: 10.1103/PhysRevB.48.16929 (cited on page 15).

[18] A. I. Liechtenstein, V. I. Anisimov, and J. Zaanen. 'Density-functional theory and strong interactions: Orbital ordering in Mott-Hubbard insulators'. In: *Phys. Rev. B* 52.8 (Aug. 1995), R5467–R5470. DOI: 10.1103/PhysRevB.52.R5467 (cited on page 15).

[19] Vladimir I. Anisimov, F. Aryasetiawan, and A. I. Lichtenstein. 'First-principles calculations of the electronic structure and spectra of strongly correlated systems: The LDA + U method'. In: *J. Phys. Condens. Matter* 9.4 (1997), pp. 767–808. DOI: 10.1088/0953-8984/9/4/002 (cited on pages 15, 94).

[20] S. L. Dudarev et al. 'Electron-energy-loss spectra and the structural stability of nickel oxide: An LSDA+U study'. In: *Phys. Rev. B* 57 (3 Jan. 1998), pp. 1505–1509. DOI: 10.1103/PhysRevB.57.1505 (cited on page 15).

[21] Matteo Cococcioni. 'The LDA+ U approach: a simple Hubbard correction for correlated ground states'. In: *Correlated Electrons: From Models to Materials Modeling and Simulation; Verlag des Forschungszentrum Jülich: Jülich, Germany* (2012) (cited on page 15).

[22] Bernard Amadon, Thomas Applencourt, and Fabien Bruneval. 'Screened Coulomb interaction calculations: cRPA implementation and applications to dynamical screening and self-consistency in uranium dioxide and cerium'. In: *Phys. Rev. B* 89 (12 Mar. 2014), p. 125110. DOI: 10.1103/PhysRevB.89.125110 (cited on page 15).

[23] X. Gonze and J.-P. Vigneron. 'Density-functional approach to nonlinear-response coefficients of solids'. In: *Phys. Rev. B* 39 (18 June 1989), pp. 13120–13128. DOI: 10.1103/PhysRevB.39.13120 (cited on page 16).

[24] Xavier Gonze. 'Perturbation expansion of variational principles at arbitrary order'. In: *Phys. Rev. A* 52 (2 Aug. 1995), pp. 1086–1095. DOI: 10.1103/PhysRevA.52.1086 (cited on page 16).

[25] Xavier Gonze. 'Adiabatic density-functional perturbation theory'. In: *Phys. Rev. A* 52 (2 Aug. 1995), pp. 1096–1114. DOI: 10.1103/PhysRevA.52.1096 (cited on page 16).

[26] Xavier Gonze and Changyol Lee. 'Dynamical matrices, Born effective charges, dielectric permittivity tensors, and interatomic force constants from density-functional perturbation theory'. In: *Phys. Rev. B - Condens. Matter Mater. Phys.* 55.16 (Apr. 1997), pp. 10355–10368. DOI: 10.1103/PhysRevB.55.10355 (cited on pages 16, 22).

[27] Marek Veithen, Xavier Gonze, and Philippe Ghosez. 'First-principles study of the electro-optic effect in ferroelectric oxides'. In: *Phys. Rev. Lett.* 93.18 (2004), p. 187401. DOI: 10.1103/PhysRevLett.93.187401 (cited on page 16).

[28] Richard Van Noorden, Brendan Maher, and Regina Nuzzo. 'The top 100 papers'. In: *Nature* 514.7524 (2014), pp. 550–553. DOI: 10.1038/514550a (cited on page 17).

[29] Anubhav Jain et al. 'Commentary: The materials project: A materials genome approach to accelerating materials innovation'. In: *APL Mater.* 1.1 (2013), p. 11002. DOI: 10.1063/1.4812323 (cited on page 17).

[30] Lin Lin et al. 'SIESTA-PEXSI: Massively parallel method for efficient and accurate ab initio materials simulation without matrix diagonalization'. In: *J. Phys. Condens. Matter* 26.30 (2014), p. 305503. DOI: 10.1088/0953-8984/26/30/305503 (cited on page 17).

[31] A. Erba et al. 'Large-Scale Condensed Matter DFT Simulations: Performance and Capabilities of the CRYSTAL Code'. In: *J. Chem. Theory Comput.* 13.10 (2017), pp. 5019–5027. DOI: 10.1021/acs.jctc.7b00687 (cited on page 17).

[32] Charles Kittel. *Introduction to solid state physics*. eng. 8th ed. Hoboken, NJ: Wiley (cited on page 17).

[33] Michael F. Russo and Adri C.T. van Duin. 'Atomistic-scale simulations of chemical reactions: Bridging from quantum chemistry to engineering'. In: *Nuclear Instruments and Methods in Physics Research Section B: Beam Interactions with Materials and Atoms* 269.14 (2011). Computer Simulations of Radiation Effects in Solids, pp. 1549–1554. DOI: https://doi.org/10.1016/j.nimb.2010.12.053 (cited on page 17).

[34] Thomas P. Senftle et al. 'The ReaxFF reactive force-field: development, applications and future directions'. In: *npj Computational Materials* 2.1 (Mar. 2016), p. 15011 (cited on pages 17, 18).

[35] Young-Han Shin et al. 'Development of a bond-valence molecular-dynamics model for complex oxides'. In: *Phys. Rev. B* 71 (5 Feb. 2005), p. 054104. DOI: 10.1103/PhysRevB.71.054104 (cited on page 17).

[36] Ian David Brown. 'Recent Developments in the Methods and Applications of the Bond Valence Model'. In: *Chem. Rev.* 109.12 (Dec. 2009), pp. 6858–6919. DOI: 10.1021/cr900053k (cited on page 17).

[37] P J D Lindan and M J Gillan. 'Shell-model molecular dynamics simulation of superionic conduction in CaF2'. In: *Journal of Physics: Condensed Matter* 5.8 (Feb. 1993), pp. 1019–1030. DOI: 10.1088/0953-8984/5/8/005 (cited on page 17).

[38] M. Sepliarsky et al. 'Atomic-level simulation of ferroelectricity in oxide materials'. In: *Current Opinion in Solid State and Materials Science* 9.3 (2005), pp. 107–113. DOI: https://doi.org/10.1016/j.cossms.2006.05.002 (cited on page 17).

[39] K. M. Rabe and U. V. Waghmare. 'Localized basis for effective lattice Hamiltonians: Lattice Wannier functions'. In: *Phys. Rev. B* 52 (18 Nov. 1995), pp. 13236–13246. DOI: 10.1103/PhysRevB.52.13236 (cited on page 18).

[40] W. Zhong and David Vanderbilt. 'Effect of quantum fluctuations on structural phase transitions in $SrTiO_3$ and $BaTiO_3$'. In: *Phys. Rev. B* 53 (9 Mar. 1996), pp. 5047–5050. DOI: 10.1103/PhysRevB.53.5047 (cited on page 18).

[41] Ph. Ghosez and K. M. Rabe. 'Microscopic model of ferroelectricity in stress-free PbTiO3 ultrathin films'. In: *Applied Physics Letters* 76.19 (2000), pp. 2767–2769. DOI: 10.1063/1.126469 (cited on page 18).

[42] Silvia Tinte et al. 'Quantitative analysis of the first-principles effective Hamiltonian approach to ferroelectric perovskites'. In: *Phys. Rev. B* 67 (6 Feb. 2003), p. 064106. DOI: 10.1103/PhysRevB.67.064106 (cited on page 18).

[43] Igor A. Kornev et al. 'Finite-Temperature Properties of Multiferroic $BiFeO_3$'. In: *Phys. Rev. Lett.* 99 (22 Nov. 2007), p. 227602. DOI: 10.1103/PhysRevLett.99.227602 (cited on page 18).

[44] Jacek C. Wojdeł et al. 'First-principles model potentials for lattice-dynamical studies: General methodology and example of application to ferroic perovskite oxides'. In: *J. Phys. Condens. Matter* 25.30 (2013), p. 305401. DOI: 10.1088/0953-8984/25/30/305401 (cited on pages 18, 27, 33, 80).

[45] Carlos Escorihuela-Sayalero, Jacek C. Wojdeł, and Jorge Íñiguez. 'Efficient systematic scheme to construct second-principles lattice dynamical models'. In: *Phys. Rev. B* 95.9 (2017), p. 94115. DOI: 10.1103/PhysRevB.95.094115 (cited on pages 18, 32, 33, 80, 104, 106, 117).

[46] Pablo García-Fernández et al. 'Second-principles method for materials simulations including electron and lattice degrees of freedom'. In: *Phys. Rev. B* 93.19 (2016), p. 195137. DOI: 10.1103/PhysRevB.93.195137 (cited on pages 18, 36, 37, 80).

[47] Xavier Gonze et al. 'The Abinitproject: Impact, environment and recent developments'. In: *Computer Physics Communications* 248 (2020), p. 107042. DOI: https://doi.org/10.1016/j.cpc.2019.107042 (cited on pages 19, 103).

[48] IE Dzialoshinskii. 'Thermodynamic theory of weak ferromagnetism in antiferromagnetic substances'. In: *Soviet Physics Jetp-Ussr* 5.6 (1957), pp. 1259–1272 (cited on page 19).

[49] Sergei Prokhorenko et al. 'Large scale hybrid Monte Carlo simulations for structure and property prediction'. In: *npj Computational Materials* 4.1 (Dec. 2018), p. 80 (cited on pages 20, 103).

[50] Glenn J. Martyna, Michael L. Klein, and Mark Tuckerman. 'Nosé–Hoover chains: The canonical ensemble via continuous dynamics'. In: *The Journal of Chemical Physics* 97.4 (1992), pp. 2635–2643. DOI: 10.1063/1.463940 (cited on pages 20, 103, 104).

[51] URL: https://github.com/abinit/abiout, https://github.com/abinit/qAgate (cited on pages 20, 111, 112).

[52] Daniel Sheppard et al. 'A generalized solid-state nudged elastic band method'. In: *The Journal of Chemical Physics* 136.7 (2012), p. 074103. DOI: 10.1063/1.3684549 (cited on page 32).

[53] Philip B Stark and Robert L Parker. 'Bounded-variable least-squares: an algorithm and applications'. In: *Computational Statistics* 10 (1995), pp. 129–129 (cited on page 35).

[54] J Hubbard and Flowers Brian Hilton. 'Electron correlations in narrow energy bands'. In: *Proc. R. Soc. London. Ser. A. Math. Phys. Sci.* 276.1365 (1963), pp. 238–257. DOI: 10.1098/rspa.1963.0204 (cited on pages 37, 62).

[55] H A Jahn and E Teller. 'Stability of polyatomic molecules in degenerate electronic states - I—Orbital degeneracy'. In: *Proc. R. Soc. London. Ser. A - Math. Phys. Sci.* 161.905 (1937), pp. 220–235. DOI: 10.1098/rspa.1937.0142 (cited on pages 43, 45, 62).

[56] Robert Englman. *The Jahn-Teller effect in molecules and crystals*. John Wiley & Sons, 1972 (cited on pages 43, 62).

[57] Kugel' KI and D Khomskii. 'The jahn-teller effect and magnetism: transition metal compounds'. In: *Sov. Phys. Usp* 25 (1982), p. 231. DOI: 10.1070/PU1982v025n04ABEH004537 (cited on pages 43, 57, 62, 68).

[58] Eva Pavarini. 'Crystal-field theory, tight-binding method and jahn-teller effect'. In: *Correlated electrons: from models to materials* 2 (2012), pp. 6–2 (cited on pages 46, 48, 49).

[59] Martin Breza. 'Group-Theoretical Analysis of Jahn–Teller Systems'. In: *The Jahn-Teller Effect*. Springer, 2009, pp. 51–76 (cited on page 46).

[60] J. H. Van Vleck. 'The John-Teller effect and crystalline stark splitting for clusters of the form XY6'. In: *J. Chem. Phys.* 7.1 (1939), pp. 72–84. DOI: 10.1063/1.1750327 (cited on pages 46, 49).

[61] J. C. Slater and G. F. Koster. 'Simplified LCAO method for the periodic potential problem'. In: *Phys. Rev.* 94.6 (1954), pp. 1498–1524. DOI: 10.1103/PhysRev.94.1498 (cited on page 48).

[62] Isaac Bersuker. *The Jahn-Teller Effect*. Cambridge University Press, 2006 (cited on pages 49, 56–58).

[63] U Öpik and M H L Pryce. 'Studies of the Jahn-Teller effect. I. A survey of the static problem'. In: *Proc. R. Soc. London. Ser. A. Math. Phys. Sci.* Vol. 238. 1215. The Royal Society, 1957, pp. 425–447. DOI: 10.1098/rspa.1957.0010 (cited on page 49).

[64] Isaac B Bersuker and Victor Z Polinger. *Vibronic interactions in molecules and crystals*. Vol. 49. Springer Science & Business Media, 2012 (cited on pages 49, 56–58, 71).

[65] Boris Tsukerblat, Sophia Klokishner, and Andrew Palii. *Jahn-Teller effect in molecular magnetism: An overview*. Ed. by Horst Köppel, David R Yarkony, and Heinz Barentzen. Vol. 97. Springer Science & Business Media, 2010, pp. 555–619 (cited on page 49).

[66] Mary C. M. O'Brien and C. C. Chancey. 'The Jahn–Teller effect: An introduction and current review'. In: *Am. J. Phys.* 61.8 (1993), pp. 688–697. DOI: 10.1119/1.17197 (cited on page 49).

[67] Junjiro Kanamori. 'Crystal distortion in magnetic compounds'. In: *J. Appl. Phys.* 31.5 (1960), S14–S23. DOI: 10.1063/1.1984590 (cited on pages 49, 52, 56).

[68] John B. Goodenough. *Magnetism and the chemical bond*. eng. Interscience monographs on chemistry. Inorganic chemistry section, 1. New York, NY: Interscience, 1963 (cited on page 51).

[69] Serena Margadonna and Georgios Karotsis. 'Cooperative Jahn-Teller distortion, phase transitions, and weak ferromagnetism in the KCrF3 perovskite'. In: *J. Am. Chem. Soc.* 128.51 (2006), pp. 16436–16437. DOI: 10.1021/ja0669272 (cited on pages 51, 55).

[70] Michael W. Lufaso and Patrick M. Woodward. 'Jahn-Teller distortions, cation ordering and octahedral tilting in perovskites'. In: *Acta Crystallogr. Sect. B Struct. Sci.* 60.1 (Feb. 2004), pp. 10–20. DOI: 10.1107/S0108768103026661 (cited on page 51).

[71] A. C. Komarek et al. 'Magnetoelastic coupling in RTi O3 (R=La,Nd,Sm,Gd,Y) investigated with diffraction techniques and thermal expansion measurements'. In: *Phys. Rev. B - Condens. Matter Mater. Phys.* 75.22 (June 2007), p. 224402. DOI: 10.1103/PhysRevB.75.224402 (cited on page 51).

[72] Julien Varignon et al. 'Origin of the orbital and spin ordering in rare-earth titanates'. In: *Phys. Rev. B* 96.23 (2017), p. 235106. DOI: 10.1103/PhysRevB.96.235106 (cited on page 51).

[73] Michael A Carpenter and Christopher J Howard. 'Symmetry rules and strain/order-parameter relationships for coupling between octahedral tilting and cooperative Jahn-Teller transitions in ABX_3 perovskites. I. Theory'. In: *Acta Crystallogr. B.* 65.2 (Apr. 2009), pp. 147–159. DOI: 10.1107/S0108768109000974 (cited on pages 51, 77).

[74] M. Bacci, E. Mihókováand, and K. Polák. 'Coexistence of Jahn-Teller distortions in an symmetry:A general view including the spin-orbit interaction'. In: *Phys. Rev. B - Condens. Matter Mater. Phys.* 55.21 (June 1997), pp. 14257–14264. DOI: 10.1103/PhysRevB.55.14257 (cited on page 52).

[75] Michael A. Carpenter and Christopher J. Howard. 'Symmetry rules and strain/order-parameter relationships for coupling between octahedral tilting and cooperative Jahn–Teller transitions in ABX_3perovskites. I. Theory'. In: *Acta Crystallogr. B.* 65.2 (Apr. 2009), pp. 134–146. DOI: 10.1107/S0108768109000974 (cited on pages 52, 99).

[76] Zhuoran He and Andrew J. Millis. 'Strain control of electronic phase in rare-earth nickelates'. In: *Phys. Rev. B - Condens. Matter Mater. Phys.* 91.19 (2015), p. 195138. DOI: 10.1103/PhysRevB.91.195138 (cited on page 52).

[77] Alain Mercy et al. 'Structurally triggered metal-insulator transition in rare-earth nickelates'. In: *Nat. Commun.* 8.1 (2017), pp. 1677–. DOI: 10.1038/s41467-017-01811-x (cited on pages 53, 63, 80, 86, 93, 95).

[78] Prasanna V. Balachandran and James M. Rondinelli. 'Interplay of octahedral rotations and breathing distortions in charge-ordering perovskite oxides'. In: *Phys. Rev. B - Condens. Matter Mater. Phys.* 88.5 (Aug. 2013), p. 54101. DOI: 10.1103/PhysRevB.88.054101 (cited on page 53).

[79] Se Young Park, Anil Kumar, and Karin M. Rabe. 'Charge-Order-Induced Ferroelectricity in LaVO3/SrVO3 Superlattices'. In: *Phys. Rev. Lett.* 118.8 (Feb. 2017), p. 87602. DOI: 10.1103/PhysRevLett.118.087602 (cited on page 53).

[80] Atsushi Okazaki and Yasutaka Suemune. 'The Crystal Structure of KCuF3'. In: *J. Phys. Soc. Japan* 16.2 (1961), pp. 176–183. DOI: 10.1143/JPSJ.16.176 (cited on page 55).

[81] L. Paolasini et al. 'Coupling between Spin and Orbital Degrees of Freedom in $KCuF_3$'. In: *Phys. Rev. Lett.* 88 (10 Feb. 2002), p. 106403. DOI: 10.1103/PhysRevLett.88.106403 (cited on page 55).

[82] Peter M.M. Thygesen et al. 'Local structure study of the orbital order/disorder transition in LaMnO3'. In: *Phys. Rev. B* 95.17 (2017), p. 174107. DOI: 10.1103/PhysRevB.95.174107 (cited on pages 55, 62, 76, 77).

[83] Michael Kaplan. 'Cooperative Jahn–Teller Effect: Fundamentals, Applications, Prospects'. In: *The Jahn-Teller Effect*. Springer, 2009, pp. 653–683 (cited on pages 56, 57).

[84] R. Englman and B. Halperin. 'Cooperative dynamic Jahn-Teller effect. I. Molecular field treatment of spinels'. In: *Phys. Rev. B* 2.1 (1970), pp. 75–94. DOI: 10.1103/PhysRevB.2.75 (cited on pages 56, 62).

[85] Victor Polinger. 'Orbital Ordering Versus the Traditional Approach in the Cooperative Jahn–Teller Effect: A Comparative Study'. In: *The Jahn-Teller Effect*. Springer, 2009, pp. 685–725 (cited on page 57).

[86] Kliment Kugel and D. Khomskii. 'Crystal structure and magnetic properties of substances with orbital degeneracy'. In: *Journal of Experimental and Theoretical Physics - J EXP THEOR PHYS* 37 (Jan. 1973) (cited on page 57).

[87] Eva Pavarini and Erik Koch. 'Origin of Jahn-Teller Distortion and Orbital Order in $LaMnO_3$'. In: *Phys. Rev. Lett.* 104.8 (Feb. 2010), p. 86402. DOI: 10.1103/PhysRevLett.104.086402 (cited on pages 57, 62, 80).

[88] E. Pavarini, E. Koch, and A. I. Lichtenstein. 'Mechanism for orbital ordering in KCuF3'. In: *Phys. Rev. Lett.* 101.26 (2008), p. 266405. DOI: 10.1103/PhysRevLett.101.266405 (cited on pages 57, 80).

[89] Julien Varignon, Manuel Bibes, and Alex Zunger. 'Origins versus fingerprints of the Jahn-Teller effect in d-electron ABX_3 perovskites'. In: *Phys. Rev. Research* 1 (3 Nov. 2019), p. 033131. DOI: 10.1103/PhysRevResearch.1.033131 (cited on pages 57, 62, 69, 119).

[90] Rudolf Peierls and A. O. Barut. *More Surprises in Theoretical Physics*. Vol. 60. 10. Princeton University Press, 1992, pp. 957–958 (cited on pages 57, 62).

[91] Roald Hoffmann. 'How Chemistry and Physics Meet in the Solid State'. In: *Angew. Chemie Int. Ed. English* 26.9 (1987), pp. 846–878. DOI: 10.1002/anie.198708461 (cited on page 58).

[92] Masatoshi Imada. 'Tokura_RevModPhys_98.pdf'. In: *Rev. Mod. Phys.* 70.4 (1998), pp. 1039–1263. DOI: 10.1103/RevModPhys.70.1039 (cited on pages 58, 93).

[93] M. D. Johannes, I. I. Mazin, and C. A. Howells. 'Fermi-surface nesting and the origin of the charge-density wave in Nb Se2'. In: *Phys. Rev. B - Condens. Matter Mater. Phys.* 73.20 (2006), p. 205102. DOI: 10.1103/PhysRevB.73.205102 (cited on page 58).

[94] J. C. Slater. 'Magnetic Effects and the Hartree-Fock Equation'. In: *Phys. Rev.* 82 (4 May 1951), pp. 538–541. DOI: 10.1103/PhysRev.82.538 (cited on page 58).

[95] S V Streltsov and D I Khomskii. 'Orbital physics in transition metal compounds: new trends'. In: *Physics-Uspekhi* 60.11 (2017), pp. 1121–1146. DOI: 10.3367/ufne.2017.08.038196 (cited on pages 58, 71).

[96] Victor Polinger. 'The band Jahn-Teller effect: A new perspective on an old problem'. In: *J. Mol. Struct.* 838.1-3 (2007), pp. 13–19. DOI: 10.1016/j.molstruc.2007.01.033 (cited on pages 58, 71).

[97] R. Von Helmolt et al. 'Giant negative magnetoresistance in perovskitelike La2/3Ba1/3MnOx ferromagnetic films'. In: *Phys. Rev. Lett.* 71.14 (1993), pp. 2331–2333. DOI: 10.1103/PhysRevLett.71.2331 (cited on page 61).

[98] P. Norby et al. 'The crystal structure of lanthanum manganate(iii), LaMnO3, at room temperature and at 1273 K under N2'. In: *J. Solid State Chem.* 119.1 (1995), pp. 191–196. DOI: 10.1016/0022-4596(95)80028-N (cited on page 61).

[99] Xiangyun Qiu et al. 'Orbital correlations in the pseudocubic O and rhombohedral R phases of LaMnO3'. In: *Phys. Rev. Lett.* 94.17 (2005), p. 177203. DOI: 10.1103/PhysRevLett.94.177203 (cited on pages 61, 62).

[100] M. Baldini et al. 'Persistence of Jahn-Teller distortion up to the insulator to metal transition in LaMnO3'. In: *Phys. Rev. Lett.* 106.6 (Feb. 2011), p. 66402. DOI: 10.1103/PhysRevLett.106.066402 (cited on pages 61, 62).

[101] Tapan Chatterji et al. 'Volume collapse in LaMnO3 caused by an orbital order-disorder transition'. In: *Phys. Rev. B - Condens. Matter Mater. Phys.* 68.5 (Aug. 2003), p. 52406. DOI: 10.1103/PhysRevB.68.052406 (cited on pages 61, 77).

[102] T. Maitra, P. Thalmeier, and T. Chatterji. 'Volume collapse in LaMnO3 at the Jahn-Teller transition temperature'. In: *Phys. Rev. B - Condens. Matter Mater. Phys.* 69.13 (Apr. 2004), p. 132417. DOI: 10.1103/PhysRevB.69.132417 (cited on pages 61, 77).

[103] Mahrous R. Ahmed and G. A. Gehring. 'Volume collapse in LaMnO3 studied using an anisotropic Potts model'. In: *Phys. Rev. B - Condens. Matter Mater. Phys.* 79.17 (2009), p. 174106. DOI: 10.1103/PhysRevB.79.174106 (cited on pages 61, 77).

[104] J. Rodríguez-Carvajal et al. 'Neutron-diffraction study of the Jahn-Teller transition in stoichiometric'. In: *Phys. Rev. B - Condens. Matter Mater. Phys.* 57.6 (Feb. 1998), R3189–R3192. DOI: 10.1103/PhysRevB.57.R3189 (cited on page 61).

[105] M. C. Sánchez et al. 'Cooperative Jahn-Teller Phase Transition in [Formula presented] Studied by X-Ray Absorption Spectroscopy'. In: *Phys. Rev. Lett.* 90.4 (Jan. 2003), p. 4. DOI: 10.1103/PhysRevLett.90.045503 (cited on pages 61, 62, 93).

[106] F. Moussa et al. 'Spin waves in the antiferromagnet perovskite LaM: A neutron-scattering study'. In: *Phys. Rev. B - Condens. Matter Mater. Phys.* 54.21 (1996), pp. 15149–15155. DOI: 10.1103/PhysRevB.54.15149 (cited on pages 62, 65–67).

[107] N. N. Kovaleva et al. 'Spin-controlled mott-hubbard bands in LaMnO3 probed by optical ellipsometry'. In: *Phys. Rev. Lett.* 93.14 (2004), p. 147204. DOI: 10.1103/PhysRevLett.93.147204 (cited on pages 62, 65).

[108] A. Yamasaki et al. 'Pressure-induced metal-insulator transition in LaMnO3 is not of mott-hubbard type'. In: *Phys. Rev. Lett.* 96.16 (Apr. 2006), p. 166401. DOI: 10.1103/PhysRevLett.96.166401 (cited on page 62).

[109] N. N. Kovaleva et al. 'Low-energy Mott-Hubbard excitations in LaMnO3 probed by optical ellipsometry'. In: *Phys. Rev. B - Condens. Matter Mater. Phys.* 81.23 (2010). DOI: 10.1103/PhysRevB.81.235130 (cited on pages 62, 65, 67).

[110] A. Nucara et al. 'Optical investigation of LaMnO 3 thin films: A study of the 2-eV band'. In: *Eur. Phys. J. B* 79.4 (2011), pp. 435–441. DOI: 10.1140/epjb/e2011-10945-0 (cited on page 62).

[111] M. Sherafati et al. 'Percolative metal-insulator transition in LaMnO3'. In: *Phys. Rev. B* 93.2 (Jan. 2016), p. 24107. DOI: 10.1103/PhysRevB.93.024107 (cited on page 62).

[112] B. Halperin and R. Englman. 'Cooperative dynamic jahn-teller effect. II. Crystal distortion in perovskites'. In: *Phys. Rev. B* 3.5 (1971), pp. 1698–1708. DOI: 10.1103/PhysRevB.3.1698 (cited on page 62).

[113] G A Gehring and K A Gehring. 'Co-operative Jahn-Teller effects'. In: *Rep. Prog. Phys.* 38.1 (1975), p. 1 (cited on page 62).

[114] A. S. Moskvin. 'Disproportionation and electronic phase separation in parent manganite LaMnO3'. In: *Phys. Rev. B - Condens. Matter Mater. Phys.* 79.11 (2009), p. 115102. DOI: 10.1103/PhysRevB.79.115102 (cited on pages 62, 80, 81).

[115] Julien Varignon, Manuel Bibes, and Alex Zunger. 'Origin of band gaps in 3d perovskite oxides'. In: *Nat. Commun.* 10.1 (2019), p. 1658. DOI: 10.1038/s41467-019-09698-6 (cited on pages 63, 80, 119).

[116] Yajun Zhang et al. 'From charge- to orbital-ordered metal-insulator transition in alkaline-earth ferrites'. In: *Phys. Rev. B* 98.8 (2018). DOI: 10.1103/PhysRevB.98.081108 (cited on pages 63, 80).

[117] Jun Hee Lee et al. 'Strong coupling of jahn-teller distortion to oxygen-octahedron rotation and functional properties in epitaxially strained orthorhombic LaMnO3'. In: *Phys. Rev. B - Condens. Matter Mater. Phys.* 88.17 (Nov. 2013), p. 174426. DOI: 10.1103/PhysRevB.88.174426 (cited on page 63).

[118] Y. S. Hou, H. J. Xiang, and X. G. Gong. 'Intrinsic insulating ferromagnetism in manganese oxide thin films'. In: *Phys. Rev. B - Condens. Matter Mater. Phys.* 89.6 (Feb. 2014), p. 64415. DOI: 10.1103/PhysRevB.89.064415 (cited on pages 63, 75, 82, 88).

[119] Woo Seok Choi et al. 'LaMnO3 Thin Films Grown by Using Pulsed Laser Deposition and Their Simple Recovery to a Stoichiometric Phase by Annealing'. In: *J. Korean Phys. Soc.* 58.3(1) (2011), pp. 569–574. DOI: 10.3938/jkps.58.569 (cited on pages 63, 81–83).

[120] Zsolt Marton et al. 'Growth control of stoichiometry in LaMnO3 epitaxial thin films by pulsed laser deposition'. In: *J. Cryst. Growth* 312.20 (2010), pp. 2923–2927. DOI: 10.1016/j.jcrysgro.2010.07.013 (cited on pages 63, 81).

[121] H. S. Kim and H. M. Christen. 'Controlling the magnetic properties of LaMnO3 thin films on SrTiO3(100) by deposition in a O2/Ar gas mixture'. In: *J. Phys. Condens. Matter* 22.14 (2010), p. 146007. DOI: 10.1088/0953-8984/22/14/146007 (cited on page 63).

[122] Jaume Roqueta et al. 'Strain-Engineered Ferromagnetism in LaMnO3 Thin Films'. In: *Cryst. Growth Des.* 15.11 (2015), pp. 5332–5337. DOI: 10.1021/acs.cgd.5b00884 (cited on pages 63, 75, 81–83).

[123] X. Renshaw Wang et al. 'Imaging and control of ferromagnetism in LaMnO3/SrTiO3 heterostructures'. In: *Science (80-.).* 349.6249 (2015), pp. 716–719. DOI: 10.1126/science.aaa5198 (cited on pages 63, 81–83).

[124] John P. Perdew et al. 'Restoring the density-gradient expansion for exchange in solids and surfaces'. In: *Phys. Rev. Lett.* 100.13 (Apr. 2008), p. 136406. DOI: 10.1103/PhysRevLett.100.136406 (cited on pages 63, 94).

[125] D. Joubert. 'From ultrasoft pseudopotentials to the projector augmented-wave method'. In: *Phys. Rev. B - Condens. Matter Mater. Phys.* 59.3 (Jan. 1999), pp. 1758–1775. DOI: 10.1103/PhysRevB.59.1758 (cited on page 63).

[126] Thomas A. Mellan et al. 'Importance of anisotropic Coulomb interaction in LaMnO3'. In: *Phys. Rev. B - Condens. Matter Mater. Phys.* 92.8 (Aug. 2015), p. 85151. DOI: 10.1103/PhysRevB.92.085151 (cited on pages 63, 65, 66).

[127] Hendrik J. Monkhorst and James D. Pack. 'Special points for Brillouin-zone integrations'. In: *Phys. Rev. B* 13.12 (June 1976), pp. 5188–5192. DOI: 10.1103/PhysRevB.13.5188 (cited on pages 63, 94, 103).

[128] Branton J. Campbell et al. 'ISODISPLACE: A web-based tool for exploring structural distortions'. In: *J. Appl. Crystallogr.* 39.4 (Aug. 2006), pp. 607–614. DOI: 10.1107/S0021889806014075 (cited on pages 64, 90, 95, 97, 110, 128, 134).

[129] Dorian M. Hatch and Harold T. Stokes. 'INVARIANTS : program for obtaining a list of invariant polynomials of the order-parameter components associated with irreducible representations of a space group '. In: *J. Appl. Crystallogr.* 36.3 (June 2003), pp. 951–952. DOI: 10.1107/s0021889803005946 (cited on pages 64, 123).

[130] Paulo V.C. Medeiros, Sven Stafström, and Jonas Björk. 'Effects of extrinsic and intrinsic perturbations on the electronic structure of graphene: Retaining an effective primitive cell band structure by band unfolding'. In: *Phys. Rev. B - Condens. Matter Mater. Phys.* 89.4 (2014), p. 41407. DOI: 10.1103/PhysRevB.89.041407 (cited on page 64).

[131] Paulo V.C. Medeiros et al. 'Unfolding spinor wave functions and expectation values of general operators: Introducing the unfolding-density operator'. In: *Phys. Rev. B - Condens. Matter Mater. Phys.* 91.4 (2015), p. 41116. DOI: 10.1103/PhysRevB.91.041116 (cited on page 64).

[132] Julien Varignon et al. 'Coupling and electrical control of structural, orbital and magnetic orders in perovskites'. In: *Sci. Rep.* 5 (Sept. 2015), pp. 15364–. DOI: 10.1038/srep15364 (cited on pages 64, 98, 105).

[133] Naihua Miao et al. 'First-principles study of the thermoelectric properties of SrRuO3'. In: *J. Phys. Chem. C* 120.17 (2016), pp. 9112–9121. DOI: 10.1021/acs.jpcc.6b02514 (cited on pages 64, 105).

[134] Naihua Miao et al. 'First-principles study of the lattice dynamical properties of strontium ruthenate'. In: *Journal of Physics: Condensed Matter* 26.3 (Dec. 2013), p. 035401. DOI: 10.1088/0953-8984/26/3/035401 (cited on pages 64, 72, 105).

[135] Jacqueline B.A.A. Elemans et al. 'The crystallographic and magnetic structures of La1-xBaxMn1-xMexO3 (Me = Mn or Ti)'. In: *J. Solid State Chem.* 3.2 (1971), pp. 238–242. DOI: 10.1016/0022-4596(71)90034-X (cited on page 67).

[136] J. Jung et al. 'Determination of electronic band structures of and using optical-conductivity analyses'. In: *Phys. Rev. B - Condens. Matter Mater. Phys.* 55.23 (June 1997), pp. 15489–15493. DOI: 10.1103/PhysRevB.55.15489 (cited on pages 65, 67).

[137] T. Saitoh et al. 'Electronic structure of La1-xSrxMnO3 studied by photoemission and x-ray-absorption spectroscopy'. In: *Phys. Rev. B* 51.20 (1995), pp. 13942–13951. DOI: 10.1103/PhysRevB.51.13942 (cited on pages 65, 67).

[138] T. Arima, Y. Tokura, and J. B. Torrance. 'Variation of optical gaps in perovskite-type 3d transition-metal oxides'. In: *Phys. Rev. B* 48.23 (1993), pp. 17006–17009. DOI: 10.1103/PhysRevB.48.17006 (cited on pages 65, 67).

[139] J. Jung et al. 'Midgap states of Doping-dependent optical-conductivity studies'. In: *Phys. Rev. B - Condens. Matter Mater. Phys.* 57.18 (1998), R11043–R11046. DOI: 10.1103/PhysRevB.57.R11043 (cited on pages 65, 67).

[140] R. Krüger et al. 'Orbital ordering in LaMnO3 investigated by resonance raman spectroscopy'. In: *Phys. Rev. Lett.* 92.9 (2004), p. 97203. DOI: 10.1103/PhysRevLett.92.097203 (cited on pages 65, 67).

[141] K. Tobe et al. 'Anisotropic optical spectra in a detwinned (formula presented) crystal'. In: *Phys. Rev. B - Condens. Matter Mater. Phys.* 64.18 (2001), p. 184421. DOI: 10.1103/PhysRevB.64.184421 (cited on pages 65, 67).

[142] D. Muñoz, N. M. Harrison, and F. Illas. 'Electronic and magnetic structure of LaMnO3 from hybrid periodic density-functional theory'. In: *Phys. Rev. B - Condens. Matter Mater. Phys.* 69.8 (Feb. 2004), p. 85115. DOI: 10.1103/PhysRevB.69.085115 (cited on page 66).

[143] Claude Ederer, Chungwei Lin, and Andrew J. Millis. 'Structural distortions and model Hamiltonian parameters: From LSDA to a tight-binding description of LaMn O3'. In: *Phys. Rev. B - Condens. Matter Mater. Phys.* 76.15 (2007), p. 155105. DOI: 10.1103/PhysRevB.76.155105 (cited on page 69).

[144] Wei Ku, Tom Berlijn, and Chi Cheng Lee. 'Unfolding first-principles band structures'. In: *Phys. Rev. Lett.* 104.21 (2010), p. 216401. DOI: 10.1103/PhysRevLett.104.216401 (cited on page 69).

[145] Roman Kováčik and Claude Ederer. 'Calculation of model Hamiltonian parameters for LaMnO3 using maximally localized Wannier functions'. In: *Phys. Rev. B - Condens. Matter Mater. Phys.* 81.24 (June 2010), p. 245108. DOI: 10.1103/PhysRevB.81.245108 (cited on page 69).

[146] Roman Kováčik and Claude Ederer. 'Effect of Hubbard U on the construction of low-energy Hamiltonians for LaMnO3 via maximally localized Wannier functions'. In: *Phys. Rev. B - Condens. Matter Mater. Phys.* 84.7 (Aug. 2011), p. 75118. DOI: 10.1103/PhysRevB.84.075118 (cited on page 69).

[147] Roman Kováčik et al. 'Combined first-principles and model Hamiltonian study of the perovskite series RMnO3 (R=La,Pr,Nd,Sm,Eu, and Gd)'. In: *Phys. Rev. B* 93.7 (Feb. 2016), p. 75139. DOI: 10.1103/PhysRevB.93.075139 (cited on page 69).

[148] K. R. Poeppelmeier et al. 'Structure determination of CaMnO3 and CaMnO2.5 by X-ray and neutron methods'. In: *J. Solid State Chem.* 45.1 (1982), pp. 71–79. DOI: 10.1016/0022-4596(82)90292-4 (cited on page 72).

[149] Nicole A. Benedek et al. 'Understanding ferroelectricity in layered perovskites: New ideas and insights from theory and experiments'. In: *Dalt. Trans.* 44.23 (2015), pp. 10543–10558. DOI: 10.1039/c5dt00010f (cited on page 72).

[150] Pablo Rivero, Vincent Meunier, and William Shelton. 'Electronic, structural, and magnetic properties of LaMnO3 phase transition at high temperature'. In: *Phys. Rev. B* 93.2 (Jan. 2016), p. 24111. DOI: 10.1103/PhysRevB.93.024111 (cited on page 75).

[151] Pablo Rivero, Vincent Meunier, and William Shelton. 'Uniaxial pressure-induced half-metallic ferromagnetic phase transition in LaMnO3'. In: *Phys. Rev. B* 93.9 (2016), p. 94409. DOI: 10.1103/PhysRevB.93.094409 (cited on page 75).

[152] A. Trokiner et al. 'Melting of the orbital order in LaMnO3 probed by NMR'. In: *Phys. Rev. B - Condens. Matter Mater. Phys.* 87.12 (2013), p. 125142. DOI: 10.1103/PhysRevB.87.125142 (cited on page 77).

[153] M. H. Whangbo et al. 'Effect of metal-oxygen covalent bonding on the competition between Jahn-Teller distortion and charge disproportionation in the perovskites of high-spin d4 metal ions LaMnO3 and CaFeO3'. In: *Inorg. Chem.* 41.7 (2002), pp. 1920–1929. DOI: 10.1021/ic0110427 (cited on pages 80, 96, 128).

[154] I. I. Mazin et al. 'Charge ordering as alternative to Jahn-Teller distortion'. In: *Phys. Rev. Lett.* 98.17 (Apr. 2007), p. 176406. DOI: 10.1103/PhysRevLett.98.176406 (cited on pages 80, 93).

[155] J. S. Zhou and J. B. Goodenough. 'Paramagnetic phase in single-crystal LaMnO3'. In: *Phys. Rev. B - Condens. Matter Mater. Phys.* 60.22 (1999), R15002–R15004. DOI: 10.1103/PhysRevB.60.R15002 (cited on page 80).

[156] Li Tong Jiang et al. 'Biaxial strain engineering of charge ordering and orbital ordering in HoNiO3'. In: *Phys. Rev. B* 97.19 (2018), p. 195132. DOI: 10.1103/PhysRevB.97.195132 (cited on pages 80, 99).

[157] Q. Huang, A. Santoro, and J. Lynn. 'Structure and magnetic order in undoped lanthanum manganite'. In: *Phys. Rev. B - Condens. Matter Mater. Phys.* 55.22 (June 1997), pp. 14987–14999. DOI: 10.1103/PhysRevB.55.14987 (cited on page 81).

[158] Harold T. Stokes and Dorian M. Hatch. 'FINDSYM: Program for identifying the space-group symmetry of a crystal'. In: *J. Appl. Crystallogr.* 38.1 (Feb. 2005), pp. 237–238. DOI: 10.1107/S0021889804031528 (cited on pages 82, 128).

[159] Olivier Copie et al. 'Chemical Strain Engineering of Magnetism in Oxide Thin Films'. In: *Adv. Mater.* 29.22 (2017). DOI: 10.1002/adma.201604112 (cited on page 83).

[160] John B. Goodenough. 'Theory of the role of covalence in the perovskite-type manganites [La,M(II)]MnO3'. In: *Phys. Rev.* 100.2 (1955), pp. 564–573. DOI: 10.1103/PhysRev.100.564 (cited on page 83).

[161] John B. Goodenough. 'An interpretation of the magnetic properties of the perovskite-type mixed crystals La1-xSrxCoO3 – λ'. In: *J. Phys. Chem. Solids* 6.2-3 (1958), pp. 287–297. DOI: 10.1016/0022-3697(58)90107-0 (cited on page 83).

[162] Junjiro Kanamori. 'Superexchange interaction and symmetry properties of electron orbitals'. In: *J. Phys. Chem. Solids* 10.2-3 (1959), pp. 87–98. DOI: 10.1016/0022-3697(59)90061-7 (cited on page 83).

[163] R. K. Zheng et al. 'Effects of substrate-induced strain on transport properties of LaMnO 3 + δ and CaMnO3 thin films using ferroelectric poling and converse piezoelectric effect'. In: *Phys. Rev. B - Condens. Matter Mater. Phys.* 81.10 (2010), p. 104427. DOI: 10.1103/PhysRevB.81.104427 (cited on page 90).

[164] R. K. Zheng et al. 'Interface strain coupling and its impact on the transport and magnetic properties of LaMnO 3 thin films grown on ferroelectrically active substrates'. In: *J. Alloys Compd.* 519 (2012), pp. 77–81. DOI: 10.1016/j.jallcom.2011.12.099 (cited on page 90).

[165] Daniel I. Khomskii. *Transition metal compounds*. Cambridge University Press, 2014, pp. 1–485 (cited on page 93).

[166] Pavlo Zubko et al. 'Interface Physics in Complex Oxide Heterostructures'. In: *Annu. Rev. Condens. Matter Phys.* 2.1 (2011), pp. 141–165. DOI: 10.1146/annurev-conmatphys-062910-140445 (cited on page 93).

[167] María Luisa Medarde. 'Structural, magnetic and electronic properties of RNiO$_3$ perovskites (R = rare earth)'. In: *J. Phys. Condens. Matter* 9.8 (1997), p. 1679 (cited on page 93).

[168] Sungbin Lee, Ru Chen, and Leon Balents. 'Landau theory of charge and spin ordering in the nickelates'. In: *Phys. Rev. Lett.* 106.1 (2011), p. 16405. DOI: 10.1103/PhysRevLett.106.016405 (cited on page 93).

[169] Hyowon Park, Andrew J. Millis, and Chris A. Marianetti. 'Site-selective Mott transition in rare-earth-element nickelates'. In: *Phys. Rev. Lett.* 109.15 (2012), p. 156402. DOI: 10.1103/PhysRevLett.109.156402 (cited on page 93).

[170] Steve Johnston et al. 'Charge disproportionation without charge transfer in the rare-earth-element nickelates as a possible mechanism for the metal-insulator transition'. In: *Phys. Rev. Lett.* 112.10 (2014), p. 106404. DOI: 10.1103/PhysRevLett.112.106404 (cited on page 93).

[171] Julien Varignon et al. 'Complete phase diagram of rare-earth nickelates from first-principles'. In: *npj Quantum Mater.* 2.1 (2017), pp. 21–. DOI: 10.1038/s41535-017-0024-9 (cited on page 93).

[172] T. Kimura et al. 'Distorted perovskite with eg1 configuration as a frustrated spin system'. In: *Phys. Rev. B - Condens. Matter Mater. Phys.* 68.6 (Aug. 2003), p. 60403. DOI: 10.1103/PhysRevB.68.060403 (cited on page 93).

[173] J. B. MacChesney, R. C. Sherwood, and J. F. Potter. 'Electric and magnetic properties of the strontium ferrates'. In: *J. Chem. Phys.* 43.6 (1965), pp. 1907–1913. DOI: 10.1063/1.1697052 (cited on pages 93, 96).

[174] Shuji Kawasaki et al. 'Phase Transitions in Fe4+ (3d4)-Perovskite Oxides Dominated by Oxygen-Hole Character'. In: *J. Phys. Soc. Japan* 67.5 (1998), pp. 1529–1532. DOI: 10.1143/JPSJ.67.1529 (cited on page 93).

[175] P. Woodward, D. Cox, and E. Moshopoulou. 'Structural studies of charge disproportionation and magnetic order in $CaFeO_3$'. In: *Phys. Rev. B - Condens. Matter Mater. Phys.* 62.2 (July 2000), pp. 844–855. DOI: 10.1103/PhysRevB.62.844 (cited on pages 93, 127, 128).

[176] T. Akao et al. 'Charge-Ordered State in Single-Crystalline CaFeO3 Thin Film Studied by X-Ray Anomalous Diffraction'. In: *Phys. Rev. Lett.* 91.15 (2003), pp. 1564051–1564054. DOI: 10.1103/physrevlett.91.156405 (cited on page 93).

[177] J. Matsuno et al. 'Different routes to charge disproportionation in perovskite-type Fe oxides'. In: *Phys. Rev. B - Condens. Matter Mater. Phys.* 66.19 (Nov. 2002), pp. 1–4. DOI: 10.1103/PhysRevB.66.193103 (cited on page 93).

[178] Shankar Ghosh et al. 'Raman scattering in CaFeO3 and La0.33Sr0.67FeO3 across the charge-disproportionation phase transition'. In: *Phys. Rev. B - Condens. Matter Mater. Phys.* 71.24 (June 2005), p. 245110. DOI: 10.1103/PhysRevB.71.245110 (cited on page 93).

[179] Antonio Cammarata and James M. Rondinelli. 'Spin-assisted covalent bond mechanism in "charge-ordering" perovskite oxides'. In: *Phys. Rev. B - Condens. Matter Mater. Phys.* 86.19 (Nov. 2012), p. 195144. DOI: 10.1103/PhysRevB.86.195144 (cited on pages 93, 128).

[180] Paul C. Rogge et al. 'Electronic structure of negative charge transfer CaFeO3 across the metal-insulator transition'. In: *Phys. Rev. Mater.* 2.1 (Jan. 2018), p. 15002. DOI: 10.1103/PhysRevMaterials.2.015002 (cited on pages 94, 97).

[181] G Kresse and J Hafner. 'Ab initio'. In: *Phys. Rev. B* 47.1 (Jan. 1993), pp. 558–561. DOI: 10.1103/PhysRevB.47.558 (cited on page 94).

[182] J. Holakovský. 'A New Type of the Ferroelectric Phase Transition'. In: *Phys. Status Solidi* 56.2 (1973), pp. 615–619. DOI: 10.1002/pssb.2220560224 (cited on page 95).

[183] Takashi Takeda et al. 'Metal-semiconductor transition, charge disproportionation, and low-temperature structure of Ca(1-x)Sr(x)FeO3 synthesized under high-oxygen pressure'. In: *Solid State Sci.* 2.7 (2000), pp. 673–687. DOI: 10.1016/S1293-2558(00)01088-8 (cited on page 96).

[184] Imene Cherair et al. 'First-principles study of strain-induced Jahn–Teller distortions in BaFeO3'. In: *Journal of Physics: Condensed Matter* 30.25 (May 2018), p. 255701. DOI: 10.1088/1361-648x/aac46d.

[185] Wei Guo Yin, Dmitri Volja, and Wei Ku. 'Orbital ordering in LaMnO3: Electron-electron versus electron-lattice interactions'. In: *Phys. Rev. Lett.* 96.11 (2006), p. 116405. DOI: 10.1103/PhysRevLett.96.116405 (cited on page 99).

[186] Roushown Ali and Masatomo Yashima. 'Space group and crystal structure of the Perovskite CaTiO3 from 296 to 1720 K'. In: *J. Solid State Chem.* 178.9 (2005), pp. 2867–2872. DOI: 10.1016/j.jssc.2005.06.027 (cited on pages 101, 114).

[187] V.V. Lemanov et al. 'Perovskite CaTiO3 as an incipient ferroelectric'. In: *Solid State Communications* 110.11 (1999), pp. 611–614. DOI: https://doi.org/10.1016/S0038-1098(99)00153-2 (cited on page 101).

[188] V. Železný et al. 'Soft-Mode Behavior of Incipient Ferroelectric Perovskite CaTiO 3'. In: *Ferroelectrics* 272.1 (2002), pp. 113–118. DOI: 10.1080/713716295 (cited on page 101).

[189] Liliana Goncalves-Ferreira et al. 'Ferrielectric Twin Walls in $CaTiO_3$'. In: *Phys. Rev. Lett.* 101 (9 Aug. 2008), p. 097602. DOI: 10.1103/PhysRevLett.101.097602 (cited on page 101).

[190] Paolo Barone, Domenico Di Sante, and Silvia Picozzi. 'Improper origin of polar displacements at $CaTiO_3$ and $CaMnO_3$ twin walls'. In: *Phys. Rev. B* 89 (14 Apr. 2014), p. 144104. DOI: 10.1103/PhysRevB.89.144104 (cited on page 101).

[191] Sandra Van Aert et al. 'Direct Observation of Ferrielectricity at Ferroelastic Domain Boundaries in CaTiO3 by Electron Microscopy'. In: *Advanced Materials* 24.4 (2012), pp. 523–527. DOI: 10.1002/adma.201103717 (cited on page 101).

[192] Bjarni Gautason and Karlis Muehlenbachs. 'Oxygen Diffusion in Perovskite: Implications for Electrical Conductivity in the Lower Mantle'. In: *Science* 260.5107 (1993), pp. 518–521. DOI: 10.1126/science.260.5107.518 (cited on page 101).

[193] H. F. Kay and P. C. Bailey. 'Structure and properties of CaTiO3'. In: *Acta Crystallogr.* 10.3 (1957), pp. 219–226. DOI: 10.1107/s0365110x57000675 (cited on pages 101, 114).

[194] Yanbin Wang and Robert C. Liebermann. 'Electron microscopy study of domain structure due to phase transitions in natural perovskite'. In: *Physics and Chemistry of Minerals* 20.3 (Aug. 1993), pp. 147–158 (cited on pages 101, 114).

[195] F. Guyot et al. 'High-temperature heat capacity and phase transitions of CaTiO3 perovskite'. In: *Physics and Chemistry of Minerals* 20.3 (Aug. 1993), pp. 141–146 (cited on pages 101, 114).

[196] T Vogt and W. W Schmahl. 'The High-Temperature Phase Transition in Perovskite'. In: *Europhysics Letters (EPL)* 24.4 (Nov. 1993), pp. 281–285. DOI: 10.1209/0295-5075/24/4/008 (cited on pages 101, 114).

[197] Simon A.T. Redfern. 'High-temperature structural phase transitions in perovskite (CaTiO3)'. In: *J. Phys. Condens. Matter* 8.43 (1996), pp. 8267–8275. DOI: 10.1088/0953-8984/8/43/019 (cited on pages 101, 114).

[198] Brendan J Kennedy, Christopher J Howard, and Bryan C Chakoumakos. 'Phase transitions in perovskite at elevated temperatures - a powder neutron diffraction study'. In: *J. Phys. Condens. Matter* 11.6 (1999), pp. 1479–1488. DOI: 10.1088/0953-8984/11/6/012 (cited on pages 101, 114).

[199] Masatomo Yashima and Roushown Ali. 'Structural phase transition and octahedral tilting in the calcium titanate perovskite CaTiO3'. In: *Solid State Ionics* 180.2-3 (2009), pp. 120–126. DOI: 10.1016/j.ssi.2008.11.019 (cited on pages 101, 111–114).

[200] Yijia Gu et al. 'Phenomenological thermodynamic potential for CaTiO 3 single crystals'. In: *Phys. Rev. B - Condens. Matter Mater. Phys.* 85.6 (2012), p. 64117. DOI: 10.1103/PhysRevB.85.064117 (cited on pages 101, 102, 114).

[201] Michael A. Carpenter. 'Elastic anomalies accompanying phase transitions in (Ca,Sr)TiO3 perovskites: Part I. Landau theory and a calibration for SrTiO3'. In: *American Mineralogist* 92.2-3 (Feb. 2007), pp. 309–327. DOI: 10.2138/am.2007.2295 (cited on pages 101, 113, 114).

[202] Nicole A. Benedek and Craig J. Fennie. 'Why Are There So Few Perovskite Ferroelectrics?' In: *J. Phys. Chem. C* 117.26 (July 2013), pp. 13339–13349. DOI: 10.1021/jp402046t (cited on pages 102, 105).

[203] C. J. Eklund, C. J. Fennie, and K. M. Rabe. 'Strain-induced ferroelectricity in orthorhombic CaTiO3 from first principles'. In: *Phys. Rev. B - Condens. Matter Mater. Phys.* 79.22 (2009), p. 220101. DOI: 10.1103/PhysRevB.79.220101 (cited on pages 102, 114, 135).

[204] Qibin Zhou and Karin M. Rabe. *Strain-Induced Hybrid Improper Ferroelectricity in Simple Perovskites from First Principles*. Aug. 25, 2013. URL: https://arxiv.org/abs/1306.1839 (cited on pages 102, 114).

[205] Michael D. Biegalski et al. 'Impact of symmetry on the ferroelectric properties of CaTiO3 thin films'. In: *Appl. Phys. Lett.* 106.16 (2015), p. 162904. DOI: 10.1063/1.4918805 (cited on page 102).

[206] Ryan C. Haislmaier et al. 'Large tetragonality and room temperature ferroelectricity in compressively strained CaTiO3 thin films'. In: *APL Materials* 7.5 (2019), p. 051104. DOI: 10.1063/1.5090798 (cited on page 102).

[207] X. Gonze et al. 'First-principles computation of material properties: the ABINIT software project'. In: *Computational Materials Science* 25.3 (2002), pp. 478–492. DOI: https://doi.org/10.1016/S0927-0256(02)00325-7 (cited on page 103).

[208] X. Gonze et al. 'ABINIT: First-principles approach to material and nanosystem properties'. In: *Computer Physics Communications* 180.12 (2009). 40 YEARS OF CPC: A celebratory issue focused on quality software for high performance, grid and novel computing architectures, pp. 2582–2615. DOI: https://doi.org/10.1016/j.cpc.2009.07.007 (cited on page 103).

[209] X. Gonze et al. 'Recent developments in the ABINIT software package'. In: *Comput. Phys. Commun.* 205 (2016), pp. 106–131. DOI: 10.1016/j.cpc.2016.04.003 (cited on page 103).

[210] Zhigang Wu and R. E. Cohen. 'More accurate generalized gradient approximation for solids'. In: *Phys. Rev. B - Condens. Matter Mater. Phys.* 73.23 (June 2006), p. 235116. DOI: 10.1103/PhysRevB.73.235116 (cited on page 103).

[211] Danila Amoroso, Andrés Cano, and Philippe Ghosez. 'First-principles study of (Ba, Ca)TiO_3 and Ba(Ti, Zr)O_3 solid solutions'. In: *Phys. Rev. B* 97 (17 May 2018), p. 174108. DOI: 10.1103/PhysRevB.97.174108 (cited on pages 103, 109).

[212] A Togo and I Tanaka. 'First principles phonon calculations in materials science'. In: *Scr. Mater.* 108 (Nov. 2015), pp. 1–5 (cited on page 103).

[213] Kevin S. Knight. 'Structural and thermoelastic properties of CaTiO3 perovskite between 7K and 400K'. In: *Journal of Alloys and Compounds* 509.22 (2011), pp. 6337–6345. DOI: https://doi.org/10.1016/j.jallcom.2011.03.014 (cited on page 110).

[214] Julien Varignon, Manuel Bibes, and Alex Zunger. 'Mott gapping in 3*d* ABO_3 perovskites without Mott-Hubbard interelectronic repulsion energy U'. In: *Phys. Rev. B* 100 (3 July 2019), p. 035119. DOI: 10.1103/PhysRevB.100.035119 (cited on page 119).

[215] Zhi Wang et al. *Mass enhancement in 3d and s-p perovskites from symmetry breaking*. 2020 (cited on page 119).

[216] Fredrik Eriksson, Erik Fransson, and Paul Erhart. 'The Hiphive Package for the Extraction of High-Order Force Constants by Machine Learning'. In: *Advanced Theory and Simulations* 2.5 (2019), p. 1800184. DOI: 10.1002/adts.201800184 (cited on page 120).

[217] Albert P. Bartók et al. 'Gaussian Approximation Potentials: The Accuracy of Quantum Mechanics, without the Electrons'. In: *Phys. Rev. Lett.* 104 (13 Apr. 2010), p. 136403. DOI: 10.1103/PhysRevLett.104.136403 (cited on page 120).

[218] Wojciech J. Szlachta, Albert P. Bartók, and Gábor Csányi. 'Accuracy and transferability of Gaussian approximation potential models for tungsten'. In: *Phys. Rev. B* 90 (10 Sept. 2014), p. 104108. DOI: 10.1103/PhysRevB.90.104108 (cited on page 120).

[219] Ryosuke Jinnouchi, Ferenc Karsai, and Georg Kresse. 'On-the-fly machine learning force field generation: Application to melting points'. In: *Phys. Rev. B* 100 (1 July 2019), p. 014105. DOI: 10.1103/PhysRevB.100.014105 (cited on page 120).

[220] Ryosuke Jinnouchi et al. 'Phase Transitions of Hybrid Perovskites Simulated by Machine-Learning Force Fields Trained on the Fly with Bayesian Inference'. In: *Phys. Rev. Lett.* 122 (22 June 2019), p. 225701. DOI: 10.1103/PhysRevLett.122.225701 (cited on page 120).

[221] Ryosuke Jinnouchi, Ferenc Karsai, and Georg Kresse. 'Making free-energy calculations routine: Combining first principles with machine learning'. In: *Phys. Rev. B* 101 (6 Feb. 2020), p. 060201. DOI: 10.1103/PhysRevB.101.060201 (cited on page 120).

[222] Gianluca Giovannetti et al. 'Multiferroicity in Rare-Earth Nickelates $R\mathrm{NiO}_3$'. In: *Phys. Rev. Lett.* 103 (15 Oct. 2009), p. 156401. DOI: 10.1103/PhysRevLett.103.156401 (cited on page 127).

[223] H. H. Wieder. 'Electrical Behavior of Barium Titanatge Single Crystals at Low Temperatures'. In: *Phys. Rev.* 99 (4 Aug. 1955), pp. 1161–1165. DOI: 10.1103/PhysRev.99.1161 (cited on page 134).

[224] A. Mahmoud et al. 'Low-temperature phase of BaTiO 3: Piezoelectric, dielectric, elastic, and photoelastic properties from ab initio simulations'. In: *Phys. Rev. B - Condens. Matter Mater. Phys.* 89.4 (Jan. 2014), p. 45103. DOI: 10.1103/PhysRevB.89.045103 (cited on page 134).

[225] P. M. Woodward. 'Octahedral Tilting in Perovskites. II. Structure Stabilizing Forces'. In: *Acta Crystallographica Section B* 53.1 (Feb. 1997), pp. 44–66. DOI: 10.1107/S0108768196012050 (cited on page 135).

[226] W.T. Fu, D. Visser, and D.J.W. IJdo. 'On the Crystal Structure of BaTbO3'. In: *Journal of Solid State Chemistry* 165.2 (2002), pp. 393–396. DOI: https://doi.org/10.1006/jssc.2002.9566 (cited on page 135).

[227] S. J. May et al. 'Quantifying octahedral rotations in strained perovskite oxide films'. In: *Phys. Rev. B - Condens. Matter Mater. Phys.* 82.1 (July 2010), p. 14110. DOI: 10.1103/PhysRevB.82.014110 (cited on page 135).

[228] Xin Wan. 'Growth and characterization of CaTiO3 thin films with (111) orientation'. MA thesis. University of Twente, Apr. 3, 2008 (cited on page 135).

[229] S. Catalano et al. 'Tailoring the electronic transitions of NdNiO3 films through (111)pc oriented interfaces'. In: *APL Materials* 3.6 (2015), p. 062506. DOI: 10.1063/1.4919803 (cited on page 135).

List of Figures

List of Tables